Projector Quantum Monte Carlo Methods for Linear and Non-linear Wavefunction Ansatzes

Lauretta Rebecca Schwarz

Trinity Hall
University of Cambridge

This dissertation is submitted for the degree of
Doctor of Philosophy
at the University of Cambridge

October 2017

Projector Quantum Monte Carlo Methods for Linear and Non-linear Wavefunction Ansatzes

Lauretta Rebecca Schwarz

Abstract

This thesis is concerned with the development of a Projector Quantum Monte Carlo method for non-linear wavefunction ansatzes and its application to strongly correlated materials. This new approach is partially inspired by a prior application of the Full Configuration Interaction Quantum Monte Carlo (FCIQMC) method to the three-band ($p-d$) Hubbard model. Through repeated stochastic application of a projector FCIQMC projects out a stochastic description of the Full Configuration Interaction (FCI) ground state wavefunction, a linear combination of Slater determinants spanning the full Hilbert space. The study of the $p-d$ Hubbard model demonstrates that the nature of this FCI expansion is profoundly affected by the choice of single-particle basis. In a counterintuitive manner, the effectiveness of a one-particle basis to produce a sparse, compact and rapidly converging FCI expansion is not necessarily paralleled by its ability to describe the physics of the system within a single determinant. The results suggest that with an appropriate basis, single-reference quantum chemical approaches may be able to describe many-body wavefunctions of strongly correlated materials.

Furthermore, this thesis presents a reformulation of the projected imaginary time evolution of FCIQMC as a Lagrangian minimisation. This naturally allows for the optimisation of polynomial complex wavefunction ansatzes with a polynomial rather than exponential scaling with system size. The proposed approach blurs the line between traditional Variational and Projector Quantum Monte Carlo approaches whilst involving developments from the field of deep-learning neural networks which can be expressed as a modification of the projector. The ability of the developed approach to sample and optimise arbitrary non-linear wavefunctions is demonstrated with several classes of Tensor Network States all of which involve controlled approximations but still retain systematic improvability towards exactness. Thus, by applying the method to strongly-correlated Hubbard models, as well as *ab-initio* systems, including a fully periodic *ab-initio* graphene sheet, many-body wavefunctions and their one- and two-body static properties are obtained. The proposed approach can handle and simultaneously optimise large numbers of variational parameters, greatly exceeding those of alternative Variational Monte Carlo approaches.

For my parents

Preface

This dissertation contains an account of research carried out in the period between October 2013 and July 2017 in the Theoretical Sector of the Department of Chemistry in the University of Cambridge under the supervision of Prof. Ali Alavi, F.R.S. The following sections of this thesis are included in work which has either been published or is to be published:

Chapter 4 : L. R. Schwarz, G. H. Booth and A. Alavi, *Insights into the structure of many-electron wave functions of Mott-insulating antiferromagnets: The three-band Hubbard model in full configuration interaction quantum Monte Carlo*, Physical Review B, 91, 045139 (2015)

Chapter 5 and 6 : L. R. Schwarz, A. Alavi and G. H. Booth, *Projector Quantum Monte Carlo Method for Nonlinear Wave Functions*, Physical Review Letters, 118, 176403 (2017)

Chapter 7 : In preparation.

This dissertation is the result of my own work and includes nothing which is the outcome of work done in collaboration except where indicated otherwise. This thesis is not substantially the same as any that I have submitted, or, is being concurrently submitted for a degree or diploma or other qualification at the University of Cambridge or any other University or similar institution. I further state that no substantial part of my thesis has already been submitted, or, is being concurrently submitted for any such degree, diploma or other qualification at the University of Cambridge or any other University or similar institution. This dissertation does not exceed $60,000$ words in length, including abstract, tables, and footnotes, but excluding table of contents, photographs, diagrams, figure captions, list of figures, list of abbreviations, bibliography, appendices and acknowledgements.

Lauretta Rebecca Schwarz
October 2017

Acknowledgements

First, I would like to thank my supervisor, Ali Alavi, for all of his many ideas and enthusiasm. I am very grateful for the continual support that he provided, whilst giving me the space to explore my own ideas and creating an inspiring atmosphere to work in. The many inspiring discussions with him and his wide knowledge have been invaluable, and I appreciate all that he has done.

Another person whom I cannot thank enough is George Booth. The huge amount of knowledge and advice that he has passed on to me has been invaluable. I am grateful not only for proof-reading this thesis and the many helpful discussions, but also for his guidance and support. I would also like to thank Charlie Scott for proof-reading parts of this thesis and Robert Thomas for many inspiring discussions, as well as the past and present members of the Alavi group for creating such a pleasant environment to work in.

Moreover, it is a pleasure to acknowledge the Engineering and Physical Sciences Research Council for funding this work, and the Max Planck Society for the provision of high-performing computing facilities.

Last but not least, I would like to thank my parents for their loving support which means so much to me. Their love and encouragement has continually accompanied and helped me on my way.

Table of contents

List of figures **xv**

List of tables **xvii**

1 Introduction **1**

2 Theoretical Background **9**

2.1 Introduction 9

2.2 An Alternative Formalism: Second Quantisation 13

2.2.1 The Fock Space 13

2.2.2 Elementary Operators 15

2.3 Hartree-Fock Theory 18

2.4 Electron Correlation 22

2.5 Full Configuration Interaction 25

2.6 Further Approximate Solution Methods 28

2.7 Beyond Traditional Quantum Chemical Methods: Tensor Network States Approaches 33

2.7.1 Entanglement Entropy and Area Laws 33

2.7.2 Decomposing the FCI Wavefunction Ansatz 34

2.7.3 Tensor Network States in One Dimension: Matrix Product States 35

2.7.4 The Area Law and Efficient Approximability 38

2.7.5 Tensor Network States in Two Dimensions: Projected Entangled Pair States 41

2.7.6 Optimisation of MPS, PEPS, ... 43

3 Zero-temperature Ground State Quantum Monte Carlo Methods **47**

3.1 Variational Quantum Monte Carlo Approaches 47

3.2 Projector Quantum Monte Carlo Approaches 51

3.3 Full Configuration Interaction Quantum Monte Carlo: FCIQMC 55

3.3.1 Derivation of FCIQMC Equations 56
3.3.2 Stochastic Implementation of FCIQMC 60
3.3.3 Energy Estimators 62
3.3.4 The Fermion Sign Problem and the Importance of Annihilation 63
3.3.5 The Initiator Approximation 66
3.3.6 Non-integer Real-weight Walkers 71
3.3.7 The Semi-stochastic Adaptation 72
3.4 Handling Stochastic Estimators 73

4 Application of i-FCIQMC to Strongly Correlated Systems 75
4.1 Model Hamiltonians 76
4.1.1 The Hubbard Model 76
4.1.2 The three-band $(p-d)$ Hubbard Model 78
4.2 Geometries and Cluster Size 83
4.3 The three-band Hubbard Model in FCIQMC 83
4.3.1 The Choice of Single-Particle Basis Sets 84
4.3.2 An i-FCIQMC Study of the Many-Body Ground State Wavefunctions 86
4.3.3 Orbital Occupation Numbers and Correlation Entropy 90
4.3.4 Subspace Diagonalisations and CI Expansions 93
4.3.5 Conclusions 95

5 A Projector Quantum Monte Carlo Method for Non-linear Wavefunctions 97
5.1 Non-linear Projector Quantum Monte Carlo Method: Combining Variational and Projector Quantum Monte Carlo 99
5.2 Derivation: Lagrangian Minimisation 99
5.3 Sampling of the Lagrangian Gradient 101
5.4 Momentum Methods: Nesterov's Accelerated Gradient Descent 111
5.5 Matrix Polynomials - Closing a Circle of Connections 114
5.6 Step Size Adaptation: RMSprop 118
5.7 Wavefunction Properties 119
5.8 A Technical Point: Wavefunction Normalisation, Step Sizes and Parameter Updates 124
5.9 Comparison to State-of-the-art VMC Methods 125

6 Applications of the Projector Quantum Monte Carlo Method for Non-linear Wavefunctions to Correlator Product State Wavefunctions 127

6.1 The Correlator Product State Wavefunction Ansatz 129
6.2 Wavefunction Amplitudes and Derivatives 131
6.3 2D Hubbard Model 132
6.4 1D Hubbard Model 136
6.5 Linear H_{50} Chain 141
6.6 Graphene Sheet 143
6.7 Conclusions 147

7 Projector Quantum Monte Carlo Method for Tensor Network States 149

7.1 The Computational Challenge of PEPS Wavefunctions - Can It Be Tackled Stochastically ? 151
7.2 The PEPS and MPS Wavefunctions Ansatz 152
7.3 Wavefunctions Amplitudes and Derivatives 154
7.4 A Sampling Approach for Wavefunction Amplitudes and Derivatives . . 155
7.5 Investigation of TNS Projection Sampling Approach 158
7.6 Applications for MPS and PEPS Wavefunctions 165
7.7 Conclusions 169

8 Concluding Remarks and Continuing Directions 171

Appendix A Comparison of Lagrangian and Ritz Functional Derivatives 177

References 179

List of figures

2.1 Excitation level classification of configurations 27
2.2 Construction of MPS 36
2.3 Construction of PEPS 40

3.1 An example FCIQMC calculation 65
3.2 A comparison of FCIQMC and i-FCIQMC simulations 68
3.3 Convergence of initiator error 70

4.1 Phase conventions for three-band $(p-d)$ Hubbard model 80
4.2 Clusters on $2D$ square lattice 83
4.3 Convergence of ground state energy for three-band Hubbard model with total walker number in i-FCIQMC 86
4.4 Spin-spin correlation function from i-FCIQMC ground state wavefunction of three-band $(p-d)$ Hubbard model 88
4.5 Restricted and unrestricted Hartree-Fock band structures and density of states for three-band Hubbard model 89
4.6 Orbital occupation numbers and mean-field orbital energies for different single-particle basis sets 90
4.7 Illustration of selected RHF and UHF spin orbitals for three-band $(p-d)$ Hubbard model 91
4.8 Magnitude of coefficients in FCI expansion with respect to determinant energy for four different basis sets 94

5.1 Comparison of momentum methods 113
5.2 Comparison of projections 118

6.1 Illustration of correlators 133
6.2 Convergence of CPS wavefunction for $2D$ Hubbard model 135
6.3 Convergence of energy of CPS wavefunctions for $1D$ Hubbard model . . 137

6.4 Percentage of DMRG correlation energy captured by CPS wavefunction for symmetric dissociation of H_{50} 143
6.5 Illustration of correlators and CPS wavefunction for graphene sheet . . 144
6.6 Spin correlation functions for graphene sheet 146

7.1 Illustration of a PEPS network 152
7.2 Convergence of stochastic energy estimates with number of samples . . 160
7.3 Convergence of stochastic energy estimates with number of samples for auxiliary and physical indices 163
7.4 Convergence of ground state energy for $1D$ 1×10 Hubbard model . . . 165

List of tables

2.1 Slater-Condon rules 28

3.1 Summary of most commonly used PMC methods 52

4.1 Parameters for three-band Hubbard model 79
4.2 Properties of ground state wavefunctions for three-band Hubbard model 87

6.1 Ground state energies for $2D$ Hubbard model 134
6.2 Ground state energies and RDM properties for $1D$ Hubbard model . . 140
6.3 Symmetric dissociation of H_{50} 142
6.4 Energies and RDM properties for 4×4 graphene sheet 145

7.1 Ground state energies for $1D$ 1×10, 1×14 and 1×22 Hubbard model 166
7.2 Ground state energy for $2D$ 4×4 Hubbard model 169

Chapter 1

Introduction

It was not until the unexpected discovery of high-temperature superconductivity in cuprates by J. G. Bednorz and K. A. Müller in 1986[1, 2] that the field of strongly correlated electrons received the attention that it deserves. Soon after their discovery, it became clear that in order to understand the normal state properties of these materials and, in particular, the phenomenon of superconductivity deeper insight into the strong correlations that prevail in these systems is required[3–5].

In strongly correlated materials different physical interactions involving spins, charges, orbitals and the lattice of the system are strongly coupled to each other and give rise to a variety of electronic phases[6–8] which are typically close energy, thereby leading to complex phase diagrams. The cooperation, competition, or a combination of both, amongst these correlated electronic phases can result in unexpected electronic phenomena and non-linear responses to external fields as these systems are very sensitive to small changes in their surroundings, an observation that has been made in many experimental studies and numerous investigations of model systems[9–11]. This rich variety of phenomena resulting from strong correlation effects includes not only the high temperature superconductivity in layered copper oxides and iron pnictides, but also colossal magneto-resistance effects in manganese oxide, as well as heavy fermion phenomena in lanthanide and actinide intermetallic compounds, to name just a few[12, 13]. Typically, strongly correlated systems comprise materials in which transition metals, lanthanides or actinides with partially filled d- or f-shells play an active role. On the one hand, these electrons in open d- or f-shell are spatially localised and thus display atomic-like behaviour. On the other hand, they also participate in chemical bonding to differing extends and can act in a band-like fashion in some cases. As a consequence, they are located in an intermediate regime between localised and delocalised electrons[13] and it is this competition between localisation and delocalisation, that is between kinetic energy and electron-electron interaction, which lies at the heart of the strong correlation problem[14] and gives rise to the new low-energy scales generated by strong correlations[3]. Usually, many of these strongly correlated materials consist of simple components such as transition metal oxides which often adopt the perovskite structure whereby a transition metal ion is surrounded by an octahedral oxygen cage. Yet, when these simple building blocks are brought together they interact in a highly complex manner such that their collective behaviour is difficult to predict a priori based on their individual properties. The strong correlations prevailing in these systems imply that the collective states cannot be understood based on a one-electron (or even one-quasiparticle) approximation. The latter are therefore of no use and more sophisticated approaches are needed to gain insight and rationalise the intriguing electronic phenomena and non-linear responses that emerge in these materials. Potentially, this behaviour can also form the basis for the design and development of novel types of electronics with new functionalities for which purpose understanding, controlling and predicting the emergent complexity of strongly correlated electron systems is essential. Examples of these potential applications include the surface and catalytic properties of transition metal and rare earth oxides[15], molecular magnetic materials[16] and cathode materials of lithium batteries[17].

On the theory side, the foundations of quantum mechanics were established during the first half of the twentieth century. In 1926, Erwin Schrödinger rederived Bohr's semi-classical energy spectrum for hydrogen-like atoms within a quantum mechanical framework[18] and concluded that each eigenstate can be uniquely labelled by three quantum numbers. In order to explain spectra of more complicated atoms, Pauli introduced a fourth degree of freedom and stated that no two electrons can share the same four quantum numbers[19], a principle which is known as Pauli's exclusion principle today. Whilst Uhlenbeck and Goudsmit identified this fourth quantum number as the spin projection of the electron[20], Heisenberg introduced quantum mechanical treatments of many-body problems[21]. These and many other contributions and advances of quantum mechanics lay the foundations for the development of electronic structure theory. More generally, for any physical system, the Schrödinger equation[22] defines the allowed states of the system and their evolution in time and solving it leads to the wavefunction which in the Copenhagen interpretation of quantum mechanics represents the most complete description of a physical system. Yet, it was soon realised that this would only be the beginning of the problem, as Paul Dirac said in 1929[23]:

> *The general theory of quantum mechanics is now almost complete, the imperfections that still remain being in connection with the exact fitting*

> *in of the theory with relativity ideas. These give rise to difficulties only when high-speed particles are involved, and are therefore of no importance in the consideration of atomic an molecular structure and ordinary chemical reactions, in which it is, indeed, usually sufficiently accurate if one neglects relativity variation of mass with velocity and assumes only Coulomb forces between the various electrons and atomic nuclei. The underlying physical laws necessary for the mathematical theory of a large part of physics and the whole of chemistry are thus completely known, and the difficulty is only that the exact application of these laws leads to equations much too complicated to be soluble. It therefore becomes desirable that approximate practical methods of applying quantum mechanics should be developed, which can lead to an explanation of the main features of complex atomic systems without too much computation.*

Nevertheless exact or approximate solutions to the corresponding equations are crucial for understanding the collective behaviour of interacting elementary particles and the variety of complex phenomena emerging from this. Electronic structure theory is therefore concerned with the development of theories which attempt to find approximate solutions to the underlying exact equations, with varying degrees of accuracy and associated computational cost. Over the last century, this has resulted in a huge array of methods with different levels of approximations to balance the competing demands of accuracy and tractable computational cost. In the realm of strongly correlated electrons, developments of various electronic structure approaches have concentrated on methods which require no assumption of the explicit form of the full many-body wavefunction since it represents a computationally expensive object.

Thus, *ab-initio* electronic structure calculations are dominated by density functional theory (DFT)[24] which is, however, a ground state theory and therefore fails, often qualitatively. In particular, this is the case for strongly-correlated systems where low-energy excitations need to be taken into account appropriately. This failure is inherent and independent of any approximations that are involved in the potential of the Kohn-Sham equation[3]. An example for such a failure is the local density approximation (LDA)[25] within DFT which despite its success for conventional metallic systems is inadequate for strongly correlated systems since it assumes the potential of the Kohn-Sham equations to be determined by the local density. This assumption breaks down when the latter has a strong spatial dependence as it is the case in strongly correlated materials with their strongly fluctuating charge and spin degrees of freedom[3, 9]. Qualitative failures of LDA are widely observed for the Mott insulating phase of many transition metal compounds, as well as for phases of correlated metals near the Mott insulator. Examples of the inability of LDA to reproduce an insulating (or semiconducting) phase include La_2CuO_4, $YBa_2Cu_3O_6$, NiS, NiO and MnO[9, 26, 27]. Nonetheless, semi-empirical methods have had some successes like the renormalised band-structure method[28]. Several approaches have also been proposed to incorporate strong correlation in the LDA method such as LDA+U[29] and LDA-SIC[30]. In contrast to LDA, both methods yield a correct antiferromagnetic insulator as ground state for La_2CuO_4, but the origin of the insulating gap is not correct. Being a ground state method, DFT is not guaranteed to reproduce excitations well which are, however, often crucial for the properties of strongly correlated systems and many cases exist where DFT calculations involving standard approximations lead to unacceptable errors. For example, excitation energies between different states of transition metal, as well as rare earth and lanthanide atoms are often predicted poorly, differing from measured values by about 2 eV[3]. Another method applied to strongly correlated electron systems is the hybrid LDA+DMFT (Dynamical Mean Field Theory) method[31]. In this approach, the electron self-energy is calculated by DMFT theory in the limit of infinite dimension and is **k**-independent[10] which is why the LDA+DMFT approach provides no viable route to the correct band dispersion. Extensions of the original DMFT method to cluster DMFT[32] go into the right direction, but the clusters that can be treated are relatively small.

Since reliable *ab-initio* methods for strongly correlated methods are still at their beginning, another widely used theoretical approach is based on simplifying model Hamiltonians which seem to better capture the essence and unravel the physical effects of correlated systems. The one most studied is the Hubbard Hamiltonian[33, 9], which describes the dynamics of electrons on a lattice whereby each lattice site can at most accommodate two electrons of opposite spin in its associated orbitals. The complexity of a full Hamiltonian for this system is thus reduced down to only two parameters: a kinetic energy term t which represents the hopping of electrons between nearest-neighbour lattice sites and an on-site Coulomb repulsion term U which accounts for the repulsion between electrons that reside on the same lattice site. The simplifications introduced by this ansatz compared to an *ab-initio* Hamiltonian are enormous. Nevertheless, important insight can be gained by studying Hubbard model systems, in particular at or close to half filling. A variety of techniques have been applied for the study of Hubbard systems with emphasis on two dimensions ($2D$). The reason for this is that the $2D$ Hubbard model is claimed to possess all the relevant physics for high-T_C superconductivity. Despite the simplicity of the model Hamiltonian, the latter is still very difficult to solve accurately and many questions still remain unanswered. An example for this is the much studied Mott-Hubbard metal-to-insulator phase transition at half filling when $U >> t$ for which it is not known at which critical ratio of $\frac{U}{t}$ this phase transition occurs at $T = 0$[34]. For a slightly more realistic picture, the Hubbard model Hamiltonians can also be refined by addition of further orbitals and parameters. This leads for example to the three-band or five-band Hubbard model which act as model for Cu$-$O planes in high-T_C cuprates. Hybrid approaches have also been developed in which LDA is used to construct Wannier functions and compute parameters of a multi-band Hubbard model. The latter is treated by a generalised tight-binding method which combines exact diagonalisation of a small cluster with perturbation treatment of the inter-cluster hopping and interactions. This approach has been used to find the size of the gap in La_2CuO_4[35].

In spite of its success, DFT and its various hybrid approaches have some weaknesses which are difficult to amend. A general drawback is that the true exchange-correlation potential is unknown and all results of DFT calculations depend on the choice of approximation to it. Any approximation to the exchange-correlation potential is essentially uncontrolled and therefore difficult to improve systematically which represents a major issue for calculations of strongly correlated electrons. Because of the issues associated with DFT and its hybrid approaches there is also growing interest in wavefunction-based methods[36–38]. Initially these methods were only used to treat small molecules, although the studied systems increased in size. Owing to a fruitful combination of the advent in computer technology and methodological development, quantum chemical methods have made impressive progress and system sizes increased to several hundred atoms[39]. In contrast to DFT, wavefunction-based methods provide a rigorous framework for addressing correlation problems which avoid any uncontrolled approximations. These approaches explicitly construct many-body wavefunctions at increasing levels of sophistication and accuracy. However, W. Kohn put forward the argument that the many-electron wavefunction is not a legitimate concept for large systems with large electron numbers, $N \gtrsim 10^3$[40, 41]. Electronic wavefunctions are thus said to face the ‘exponential wall’ problem, another formulation of the fact that the number of all possible classical configurations of particles grows exponentially with system size, and so does the Hilbert space that the exact wavefunction lives in. Yet, electronic structure methods based on many-body wavefunctions have found a multitude of ways to circumvent this ‘exponential wall’ problem. Standard quantum chemical methods provide thus an appropriate framework for a rigorous treatment of the ubiquitous short-range correlations and of a realistic representation of the crystalline environment. The success of these quantum chemical methods is founded on an accurate description in real space of the correlation hole around an electron which is of local character[42, 43] apart from special cases such as marginal Fermi-liquid behaviour or superconductivity where the long-range part of the correlation hole becomes crucial[41]. Since the correlation hole is a local object, wavefunction-based approaches can limit its description to a finite periodic cluster out of the infinite solid which is large enough to account for crucial short-range correlations. Typically, partially filled d- or f-shells require a multi-configurational wavefunction representation. This can be obtained with the Complete Active Space Self-Consistent Field (CASSCF) method which in general provides a good description for strong correlation effects. In these treatments, the crystalline environment is described by an effective one-electron potential which is calculated with prior Hartree-Fock evaluations for the periodic system. Although the Hartree-Fock approximation is a mean-field treatment, charge distributions are described quite well by it as they are relatively unaffected by correlation effects, even when the latter are strong. These methods have been used to describe the ground state of strongly correlated systems such as $LaCoO_3$ and LiFeAs, as well as the Zhang-Rice-like electron removal band for CuO_2 planes in La_2CuO_4[44]. Further successful examples include the application of the method of increments, which evaluates the correlation energy by decomposing it into increments[45, 46], to transition metal and rare-earth oxides[47–49].

Wavefunction-based approaches are therefore a field with high potential in the future. Although they tend to be more computationally expensive, they represent promising alternatives to DFT-based methodologies given that all approximations are fully controlled and can be successively and systematically improved. In addition, many-body wavefunctions represent the best framework to obtain deeper insight into correlation effects of a system and a better understanding of its most important microscopic processes. Over the last century, developments and applications involving well-chosen and controlled approximations have yielded wavefunctions whose observables are in excellent agreement with experimental measurements. Thus, a major motivation for advances in electronic structure theory has been the aim to arrive at these wavefunctions at a tractable computational cost. This has lead to a vast array of wavefunction-based methods at different levels of accuracy when balancing the competing demands of computational cost and accuracy. A summary of those which are most relevant to this thesis is given in Chapter 2. A set of promising techniques that may pave the way to arrive at this delicate balance are Quantum Monte Carlo (QMC) approaches[50, 51] which broadly split in two main categories, Variational and Projector Quantum Monte

Carlo methods. These represent an array of versatile and accurate stochastic methods which treat quantum many-body systems by sampling the space stochastically, as detailed in Chapter 3 which lays the necessary groundwork for the research presented in the later chapters. Amongst these QMC approaches, one promising emerging technique is the Full Configuration Interaction Quantum Monte Carlo (FCIQMC) method[52], a Projector Quantum Monte Carlo approach which samples both the projector and the exact wavefunction in Fock space, a linear superposition of all classical configurations. As such, FCIQMC is a high-accuracy technique and thus ideally suitable for gaining a fundamental understanding of the structure and important components in the quantum many-body wavefunction of a system which then also aids the development of more approximate approaches. A study in this spirit is presented in Chapter 4 for a prototypical strongly correlated system, the strongly correlated three-band ($p - d$) Hubbard model. In this investigation, FCIQMC is used to examine how the structure of the exact wavefunction is affected by the choice of underlying single-particle basis spanning the Hilbert space and what the implications for other more approximate methods are. Even though the high accuracy of FCIQMC represents a significant advantage, the size of the Hilbert space conceals exponential complexity in the exact wavefunction ansatz and the associated computational cost can often limit the applicability of FCIQMC, in particular when considering large systems.

This challenge has inspired the research that the remaining chapters of this thesis are concerned with: the development of a Projector Quantum Monte Carlo method for non-linear wavefunction ansatzes. This novel approach reformulates the projected imaginary time evolution of FCIQMC in terms of a Lagrangian minimisation which naturally admits non-linear wavefunctions ansatzes. The latter more traditionally inhabit the realm of Variational Quantum Monte Carlo approaches where their polynomial complexity circumvents the exponential scaling of the Hilbert space, and hence the 'exponential wall' problem. Chapter 5 gives a thorough derivation and exposition of this approach which blurs the line between traditional Variational and Projector Quantum Monte Carlo methods. At the same time, it includes developments from the field of deep-learning neural network which can be viewed as a modification of the propagator of the wavefunction dynamics. In addition, the dynamics of the wavefunction evolution also grant access to the one- and two-body static properties of the quantum many-body wavefunction. Chapter 6 and 7 are dedicated to applications which demonstrate the ability of this approach to sample and optimise arbitrary non-linear wavefunction parameterisations with different forms of Tensor Network State ansatzes[53–55]. This set of powerful wavefunction parameterisations has been shown to provide efficient representations of the quantum many-body wavefunction with their success rooted in their ability to capture the natural structure of quantum correlations. Whilst Chapter 6 focuses on Correlator Product State wavefunctions, Chapter 7 considers Matrix Product States, the underlying variational class of the highly successful Density Matrix Renormalisation Group (DMRG)[56] approach, and their generalisations to higher dimensions, Projected Entangled Pair States. All of these wavefunction ansatzes involve controlled approximations and retain systematic improvability towards exactness. Thus, these parameterisations are used in Chapters 6 and 7 to find many-body wavefunctions and their one- and two-body static properties for a range of Hubbard lattice models and *ab-initio* systems. The number of variational parameters that are handled and simultaneously optimised within these applications exceeds those of alternative state-of-the-art Variational Quantum Monte Carlo methods, again demonstrating the ability of this novel approach to efficiently treat and optimise arbitrary non-linear wavefunction ansatzes.

Chapter 2

Theoretical Background

2.1 Introduction

The first postulate of quantum mechanics states that all possible information on any quantum mechanical system of interacting particles is contained within its wavefunction Ψ. The time-dependent Schrödinger equation,

$$i\hbar\frac{\partial}{\partial t}\Psi = \hat{\mathcal{H}}\Psi, \tag{2.1}$$

together with an appropriate set of boundary conditions entirely determines this wavefunction, and hence the state of the system and its evolution in time. It is therefore a primary objective of molecular quantum mechanics to find a solution to the non-relativistic time-independent Schrödinger equation [18]

$$\hat{\mathcal{H}}\Psi = \mathcal{E}\Psi \tag{2.2}$$

where $\hat{\mathcal{H}}$ is the Hamiltonian operator for a system whose state is described by the wavefunction Ψ with total energy $\mathcal{E}$. For a system of N_{nuc} nuclei and N electrons, this Hamiltonian (in atomic units $\hbar = e = m_e = 4\pi\epsilon_0 = 1$), is given by [57]:

$$\hat{\mathcal{H}} = -\sum_{i=1}^{N}\frac{1}{2}\nabla_i^2 - \sum_{A=1}^{N_{\text{nuc}}}\frac{1}{2M_A}\nabla_A^2 - \sum_{i=1}^{N}\sum_{A=1}^{N_{\text{nuc}}}\frac{Z_A}{r_{iA}} + \sum_{i=1}^{N}\sum_{j>i}^{N}\frac{1}{r_{ij}} + \sum_{A=1}^{N_{\text{nuc}}}\sum_{B>A}^{N_{\text{nuc}}}\frac{Z_A Z_B}{R_{AB}}, \tag{2.3}$$

where $r_{ij} = |\mathbf{r}_i - \mathbf{r}_j|$ is the distance between electrons i and j, $r_{iA} = |\mathbf{r}_i - \mathbf{R}_A|$ the distance between electron i and nucleus A with mass M_A and atomic number Z_A, and $R_{AB} = |\mathbf{R}_A - \mathbf{R}_B|$ the distance between nuclei A and B. Whilst the first two terms account for the kinetic energy of electrons and nuclei, the third term describes the Coulomb attraction between electrons and nuclei. The electron-electron and nuclear-nuclear repulsion are represented by the last two terms, respectively.

Due to the large difference between nuclear and electronic masses, the electrons are expected to adjust almost instantaneously to changes in the nuclear positions, such that the $\sum_{A=1}^{N_{\text{nuc}}} \frac{1}{2M_A}\nabla_A^2$ term can be considered negligible. Electronic structure methods therefore typically invoke the Born-Oppenheimer approximation [58] which decouples the electronic motion from the nuclear motion by expressing the total wavefunction as product of electronic and nuclear components,

$$\Psi(\mathbf{r}, \mathbf{R}) = \Psi_{\text{elec}}(\mathbf{r}; \mathbf{R})\Psi_{\text{nuc}}(\mathbf{R}). \tag{2.4}$$

The electronic wavefunction Ψ_{elec} represents a solution to the electronic Schrödinger equation

$$\hat{\mathcal{H}}_{\text{elec}}\Psi_{\text{elec}}(\mathbf{r}; \mathbf{R}) = \mathcal{E}_{\text{elec}}(\mathbf{R})\Psi_{\text{elec}}(\mathbf{r}; \mathbf{R}), \tag{2.5}$$

$$\hat{\mathcal{H}}_{\text{elec}} = -\sum_{i=1}^{N} \frac{1}{2}\nabla_i^2 - \sum_{i=1}^{N}\sum_{A=1}^{N_{\text{nuc}}} \frac{Z_A}{r_{iA}} + \sum_{i=1}^{N}\sum_{j>i}^{N} \frac{1}{r_{ij}} + E_{\text{nuc}}. \tag{2.6}$$

This electronic Schrödinger equation describes the motion of N electrons in a field of N_{nuc} fixed nuclei whose kinetic energy is neglected and whose repulsion contributes a constant value $E_{\text{nuc}} = \sum_{A=1}^{N_{\text{nuc}}}\sum_{B>A}^{N_{\text{nuc}}} \frac{Z_A Z_B}{R_{AB}}$ to the electronic energy $\mathcal{E}_{\text{elec}}$. This common approximation has been shown to produce potential energy surfaces with accurate molecular properties. It is, however, worth noting that the approximation can break down in systems with closely lying electronic states due to coupling between these states and the nuclear kinetic energy neglected in the Born-Oppenheimer approximation [59, 60]. Nevertheless, the electronic Schrödinger equation is the basis of the majority of problems in quantum chemistry. In particular, any discussion of the Hamiltonian within this thesis is with respect to the Born-Oppenheimer separated electronic Hamiltonian, unless otherwise stated, and the ‘elec’ subscript is omitted from this point onwards.

In practice, it is extremely difficult to solve 2.5 for the exact Ψ and analytical solutions can only be found for a few simple one-electron systems such as the H atom or the $H_2{}^+$ molecule. For more complicated systems, approximations must be introduced whilst incorporating as many of the symmetries and characteristics of the exact wavefunction as possible in the approximate wavefunction to ensure that it gives a reasonable description of the system. Many of these properties can be introduced by ensuring that the wavefunction represents an eigenfunction of the corresponding operators which commute with $\hat{\mathcal{H}}$ such as the number operator ($\hat{\mathcal{N}}$), or the total ($\hat{\mathcal{S}}^2$) and projected spin operators ($\hat{\mathcal{S}}_z$) in non-relativistic theory.

One of the most fundamental characteristics which should be included at each level of theory arises as a consequence of the fundamental nature of the spin that each particle is associated with. Since the Hamiltonian is invariant to interchange of indistinguishable particles, its eigenfunctions can be separated in two symmetry classes: those wavefunctions which are symmetric and those which are anti-symmetric with respect to identical particle exchange. The spin-statistics theorem [61, 62] states that integer spin particles, called bosons, obey Bose-Einstein statistics and half-integer spin particles, referred to as fermions, obey Fermi-Dirac statistics. Hence, for bosons the general many-body wavefunction is symmetric with respect to interchange of any two indistinguishable particles, whilst for fermions it is anti-symmetric with respect to interchange of any two indistinguishable particles. From the anti-symmetric nature of the fermionic wavefunction, the Pauli exclusion principle [19, 63, 64] follows which, in its general form, states that two or more identical fermions such as electrons cannot occupy the same (pure) quantum mechanical state. In general, writing the function which completely describes a single electron i as product of a spatial and a spin component that depend on the spatial and spin coordinates of the electron, collectively denoted by:

$$\mathbf{x}_i = \{\mathbf{r}_i, \sigma_i\}\,, \tag{2.7}$$

where

$$\sigma = \{\alpha; \beta\}\,, \tag{2.8}$$

the anti-symmetry and Pauli principle can thus be described as

$$\Psi(\mathbf{x}_1, \mathbf{x}_2, \ldots, \mathbf{x}_i, \ldots, \mathbf{x}_j, \ldots, \mathbf{x}_N) = -\Psi(\mathbf{x}_1, \mathbf{x}_2, \ldots, \mathbf{x}_j, \ldots, \mathbf{x}_i, \ldots, \mathbf{x}_N). \tag{2.9}$$

The simplest, non-trivial function which satisfies this requirement is a Slater determinant [65]

$$D_{\mathbf{i}} = \frac{1}{\sqrt{N!}} \begin{vmatrix} \phi_1(\mathbf{x}_1) & \phi_1(\mathbf{x}_2) & \ldots & \phi_1(\mathbf{x}_N) \\ \phi_2(\mathbf{x}_1) & \phi_2(\mathbf{x}_2) & \ldots & \phi_2(\mathbf{x}_N) \\ \vdots & \vdots & \ddots & \vdots \\ \phi_n(\mathbf{x}_1) & \phi_n(\mathbf{x}_2) & \ldots & \phi_N(\mathbf{x}_N) \end{vmatrix}. \tag{2.10}$$

Within this formalism interchanging the coordinates of two electrons is equivalent to interchanging two rows of the Slater determinant which changes the sign of the determinant as required by the anti-symmetry principle. If two electrons share the same spin and spatial coordinates, corresponding to two identical columns in the Slater determinant, the latter vanishes. At the same time, this characteristic creates a region of low probability for electrons with like spin at small separation distances. This represents a manifestation of Fermi correlation which is automatically incorporated into a wavefunction written as a Slater determinant. Alternatively, the Slater determinant can also be expressed in terms of an antisymmetrising operator $\hat{\mathcal{A}}$ acting on a Hartree product

$$D_{\mathbf{i}} = \hat{\mathcal{A}}[\phi_1(\mathbf{x}_1)\phi_2(\mathbf{x}_2)\dots\phi_N(\mathbf{x}_N)], \tag{2.11}$$

where

$$\hat{\mathcal{A}} = \frac{1}{\sqrt{N!}}\sum_{p=0}^{N-1}(-1)^p\hat{\mathcal{P}}_p = \frac{1}{\sqrt{N!}}\left[1 - \sum_{i\neq j}\hat{\mathcal{P}}_{ij} + \sum_{i\neq j\neq k}\hat{\mathcal{P}}_{ijk} - \dots\right] \tag{2.12}$$

with $\hat{\mathcal{P}}_p$ the permutation operator which generates all possible permutations of p electronic coordinates. The functions $\{\phi_i\}$ represent single particle spin orbitals which describe the distribution of a single electron. Each ϕ_i depends on the spin and spatial coordinates $\mathbf{x}$ of only one electron and is written as a product of a spatial orbital and a spin function

$$\phi_i(\mathbf{x}) = \phi_{i,s}(\mathbf{r},\sigma) = \phi_I(\mathbf{r})\delta_{s,\sigma}. \tag{2.13}$$

Whereas two spin orbitals with the same spatial function but different spin part are always orthogonal $\langle\phi_{i,\alpha}(\mathbf{x})|\phi_{i,\beta}(\mathbf{x})\rangle = 0$, the set of spatial orbitals $\{\phi_I(\mathbf{r})\}$ are usually chosen to be orthonormal $\langle\phi_I(\mathbf{r})|\phi_J(\mathbf{r})\rangle = \delta_{IJ}$ but need not necessarily be.

Since the Hamiltonian and the antisymmetrising operator are both linear operators, a linear combination of Slater determinants

$$\Psi = \sum_{\mathbf{i}} C_{\mathbf{i}}D_{\mathbf{i}} \tag{2.14}$$

creates a more flexible many-body wavefunction whilst still maintaining the required antisymmetry properties. Wavefunctions written in the form of a single Slater determinant or any linear combination of Slater determinants constitute the basis of the

Hartree-Fock and Configuration Interaction methods, respectively. Working in a Slater determinant basis requires keeping track of the occupations of the single particles states with a certain number of fermions and the appropriate sign factors arising from the respective permutation. Dirac and Fock established a formalism with this functionality, referred to as Second Quantisation [66, 67].

2.2 An Alternative Formalism: Second Quantisation

The Hamiltonian in 2.5 is represented in First Quantisation, a formulation in which observables are represented by operators and states by functions. In the language of Second Quantisation [37, 68–70], both wavefunctions and operators are uniquely described by a single set of elementary operators. One of the major differences between first and second quantisation is that while the total number of particles is restricted in first quantisation, second quantisation does not impose such a restriction. In its first quantisation representation, the N-particle wavefunction is expanded in a basis of vectors that span the N-particle Hilbert space $\mathcal{H}_N$. In the trivial case of no particles, $N = 0$, $\mathcal{H}_N$ is equal to $\mathbb{C}$, and in the case of a single particle $N = 1$, $\mathcal{H}_N$ is spanned by the set of single particle spin orbitals ϕ_i $(i = 1, 2, \ldots \infty)$ with inner product $\langle \phi_i | \phi_j \rangle = \delta_{ij}$. For a general N-particle system, $\mathcal{H}_N$ is the N-fold tensor product of $\mathcal{H}_1$

$$\mathcal{H}_N = \mathcal{H}_1^{\otimes N}. \tag{2.15}$$

In the case of bosons, this tensor product is symmetrised after tensor multiplication, and in the case of fermions it is antisymmetrised, thereby implying that the fermionic $\mathcal{H}_N$ is spanned by the set of all N-particle Slater determinants. Since this thesis is only concerned with fermionic particles the following discussion will be restricted to fermions.

2.2.1 The Fock Space

Since in second quantisation the number of particles is not a constant, a state vector in its second quatised form is a basis vector of an abstract linear vector space called Fock space $\mathcal{F}_\infty$ comprising all states containing zero to infinitely many particles. This

Fock space is defined as the direct sum of N-particle Hilbert spaces

$$\mathcal{F}_\infty = \bigoplus_{N=0}^{\infty} \mathcal{H}_N. \tag{2.16}$$

Since $\mathcal{F}_\infty$ may be decomposed into subspaces of N-particles Hilbert spaces which in turn are spanned by N-particle Slater determinants, the span of $\mathcal{F}_\infty$ includes Slater determinants but for all particle numbers ranging from 0 to ∞. The basis vectors of the Fock space are occupation number vectors defined as

$$|\mathbf{n}\rangle = |n_1, n_2, \ldots\rangle\,, \quad n_i = \begin{cases} 1 & \phi_i \text{ occupied} \\ 0 & \phi_i \text{ unoccupied} \end{cases}, \quad \sum_{i=1}^{\infty} n_i < \infty, \tag{2.17}$$

which is an alternative representation for a Slater determinant constructed from the set of one-particle functions $\{\phi_i\}$. The occupation number n_i is equal to 1 if ϕ_i is present in the determinant and 0 if it is absent. Spaces $\mathcal{F}_N$ with at most N particles,

$$\mathcal{F}_N = \bigoplus_{n=0}^{N} \mathcal{H}_n. \tag{2.18}$$

are subspaces of the Fock space $\mathcal{F}_\infty$ and likewise spanned by $|\mathbf{n}\rangle$ satisfying the constraint

$$\sum_{i=1}^{\infty} n_i \leq N. \tag{2.19}$$

Whilst the $|\mathbf{n}\rangle$ of the Fock space $\mathcal{F}_\infty$ and its subspaces $\mathcal{F}_N$ are created from an infinite set of functions ϕ_i, in practice only finite basis set with M spin orbitals can be employed. This further restricts the space to those 2^M-dimensional subspaces

$$\mathcal{F}_{N,M} = \bigoplus_{n=0}^{N} \mathcal{H}_{n,M}. \tag{2.20}$$

spanned by those occupation number vectors that satisfy

$$|\mathbf{n}\rangle = |n_1, n_2, \ldots, n_m\rangle\,, \quad \sum_{i=1}^{M} n_i \leq N. \tag{2.21}$$

For a given spin orbital basis, a one-to-one mapping between Slater determinants in canonical order and occupation number vectors in the Fock space exist. However, in contrast to determinants occupation number vectors have no spatial structure but are basis vectors of an abstract vector space, representing an orthonormal and complete basis with inner product,

$$\langle \mathbf{m} | \mathbf{n} \rangle = \delta_{\mathbf{m},\mathbf{n}} = \prod_{i=1}^{M} \delta_{m_i,n_i}, \tag{2.22}$$

and resolution of the identity defined as

$$\hat{\mathcal{I}} = \sum_{\mathbf{k}} |\mathbf{k}\rangle \langle \mathbf{k}| \,. \tag{2.23}$$

The subspace $\mathcal{H}_0$ with no particles contains a single basis vector, the true vacuum state

$$|0\rangle = |0_1.0_2, \ldots\rangle = 1 \in \mathbb{C} = \mathcal{H}_0 \subset \mathcal{F}_\infty, \tag{2.24}$$

which is normalised to unity $\langle 0|0\rangle = 1$.

2.2.2 Elementary Operators

In second quantisation, all states and operators can be constructed from the set of elementary creation and annihilation operators. Whereas the creation operator $a_p^\dagger$ creates a fermion in spin orbitals p, its Hermitian adjoint, the annihilation operator a_p annihilates a fermion in spin orbital p. These operators satisfy the anticommutation rules

$$\left\{a_p, a_q^\dagger\right\} = a_p a_q^\dagger + a_q^\dagger a_p = \delta_{pq} \tag{2.25}$$

$$\{a_p, a_q\} = \left\{a_p^\dagger, a_q^\dagger\right\} = 0, \tag{2.26}$$

from which all properties of the operators follow. These anticommutation relations ensure that, in accordance with Pauli's exclusion principle, a single-particle state cannot be occupied with more than one fermion, $a_p^\dagger a_p^\dagger = -a_p^\dagger a_p^\dagger = 0$, as well as, the antisymmetry for multiple fermions $a_p^\dagger a_q^\dagger = -a_q^\dagger a_p^\dagger$. Furthermore, the anticommutation rules imply that if a creation operator $a_p^\dagger$ (annihilation operator a_p) acts on an occupation number vector $|\mathbf{n}\rangle$, it populates (depopulates) the spin orbital ϕ_p if it is unoccupied

(occupied) in $|\mathbf{n}\rangle$

$$a_p^\dagger \left|n_1, \ldots, n_{p-1}, n_p, n_{p+1}, \ldots\right\rangle = \begin{cases} \Gamma_p^{\mathbf{n}} \left|n_1, \ldots, n_{p-1}, 1_p, n_{p+1}, \ldots\right\rangle & \text{if } n_p = 0_p \\ 0 & \text{if } n_p = 1_p, \end{cases} \tag{2.27}$$

$$a_p \left|n_1, \ldots, n_{p-1}, n_p, n_{p+1}, \ldots\right\rangle = \begin{cases} \Gamma_p^{\mathbf{n}} \left|n_1, \ldots, n_{p-1}, 0_p, n_{p+1}, \ldots\right\rangle & \text{if } n_p = 1_p \\ 0 & \text{if } n_p = 0_p, \end{cases} \tag{2.28}$$

with the phase factor

$$\Gamma_p^{\mathbf{n}} = \prod_{q=1}^{p-1} (-1)^{n_q}. \tag{2.29}$$

Since for a general occupation number vector the unoccupied spin orbitals can be identified from the occupied ones, explicit reference to the former may be avoided altogether by writing the occupation number vector as a string of creation operators in canonical order (i.e. in the same order as in the occupation number vector) acting on the vacuum state:

$$|\mathbf{n}\rangle = \left[\prod_{p=1}^{\infty} (a_p^\dagger)^{n_p}\right] |0\rangle\,. \tag{2.30}$$

Due to the definition of the elementary creation and annihilation operators and their respective anticommutation relation, the antisymmetry properties of the wavefunction are incorporated in the algebraic properties of the operators. By analogy, similar creation $b_p^\dagger$ and annihilation b_p operators can be introduced for bosons which satisfy the commutation rules $[b_p, b_q^\dagger] = b_p b_q^\dagger - b_q^\dagger b_p = \delta_{pq}$ and $[b_p, b_q] = [b_p^\dagger, b_q^\dagger] = 0$ to transfer the symmetry properties of the bosonic wavefunction into the algebraic properties of the operator. Second quantisation allows both states and operators to be expressed in terms of creation and annihilation operators in a unified way. As expectation values of observables are independent of the representation of operators and states, an operator in Fock space can be derived by requiring its matrix elements between occupation number vectors to be equal to the respective matrix elements between Slater determinants of the operator in its first quantised form. In first quantisation, the operators are exact and independent of the spin orbital basis, but explicitly depend on the number of particles, and the dependence on the spin orbital basis is incorporated into the Slater determinants. In contrast, in the second quantisation formalism, the occupation number vectors contain no reference to the spin orbital basis. Still, the operators are projections of the exact operators onto the spin orbital basis, and hence basis-dependent, but independent of the number of particles. Thus, the second-quantisation representation of the electronic Hamiltonian in 2.5 is given by [37]:

$$\hat{\mathcal{H}} = \hat{h} + \hat{g} + E_{\text{nuc}} = \sum_{pq} h_{pq} a_p^\dagger a_q + \frac{1}{2} \sum_{pqrs} g_{pqrs} a_p^\dagger a_q^\dagger a_s a_r + E_{\text{nuc}} \tag{2.31}$$

with the one- and two-particle integrals defined as

$$h_{pq} = \langle p|\hat{h}|q\rangle = \int \phi_p^*(\mathbf{x}_i) \left(-\frac{1}{2}\nabla_i^2 - \sum_{A=1}^{N_{\text{nuc}}} \frac{Z_A}{r_{iA}} \right) \phi_q(\mathbf{x}_i) d\mathbf{x}_i \tag{2.32}$$

$$g_{pqrs} = \langle pq|rs\rangle = \int\int \phi_p^*(\mathbf{x}_i)\phi_q^*(\mathbf{x}_j) \frac{1}{r_{ij}} \phi_r(\mathbf{x}_i)\phi_s(\mathbf{x}_j) d\mathbf{x}_i d\mathbf{x}_j \tag{2.33}$$

$$E_{\text{nuc}} = \sum_{A=1}^{N_{\text{nuc}}} \sum_{B>A}^{N_{\text{nuc}}} \frac{Z_A Z_B}{R_{AB}}. \tag{2.34}$$

Within this second-quantisation formulation, if applied to a state vector, the Hamiltonian operator generates a linear combination of the original state and further states constructed by single- and double particle excitations from this state vector. Each such excitation is associated with an amplitude h_{pq} and g_{pqrs} representing the probability of this event occurring. In the limit of a complete set of spin orbital, the exact eigenstate Ψ of the Hamiltonian can be represented by a linear expansion in terms of the occupation number vectors of the Fock space $\mathcal{F}_\infty$ when no restriction with respect to particle number, point-group symmetry or projection of the total spin are enforced. Yet, even if the total number of electrons is restricted to $N = N_\alpha + N_\beta$ with N_α and N_β the number of α and β spin particles, the number of terms in the linear combination becomes infinite due to the infinite basis set. Therefore, the approximation of a finite spin orbital basis of size M is introduced. Even within this framework, it is exceedingly difficult in practice to solve for the exact eigenstate Ψ of the Hamiltonian since the $\frac{1}{r_{ij}}$ term encapsulates the correlation of N interacting particles. The pursuit of accurate approximations to the solution of the Schrödinger equation is therefore the driving force of development in electronic structure theory. Within the plethora of different approaches, many wavefunction-based methods still resort to Slater determinants as reference functions due to their favourable characteristic of enforcing antisymmetry in the wavefunction.

2.3 Hartree-Fock Theory

Hartree-Fock (HF) Theory[71–73] represents a cornerstone of electronic structure theory. It is not only a useful approximation in its own right, but also often serves as starting point for more accurate electronic structure methods. HF theory seeks the best single Slater determinant description of Ψ by optimising its energy with respect to variations in the molecular (MO) spin orbitals occupying the determinant. Whilst optimisation of the HF wavefunction can be formulated as an orbital rotation problem that can be solved using standard techniques of numerical analysis, there exists an alternative approach which more clearly reflects the physical contents of the HF state Ψ_{HF}: canonical Hartree-Fock theory. Since a single determinant wavefunction represents a state where each electron behaves as independent particle (subject to Fermi correlation), the optimal determinant, Ψ_{HF}, can be constructed from a set of independent-particle spin orbitals each of which represents an eigenfunction of an effective one-electron Schrödinger equation. This set of effective one-electron Schrödinger equation, known as Hartree-Fock equations, are specified by the Fock operator

$$\hat{f} = \sum_{pq} f_{pq} a_p^\dagger a_q, \tag{2.35}$$

where f_{pq} denotes the elements of the Fock matrix. The Fock operator

$$\hat{f} = \hat{h} + \hat{V} \tag{2.36}$$

retains the one-electron part $\hat{h}$ of the true Hamiltonian in 2.31, but replaces the two-electron part $\hat{g}$ in 2.31 by an effective one-electron potential, also referred to as Fock potential

$$\hat{V} = \sum_{pq} \sum_{i} (2g_{piqi} - g_{piiq}) a_p^\dagger a_q. \tag{2.37}$$

Whereas the sums over p and q run over the full set of spin orbitals, the sum over i only includes occupied spatial orbitals and the Fock potential thus depends on the form of occupied spin orbitals. While the first term in 2.37 describes the classical Coulomb interaction of the electron with the charge distribution of the occupied spin orbitals, the second term, called exchange term, corrects the classical electrostatic interaction for Fermi correlation. The one-electron eigenfunctions of the Fock operator

$$\hat{f} a_p^\dagger \left|0\right\rangle = \epsilon_p a_p^\dagger \left|0\right\rangle \tag{2.38}$$

are called canonical spin orbitals and their associated eigenvalues represent the eigenvalues of the Fock matrix

$$f_{pq} = \delta_{pq}\epsilon_p \tag{2.39}$$

which is diagonal in this canonical representation. However, the canonical spin orbitals are not only the eigenvectors of the Fock matrix, but at the same time they represent the orbitals from which the Fock matrix is constructed, thereby implying that the Hartree-Fock equations constitute a set of non-linear equations that are not true eigenvalue equations but more appropriately described as pseudo-eigenvalue equations. The HF equations can therefore only be solved in an iterative manner whereby, starting from an initial guess, the Fock matrix is repeatedly reconstructed and rediagonalised until self-consistency is achieved and the spin orbitals from which the Fock matrix is constructed are identical to those generated by its diagonalisation. This iterative procedure is known as self-consistent field (SCF) method[74].

In the classical Roothaan-Hall formulation of Hartree-Fock theory[75, 37], the molecular orbitals (MO) ϕ_p are expanded in a finite basis of M orthonormal atomic spin orbitals (AO) $\{\chi_\mu\}$

$$\phi_p = \sum_\mu \chi_\mu C_{\mu p}. \tag{2.40}$$

The expansion coefficients $C_{\mu p}$ are treated as variational parameters for optimisation of the HF energy, the expectation value with the true Hamiltonian operator $\hat{H}$,

$$E_{\mathrm{HF}}(\mathbf{C}) = \min \langle \Psi_{\mathrm{HF}} | \hat{H} | \Psi_{\mathrm{HF}} \rangle \,, \tag{2.41}$$

which can be written as

$$E_{\mathrm{HF}}(\mathbf{C}) = \sum_i^N h_{ii} + \frac{1}{2}\sum_i^N \sum_j^N (g_{ijij} - g_{ijji}) + E_{\mathrm{nuc}}, \tag{2.42}$$

and the indices i and j denote occupied orbitals. Minimisation of this energy subject to the constraint that the molecular orbitals remain orthonormal

$$\langle \phi_i | \phi_j \rangle = \delta_{ij}, \tag{2.43}$$

can be reformulated by introducing the Hartree-Fock Lagrangian

$$L(\mathbf{C}) = E_{\mathrm{HF}}(\mathbf{C}) - \sum_{ij} \lambda_{ij}(\langle\phi_i|\phi_j\rangle - \delta_{ij}), \tag{2.44}$$

where λ_{ij} denote the set of Lagrange multipliers. The variational conditions on the HF energy can thus be equivalently expressed in the unconstrained form

$$\frac{\partial L(\mathbf{C})}{\partial C_{\mu k}} = 0, \tag{2.45}$$

which results in the conditions for the optimised HF state

$$f_{\mu k} = \sum_{j} S_{\mu j}\lambda_{jk}, \tag{2.46}$$

where $S_{\mu j}$ represents the overlap between atomic orbital χ_μ and molecular orbital ϕ_j. Multiplication from the left by a set of molecular orbitals demonstrates that the elements of the Fock operator correspond the the Lagrange multipliers

$$f_{ik} = \lambda_{ik}. \tag{2.47}$$

Since the matrix λ is Hermitian, it may be diagonalised by an orthogonal transformation among the occupied orbitals $\lambda = \mathbf{U}\epsilon\mathbf{U}^{\mathbf{T}}$. The HF state is invariant to such transformations, and the set of occupied spin orbitals can be rotated into the basis of canonical spin orbitals which are defined by their diagonalisation of the Fock matrix

$$f_{ik} = \delta_{ik}\epsilon_i. \tag{2.48}$$

In this canonical representation, the variational conditions in 2.46 can be expressed in the form

$$\sum_{\nu} f^{\mathrm{AO}}_{\mu\nu} C_{\nu k} = \epsilon_k \sum_{\nu} S_{\mu\nu} C_{\nu k}, \tag{2.49}$$

where the elements of the AO Fock matrix may be entirely evaluated in terms of the AO basis set spin orbitals

$$f^{\mathrm{AO}}_{\mu\nu} = h_{\mu\nu} + \sum_{\rho\sigma} D^{\mathrm{AO}}_{\rho\sigma}(g_{\mu\rho\nu\sigma} - g_{\mu\rho\sigma\nu}), \tag{2.50}$$

with the one-electron density matrix defined as

$$D^{\mathrm{AO}}_{\rho\sigma} = \sum_{i}^{N} C^{*}_{\rho i} C_{\sigma i}. \tag{2.51}$$

The eigenvalue ϵ_i represents the Fock energy of the respective canonical spin orbital ϕ_i,

$$\epsilon_i = h_{ii} + \sum_{j}^{N} (g_{ijij} - g_{ijji}). \tag{2.52}$$

The final HF wavefunction Ψ_{HF} is then constructed from the N lowest energy orbitals of these spin orbitals, and expressing them as Slater determinant with its energy given by the HF energy in 2.42. In this HF picture, the N electrons move independently of one another in an electrostatic field created by the stationary nuclei and by the charge distributions of all the remaining electrons, appropriately modified to account for Fermi correlation arising from the Pauli antisymmetry principle. The occupied (ϵ_i) and virtual (ϵ_a) spin orbital energies may be interpreted as ionisation potential $-\epsilon_i$ for removing an electron from the occupied spin orbital ϕ_i and electron affinity $-\epsilon_a$ for adding an electron to the virtual spin orbital ϕ_a (Koopmans' theorem). The HF variational conditions in matrix form

$$\mathbf{f}^{\mathrm{AO}}\mathbf{C} = \mathbf{SC}\epsilon. \tag{2.53}$$

are also known as the Roothaan-Hall equations[75] within the context of Restricted Hartree-Fock (RHF) theory. The latter assumes a set of restricted spin orbitals which impose the constraint that the spatial functions for α and β pairs of spin orbitals of the same spatial orbital are the same

$$\phi_{i,\alpha}(\mathbf{x}) = \phi_I(\mathbf{r})\alpha(\sigma) \tag{2.54}$$

$$\phi_{i,\beta}(\mathbf{x}) = \phi_I(\mathbf{r})\beta(\sigma). \tag{2.55}$$

This symmetry is broken in the Unrestricted Hartree-Fock (UHF) formalism which uses unrestricted spin orbitals that allow different spatial functions for paired spin orbitals of the same spatial orbital

$$\phi_{i,\alpha}(\mathbf{x}) = \phi^{\alpha}_I(\mathbf{r})\alpha(\sigma) \tag{2.56}$$

$$\phi_{i,\beta}(\mathbf{x}) = \phi^{\beta}_I(\mathbf{r})\beta(\sigma). \tag{2.57}$$

This leads to the Poble-Nesbet equations[76], a generalisation of the Roothaan-Hall equation, which must be solved simultaneously,

$$\mathbf{f}^{\mathrm{AO},\alpha}\mathbf{C}^{\alpha} = \mathbf{S}\mathbf{C}^{\alpha}\epsilon^{\alpha} \tag{2.58}$$

$$\mathbf{f}^{\mathrm{AO},\beta}\mathbf{C}^{\beta} = \mathbf{S}\mathbf{C}^{\beta}\epsilon^{\beta}. \tag{2.59}$$

This additional flexibility may lead to a lower UHF energy compared to the RHF value. However, whilst the use of restricted spin orbitals ensures that the RHF state is also an eigenfunction of the total ($\hat{\mathcal{S}}^2$) and projected spin operators ($\hat{\mathcal{S}}_z$), relaxation of this constraint in the UHF approach can introduce spin contaminations in the UHF wavefunction which is thus no longer an eigenfunction of $\hat{\mathcal{S}}^2$.

Bearing in mind the bold approximation introduced by the effective one-body treatment, HF total electronic energies and properties can perform remarkably well for some molecular systems when comparing to experimental data. Its results are best for weakly correlated and single reference systems where the exact wavefunction is well approximated by a single HF determinant such as first row atoms or dimers at equilibrium geometry. However, the ability of HF theory to produce accurate, or even only qualitatively correct, descriptions is limited for most applications, for example, in the case of N_2 the ordering of its ionisation potentials is predicted qualitatively incorrect[57]. Furthermore, the RHF method fails to describe the dissociation of dimers into open-shell fragments, even for the simplest case of $H_2 \rightarrow 2\,H$. While the UHF approach gives a qualitatively correct description in the dissociation limit, the resulting binding curves are not accurate[37]. In general, the HF wavefunction performs very poorly in more correlated systems due to the mean-field treatment of interactions between electrons. More sophisticated approaches are therefore needed for the treatment of instantaneous electron-electron interactions, also known as electron correlation.

2.4 Electron Correlation

The broad term electron correlation describes the behaviour of N interacting electrons and their instantaneous electron-electron interactions in a many-body state, embodied in the $\frac{1}{r_{ij}}$ term in the Hamiltonian (Eq. 2.5). In other words, electron correlation effects loosely denote corrections to the independent electron picture of the HF approximation that are necessary to reach the limit of the exact wavefunction which is a linear combination of all occupation number vectors (representing Slater determinants for fermions) in the N-particle Hilbert space spanned by the complete single-particle basis set. As such, the theoretical concept of the correlation energy is introduced which is defined as the difference between the exact non-relativistic electronic energy of the system ($\mathcal{E}_0$) and the HF energy (E_{HF}) in the limit that the basis set approaches completeness[37, 57]

$$E_{\mathrm{corr}} = \mathcal{E}_0 - E_{\mathrm{HF}}. \tag{2.60}$$

In practice, the complete basis set has to be limited to a finite number of M one-particle basis functions and the basis set correlation energy is thus defined as the difference between the Hartree-Fock energy in this basis and the lowest possible energy of a wavefunction formed within the variational flexibility available in this incomplete basis. As the basis set approaches completeness, the basis set correlation energy tends towards the true correlation energy.

Since the HF state is a single Slater determinant, it is an antisymmetric superposition of products of one-particle functions. Although this antisymmetrisation of the HF wavefunction incorporates one mode of correlation, Fermi correlation, which introduces Fermi holes for electron pairs of parallel spin, Ψ_{HF} is nevertheless defined to be an uncorrelated many-particle state.

Disregarding Fermi correlation, it is conceptually convenient to distinguish between different types of electron correlation: static and dynamical correlation. Dynamical correlation arises from the Coulomb repulsion and describes the instantaneous detailed correlated motion of the electrons due to their mutual repulsion. It is often useful to separate long-range and short-range dynamical correlation effects. Short-range dynamical correlation manifests itself in the appearance of cusps in the exact wavefunction when particles coincide. In this limit, the Hamiltonian in 2.5 becomes singular in the attraction terms for $r_{iA} = 0$ and in the repulsion term for $r_{ij} = 0$. These singularities must be balanced by the kinetic energy of the wavefunction to ensure that the local energy $E(\mathbf{r}_i, \mathbf{r}_j) = \frac{\hat{\mathcal{H}}\Psi(\mathbf{r}_i,\mathbf{r}_j)}{\Psi(\mathbf{r}_i,\mathbf{r}_j)}$ remains constant and equal to the eigenvalue $\mathcal{E}$. It can be shown that the first derivative of the wavefunction must therefore satisfy[37, 77–79]

$$\lim_{r_{iA}\to 0}\left(\frac{\partial\Psi}{\partial r_{iA}}\right) = -Z_A\Psi(r_{iA}=0) \tag{2.61}$$

$$\lim_{r_{ij}\to 0}\left(\frac{\partial\Psi}{\partial r_{ij}}\right) = \frac{1}{2}\Psi(r_{ij}=0), \tag{2.62}$$

The first of these conditions represents the nuclear cusp condition and describes the behaviour of the wavefunction in the vicinity of a nucleus. Likewise, the second condition is referred to as (electronic) Coulomb cusp condition and establishes the behaviour of the wavefunction when electrons coincide. Whilst Eq. 2.62 considers anti-parallel spin electrons, the case is slight different for parallel spin electrons. For the latter, the situation is somewhat improved since the wavefunction vanishes when like spin electrons coalesce due to the need to satisfy the Pauli principle. In these cases of parallel spin electrons, the cusp condition is similar to equation 2.62 but with the factor of $\frac{1}{2}$ replaced by $\frac{1}{4}$. Regardless of their precise mathematical formulation, all of these cusps in the wavefunction are difficult to approximate by means of a superposition of Slater determinants and a good description of dynamical correlation and the wavefunction cusps is only achieved in the limit of a large expansion in Slater determinant space[80]. This slowly converging expansion is therefore a limitation that is shared by all Fock-space methods and necessitates the use of very large basis sets to accurately capture dynamical correlation. In contrast, long-range dynamical correlations can usually be adequately accounted for by inclusion of a relatively small number of determinants.

Static correlation – also known as nondynamical or near-degeneracy correlation – arises from near-degeneracies among configurations (determinants) which interact strongly and cannot be treated in isolation. In this case, many determinants contribute significantly to the wavefunction and are needed for a description of the qualitative behaviour of the system.

The two modes of correlation can be illustrated with two examples. The helium atom represents a system where correlations are considered to be solely of dynamical nature. Similarly, H_2 at equilibrium geometry displays dynamical correlation effects. In contrast, in the molecular dissociation limit the electrons in H_2 are too far apart for significant dynamical correlation effects, yet, due to the degeneracy of the bonding and anti-bonding configurations it is regarded as static correlation problem. In the intermediate region, the linear combination of determinants serves the double purpose of describing effects of Coulomb repulsion and the near-degeneracy of configurations and no clear distinction between the two effects can be drawn. Static correlation effects generally require a multireference approach where many determinants are included in the reference wavefunction, in contrast to single-reference methods which only add correlation corrections onto a single determinant such as the HF determinant. These methods rely on the assumption that this one reference determinant provides a reasonable qualitative description of the system and are therefore likely to fail in systems with significant static correlation. Single-reference methods are usually appropriate for a treatment of long-range dynamical correlations whereas short-range dynamical correlations are exceedingly difficult to account for and might need treatment with explicitly correlated methods[81] which go beyond the Fock space description and multiply the determinant expansion by a suitable correlating function $\gamma(r_{ij})$ which imposes the correct Coulomb-cusp behaviour.

2.5 Full Configuration Interaction

The exact eigenstate of the non-relativistic, Born-Oppenheimer Hamiltonian (Eq. 2.31) for a given single-particle basis set is represented by a wavefunction expressed as linear combination of all occupation number vectors in the direct-product basis of single-particle Hilbert spaces

$$\Psi_{\text{FCI}} = \sum_{n_1 n_2 \dots n_m}^{q} C_{n_1 n_2 \dots n_m} \left| n_1 n_2 \dots n_m \right\rangle = \sum_{\mathbf{n}} C_{\mathbf{n}} \left| \mathbf{n} \right\rangle . \tag{2.63}$$

q denotes the dimension of the local Hilbert space and assumes a value of 2 for spin orbitals corresponding to the set of unoccupied and occupied single-particle state $\{\left|0\right\rangle, \left|1\right\rangle\}$. The sum is restricted to include only those states which conserve the number of alpha and beta spin electrons $N = N_\alpha + N_\beta$ in the system such that the occupation number vectors represent Slater determinants of the N-particle Hilbert space. This is the wavefunction ansatz of Full Configuration Interaction (FCI) which includes all static and dynamical correlation exactly within the variational flexibility afforded by the finite basis set[82–84]. The optimal set of expansion coefficients $\{C_{\mathbf{n}}\}$ can be found by variationally minimising the energy

$$E_{\text{FCI}}(\{C_{\mathbf{n}}\}) = \min \langle \Psi_{\text{FCI}} | \hat{\mathcal{H}} | \Psi_{\text{FCI}} \rangle \tag{2.64}$$

subject to the constraint that the wavefunction remains normalised $\langle \Psi_{\text{FCI}} | \Psi_{\text{FCI}} \rangle = 1$. This constraint optimisation can be performed via Lagrange's method of undetermined multipliers

$$\begin{aligned}
\mathcal{L}[\{C_{\mathbf{n}}\}] &= \langle \Psi_{\text{FCI}} | \hat{\mathcal{H}} | \Psi_{\text{FCI}} \rangle - E(\langle \Psi_{\text{FCI}} | \Psi_{\text{FCI}} \rangle - 1) && (2.65)\\
&= \sum_{\mathbf{mn}} C_{\mathbf{m}} C_{\mathbf{n}} \langle \mathbf{m} | \hat{\mathcal{H}} | \mathbf{n} \rangle - E(\sum_{\mathbf{mn}} C_{\mathbf{m}} C_{\mathbf{n}} \langle \mathbf{m} | \mathbf{n} \rangle - 1) && (2.66)\\
&= \sum_{\mathbf{mn}} C_{\mathbf{m}} C_{\mathbf{n}} H_{\mathbf{mn}} - E(\sum_{\mathbf{n}} C_{\mathbf{n}}^2 - 1). && (2.67)
\end{aligned}$$

Setting the derivative with respect to an arbitrary coefficient, $C_{\mathbf{k}}$, to zero, the stationary condition becomes (assuming $\hat{\mathcal{H}}$ to be a real Hermitian operator and Ψ_{FCI} to be a real wavefunction)

$$\frac{\partial \mathcal{L}}{\partial C_{\mathbf{k}}} = \sum_{\mathbf{m}} C_{\mathbf{m}} H_{\mathbf{mk}} + \sum_{\mathbf{n}} C_{\mathbf{n}} H_{\mathbf{kn}} - 2EC_{\mathbf{k}} = 0 \tag{2.68}$$

$$\sum_{\mathbf{m}} H_{\mathbf{nm}} C_{\mathbf{m}} - EC_{\mathbf{n}} = 0 \tag{2.69}$$

$$(H_{\mathbf{nn}} - E)C_{\mathbf{n}} + \sum_{\mathbf{m} \neq \mathbf{n}} H_{\mathbf{nm}} C_{\mathbf{m}} = 0. \tag{2.70}$$

These stationary conditions for all $\mathbf{k}$ can be written compactly in matrix notation as

$$(\mathbf{H} - E\mathbf{I})\mathbf{C} = 0 \tag{2.71}$$

$$\mathbf{HC} = E\mathbf{C}, \tag{2.72}$$

which is a standard Hermitian eigenvalue problem for the Hamiltonian matrix $\mathbf{H}$. Thus, minimisation of the expectation value of the energy by variational optimisation of the expansion coefficients of the linear parameterisation results in the original eigenvalue formulation of the Schrödinger equation.

Exact diagonalisation of the Hamiltonian in the basis of N_{FCI} Slater determinants leads to the set of N_{FCI} eigenpairs whereby the m-th eigenfunction can be identified with the m-th state and the corresponding m-th eigenvalue with its respective energy. Due to the linearity of the variational expansion, the m-th eigenvalue provides a rigorous upper bound to the energy of the m-th exact solution to the Schrödinger equation. In the limit of a complete underlying one-particle basis, the exact wavefunctions and their energies are recovered.

The FCI wavefunction can also be thought of as generated from a single reference configuration, typically the HF state vector which tends to dominate the FCI wavefunction in many systems. These generation processes create a series of occupation number vectors by vacating states that are occupied in the reference state and occupying states which are unoccupied in the reference vector instead. These generated occupation number vectors can thus be characterised according to how many particles in the reference state have been excited from one single-particle state to another. In this manner, the occupation number vectors are referred to as single (S), double (D), triple

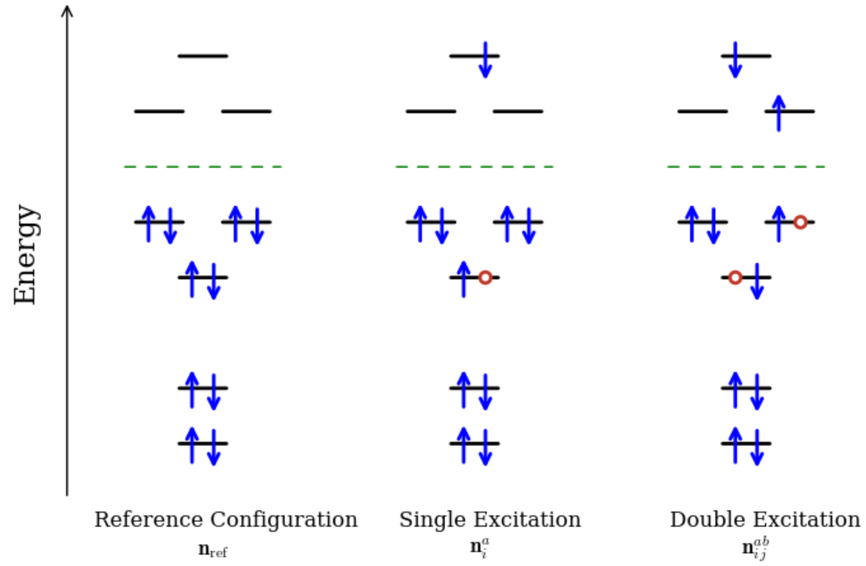

Fig. 2.1 Illustration of the excitation level classification of configurations. The full Hilbert space is spanned by the configurations which can be generated by distributing the N particles amongst the M single particle states. These configurations are classified by their excitation level from the reference configuration $\mathbf{n}_{\mathrm{ref}}$, with an m-fold excitation exciting m particles from the occupied states $i, j, k, \ldots$ in $\mathbf{n}_{\mathrm{ref}}$ to the unoccupied states $a, b, c \ldots$ in $\mathbf{n}_{\mathrm{ref}}$. Single excitations are denoted by $\mathbf{n}_i^a$, double excitations by $\mathbf{n}_{ij}^{ab}$, etc. In the case that the reference configuration represents the Hartree-Fock Slater determinant $\mathbf{n}_{\mathrm{ref}} = \mathbf{n}_{\mathrm{HF}}$ constructed from the lowest N HF spin orbitals, all excited determinants are higher in energy than $\mathbf{n}_{\mathrm{HF}}$ as the excitation process involves exciting particles (blue arrows) into spin orbitals above the Hartree-Fock Fermi energy (green dotted line), thereby introducing holes (red circles) below this energy.

(T), quadruple (Q), ..., N-fold excitations of the reference configuration (Figure 2.1).

$$\Psi_{\mathrm{FCI}} = C_{\mathbf{n}_{\mathrm{ref}}} |\mathbf{n}_{\mathrm{ref}}\rangle + \sum_{ia} C_{\mathbf{n}_i^a} |\mathbf{n}_i^a\rangle + \sum_{\substack{i<j \\ a<b}} C_{\mathbf{n}_{ij}^{ab}} |\mathbf{n}_{ij}^{ab}\rangle + \sum_{\substack{i<j<k \\ a<b<c}} C_{\mathbf{n}_{ijk}^{abc}} |\mathbf{n}_{ijk}^{abc}\rangle + \ldots \tag{2.73}$$

$$= \sum_{\mathbf{n}} C_{\mathbf{n}} |\mathbf{n}\rangle \tag{2.74}$$

Since the Hamiltonian operator contains only one- and two-body terms, it only connects occupation number vectors which are at most two-particle substitutions of each other. A general matrix element $H_{\mathbf{mn}} = \langle\mathbf{m}|\hat{\mathcal{H}}|\mathbf{n}\rangle$ can be evaluated using the Slater-Condon rules[85, 86], as given in Table 2.1. The diagonal elements of the Hamiltonian matrix $H_{\mathbf{nn}}$ are energies of the occupation number vectors $|\mathbf{n}\rangle$. As a result, the Hamiltonian matrix is diagonally dominant in this basis, and since each occupation number vector is only connected to $\mathcal{O}[N^2M^2]$ other occupation number vectors, it is a sparse matrix. However, a difficulty of the FCI method is that the

Differing orbitals	One-electron term	Two-electron term
None	$\sum_i \langle i\vert\hat{h}\vert i\rangle$	$\sum_{i<j}[\langle ij\vert ij\rangle - \langle ij\vert ji\rangle]$
$i \to a$	$\langle i\vert\hat{h}\vert a\rangle$	$\sum_j[\langle ij\vert aj\rangle - \langle ij\vert ja\rangle]$
$ij \to ab$	0	$\langle ij\vert ab\rangle - \langle ij\vert ba\rangle$
> 2	0	0

Table 2.1 The Slater-Condon rules[85, 86] for evaluating the matrix elements between Slater determinants.

number of occupation number vectors in the Hilbert space grows factorially with the number of single particle states M and particles $N = N_\alpha + N_\beta$,

$$N_{\text{FCI}} = \binom{\frac{M}{2}}{N_\alpha} \times \binom{\frac{M}{2}}{N_\beta}, \tag{2.75}$$

and exact diagonalisation of the Hamiltonian in this basis is thus NP-complete (in M). Although the size of this space may be reduced somewhat by symmetry, storage and subsequent diagonalisation of the full Hamiltonian is prohibitively expensive for all but the most trivial systems. In order to alleviate some of the computational expense, iterative diagonalisation techniques such as the Lanczos or Davidson method[87–89] are used which exploit the sparseness of the matrix to extract only selected eigenpairs. In addition, the matrix elements can be evaluated ‘on the fly’, resulting in a direct CI calculation[90]. However, despite these advancements, the FCI wavefunction rapidly becomes intractable which makes systems of only moderate size too expensive to study at this level of theory with an N_2 system in a space of $\mathcal{O}[10^{10}]$ determinants amongst the largest applications to date[91]. As a result, even though FCI is exact for a given single-particle basis, FCI calculations for small systems generally serve as useful benchmarks for other methods, exhibiting their strengths and weaknesses in a transparent manner.

2.6 Further Approximate Solution Methods

Since exact diagonalisation scales binomially with system size, exact eigenstates in the form of an FCI wavefunction can only be obtained for small systems, approximate solution methods need to be employed instead. This section attempts to provide a minimal overview over the many techniques available each of which has its own delicate compromise between desired accuracy and affordable computational cost.

Dynamical correlation can be captured by post Hartree-Fock methods, which start from the HF Slater determinant and its optimised HF orbitals and add dynamical correlation onto the single configuration reference. One of the most economical post HF-methods is Møller-Plesset perturbation theory (MPx)[92] which partitions the Hamiltonian into an exactly solvable reference Hamiltonian, chosen to be the Fock operator, and a perturbing correction, the difference between the true Hamiltonian and the Fock operator. The associated energy and wavefunction of this Hamiltonian are expanded out as Taylor series and the terms can be solved for to give the x-th order correction to the energy, whereby the HF state and energy represent the zero-order wavefunction and the sum of zero- and first-order corrections. By adding the second-order correction, the second-order Møller-Plesset (MP2) energy is obtained[37]

$$E_{\mathrm{MP2}} = E_{\mathrm{HF}} + \sum_{a>b,i>j} \frac{|\langle \mathbf{n}_{\mathrm{HF}}|\hat{\mathcal{H}}|\mathbf{n}_{ij}^{ab}\rangle|^2}{\epsilon_a + \epsilon_b - \epsilon_i - \epsilon_j}, \tag{2.76}$$

which provides surprisingly accurate, size-extensive, yet non-variational, correction at low cost[93]. Higher order correction terms are costly, and the MP series does not converge unconditionally[94]. Additionally, the dominance of the single determinant reference makes MP2 ill suited for systems with significant static correlation.

A further standard model which incorporates effects of correlation, mostly of dynamical nature, is the Configuration Interaction (CI) method[95] which arises naturally from FCI ansatz by truncating the wavefunction expansion to a subset of occupation number vectors of the full N-electron Hilbert space. The cost limitations of FCI are thus reduced by truncating its space at a given excitation level with respect to a reference occupation number vector, typically the HF state. This results in a series of CI methods denoted by CIS, CISD, CISDT, CISDTQ . . . with a hierarchy of successively more accurate wavefunction by including up to single, double, triple, quadruple, . . . excitations of the reference determinant[96]. This truncation is variational, the FCI energy is approached monotonically from above and the FCI wavefunction is recovered as the truncation level is increased to the N-th level. The advantage of an iterative CI diagonalisation is that its cost scales polynomially with excitation level n as $\mathcal{O}[N^{2n+2}]$. It is interesting to note that if the HF determinant is used as reference occupation number vector the inclusion of only single-excitations has no effect due to the zero Hamiltonian matrix elements connecting the HF occupation number vector and its single excitations according to the Brillouin theorem[97, 98]. In general, lower order excited configurations are often more important than higher orders and for single-reference systems, where the reference configuration provides a good zero-order approximation, the series will rapidly converge[99]. Since these CI methods start from a single reference, they efficiently describe dynamical correlation but are likely to fail for multireference systems due to the difficulty building in static correlation in an expansion localised around a single occupation number vector. Inclusion of higher excitation levels in the series can retrieve more of the static correlation but at the same time also substantially increases the cost of a calculation. All truncated CI methods suffer from their lack of size extensivity and size consistency, meaning their energies do not scale correctly with system size and an ever smaller fraction of the correlation energy is captured as system sizes increase[100, 37, 101]. Additionally, the CI wavefunction converges slowly with number of variational parameters towards the FCI limit, partly due to the difficulties encountered when describing Coulomb cusps by determinantal expansions.

One of the most efficient and accurate post-HF methods is Coupled Cluster Theory (CC)[102–106] which expresses the wavefunction as non-linear parameterisation of Slater determinants in product form

$$\Psi_{\mathrm{CC}} = \left[\prod_{i,a}(1+\hat{X}_i^a)\right]\left[\prod_{a>b,i>j}(1+\hat{X}_{ij}^{ab})\right]\ldots\left|\mathbf{n}_{\mathrm{ref}}\right\rangle, \tag{2.77}$$

where $\hat{X}_i^a = t_i^a a_a^\dagger a_i$ is an excitation operator with coefficient t_i^a. An alternative formulation of the CC wavefunction is given by its exponential ansatz in terms of the cluster operator $\hat{T}$

$$\Psi_{\mathrm{CC}} = e^{\hat{T}}\left|\mathbf{n}_{\mathrm{ref}}\right\rangle = \exp\left(\sum_{ia} t_i^a a_a^\dagger a_i + \sum_{a>b,i>j} t_{ij}^{ab} a_a^\dagger a_b^\dagger a_i a_j + \ldots\right)\left|\mathbf{n}_{\mathrm{ref}}\right\rangle. \tag{2.78}$$

Variational optimisation of the CC wavefunction and its energy is only possible for small systems. Instead, the CC amplitudes are solved for by projecting the Schrödinger equation onto a set of states $\langle\mu|$ which spans the space of all determinants that can be obtained by linear application of the truncated cluster operator $\hat{T}$ to the reference state[37]

$$\langle\mu|e^{-\hat{T}}\hat{\mathcal{H}}e^{\hat{T}}|\mathbf{n}_{\mathrm{ref}}\rangle = 0, \tag{2.79}$$

and the resulting CC energy

$$E_{\mathrm{CC}} = \langle\mathbf{n}_{\mathrm{ref}}|e^{-\hat{T}}\hat{\mathcal{H}}e^{\hat{T}}|\mathbf{n}_{\mathrm{ref}}\rangle \tag{2.80}$$

is in general not variational. Much like CI, truncating the CC expansion at a given excitation level n produces a hierarchy of methods denoted by CCSD, CCSDT, CCSDTC, … with increasing accuracy and computational scaling of $\mathcal{O}[N^{2n+2}]$, tending towards the FCI limit for a full cluster operator[37]. In contrast to a CI expansion truncated at level n which is restricted to determinants with excitation levels $\leq n$, a truncated CC wavefunction contains contributions from all states in the Fock space as the product form allows access to higher level excitations through the cumulative effect of multiple low-level excitations. The product excitations implicitly approximate contributions of excited configurations above the truncation level up to infinite order and in the limit of a full cluster operator the FCI state is recovered, meaning that the truncated CC wavefunction may be regarded as a particular approximation to the FCI state. The product form of the CC wavefunction thus makes it manifestly separable and imposes size-extensivity. Although CCSDT and higher level truncation methods produce accurate results, their computational costs are too high for practical application, and an effective compound technique has been devised which uses perturbation theory to approximate the inclusion of connected triple contributions on to the CCSD wavefunction. This CCSD(T) method, often referred to as the 'gold standard' of *ab-initio* quantum chemistry, only increases the scaling to $\mathcal{O}[N^7]$[107] and has been shown capable of producing a range of molecular properties within 1 kcal mol^{-1} chemical accuracy once finite basis set error is removed[108]. Still, since tractable CC wavefunctions are inherently single reference, they fundamentally break down for strongly correlated system.

For systems with pronounced static correlated multireference (MR) methods provide preferred approaches. Multireference coupled cluster (MRCC) theories and alternative methods of evaluating the CC amplitudes are devised to alleviate this limitation, but have generally proved difficult to implement such that their development has been slow and is still ongoing. One means to improve a truncated CI wavefunction, which is typically based on a set of fixed orbitals generated in a preceding HF optimisation, in order to retrieve a larger fraction of static correlation is through simultaneous variational optimisation of the configuration expansion coefficients and the expansion coefficients of the spin orbitals. This approach, known as multiconfigurational self-consistent field (MCSCF)[109], results in a more flexible wavefunction than the corresponding CI wavefunction. One particularly common method is the complete active space self-consistent field (CASSCF) technique[110–112]. This approach selects a subset of occupied and virtual orbitals as active space, in which the wavefunction is solved for exactly while the remaining orbitals are kept frozen. Subsequently, the occupied, active and virtual spaces are rotated to minimise the energy[113]. This two-step cycle is repeated until convergence is achieved. This optimisation of the non-linear wavefunction parameterisation is more difficult and, in practice, MCSCF wavefunctions are restricted to small determinant expansions which are adequate for the description of static correlation but inadequate for the description of dynamical correlation. Dynamic correlation can be added on top of a MCSCF or CASSCF wavefunction by perturbation theory (CASPT2)[114–116], a multireference CI expansion (MRCI or CASCI)[117–123] or CC theory (MRCC or CASCC)[124, 125] such as canonical transformation (CT) theory[126], an approximate scheme.

In principle all static and dynamic correlation can be captured by density functional theory (DFT) which is a density-based method. This approach is based on the Hohenberg-Kohn theorem which states that the electron density uniquely determines all ground state properties of a system and that a unique universal functional of the electron density exists which can be used to find the exact electron density[24]. The most commonly applied approach is the Kohn-Sham formalism which introduces an artificial non-interacting reference system with exactly the same electron density as the true interacting system. The energy is thus written as functional of the electron density ρ and partitioned into several contributions[25]

$$E[\rho] = T_S[\rho] + \int d\mathbf{r}\rho(\mathbf{r}) \left(V_{\text{ext}}(\mathbf{r}) + \frac{1}{2}\Phi(\mathbf{r}) \right) + E_{\text{xc}}[\rho], \tag{2.81}$$

where $T_S[\rho]$ denotes the kinetic energy of the non-interacting reference system, $V_{\text{ext}}(\mathbf{r})$ the external potential, $\Phi(\mathbf{r})$ the classical Coulomb potential and $E_{\text{xc}}[\rho]$ the non-classical exchange correlation energy. The description of electron correlation in DFT is therefore entirely determined by the choice of the exchange-correlation functional. Unfortunately, the universal functional is unknown. Many approximate exchange-correlation functionals of various complexity have been designed. A simple proposal for defining $E_{\text{xc}}[\rho]$ is the Local Density Approximation (LDA) which assumes the electron density to be uniform at a local level. DFT may produce good results in some cases at little more computational cost than HF theory, or even lower costs with recent linear-scaling implementations. However, each functional is limited in its applicability to only a subset of systems and DFT results have often been shown to be outside chemical accuracy compared to experimental data. Since the exact $E_{\text{xc}}[\rho]$ is unknown, current DFT methods cannot capture all static and dynamic correlation and there is also no way of systematically improving a DFT result. It can be stated that DFT is rather poor at capturing static correlation[127].

2.7 Beyond Traditional Quantum Chemical Methods: Tensor Network States Approaches

In addition, to conventional quantum chemical post-Hartree-Fock methods, progress in quantum information theory lead to the development of sophisticated approaches which decompose the full FCI tensor to obtain highly accurate and faithful representations of the FCI wavefunction.

2.7.1 Entanglement Entropy and Area Laws

The description of quantum many-body states in strongly correlated systems are central to understanding a wealth of complex phenomena in condensed matter physics and quantum chemistry. A significant number of these systems are governed by local interactions meaning interactions whose strength decays at least exponentially with distance (beyond a distance cutoff). Naive numerical descriptions of such systems require an intractably large number of parameters since the underlying Hilbert space grows exponentially with system size, specifically

$$\dim(\mathcal{H}) = \mathcal{O}[d^n] \tag{2.82}$$

for a system of size n and local dimension d. As such, exact diagonalisation is hence NP-complete[128]. It has, however, emerged that ground states, and a number of other physical states of local Hamiltonians usually occupy a tiny submanifold of the Hilbert space, also referred to as 'natural corner of the Hilbert space'. States living in this tiny submanifold commonly satisfy an area law rooted in the locality of interactions. The latter not only implies a decay of two-body correlation functions but also stronger forms of locality which can be captured using concepts of entanglement in quantum many-body systems[53]. For this purpose, the von Neumann entanglement entropy is defined[129, 130]

$$S(\rho_{\mathcal{R}}) = -\mathrm{Tr}[\rho_{\mathcal{R}} \log_2 \rho_{\mathcal{R}}], \tag{2.83}$$

where $\rho_{\mathcal{R}}$ is the reduced density matrix of the quantum state $\psi_{\mathcal{R}}$ in the region $\mathcal{R}$. $S(\rho_{\mathcal{R}})$ represents a measure for the entanglement between the region $\mathcal{R}$ and the complementary region $\bar{\mathcal{R}}$[131] which is, however, only meaningful for pure, that is non-degenerate, states. If the two regions are not entangled, $S(\rho_{\mathcal{R}}) = 0$. Otherwise, the entropy will be larger, being bounded from above by its maximum value $S(\rho_{\mathcal{R}}) \leq |\mathcal{R}| \log_2(d)$ which scales with the size $|\mathcal{R}|$ of the region $\mathcal{R}$. For random states, this means that the entropy usually scales extensively with size $S(\rho_{\mathcal{R}}) = \mathcal{O}[|\mathcal{R}|]$[53]. It has emerged that ground states, and a number of other physical states of local and gapped Hamiltonians satisfy an area law which states that the entanglement entropy $S(\rho_{\mathcal{R}})$ for every region $\mathcal{R}$ obeys

$$S(\rho_{\mathcal{R}}) \leq \mathcal{O}[\partial|\mathcal{R}|], \tag{2.84}$$

where $\rho_{\mathcal{R}}$ is the reduced density matrix of the quantum state $\psi_{\mathcal{R}}$ in the region $\mathcal{R}$ and $\partial|\mathcal{R}|$ is the perimeter of the region $\mathcal{R}$[132, 133, 55]. Thus, the entanglement between the region $\mathcal{R}$ and its complementary region $\bar{\mathcal{R}}$, as measured by the entanglement entropy, grows only like the boundary area of $\mathcal{R}$ and not extensively like its volume. This is a consequence of the finite correlation length[134, 135] which means that only subregions in the immediate vicinity of the boundary area are correlated with subregions on the other side of the boundary. Such area laws have been proven for all gapped Hamiltonians in 1D[136–138] and it is expected that gapped local systems in higher dimensions[132] also satisfy an area law, supported by numerical examples and theoretical arguments[139], although a general proof for arbitrary dimensions is still lacking. Yet, critical quantum systems with long-ranged interactions and a spectral gap shrinking to zero with system size violate area laws, albeit their logarithmic corrections to the area law are typically small[132, 140]. In contrast to random quantum states, ground and other physical states satisfying area laws or showing only small violations thereof display thus much less entanglement which effectively quantifies the relevant number of degrees of freedom that have to be taken into account[55]. This suggests that the exact FCI wavefunction of quantum many-body states may be efficiently approximated by alternative more compact representations.

2.7.2 Decomposing the FCI Wavefunction Ansatz

Any arbitrary wavefunction like eigenstates of the Hamiltonian which lives in a Hilbert space of $(\mathbf{C}^d)^{\otimes M}$ can be parameterised as

$$|\Psi_{\text{FCI}}\rangle = \sum_{n_1,n_2,\ldots,n_M}^{d} C_{n_1\ldots n_M} |n_1\rangle \otimes |n_2\rangle \otimes \ldots \otimes |n_M\rangle \tag{2.85}$$

$$= \sum_{n_1,n_2,\ldots,n_M}^{d} C_{n_1\ldots n_M} |n_1 n_2 \ldots n_M\rangle , \tag{2.86}$$

where d denotes the dimension of the local Hilbert space of the single-particle basis states $\{|n_i\rangle\} = \{|1\rangle, |0\rangle\}$. The coefficients $C_{n_1\ldots n_M}$ are part of the full FCI tensor C, a rank M tensor with $\mathcal{O}[d^M]$ coefficients. Whilst this FCI ansatz describes $|\Psi_{\text{FCI}}\rangle$ exactly within a given single-particle basis, it grows exponentially with system size and is therefore a computationally inefficient description for growing system sizes. Efficient wavefunction ansatzes are therefore needed which reduce the complexity in the representation of $|\Psi_{\text{FCI}}\rangle$ and allow for efficient computational treatments. The existence of area laws, and hence, the reduced amount of entanglement which effectively quantifies the relevant number of degrees of freedom, suggests that physical quantum many-body states which usually live in the small 'natural corner' of the exponentially large Hilbert space may be faithfully described by an efficient parameterisation, although there may be limitations to this intuitive expectation for higher dimensional systems[141]. This concept lies at the core of Tensor Network States (TNS) parameterisations[53–55, 142] and their powerful numerical algorithms such as the Density Matrix Renormalisation Group approach (DMRG)[56, 143, 144] and its higher-dimensional analogues[55] which variationally optimise different classes of TNS[53–55, 142]. Whilst a vast array of different TNS exists, the following theoretical descriptions will focus on those which are most relevant to this thesis.

2.7.3 Tensor Network States in One Dimension: Matrix Product States

Ground states of gapped local Hamiltonians in one dimension are well described by Matrix Product States (MPS)[145] since both fulfil the area law. According to the latter, the entanglement entropy, which represents a measure for the entanglement between a region $\mathcal{R}$ and its compliment, scales as the boundary of this region $\partial|\mathcal{R}|$ which suggests that the entanglement between $\mathcal{R}$ and the remainder of the system is concentrated around the boundary between the two regions. This concept lies at the heart of the MPS ansatz for quantum many-body systems. For the purpose of describing the MPS ansatz, a one-dimensional fermionic Hubbard model with $\frac{M}{2}$ lattice sites is considered where the local Hilbert space of each lattice site comprises the states $\{n_s\} = \{|00\rangle, |\uparrow 0\rangle, |0\downarrow\rangle, |\uparrow\downarrow\rangle\}$. In order to construct an MPS for this one-dimensional system, each site is considered to be composed of two virtual subsystems, one on the left and one on the right (Figure 2.2). Furthermore, each of these virtual subsystems is part of a product state of maximally entangled pairs connecting neighbouring sites, that is the right virtual subsystem of site s and the left virtual subsystem of site $s+1$

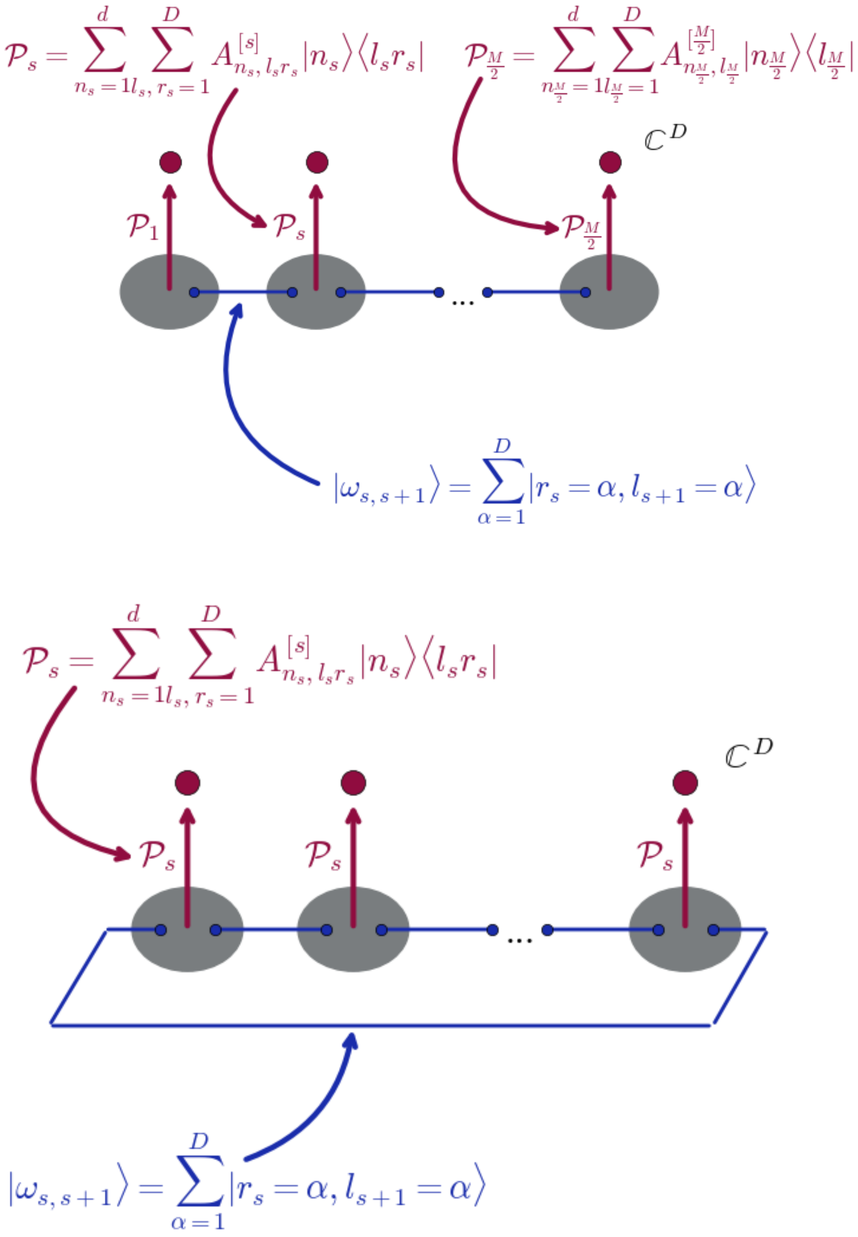

Fig. 2.2 Construction of MPS with open (top) and periodic (bottom) boundary conditions. Each lattice site is associated with two virtual subsystems (blue filled circles). Two such virtual subsystems of two neighbouring sites are placed in a maximally entangled product state $|\omega_{s,s+1}\rangle$ (blue lines). In the case of open boundary conditions, the first and last lattice sites are associated with only one virtual subsystem (top), whilst for periodic boundary conditions the left-most virtual subsystem of the first lattice site is placed in a maximally entangled state with the right-most virtual subsystem of the last lattice site (bottom). At each lattice site s, linear maps $\mathcal{P}_s$ are applied which project from the local Hilbert space of the D-dimensional virtual subsystems to the Hilbert space of the physical lattice site (red filled circles).

are in a maximally entangled state such that the state of this pair is given by

$$|\omega_{s,s+1}\rangle = \sum_{\alpha=1}^{D} |r_s = \alpha, l_{s+1} = \alpha\rangle \,, \tag{2.87}$$

where D represents the Hilbert space of the virtual subsystems. For systems with periodic boundary conditions the left-most subsystem of the first site is maximally entangled with the right-most subsystem of the last $\frac{M}{2}$-th site. In the case of open boundary conditions, the first site has only a right virtual subsystem and the last site only a left virtual system. The pure state $|\omega_{s,s+1}\rangle$ is maximally entangled in the sense that the entanglement entropy of each subsystem assumes the maximum value $\ln(D)$[53, 146]. On this system, linear maps $\mathcal{P}_s : \mathbf{C}^D \otimes \mathbf{C}^D \rightarrow \mathbf{C}^d$ at each of the $s = 1, \ldots, \frac{M}{2}$ lattice sites are applied which project from the Hilbert space of two D-dimensional subsystems to the Hilbert space of the corresponding physical lattice site. The map for each lattice site s can be written as

$$\mathcal{P}_s = \sum_{n_s=1}^{d} \sum_{l_s,r_s=1}^{D} A^{[s]}_{n_s;l_s r_s} |n_s\rangle \langle l_s r_s| \,, \tag{2.88}$$

where $A^{[s]}_{n_s;l_s r_s}$ denotes a rank-3 tensor of the lattice site s whose physical Hilbert space is of dimension d. For open boundary conditions the linear maps of the $s = 1$ and $s = \frac{M}{2}$ sites are formulated in terms of rank-2 tensors

$$\mathcal{P}_1 = \sum_{n_1=1}^{d} \sum_{r_1=1}^{D} A^{[1]}_{n_1;r_1} |n_1\rangle \langle r_1| \,, \qquad \mathcal{P}_{\frac{M}{2}} = \sum_{n_{\frac{M}{2}}=1}^{d} \sum_{l_{\frac{M}{2}}=1}^{D} A^{[\frac{M}{2}]}_{n_{\frac{M}{2}};l_{\frac{M}{2}}} |n_{\frac{M}{2}}\rangle \langle l_{\frac{M}{2}}| \,. \tag{2.89}$$

Thus, for a system with open boundary conditions, the resulting state vector is parameterised as

$$|\Psi_{\mathrm{OBC}}\rangle = \left(\bigotimes_{s=1}^{\frac{M}{2}} \mathcal{P}_s \right) \left(\bigotimes_{s=1}^{\frac{M}{2}-1} |\omega_{s,s+1}\rangle \right) \tag{2.90}$$

$$= \sum_{n_1,n_2,\ldots,n_{\frac{M}{2}}} \mathrm{Tr}[A^{[1]}_{n_1} A^{[2]}_{n_2} \ldots A^{[\frac{M}{2}]}_{n_{\frac{M}{2}}}] \, |n_1 n_2 \ldots n_{\frac{M}{2}}\rangle \tag{2.91}$$

$$= \sum_{n_1,n_2,\ldots,n_{\frac{M}{2}}} \sum_{\alpha\beta\ldots\omega=1}^{D_\alpha D_\beta \ldots D_\omega} A^{[1]}_{n_1;\alpha} A^{[2]}_{n_2;\alpha\beta} \ldots A^{[\frac{M}{2}]}_{n_{\frac{M}{2}};\omega} |n_1 n_2 \ldots n_{\frac{M}{2}}\rangle \,, \tag{2.92}$$

where $A^{[s]}_{n_s}$ represents the matrix (or vector for the first and last lattice sites) with entries $A^{[s]}_{n_s;\alpha\beta} \equiv A^{[s]}_{n_s;l_s r_s}$. Each projection onto a configuration $|n_1 n_2 \dots n_{\frac{M}{2}}\rangle$ is given by a product of matrices, hence, the name Matrix Product State (MPS). In principle, the bond dimension, that is the dimensions of the matrices, may also vary across the system ($D_\alpha \neq D_\beta \neq \dots \neq D_\omega$). Similarly, a state vector in a system with periodic boundary conditions can be written as

$$
\begin{aligned}
|\Psi_{\mathrm{PBC}}\rangle &= \left(\bigotimes_{s=1}^{\frac{M}{2}} \mathcal{P}_s\right)\left(\bigotimes_{s=1}^{\frac{M}{2}} |\omega_{s,s+1}\rangle\right) && (2.93)\\
&= \sum_{n_1,n_2,\dots,n_{\frac{M}{2}}} \mathrm{Tr}[A^{[1]}_{n_1} A^{[2]}_{n_2} \dots A^{[\frac{M}{2}]}_{n_{\frac{M}{2}}}]\, |n_1 n_2 \dots n_{\frac{M}{2}}\rangle && (2.94)\\
&= \sum_{n_1,n_2,\dots,n_{\frac{M}{2}}} \sum_{\alpha\beta\gamma\dots\omega=1}^{D_\alpha D_\beta D_\gamma \dots D_\omega} A^{[1]}_{n_1;\alpha\beta} A^{[2]}_{n_2;\beta\gamma} \dots A^{[\frac{M}{2}]}_{n_{\frac{M}{2}};\omega\alpha}\, |n_1 n_2 \dots n_{\frac{M}{2}}\rangle\,, && (2.95)
\end{aligned}
$$

with $|\omega_{\frac{M}{2},\frac{M}{2}+1}\rangle \equiv |\omega_{\frac{M}{2},1}\rangle$.

2.7.4 The Area Law and Efficient Approximability

It can be shown that for any subset of L consecutive lattice sites the entanglement entropy for a matrix product state is bounded from above by $S(\rho_L) \leq S_{\max} = 2\log_2 D$, which implies that MPS satisfy an area law by construction[53, 147]. Not only is the entanglement scaling of both MPS and ground states of gapped local Hamiltonians the same, but also an even stronger statement can be proven: all states which fulfil an area law, like ground states of gapped Hamiltonian[136, 132], as well as states which violate the area law at most logarithmically, such as critical (gapless) one-dimensional systems, can be efficiently approximated by an MPS[136, 148]. Strictly speaking, this statement follows from an area law of the Rényi entropy $S_R(\rho_{\mathcal{R}}) = \frac{1}{1-\alpha}\log_2(\mathrm{Tr}[\rho^{\alpha}_{\mathcal{R}}])$ ($\alpha \geq 0$)[149] which in the limit of $\alpha \to 1$ reduces to the von Neumann entropy (for situations where a detailed understanding has been reached, this has not been found to make a difference[53]). Specifically, for any local Hamiltonian describing a system with $\frac{M}{2}$ sites whose ground state Ψ_{exact} violates the area law at most logarithmically, an MPS $|\Psi_{\mathrm{MPS}}(D)\rangle$ with bond dimension D can be found which efficiently approximated Ψ_{exact} up to an error

$$
||\,|\Psi_{\mathrm{exact}}\rangle - |\Psi_{\mathrm{MPS}}(D)\rangle\,||^2 \leq \epsilon. \tag{2.96}
$$

It can be proven rigorously, that in order to achieve a desired accuracy ϵ, the required bond dimension D scales polynomially in $\frac{M}{2}$ and $\frac{1}{\epsilon}$[150, 53]. It is worth noting that this MPS representation $|\Psi_{\mathrm{MPS}}\rangle$ can be obtained numerically in a time that grows polynomial with system size for ground states of gapped local Hamiltonians[151]. Owing to these properties the MPS ansatz provides an extremely accurate approximation to natural states of physical systems already at low values of D. At the same time, the $\mathcal{O}[d^{\frac{M}{2}}]$ complexity of the exact FCI wavefunction ansatz is drastically reduced to the $\mathcal{O}[\frac{M}{2}dD^2]$ complexity of an MPS wavefunction of bond dimension D[53]. The latter only scales linearly in system size $\frac{M}{2}$ for constant D as opposed to exponentially in $\frac{M}{2}$. Whilst $D = 1$ yields a product state, a variant of a mean-field approach, with increasing D a larger region of the full Hilbert space is spanned by the MPS ansatz which usually increases the quality of $|\Psi_{\mathrm{MPS}}\rangle$ as approximation to natural states. Allowing D to grow exponentially towards the middle of the system, $(1 \times d), (d \times d^2), \ldots, (d^{\frac{M}{2}-1} \times d^{\frac{M}{2}}), (d^{\frac{M}{2}} \times d^{\frac{M}{2}-1}) \ldots, (d^2 \times d), (d \times 1)$ (for open boundary conditions), the MPS ansatz will eventually span the full Hilbert space[144, 152]. Yet, MPS are only able to describe correlation functions which decay exponentially with distance, meaning that the correlation length of matrix product states is always finite. Thus, they cannot represent algebraically decaying correlation functions, implying that they cannot reproduce properties of critical or scale-invariant systems where the correlation length is known to diverge[54, 153]. Nevertheless, for sufficiently large bond dimensions, MPS can also efficiently approximate states with algebraically decaying correlation functions but other tensor network ansatzes like the Multiscale Entanglement Renormalisation Ansatz (MERA)[154] display a more favourable scaling in system size in these cases[53, 142].

Although $|\Psi_{\mathrm{MPS}}\rangle$ is an efficient description of the relevant quantum many-body state $|\Psi\rangle$, this is not sufficient for the MPS parameterisation to represent an efficient variational ansatz. Crucially, $|\Psi_{\mathrm{MPS}}\rangle$ also needs to allow for efficient extraction of information, usually in the form of correlation functions, expectation values of observables, $\langle\Psi|\hat{\mathcal{O}}|\Psi\rangle$, etc. For an MPS ansatz, these quantities can be efficiently evaluated in $\mathcal{O}[\frac{M}{2}d^2D^3]$ and $\mathcal{O}[\frac{M}{2}d^2D^5]$ time for open and periodic boundary conditions, respectively[55].

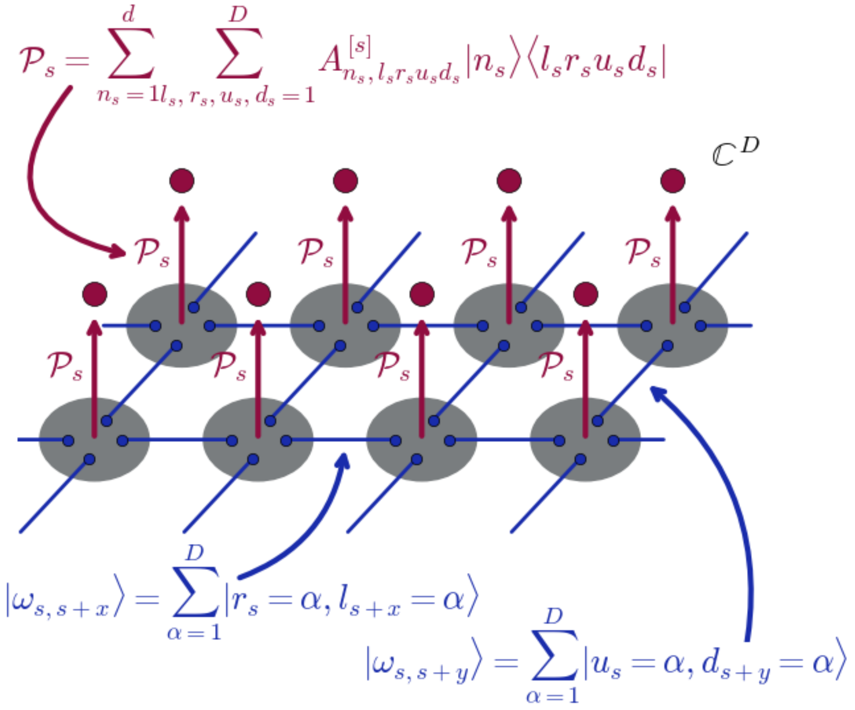

Fig. 2.3 Construction of PEPS. Each lattice site is associated with four virtual subsystems (blue filled circles). Each such virtual subsystem is placed in a maximally entangled product state, $|\omega_{s,s+x}\rangle$ and $|\omega_{s,s+y}\rangle$, (blue lines) with the corresponding virtual subsystem of the adjacent lattice site. At each lattice site s, linear maps $\mathcal{P}_s$ are applied which project from the local Hilbert space of the four virtual subsystems to the Hilbert space of the physical lattice site s (red filled circles).

2.7.5 Tensor Network States in Two Dimensions: Projected Entangled Pair States

The concept of tensor network states is not confined to one dimension but a large variety of tensor network states, also in higher dimensional systems, exists. A natural generalisation of Matrix Product States to higher-dimensional systems are Projected Entangled Pair States (PEPS)[53–55, 142, 155] which can be constructed in the same way as MPS by distributing maximally entangled states between neighbouring sites and on each site and applying linear maps from the virtual space of subsystems to the physical Hilbert space. For concreteness, a two-dimensional square lattice with periodic boundary conditions is considered. Each site of this lattice is thought to be composed of four virtual D-dimensional subsystems each of which is placed in a maximally entangled state with the corresponding subsystem of the adjacent site (Figure 2.3). Thus, labelling the states of the left, right, up and down virtual system at lattice site s by l_s, r_s, u_s and d_s, respectively, the maximally entangle pairs between two sites which are horizontally $(+x)$ and vertically $(+y)$ displaced by one unit give rise to the maximally entangled states

$$|\omega_{s,s+x}\rangle = \sum_{\alpha=1}^{D} |r_s = \alpha, l_{s+x} = \alpha\rangle \qquad |\omega_{s,s+y}\rangle = \sum_{\alpha=1}^{D} |u_s = \alpha, d_{s+y} = \alpha\rangle \,, \tag{2.97}$$

respectively. At each site of the system, linear maps $\mathcal{P}_s : \mathbb{C}^D \otimes \mathbb{C}^D \otimes \mathbb{C}^D \otimes \mathbb{C}^D \to \mathbb{C}^d$ are applied which project from the Hilbert space of the four virtual subsystems at site s to the physical Hilbert space of the lattice site. These local linear maps are given by

$$\mathcal{P}_s = \sum_{n_s=1}^{d} \sum_{l_s,r_s,u_s,r_s=1}^{D} A^{[s]}_{n_s;l_s r_s u_s d_s} |n_s\rangle \langle l_s r_s u_s d_s| \,, \tag{2.98}$$

such that the resulting PEPS state vector can be written as

$$\begin{aligned}
|\Psi_{\text{PEPS}}\rangle &= \left(\bigotimes_{s=1}^{\frac{M}{2}} \mathcal{P}_s \right) \left(\bigotimes_{s=1}^{\frac{M}{2}} |\omega_{s,s+x}\rangle \otimes |\omega_{s,s+y}\rangle \right) &(2.99)\\
&= \sum_{n_1 n_2 \dots n_{\frac{M}{2}}} \mathrm{Tr}[A^{[1]}_{n_1} A^{[2]}_{n_2} \dots A^{[\frac{M}{2}]}_{n_{\frac{M}{2}}}] \, |n_1 n_2 \dots n_{\frac{M}{2}}\rangle &(2.100)\\
&= \sum_{n_1 n_2 \dots n_{\frac{M}{2}}} \sum_{\alpha\beta\gamma\delta\dots\omega}^{D_\alpha D_\beta D_\gamma D_\delta \dots D_\omega} A^{[1]}_{n_1;\alpha\beta\gamma\omega} A^{[2]}_{n_2;\delta\alpha\lambda\eta} \dots A^{[\frac{M}{2}]}_{n_{\frac{M}{2}};\epsilon\zeta\omega\nu} \, |n_1 n_2 \dots n_{\frac{M}{2}}\rangle \,, &(2.101)
\end{aligned}$$

where $A^{[s]}_{n_s}$ denotes the rank-4 tensor with entries $A^{[s]}_{n_s;\alpha\beta\gamma\delta} \equiv A^{[s]}_{n_s;l_s r_s u_s d_s}$. Likewise, a PEPS wavefunction for systems with open boundary conditions can be constructed with modified linear maps for the lattice sites at the edges which are obtained by replacing the rank-5 tensor for a general lattice site by rank-4 tensors for the edges and rank-3 tensors for the corners. More generally, the outlined construction of a PEPS state can be generalised to any lattice shape and dimension[55].

Given their analogy to MPS, PEPS share many properties with their one dimensional counterparts. Hence, they also obey area laws by construction since the entanglement entropy of a region $\mathcal{R}$ with its complement is bounded from above by $\mathcal{O}[N_{\text{bonds}} \log_2 D]$ where N_{bonds} denotes the number of bonds that the boundary $\partial|\mathcal{R}|$ covers[132, 53]. By analogy to MPS, any state can be written as a PEPS provided the bond dimension D is large enough with the full Hilbert space being covered if D grows exponentially in system size[53, 54]. Moreover, PEPS can efficiently approximate ground states of gapped local Hamiltonian provided that the density of states grows at most polynomially with energy[156, 157]. Unlike for MPS, a strong statement on how well PEPS can approximate general states is lacking and ground states of non-local Hamiltonians exist which satisfy the area law but cannot be represented efficiently by PEPS[141]. Yet, numerical evidence[158] suggests that PEPS with a reasonably small and finite D approximate low-energy states of two-dimensional quantum many-body systems well[54]. At finite temperatures, they have also been shown to efficiently approximate thermal states[157, 159]. In contrast to MPS, PEPS can describe algebraically decaying correlations, a typical characteristic of critical points[148]. In principle, they are therefore suitable to describe both, states with finite and infinite correlation lengths, that is gapped phases, as well as critical states.

Still, the extraction of information from a PEPS state is computationally much harder. Contrary to MPS, PEPS cannot be contracted exactly in an efficient manner. Irrespective of the contraction order, the contraction will at some point involve an object with a number of indices that is proportional to $\sqrt{\frac{M}{2}}$, and hence an exponential number of parameters. The contraction is therefore an exponentially hard problem and always requires $\mathcal{O}[\exp(\frac{M}{2})]$ time[54]. Strictly speaking, from the point of view of computationally complexity, the contraction of a PEPS network is contained with the complexity class $\sharp P$[160]. Yet, this obstacle can be overcome with approximate contraction techniques which involve small and ideally controlled errors. One of these approximate contraction schemes[155] works through the network and contracts each column with the subsequent one while the bond dimensions of the new tensors are approximated by αD^2 for some α. By iterating this procedure column by column, the whole network is contracted whilst the size of the tensors always stays bounded. Although this represents an efficient approximate contraction scheme for PEPS, the scaling with D is much less favourable than in one dimension. The most simplest approaches display $\mathcal{O}[D^{12}]$ scaling which can be improved down to $\mathcal{O}[D^{8}]$. This approximate contraction method is therefore limited to much smaller bond dimensions D in comparison the contraction of an MPS ansatz. The approximation is typically very accurate provided that the system is short-range correlated and the introduced error is well controlled. In fact, the accuracy of the approach is rather limited by the bond dimension D that is needed for a good approximation to the ground state. Another approximate contraction scheme[161–163] based on renormalisation ideas approximates block of tensors by one tensor whose bond dimension is appropriately truncated. This approach relies on approximations to the environment, i.e. the remaining network. Whilst the introduced errors are less controlled and the accuracy of the approximations are worse, the scaling in D is more favourable and allows for larger D and thus potentially better approximations to the ground state[142].

2.7.6 Optimisation of MPS, PEPS, ...

Variationally finding the best description of the ground state in terms of a tensor network is equivalent to minimising

$$\min_{|\Psi\rangle \in \text{TNS family}} \frac{\langle\Psi|\hat{\mathcal{H}}|\Psi\rangle}{\langle\Psi|\Psi\rangle}, \tag{2.102}$$

or using a Lagrange multiplier λ to ensure normalisation

$$\min_{|\Psi\rangle \in \text{TNS family}} \left(\langle\Psi|\hat{\mathcal{H}}|\Psi\rangle - \lambda\,\langle\Psi|\Psi\rangle\right), \tag{2.103}$$

where $|\Psi\rangle \in$ TNS family implies that $|\Psi\rangle$ is parameterised as one of the class of tensor networks states such as MPS, PEPS, … Since the simultaneous optimisation of all parameters amounts to a highly non-linear and non-convex global optimisation, this minimisation problem is broken down into a sequence of linear optimisations of the tensors $\left\{A^{[s]}\right\}$ of the TNS. To this end, starting from a randomly chosen tensor at site k, the energy is minimised with respect to $A^{[k]}$, whilst all other tensors $\left\{A^{[s]}\right\}$, $s \neq k$, are held fixed

$$E^{[k]} := \frac{\langle\Psi|\hat{\mathcal{H}}|\Psi\rangle}{\langle\Psi|\Psi\rangle} = \frac{\langle A^{[k]}|K_1|A^{[k]}\rangle}{\langle A^{[k]}|K_2|A^{[k]}\rangle}, \tag{2.104}$$

where K_1 and K_2 represent the kernels of the respective quadratic forms and $|A^{[k]}\rangle$ denotes the vectorised form of the rank-n tensor $A^{[s]}_{n_s;\alpha\beta\dots}$ with the n indices $(n_s, \alpha, \beta, \dots)$ combined into a single one. In fact, the solution to this quadratic and convex optimisation problem is given by the eigenvalue problem $K_1 |A^{[k]}\rangle = E^{[k]} K_2 |A^{[k]}\rangle$[142, 164, 165]. In this way, by iteratively sweeping back and forth through the system and sequentially optimising the tensor at each site, convergence onto a state with low energy is reached.

If this minimisation is performed for an MPS with open boundary conditions, nothing but the extremely successful Density Matrix Renormalisation Group (DMRG)[56, 166, 167] is recovered. Originally, DMRG was invented by White in the field of condensed matter theory. Within this context, DMRG was historically formulated as a renormalisation algorithm based on keeping the states that are most relevant for the entanglement of the system and framed in the language of analysis of reduced density operators over subsystems of the chain. Later Östlund and Rommer discovered its underlying variational class, the MPS[168, 169], implying that DMRG can be reformulated as a variational method within the ansatz space of D-dimensional MPS. Although such a variational minimisation of an MPS can get stuck in principle[164, 165], the procedure works extremely well in practice and generally converges onto the lowest energy $|\Psi_{\text{MPS}}\rangle$, essentially up to machine precision[153, 144, 55] when considering MPS for one dimensional systems. For MPS in particular, many approaches have been devised in order to arrive at an efficient algorithmic realisation of the basic optimisation method and improve upon it. Firstly, the gauge degrees of freedom of the matrix product state are exploited to arrive at an MPS representation in its canonical form which is crucial in practical implementations in order to avoid ill-conditioned matrices[53, 170, 144]. Secondly, each step along the sweep can involve optimising the tensors of pairs of sites, a so-called double variational site, which improves convergence and a better control of the error[53]. In addition to MPS, this variational minimisation approach has also been successfully applied to finite PEPS[155, 55], as well as Tree Tensor Networks (TTN)[171, 172] and MERA[173].

Beyond variational optimisation, tensor network state wavefunctions can also be found with imaginary time evolution approaches whereby an initial state is evolved in imaginary time with the Hamiltonian of interest

$$|\Psi_\tau\rangle = \lim_{\tau\to\infty} \frac{e^{-\tau\hat{\mathcal{H}}} |\Psi_0\rangle}{||e^{-\tau\hat{\mathcal{H}}} |\Psi_0\rangle ||}, \tag{2.105}$$

which results in a projection onto the ground state in the limit of $\tau \to \infty$. A large variety of such imaginary time evolution methods for obtaining ground states exist, including variants of the time-evolving block decimation (TEBD) approach[174–176], as well as techniques based on the time-dependent variational principle[177] and concatenated tensor networks[178]. Even though state-of-the-art PEPS optimisations rely on imaginary time evolution[158, 161, 179, 55] whose long imaginary time limit is realised by applying small time steps $\delta\tau$ with a Trotter-Suzuki decomposition of the imaginary time operator, the considerable computational cost associated with a PEPS wavefunction means that ground state optimisations are more challenging in comparison to their MPS analogous. In practice, additional approximations have to be introduced whereby the PEPS bond dimensions are truncated in an approximate way after each time step. The truncation can be achieved with a number of different schemes[161, 158, 179, 155] each of which provides its own detailed balance between accuracy and efficiency and arriving at an efficient PEPS optimisations with a good compromise between their competing demands still remains challenging[54]. By implementing real time[167, 176] instead of imaginary time evolution these approaches also provide insights into the non-equilibrium dynamics of strongly correlated quantum systems. Thus, thermal states[174, 159] are accessible, as well as time-dependent correlation functions and expectation values of the form $\langle\Psi|e^{it\hat{\mathcal{H}}}\hat{\mathcal{O}}e^{-i\hat{\mathcal{H}}t}|\Psi\rangle$ to study system far from equilibrium[176, 180, 181, 53].

Moreover, bulk systems can be studied without finite size and boundary errors with infinite MPS (iMPS) and infinite PEPS (iPEPS)[158, 182], formulations of MPS and PEPS in the thermodynamic limit (possibly with a broken symmetry with finite period), where a finite unit cell of tensors is repeated through the infinite lattice such as in the iDMRG[183, 184] and iTEBD[158, 185] methods. Furthermore, in the case of tensor network classes such as MPS or PEPS, convergence with respect to the bond dimension D has to be established in order to arrive at the true ground state energy in the infinite D limit. Since increasing the bond dimension D results in tensor networks spanning subspaces of the full Hilbert space which are simultaneously supersets of the previous ones, the quality of the approximate tensor network state improves monotonically. In the limit $D \to \infty$ the exact tensor network state representation of $|\Psi\rangle$ is recovered which allows for reliable extrapolations of the energy to the FCI limit[186–189].

Even though all of the approaches outlined above have been successfully applied to MPS and PEPS, the latter class of tensor networks displays a worse scaling in bond dimensions D, and thus a higher computational cost, than their one dimensional analogues and are therefore typically restricted to smaller values of D in practical application. For this reason, methods with PEPS in two dimensions often achieve worse accuracy than DMRG calculations using MPS as wavefunction ansatz whereby the two dimensional system is mapped onto a one dimensional system with long-ranged interactions. Reasonable system sizes for PEPS are therefore still roughly the same as those which can be treated with two dimensional DMRG approaches[190, 191].

Chapter 3

Zero-temperature Ground State Quantum Monte Carlo Methods

An alternative approach for solving the Schrödinger equation comes from Quantum Monte Carlo (QMC) methods [192–194, 50, 51, 195] which are a group of accurate and versatile stochastic techniques for treating quantum many-body systems. These approaches represent efficient methods to evaluate complex integrals in the high dimensional space of quantum many-particle systems by sampling the integrand statistically and averaging the sampled values. Regardless of the dimensionality, the statistical error in the estimated integral decreases as $N_{\mathrm{MC}}^{-\frac{1}{2}}$ with the number of samples N_{MC}, a consequence of the central limit theorem. There are many different QMC methods of which the two most commonly applied classes are Variational Quantum Monte Carlo (VMC) and various Projector Quantum Monte Carlo (PMC) methods. These QMC methods can equally well be used for finite discrete Hilbert spaces, infinite continuous Hilbert spaces or even for spaces with both continuous and discrete degrees of freedom. In the following, notation appropriate for discrete spaces (sums, matrices, etc.) will be used interchangeably with notation appropriate for continuous spaces (integrals, integral kernels etc.).

3.1 Variational Quantum Monte Carlo Approaches

Typical VMC methods [50, 167, 51] combine the variational principle with Monte Carlo evaluation of integrals by rewriting the expectation value of any general Hermitian operator $\hat{\mathcal{O}}$ such as the Hamiltonian $\hat{\mathcal{H}}$ with respect to a trial wavefunction $|\Psi_{\mathrm{T}}\rangle$. Hence, by making use of the resolution of the identity $\hat{\mathcal{I}} = \sum_{\mathbf{n}} |\mathbf{n}\rangle \langle\mathbf{n}|$ the variational energy can be expressed as

$$E_{\mathrm{VMC}} = \frac{\langle \Psi_{\mathrm{T}} | \hat{\mathcal{H}} | \Psi_{\mathrm{T}} \rangle}{\langle \Psi_{\mathrm{T}} | \Psi_{\mathrm{T}} \rangle} \tag{3.1}$$

$$= \frac{\sum_{\mathbf{n}} \langle \Psi_{\mathrm{T}} | \mathbf{n} \rangle \langle \mathbf{n} | \hat{\mathcal{H}} | \Psi_{\mathrm{T}} \rangle}{\sum_{\mathbf{n}} \langle \Psi_{\mathrm{T}} | \mathbf{n} \rangle \langle \mathbf{n} | \Psi_{\mathrm{T}} \rangle} \tag{3.2}$$

$$= \left(\sum_{\mathbf{n}} \frac{\langle \Psi_{\mathrm{T}} | \mathbf{n} \rangle \langle \mathbf{n} | \Psi_{\mathrm{T}} \rangle \frac{\langle \mathbf{n} | \hat{\mathcal{H}} | \Psi_{\mathrm{T}} \rangle}{\langle \mathbf{n} | \Psi_{\mathrm{T}} \rangle}}{P[\langle \mathbf{n} | \Psi_{\mathrm{G}} \rangle]} P[\langle \mathbf{n} | \Psi_{\mathrm{G}} \rangle] \right) \left(\sum_{\mathbf{n}} \frac{\langle \Psi_{\mathrm{T}} | \mathbf{n} \rangle \langle \mathbf{n} | \Psi_{\mathrm{T}} \rangle}{P[\langle \mathbf{n} | \Psi_{\mathrm{G}} \rangle]} P[\langle \mathbf{n} | \Psi_{\mathrm{G}} \rangle] \right)^{-1} \tag{3.3}$$

$$= \frac{\sum_{\mathbf{n}} E_{\mathrm{L}}(\mathbf{n}) \frac{\langle \Psi_{\mathrm{T}} | \mathbf{n} \rangle \langle \mathbf{n} | \Psi_{\mathrm{T}} \rangle}{P[\langle \mathbf{n} | \Psi_{\mathrm{G}} \rangle]} P[\langle \mathbf{n} | \Psi_{\mathrm{G}} \rangle]}{\sum_{\mathbf{n}} \frac{\langle \Psi_{\mathrm{T}} | \mathbf{n} \rangle \langle \mathbf{n} | \Psi_{\mathrm{T}} \rangle}{P[\langle \mathbf{n} | \Psi_{\mathrm{G}} \rangle]} P[\langle \mathbf{n} | \Psi_{\mathrm{G}} \rangle]} \tag{3.4}$$

$$\equiv \frac{\left[\frac{1}{N_{\mathrm{MC}}} \sum_{k=1}^{N_{\mathrm{MC}}} E_{\mathrm{L}}(\mathbf{n}_k) \frac{\langle \Psi_{\mathrm{T}} | \mathbf{n}_k \rangle \langle \mathbf{n}_k | \Psi_{\mathrm{T}} \rangle}{P[\langle \mathbf{n}_k | \Psi_{\mathrm{G}} \rangle]} \right]_{P[\langle \mathbf{n} | \Psi_{\mathrm{G}} \rangle]}}{\left[\frac{1}{N_{\mathrm{MC}}} \sum_{k=1}^{N_{\mathrm{MC}}} \frac{\langle \Psi_{\mathrm{T}} | \mathbf{n}_k \rangle \langle \mathbf{n}_k | \Psi_{\mathrm{T}} \rangle}{P[\langle \mathbf{n}_k | \Psi_{\mathrm{G}} \rangle]} \right]_{P[\langle \mathbf{n} | \Psi_{\mathrm{G}} \rangle]}} \tag{3.5}$$

$$\equiv \frac{\left\langle E_{\mathrm{L}}(\mathbf{n}_k) \frac{\langle \Psi_{\mathrm{T}} | \mathbf{n}_k \rangle \langle \mathbf{n}_k | \Psi_{\mathrm{T}} \rangle}{P[\langle \mathbf{n}_k | \Psi_{\mathrm{G}} \rangle]} \right\rangle_{P[\langle \mathbf{n} | \Psi_{\mathrm{G}} \rangle]}}{\left\langle \frac{\langle \Psi_{\mathrm{T}} | \mathbf{n}_k \rangle \langle \mathbf{n}_k | \Psi_{\mathrm{T}} \rangle}{P[\langle \mathbf{n}_k | \Psi_{\mathrm{G}} \rangle]} \right\rangle_{P[\langle \mathbf{n} | \Psi_{\mathrm{G}} \rangle]}}, \tag{3.6}$$

where the local energy $E_{\mathrm{L}}(\mathbf{n}) = \frac{\langle \mathbf{n} | \hat{\mathcal{H}} | \Psi_{\mathrm{T}} \rangle}{\langle \mathbf{n} | \Psi_{\mathrm{T}} \rangle}$ has been introduced. The form of $|\Psi_{\mathrm{T}}\rangle$ needs to be such that the local energy $E_{\mathrm{L}}(\mathbf{n})$ is efficiently computable, typically in $\mathcal{O}[N^3]$ time or even better. The notation in the last two lines indicates that the full deterministic sums over all states $\mathbf{n}$ in the Hilbert space are stochastically evaluated by drawing N_{MC} samples of the appropriately reweighted local energy $E_{\mathrm{L}}(\mathbf{n})$ from the normalised probability distribution $P[\langle \mathbf{n} | \Psi_{\mathrm{G}} \rangle]$ which is a suitable function of a guiding wavefunction $|\Psi_{\mathrm{G}}\rangle$, such as the most commonly applied probability density

$$P[\langle \mathbf{n} | \Psi_{\mathrm{G}} \rangle] = \frac{|\, \langle \mathbf{n} | \Psi_{\mathrm{G}} \rangle \,|^2}{\sum_{\mathbf{m}} |\, \langle \mathbf{m} | \Psi_{\mathrm{G}} \rangle \,|^2}. \tag{3.7}$$

A well chosen function as probability density can significantly reduce the statistical error in the MC estimate [196–198], a process which is also referred to as importance sampling. In general, the requirement on $|\Psi_{\mathrm{G}}\rangle$ is such that the probability density assumes a non-zero value $P[\langle \mathbf{n} | \Psi_{\mathrm{G}} \rangle] \neq 0$ if the exact wavefunction $|\Psi_{\mathrm{E}}\rangle$ has $\langle \mathbf{n} | \Psi_{\mathrm{E}} \rangle \neq 0$. Algorithmically, this sampling process is often realised using the Metropolis-Hastings algorithm [199, 200] which generates a sequence of configurations $\{\mathbf{n}\}$ distributed according to the desired probability $P[\langle \mathbf{n} | \Psi_{\mathrm{G}} \rangle]$. Since the estimate of E_{VMC} is evaluated as the mean of the random variable $E_{\mathrm{L}}(\mathbf{n})$ over the visited configurations, its value depends only on the trial wavefunction. Yet, the statistical error in this estimate depends on both Ψ_T and Ψ_G. Although the trial and guiding wavefunction assume a different role, they are usually chosen to be the same function $\Psi_\mathrm{G} = \Psi_\mathrm{T}$. In some circumstances, it might be beneficial to choose $\Psi_\mathrm{G} \neq \Psi_\mathrm{T}$. Reasons for such a choice include cases when Ψ_T needs to be sparse for efficient evaluation of local estimators or when the variance in estimates of expectation values needs to be reduced. This approach is very general and can be extended to any general Hermitian operator $\hat{\mathcal{O}}$ and its estimator $\langle O\rangle$, whereby the local energy is replaced by the corresponding local estimator that is analogously defined by

$$O_\mathrm{L}(\mathbf{n}) = \frac{\langle \mathbf{n}|\hat{\mathcal{O}}|\Psi_\mathrm{T}\rangle}{\langle \mathbf{n}|\Psi_\mathrm{T}\rangle}. \tag{3.8}$$

An important characteristic of the probability distribution in Eq. 3.7 in the case that $\Psi_\mathrm{G} = \Psi_\mathrm{T}$ is the zero-variance property[201]. In the limit that the trial wavefunction Ψ_T tends towards the exact eigenstate Ψ_E of the Hamiltonian $\hat{\mathcal{H}}$, $\hat{\mathcal{H}}\,|\Psi_\mathrm{T}\rangle = E_\mathrm{E}\,|\Psi_\mathrm{T}\rangle$, the local energy $E_\mathrm{L}(\mathbf{n})$ is constant

$$E_\mathrm{L}(\mathbf{n}) = \frac{\langle \mathbf{n}|\hat{\mathcal{H}}|\Psi_\mathrm{T}\rangle}{\langle \mathbf{n}|\Psi_\mathrm{T}\rangle} = E_\mathrm{E}\frac{\langle \mathbf{n}|\Psi_\mathrm{T}\rangle}{\langle \mathbf{n}|\Psi_\mathrm{T}\rangle} = E_\mathrm{E}. \tag{3.9}$$

and therefore independent of $\mathbf{n}$. The estimator E_VMC therefore coincides with the exact eigenvalue E_E and its statistical error vanishes, as the variance

$$\sigma^2(\hat{\mathcal{H}}) = \frac{\langle \Psi_\mathrm{T}|(\hat{\mathcal{H}} - E_\mathrm{VMC})^2|\Psi_\mathrm{T}\rangle}{\langle \Psi_\mathrm{T}|\Psi_\mathrm{T}\rangle} = 0. \tag{3.10}$$

in $E_\mathrm{L}(\mathbf{n})$ is zero in the limit that $|\Psi_\mathrm{T}\rangle = |\Psi_\mathrm{E}\rangle$. The energy estimator E_VMC is thus also referred to as zero-variance estimator. Likewise, expectation values of operators that commute with the Hamiltonian also represent zero-variance estimators.

A typical trial wavefunction $|\Psi_\mathrm{T}\rangle$ is written in form of a Slater-Jastrow function[202, 203]

$$|\Psi_\mathrm{T}\rangle = J\sum_{\mathbf{n}} d_\mathbf{n} D^\alpha_\mathbf{n} D^\beta_\mathbf{n}, \tag{3.11}$$

where $D^\alpha_\mathbf{n}$ denotes a Slater determinant constructed from α spin orbitals and the linear combination of Slater determinants determines the $3N-1$ nodal surface of the wavefunction. The correlating Jastrow factor is given by

$$J = \exp\left(f(\mathbf{r}, \mathbf{p})\right) \tag{3.12}$$

where $f(\mathbf{r}, \mathbf{p})$ consists of a set of functions which explicitly depend on the many interparticle distances and thereby includes the cusp conditions but does not augment the original nodal surface of the Slater determinants. The accuracy of the trial wavefunction is increased by variational optimisation of the parameters $\mathbf{p}$ in $|\Psi_{\mathrm{T}}(\mathbf{p})\rangle$ by minimising the VMC energy $E_{\mathrm{VMC}}(\mathbf{p})$ of the trial wavefunction or the variance $\sigma^2(\hat{\mathcal{H}}, \mathbf{p})$ in the local energy $E_{\mathrm{L}}(\mathbf{n})$[204]. Due to the variational principle, the energy $E_{\mathrm{VMC}}(\mathbf{p})$ will always be an upper bound to the true energy E_{E}, but without knowledge of the exact eigenstate, it is hard to judge how accurate the variational approximation is. In contrast, the smallest possible variance in $E_{\mathrm{L}}(\mathbf{n})$, which is equal to zero, is known a priori and thus a good criterion for the accuracy of a trial wavefunction. Variance minimisation methods [205–207] define a cost function that represents a linear combination of energy and variance each of which can be reweighted or unweighted

$$\mathcal{C}[\mathbf{p}] = c_e E_{\mathrm{VMC}}(\mathbf{p}) + c_v \sigma^2(\hat{\mathcal{H}}, \mathbf{p}) + c_{ew} E_{\mathrm{VMC}}(\mathbf{p})_w + c_{vw} \sigma^2(\hat{\mathcal{H}}, \mathbf{p})_w, \tag{3.13}$$

where c_e, c_v, c_{ew} and c_{vw} determine the relative weight of each cost. In this context, weighted refers to changing the relative weight of each configuration by a factor $\frac{P[\langle \mathbf{n}|\Psi_{\mathrm{T}}'\rangle]}{P[\langle \mathbf{n}|\Psi_{\mathrm{T}}\rangle]}$ based on the changes of the trial wavefunction to account for changes in the probability distribution. Minimisation of this cost function with any suitable algorithm locates the optimal parameters. Current state-of-the-art wavefunction optimisation methods [208] are the Stochastic Reconfiguration (SR) [209–213] and Linear Method (LM) [214–217] which can treat large numbers of non-linear wavefunction parameters so as to minimise the energy of the trial wavefunction. Both methods optimise the trial wavefunction in a subspace Ω of the full Hilbert space which is the tangent space spanned by the wavefunction $|\Psi_{\mathrm{T}}(\mathbf{p})\rangle$ and its first derivatives with respect to the variational parameters

$$\Omega = \mathrm{span}\left(|\Psi_{\mathrm{T}}^0\rangle, |\Psi_{\mathrm{T}}^1\rangle, |\Psi_{\mathrm{T}}^2\rangle, \ldots\right) \tag{3.14}$$

where $|\Psi_{\mathrm{T}}^0\rangle \equiv |\Psi_{\mathrm{T}}\rangle$ and $|\Psi_{\mathrm{T}}^i\rangle \equiv \frac{\partial|\Psi_{\mathrm{T}}\rangle}{\partial p_i}$ for $i > 0$. The SR method can be regarded as approximate imaginary time evolution since it repeatedly applies the operator $\hat{\mathcal{T}} = \hat{\mathcal{I}} - \tau\hat{\mathcal{H}}$, the first order expansion of the imaginary time evolution operator $e^{-\tau\hat{\mathcal{H}}}$, where τ is a small number. The result of each operation with $\hat{\mathcal{T}}$ on $|\Psi_{\mathrm{T}}\rangle$ is projected into the subspace Ω to obtain a new wavefunction expanded in this subspace,

$|\Psi'_{\mathrm{T}}\rangle = \sum_i x_i \, |\Psi^i_{\mathrm{T}}\rangle$. The expansion coefficients x_i can be found by solving the system of linear equations

$$\langle \Psi^i_{\mathrm{T}} | (\hat{\mathcal{I}} - \tau \hat{\mathcal{H}}) | \Psi_{\mathrm{T}} \rangle = \sum_j \langle \Psi^i_{\mathrm{T}} | \Psi^j_{\mathrm{T}} \rangle \, x_j. \tag{3.15}$$

The improved parameters are obtained $p_i^{'} = p_i + \frac{x_i}{x_0}$, after which the subspace Ω is redefined for the new improved wavefunction. This procedure is repeated until the energy of the wavefunction has converged. An alternative method which optimises the wavefunction in the same subspace Ω is the Linear Method (LM) which can be viewed as an approximate Newton method with a built in stabilisation. Instead of imaginary time propagation, the LM method optimises $|\Psi_{\mathrm{T}}\rangle$ in the subspace Ω by finding the lowest energy eigenstate $\mathbf{x}$ in Ω determined by the generalised eigenvalue problem

$$\sum_j \langle \Psi^i_{\mathrm{T}} | \hat{\mathcal{H}} | \Psi^j_{\mathrm{T}} \rangle \, x_j = E \sum_k \langle \Psi^i_{\mathrm{T}} | \Psi^k_{\mathrm{T}} \rangle \, x_k. \tag{3.16}$$

After solving this generalised eigenvalue problem, the variables $\mathbf{p}$ are updated in the same manner as in the SR method. If the changes to the parameters are too large, they become unphysical and need to be scaled down by a line search or rotated and scaled down by adding a diagonal shift. Efficient techniques have been developed to increase the efficiency of the SR and LM method and their capability of treating large numbers of parameters [208].

3.2 Projector Quantum Monte Carlo Approaches

An improvement to the VMC energy can be achieved with PMC methods which represent stochastic implementations of the power method, an iterative method for determining the dominant eigenpair with the largest absolute eigenvalue of a matrix. These stochastic approaches are used to find expectation values of operators for the dominant eigenstate of a matrix or integral kernel that lives in a Hilbert space which can be discrete, infinite continuous or even contain both continuous and discrete degrees of freedom. PMC methods are useful when the Hilbert space is so large that deterministic iterative diagonalisation techniques are unfeasible due to their large memory requirements for storing a single vector. PMC methods drastically reduce this memory requirement by storing only a stochastic sample of the vector elements, also referred to as ensemble of walkers, and computing expectation values as a time average. The dominant eigenstate $|\Psi_{\mathrm{E}}\rangle$ with largest eigenvalue in magnitude E_0 of a Hermitian

Method	Projector	1-particle basis	Quantisation
DMC[218–222]	$e^{-\tau(\hat{\mathcal{H}}-E_0\hat{\mathcal{I}})}$	$\mathbf{r}$	1st
GFMC[223–225]	$e^{-\tau(\hat{\mathcal{H}}-E_0\hat{\mathcal{I}})}$ (samp. τ)	$\mathbf{r}$	1st
FCIQMC[52, 226]	$\hat{\mathcal{I}} - \tau(\hat{\mathcal{H}} - E_0\hat{\mathcal{I}})$	ϕ_i^{orthog}	2nd
AFQMC[227]	$e^{-\tau(\hat{\mathcal{H}}-E_0\hat{\mathcal{I}})}$	$\phi_i^{\text{nonorthog}}$	2nd

Table 3.1 Summary of the most commonly used PMC methods. The annotation ‘samp. τ’ indicates that the value of τ is sampled from a probability density.

operator is obtained by repeated application of a projector $\hat{\mathcal{P}}$ on an initial trial state $|\Psi_{\mathrm{T}}^{(0)}\rangle$ with non-zero overlap with $|\Psi_{\mathrm{E}}\rangle$:

$$\lim_{k\to\infty} (\hat{\mathcal{P}})^k \, |\Psi_{\mathrm{T}}^{(0)}\rangle = \lim_{k\to\infty} |\Psi_{\mathrm{E}}\rangle \, E_0^k \, \langle\Psi_{\mathrm{E}}|\Psi_{\mathrm{T}}^{(0)}\rangle \,. \tag{3.17}$$

Since a projector $\hat{\mathcal{P}}$ of a Hermitian operator can be any function of the operator which has one eigenvalue equal to one and all remaining eigenvalues of absolute magnitude smaller than one, there is a variety of choices for the determination of the ground state of the Hamiltonian $\hat{\mathcal{H}}$. Consequently, several PMC methods exist which, apart from many small details, differ not only in the form of their projectors but also in their choice of basis states that is whether a continuous real space spanned by first quantised states of particle coordinates or a discrete occupation number space spanned by second quantised states of occupation number vectors is employed.

Table 3.1 gives a summary of the most commonly applied PMC methods. For example, Diffusion Monte Carlo (DMC) [218–222] uses the exponential projector $\hat{\mathcal{P}} = e^{-\tau(\hat{\mathcal{H}}-E_0\hat{\mathcal{I}})}$, also known as imaginary time propagator, in a 1st quantised basis of particle coordinates. Even though there is no theoretical upper limit on τ for the exponential projector, small values of τ are used, since the explicit expressions arising from a Suzuki-Trotter decomposition of the imaginary time propagator become only exact in the limit $\tau \to 0$[228]. Green Function Monte Carlo (GFMC) [223–225], a generalisation of DMC, does not contain any time step error and is therefore able to produce accurate energies for small systems but incurs a greater computational expense than DMC. Auxiliary Field Quantum Monte Carlo (AFQMC) [227] uses the Hubbard-Stratonovich transformation[229] of the projector $\hat{\mathcal{P}} = e^{-\tau(\hat{\mathcal{H}}-E_0\hat{\mathcal{I}})}$ to map the many-body problem of interacting particles onto a system of non-interacting particles coupled to a fluctuating external auxiliary field, whilst Monte Carlo sampling is employed to average over different field configurations[230, 231]. Like AFQMC, Full Configuration Interaction Quantum Monte Carlo (FCIQMC)[52, 226] works in the

2nd quantised basis of occupation number vectors, but employs the linear projector $\hat{\mathcal{P}} = \hat{\mathcal{I}} - \tau(\hat{\mathcal{H}} - E_0\hat{\mathcal{I}})$ instead. In particular, this linear projector can only be used for Hamiltonians with bounded spectra given that the τ is bounded by $\tau < \frac{2}{(E_{\max}-E_0)}$ with E_0 and $E_{\max}$ being the minimum and maximum eigenvalues, respectively. The expectation values of the Hamiltonian and of any Hermitian operator which commutes with the Hamiltonian are expressed as mixed estimators

$$\begin{aligned}
\langle O\rangle &= \frac{\langle\Psi_{\mathrm{E}}|\hat{\mathcal{O}}|\Psi_{\mathrm{T}}\rangle}{\langle\Psi_{\mathrm{E}}|\Psi_{\mathrm{T}}\rangle} && (3.18)\\
&= \frac{\sum_{\mathbf{n}}\langle\Psi_{\mathrm{E}}|\mathbf{n}\rangle\langle\mathbf{n}|\hat{\mathcal{O}}|\Psi_{\mathrm{T}}\rangle}{\sum_{\mathbf{n}}\langle\Psi_{\mathrm{E}}|\mathbf{n}\rangle\langle\mathbf{n}|\Psi_{\mathrm{T}}\rangle} && (3.19)\\
&= \left(\sum_{\mathbf{n}}\frac{\langle\Psi_{\mathrm{E}}|\mathbf{n}\rangle\langle\mathbf{n}|\Psi_{\mathrm{T}}\rangle\frac{\langle\mathbf{n}|\hat{\mathcal{O}}|\Psi_{\mathrm{T}}\rangle}{\langle\mathbf{n}|\Psi_{\mathrm{T}}\rangle}}{P[\langle\mathbf{n}|\Psi_{\mathrm{G}}\rangle]}P[\langle\mathbf{n}|\Psi_{\mathrm{G}}\rangle]\right)\left(\sum_{\mathbf{n}}\frac{\langle\Psi_{\mathrm{E}}|\mathbf{n}\rangle\langle\mathbf{n}|\Psi_{\mathrm{T}}\rangle}{P[\langle\mathbf{n}|\Psi_{\mathrm{G}}\rangle]}P[\langle\mathbf{n}|\Psi_{\mathrm{G}}\rangle]\right)^{-1} && (3.20)\\
&= \frac{\sum_{\mathbf{n}}O_{\mathrm{L}}(\mathbf{n})\frac{\langle\Psi_{\mathrm{E}}|\mathbf{n}\rangle\langle\mathbf{n}|\Psi_{\mathrm{T}}\rangle}{P[\langle\mathbf{n}|\Psi_{\mathrm{G}}\rangle]}P[\langle\mathbf{n}|\Psi_{\mathrm{G}}\rangle]}{\sum_{\mathbf{n}}\frac{\langle\Psi_{\mathrm{E}}|\mathbf{n}\rangle\langle\mathbf{n}|\Psi_{\mathrm{T}}\rangle}{P[\langle\mathbf{n}|\Psi_{\mathrm{G}}\rangle]}P[\langle\mathbf{n}|\Psi_{\mathrm{G}}\rangle]} && (3.21)\\
&\equiv \frac{\left[\frac{1}{N_{\mathrm{MC}}}\sum_{k=1}^{N_{\mathrm{MC}}}O_{\mathrm{L}}(\mathbf{n}_k)\frac{\langle\mathbf{n}_k|\Psi_{\mathrm{T}}\rangle}{P[\langle\mathbf{n}_k|\Psi_{\mathrm{G}}\rangle]}\right]_{P[\langle\mathbf{n}|\Psi_{\mathrm{G}}\rangle]\langle\Psi_{\mathrm{E}}|\mathbf{n}\rangle}}{\left[\frac{1}{N_{\mathrm{MC}}}\sum_{k=1}^{N_{\mathrm{MC}}}\frac{\langle\mathbf{n}_k|\Psi_{\mathrm{T}}\rangle}{P[\langle\mathbf{n}_k|\Psi_{\mathrm{G}}\rangle]}\right]_{P[\langle\mathbf{n}|\Psi_{\mathrm{G}}\rangle]\langle\Psi_{\mathrm{E}}|\mathbf{n}\rangle}} && (3.22)\\
&\equiv \frac{\left\langle O_{\mathrm{L}}(\mathbf{n}_k)\frac{\langle\mathbf{n}_k|\Psi_{\mathrm{T}}\rangle}{P[\langle\mathbf{n}_k|\Psi_{\mathrm{G}}\rangle]}\right\rangle_{P[\langle\mathbf{n}|\Psi_{\mathrm{G}}\rangle]\langle\Psi_{\mathrm{E}}|\mathbf{n}\rangle}}{\left\langle\frac{\langle\mathbf{n}_k|\Psi_{\mathrm{T}}\rangle}{P[\langle\mathbf{n}_k|\Psi_{\mathrm{G}}\rangle]}\right\rangle_{P[\langle\mathbf{n}|\Psi_{\mathrm{G}}\rangle]\langle\Psi_{\mathrm{E}}|\mathbf{n}\rangle}}, && (3.23)
\end{aligned}$$

where the factor $\langle\Psi_{\mathrm{E}}|\mathbf{n}\rangle$ has been subsumed in the probability density $P[\langle\mathbf{n}|\Psi_{\mathrm{G}}\rangle]\langle\Psi_{\mathrm{E}}|\mathbf{n}\rangle$ underlying the sampling process. Usually, the probability distribution

$$P[\langle\mathbf{n}|\Psi_{\mathrm{G}}\rangle]\langle\Psi_{\mathrm{E}}|\mathbf{n}\rangle = \frac{\langle\mathbf{n}|\Psi_{\mathrm{G}}\rangle\langle\Psi_{\mathrm{E}}|\mathbf{n}\rangle}{\sum_{\mathbf{m}}\langle\mathbf{m}|\Psi_{\mathrm{G}}\rangle\langle\Psi_{\mathrm{E}}|\mathbf{m}\rangle} \tag{3.24}$$

is used for the evaluation of the expectation value as average over the ensemble of walkers. Although the exact wavefunction Ψ_{E} appearing in the expressions for expectation values is unknown, it can be sampled by repeated application of the projector $\hat{\mathcal{P}}$ or its importance-sampled version. Provided that no approximations are introduced, the PMC estimate has no bias, independent of the guiding and trial wavefunction which only affect the statistical error in the MC estimate. As in the case of VMC, if $\Psi_{\mathrm{G}} = \Psi_{\mathrm{T}}$, which is a common choice, the PMC mixed estimator represents a zero-variance estimator in the limit $\Psi_\mathrm{T} \to \Psi_\mathrm{E}$ and the bias and statistical error in the estimate vanish.

Although PMC methods are exact in principle, in practice, they all suffer from the fermion sign problem when treating fermionic and frustrated systems. The fermion sign problem is related to the fermionic nature of the wavefunction which necessitates positive and negative (or more generally complex) wavefunction amplitudes to be sampled. In all PMC methods, this means that an undesired state grows relative to the fermionic state of interest when a system is evolved by repeated stochastic application of a projector. As a result, the computational cost grows exponentially with system size and the fermion sign problem poses an NP-complete problem[128]. The sign problem manifests itself differently in the various PMC methods. For PMC methods which work in the 1st quantised space of electronic coordinate the dominant state of the projector corresponds to a nodeless bosonic solution. For projector methods working in a 2nd quantised basis the severity of the sign problem is reduced[232]. Although the intrinsic anti-symmetry of the space prevents collapse onto a bosonic solutions, the dominant state of the projector causes an exponentially decreasing signal-to-noise ratio[233]. Many PMC methods therefore employ approximation such as the fixed-node (FN) [218, 234] (or fixed-phase in the case of complex wavefunctions) approximation in DMC or the phaseless approximation [227] in AFQMC. The FN approximation imposes the antisymmetry as constraint upon the solution in the form a $3N-1$ dimensional nodal hypersurface on which the wavefunction is zero and across which it changes sign. The stochastic projection is thus performed subject to the constraint that the projected state has the same nodes as $|\Psi_\mathrm{T}\rangle$ by fixing the phase of the walkers relative to the trial state. In most circumstances $|\Psi_\mathrm{T}\rangle$ is necessarily approximate and the nodes introduce a systematic error in the sampled wavefunction, as well as a systematic bias in expectation values whose quality is intrinsically limited by the quality of the trial wavefunction. In the limit that the nodal surface of the trial state is exact the exact ground state wavefunction is recovered, the bias in expectation values vanishes, and any estimator of an operator that commutes with the Hamiltonian represents a zero-variance estimator. Since the accuracy and efficiency of approximate PMC methods depend crucially on the quality of the trail state, it is common practice to first optimise the trial wavefunction in a VMC optimisation prior to a PMC calculation. It is clear that the principal limitation for both approximate PMC and VMC methods is this fixed-node error, which will always raise the energy and represent a variational upper bound to the exact energy[221]. It has been found difficult to improve upon this limitation, increase the accuracy of the nodal surface and retrieve more of the correlation energy in a systematic and controlled manner through techniques such as backflow corrections[235, 236] or release-node methods [220, 237]. These more sophisticated approaches can significantly improve energy calculated by DMC, reducing typical systematic biases from $\sim$ 3kcal mol^{-1} to within chemical accuracy of 1kcal mol^{-1}[238, 239].

3.3 Full Configuration Interaction Quantum Monte Carlo: FCIQMC

Full Configuration Interaction Quantum Monte Carlo (FCIQMC)[52, 240] is a new wavefunction-based projector method which seeks the solution to the imaginary-time Schrödinger equation. It combines the accuracy of the FCI ansatz with the computational efficiency of Monte Carlo sampling of the projector and wavefunction to realise a stochastic implementation of the power method[233, 51]. The coefficients in the FCI wavefunction ansatz are stochastically represented by a set of discrete, signed walkers within the complete Hilbert space spanned by Slater determinants. In the limit of a sufficiently large number of walkers, the long-time average of walker distribution is equal to the FCI wavefunction, the exact solution for a given single-particle basis. Although the choice of a finite one-particle basis introduces a finite basis set error and limits the physical accuracy of FCIQMC, working in the intrinsically antisymmetric 2nd quantised space of occupation number vectors alleviates the Fermion sign problem[232]. In contrast to many other PMC methods which introduce approximations to circumvent the sign problem that are, however, difficult to improve upon in a systematic and controlled manner, FCIQMC employs effective cancellation algorithms to control the sign problem instead. The exact wavefunction therefore emerges spontaneously in FCIQMC without any a priori wavefunction information. By sampling the wavefunction and evaluating expectation values as time average over stochastic snapshots, FCIQMC only needs storage of non-zero coefficients in the FCI expansion which is often a tiny fraction of the whole Hilbert space, thereby circumventing the memory bottleneck experienced by deterministic iterative diagonalisation techniques. FCIQMC has been shown to reproduce FCI energies for a range of systems well within chemical accuracy. Owing to its reduced computation cost, FCIQMC is capable of treating systems many orders of magnitude larger than those used in existing more traditional FCI approaches. FCIQMC and its variants have been found successful in studies of atomic and molecular systems[241–244], model systems such as the homogeneous electron gas[245] and hubbard models[246], as well as solid-state systems[247]. More recently, developments have also enabled the extension to excited states[248–252], systems at finite temperature[248], the calculations of molecular properties[253, 254], the use of FCIQMC as an FCI-solver in a Multi-Configurational Self-Consistent Field framework, resulting in a stochastic CASSCF approach[255, 256], as well as the application of explicitly correlated methods which reduce the error arising from the use of a finite basis set[257, 258]. Additionally, FCIQMC has also led to further stochastic approaches which aim at solving other types of quantum chemical equations such as the Coupled-Cluster Monte Carlo method[259] and the Density Matrix Quantum Monte Carlo technique[260].

3.3.1 Derivation of FCIQMC Equations

The rational basis for the approach taken by many PMC methods is that the time-dependent Schrödinger equation

$$i\frac{\partial\Psi(\mathbf{r},t)}{\partial t} = \hat{\mathcal{H}}\Psi(\mathbf{r},t) \tag{3.25}$$

can also be viewed as a generalised diffusion equation. If the Hamiltonian of the system does not vary with time, the solutions of the time-dependent Schrödinger equation are of the form

$$\Psi(\mathbf{r},t) = \sum_i c_i(t=0)e^{-i\epsilon_i t}\psi_i(\mathbf{r}), \tag{3.26}$$

where ϵ_i and $\psi_i(\mathbf{r})$ represent the eigenvalues and eigenfunctions of the corresponding time-independent equation. By means of a Wick rotation[68], the time-dependent Schrödinger is transformed into the imaginary-time Schrödinger equation, with $\tau = it$

$$-\frac{\partial\Psi(\mathbf{r},\tau)}{\partial t} = \hat{\mathcal{H}}\Psi(\mathbf{r},\tau), \tag{3.27}$$

thereby converting it to an ordinary differential equation whose solution is formally given by

$$\Psi(\mathbf{r},\tau) = e^{-\tau\hat{\mathcal{H}}}\left|\Psi(\mathbf{r},\tau=0)\right\rangle. \tag{3.28}$$

The Schrödinger equation may thus be integrated in imaginary time to large values of τ yielding a solution to the time-independent Schrödinger equation. By expanding the initial wavefunction $|\Psi(\mathbf{r},\tau=0)\rangle$ in the complete set of orthogonal eigenstates of the

Hamiltonian, $\hat{\mathcal{H}} \left|\Psi_i(\mathbf{r})\right\rangle = E_i \left|\Psi_i(\mathbf{r})\right\rangle$, such that,

$$\left|\Psi(\mathbf{r}, \tau = 0)\right\rangle = \sum_i C_i(\tau = 0) \left|\Psi_i(\mathbf{r})\right\rangle , \tag{3.29}$$

and introducing an arbitrary energy offset, E_{off}, the wavefunction can be written as

$$\Psi(\mathbf{r}, \tau) = \sum_i C_i(\tau = 0) e^{-\tau(\hat{\mathcal{H}} - E_{\text{off}})} \left|\Psi_i(\mathbf{r})\right\rangle , \tag{3.30}$$

which describes the evolution of the individual eigenfunctions of the system in imaginary time. Using the spectral expansion of the operator[50],

$$e^{-\tau\hat{\mathcal{H}}} = \sum_j \left|\Psi_j(\mathbf{r})\right\rangle e^{-\tau E_j} \left\langle\Psi_j(\mathbf{r})\right| , \tag{3.31}$$

the decay of high-energy states relative to low-energy states becomes obvious

$$\Psi(\mathbf{r}, \tau) = \sum_{ij} C_i(\tau = 0) \left|\Psi_j(\mathbf{r})\right\rangle e^{-\tau(E_j - E_{\text{off}})} \left\langle\Psi_j(\mathbf{r})|\Psi_i(\mathbf{r})\right\rangle \tag{3.32}$$

$$= \sum_i C_i(\tau = 0) e^{-\tau(E_i - E_{\text{off}})} \left|\Psi_i(\mathbf{r})\right\rangle . \tag{3.33}$$

If E_{off} is equal to the ground state energy E_0, all states with energy $E_i > E_0$ decay exponentially, with the rate of decay determined by their energy relative to the ground state energy. In the long imaginary-time limit, the wavefunction will be dominated by the lowest energy state

$$\Psi(\mathbf{r}, \tau \to \infty) = \lim_{\tau \to \infty} \sum_i C_i(\tau = 0) e^{-\tau(E_i - E_{\text{off}})} \left|\Psi_i(\mathbf{r})\right\rangle \tag{3.34}$$

$$= C_0(\tau = 0) e^{-\tau(E_0 - E_{\text{off}})} \left|\Psi_0(\mathbf{r})\right\rangle + \mathcal{O}[e^{-\tau(E_i - E_{\text{off}})}], \tag{3.35}$$

where $\{\left|\Psi_0(\mathbf{r})\right\rangle, E_0\}$ represents the lowest energy eigenpair, provided that the initial wavefunction $\left|\Psi(\mathbf{r}, \tau = 0)\right\rangle$ has non-zero overlap with $\left|\Psi_0(\mathbf{r})\right\rangle$.

FCIQMC parameterises the wavefunction in the same manner as FCI which expands the wavefunction in the basis of occupation number vectors representing Slater determinants spanning the complete N-particle Hilbert space

$$\Psi = \sum_{\mathbf{n}} C_{\mathbf{n}} \left|\mathbf{n}\right\rangle . \tag{3.36}$$

Substituting this into the imaginary-time Schrödinger equation (Eq. 3.27) and introducing an energy offset E_{off} to allow for a stationary solution in the long τ limit, gives

$$\sum_{\mathbf{n}} \frac{dC_{\mathbf{n}}(\tau)}{d\tau} |\mathbf{n}\rangle = -\sum_{\mathbf{n}} C_{\mathbf{n}}(\tau)(\hat{\mathcal{H}} - E_{\text{off}}) |\mathbf{n}\rangle \,, \tag{3.37}$$

which if multiplied by $\langle \mathbf{m}|$

$$\sum_{\mathbf{n}} \frac{dC_{\mathbf{n}}(\tau)}{d\tau} \langle \mathbf{m}|\mathbf{n}\rangle = -\sum_{\mathbf{n}} C_{\mathbf{n}}(\tau) \langle \mathbf{m}|(\hat{\mathcal{H}} - E_{\text{off}})|\mathbf{n}\rangle \,, \tag{3.38}$$

reduces to

$$\frac{dC_{\mathbf{m}}(\tau)}{d\tau} = -\sum_{\mathbf{n}} [H_{\mathbf{mn}} - \delta_{\mathbf{mn}} E_{\text{off}})] C_{\mathbf{n}}(\tau). \tag{3.39}$$

In FCIQMC, the energy offset E_{off} is typically split into a reference energy E_{ref} and a shift parameter E_S

$$\frac{dC_{\mathbf{m}}(\tau)}{d\tau} = -\left[\sum_{\mathbf{n}\neq\mathbf{m}} H_{\mathbf{mn}} C_{\mathbf{n}}(\tau)\right] - (H_{\mathbf{mm}} - E_{\text{ref}} - E_S) C_{\mathbf{m}}(\tau). \tag{3.40}$$

In order to demonstrate the deep connection to other projector methods and the power method, Eq. 3.40 can also be obtained through application of the projector $\hat{\mathcal{P}} = \hat{\mathcal{I}} - \delta\tau(\hat{\mathcal{H}} - (E_{\text{ref}} + E_S)\hat{\mathcal{I}})$ onto a wavefunction where $\delta\tau$ is viewed as a short time step in imaginary time τ, such that the k-th application of the projector $\hat{\mathcal{P}}$ onto an arbitrary coefficient $C_{\mathbf{m}}$ gives

$$\begin{aligned}
C_{\mathbf{m}}^{(k)} &= \langle \mathbf{m}|\Psi^{(k)}\rangle && (3.41)\\
&= \sum_{\mathbf{n}} \langle \mathbf{m}|C_{\mathbf{n}}^{(k)}|\mathbf{n}\rangle && (3.42)\\
&= \sum_{\mathbf{n}} \langle \mathbf{m}|[\hat{\mathcal{I}} - \delta\tau(\hat{\mathcal{H}} - (E_{\text{ref}} + E_S)\hat{\mathcal{I}})] C_{\mathbf{n}}^{(k-1)}|\mathbf{n}\rangle && (3.43)\\
&= \langle \mathbf{m}|[\hat{\mathcal{I}} - \delta\tau(\hat{\mathcal{H}} - (E_{\text{ref}} + E_S)\hat{\mathcal{I}})] C_{\mathbf{m}}^{(k-1)}|\mathbf{m}\rangle && (3.44)\\
&\qquad + \sum_{\mathbf{n}\neq\mathbf{m}} \langle \mathbf{m}|[\hat{\mathcal{I}} - \delta\tau(\hat{\mathcal{H}} - (E_{\text{ref}} + E_S)\hat{\mathcal{I}})] C_{\mathbf{n}}^{(k-1)}|\mathbf{n}\rangle && (3.45)\\
&= C_{\mathbf{m}}^{(k-1)} - \delta\tau H_{\mathbf{mm}} C_{\mathbf{m}}^{(k-1)} + \delta\tau(E_{\text{ref}} + E_S) C_{\mathbf{m}}^{(k-1)} - \sum_{\mathbf{n}\neq\mathbf{m}} \delta\tau H_{\mathbf{mn}} C_{\mathbf{n}}^{(k-1)}. && (3.46)
\end{aligned}$$

Substituting this into the derivative of the coefficient with respect to imaginary time

$$\frac{dC_{\mathbf{m}}}{d\tau} = \lim_{\delta\tau\to 0} \frac{C_{\mathbf{m}}^{(k)} - C_{\mathbf{m}}^{(k-1)}}{\delta\tau} \tag{3.47}$$

gives

$$\frac{dC_{\mathbf{m}}}{d\tau} = \lim_{\delta\tau\to 0} \frac{1}{\delta\tau} \Bigg(C_{\mathbf{m}}^{(k-1)} - \delta\tau H_{\mathbf{mm}} C_{\mathbf{m}}^{(k-1)} + \delta\tau(E_{\mathrm{ref}} + E_S) C_{\mathbf{m}}^{(k-1)} \tag{3.48}$$

$$- \sum_{\mathbf{n}\neq\mathbf{m}} \delta\tau H_{\mathbf{mn}} C_{\mathbf{n}}^{(k-1)} - C_{\mathbf{m}}^{(k-1)} \Bigg) \tag{3.49}$$

$$= \lim_{\delta\tau\to 0} \left(- \left[\sum_{\mathbf{n}\neq\mathbf{m}} H_{\mathbf{mn}} C_{\mathbf{n}}^{(k-1)} \right] - H_{\mathbf{mm}} C_{\mathbf{m}}^{(k-1)} + (E_{\mathrm{ref}} + E_S) C_{\mathbf{m}}^{(k-1)} \right) \tag{3.50}$$

$$= - \left[\sum_{\mathbf{n}\neq\mathbf{m}} H_{\mathbf{mn}} C_{\mathbf{n}}^{(k-1)} \right] - (H_{\mathbf{mm}} - E_{\mathrm{ref}} - E_S) C_{\mathbf{m}}^{(k-1)}, \tag{3.51}$$

which exactly matches Eq. 3.40. The linear projector $\hat{\mathcal{P}} = \hat{\mathcal{I}} - \delta\tau(\hat{\mathcal{H}} - (E_{\mathrm{ref}} + E_S)\hat{\mathcal{I}})$ represents the Taylor expansion of the $e^{-\delta\tau\hat{\mathcal{H}}}$ operator with imaginary time τ discretised into B time steps $\delta\tau$, such that $e^{-B\delta\tau\hat{\mathcal{H}}} = e^{-\tau\hat{\mathcal{H}}}$. Since the imaginary time propagator $e^{-\tau\hat{\mathcal{H}}}$ represents the formal solution to the Schrödinger equation and shares the same eigenfunctions as the linear projector, repeated application of $\hat{\mathcal{P}} = \hat{\mathcal{I}} - \delta\tau(\hat{\mathcal{H}} - (E_{\mathrm{ref}} + E_S)\hat{\mathcal{I}})$ will project out the ground state of any non-orthogonal trial state.

Once this initial state has been evolved in imaginary time for a sufficiently long period, corresponding to sufficiently many repeated application of the projector, the wavefunction is proportional to the dominant eigenstate of the system, at which point the coefficients should all be stationary and $\frac{dC_{\mathbf{m}}}{d\tau} = 0\ \forall \mathbf{m}$ and Eq. 3.40 becomes

$$- \sum_{\mathbf{n}} [H_{\mathbf{mn}} - (E_{\mathrm{ref}} + E_S)\delta_{\mathbf{mn}}] C_{\mathbf{n}} = 0 \tag{3.52}$$

$$\sum_{\mathbf{n}} H_{\mathbf{mn}} C_{\mathbf{n}} = (E_{\mathrm{ref}} + E_S) C_{\mathbf{m}}, \tag{3.53}$$

which returns the time-independent Schrödinger equation for the system in form of a standard Hermitian eigenvalue problem, where $\mathbf{C}$ represents the dominant eigenstate of $\mathbf{H}$ with energy $(E_{\mathrm{ref}} + E_S)$.

3.3.2 Stochastic Implementation of FCIQMC

The set of coupled differential equations in Eq. 3.40 describes the evolution of the wavefunction parameters in imaginary time which in the long-imaginary time limit projects out the lowest energy eigenstate of the system. In FCIQMC, a stochastic algorithm[52, 240, 261] realises a finite difference formulation of Eq. 3.40 whereby the wavefunction is represented stochastically by an ensemble of discrete signed walkers which live in the complete N-particle Hilbert space, and are propagated iteratively with small time steps $\delta\tau$. Each walker, α, possesses an associated sign $s_\alpha = \pm 1$ and the instantaneous coefficients, $\{C_{\mathbf{n}}\}$, in the wavefunction expansion is defined to be proportional to the signed sum, $N_{\mathbf{n}}$, of the signed walkers on each Slater determinant,

$$C_{\mathbf{n}} \propto N_{\mathbf{n}} = \sum_{\alpha \in |\mathbf{n}\rangle} s_\alpha \tag{3.54}$$

Representing the wavefunction in this discretised form significantly compresses the information needed to store a stochastic snapshot of the wavefunction. The total number of walkers, N_w, is given by

$$L_1 \propto N_w = \sum_{\mathbf{n}} |N_{\mathbf{n}}|, \tag{3.55}$$

which is thus proportional to the L_1-norm of the wavefunction. Each iteration which propagates the walker population by a time step $\delta\tau$ comprises spawning and death attempts followed by annihilation events. These processes are explained in detail in the following.

Spawning

Every walker attempts to spawn a child from its determinant $|\mathbf{n}\rangle$ onto a connected determinant $|\mathbf{m}\rangle$ which is generated with a normalised probability $p_{\text{gen}}(\mathbf{m}|\mathbf{n}, \mathbf{H})$. In this context, a connection between two configurations refers to a non-zero connecting Hamiltonian matrix element $H_{\mathbf{mn}} \neq 0$. An attempt is made to spawn a new child walker on $|\mathbf{m}\rangle$ with an acceptance probability

$$p_s(\mathbf{m}|\mathbf{n}) = \frac{\delta\tau |H_{\mathbf{mn}}|}{p_{\text{gen}}(\mathbf{m}|\mathbf{n}, \mathbf{H})}. \tag{3.56}$$

This stochastic spawning attempt necessitates the generation of a random number r in the interval $[0, 1)$. When $p_s(\mathbf{m}|\mathbf{n}) < 1$ the spawning attempt is accepted if $p_s(\mathbf{m}|\mathbf{n}) > r$. When $p_s(\mathbf{m}|\mathbf{n}) > 1$, $\lfloor p_s(\mathbf{m}|\mathbf{n}) \rfloor$ walkers are spawned deterministically and one further walker is created with probability $p_s(\mathbf{m}|\mathbf{n}) - \lfloor p_s(\mathbf{m}|\mathbf{n}) \rfloor$ in the manner described above. [1] The sign of the child walker is determined by $\mathrm{sign}(-H_{\mathbf{mn}} N_{\mathbf{n}})$. The spawning step is designed to give a stochastic representation of the first term in Eq. 3.40 involving off-diagonal Hamiltonian matrix elements

$$\frac{dC_{\mathbf{m}}(\tau)}{d\tau} = \underbrace{-\left[\sum_{\mathbf{n}\neq\mathbf{m}} H_{\mathbf{mn}} C_{\mathbf{n}}(\tau)\right]}_{\text{spawning}} -(H_{\mathbf{mm}} - E_{\text{ref}} - E_S) C_{\mathbf{m}}(\tau). \tag{3.57}$$

The generation of connected determinants represents an integral part that is crucial for the efficiency of the algorithm. Whilst it is perfectly valid to use a uniform distribution[261] for $p_{\text{gen}}(\mathbf{m}|\mathbf{n}, \mathbf{H})$ this may become rather inefficient as each determinant is connected to $\mathcal{O}[N^2 M^2]$ others. Instead, distributions which favour preferential generation of determinants with a strong connection $|H_{\mathbf{mn}}|$ will significantly enhance efficiency, in particular in larger spaces[262, 263].

Death / Cloning

Each parent walker present at the beginning of the iteration (i.e. not including the newly spawned child walkers) attempts to die or clone itself with probability

$$p_d(\mathbf{n}) = \delta\tau (H_{\mathbf{nn}} - E_{\text{ref}} - E_S). \tag{3.58}$$

If $p_d(\mathbf{n}) > 0$, the walker dies with probability $p_d(\mathbf{n})$ (the attempt to die is successful if $p_d(\mathbf{n}) > r$ where r is a random number in the interval $[0, 1)$). It is removed from the simulation and the population on $|\mathbf{n}\rangle$ is reduced accordingly. If $p_d(\mathbf{n}) < 0$, the parent walker instead attempts to clone itself with probability $|p_d(\mathbf{n})|$ and the population on $|\mathbf{n}\rangle$ is increased if successful. Cloning attempts are rare events and usually occur in association with low energy determinants and positive values of E_S. The death step is designated to account for the second term in Eq. 3.40 comprising diagonal Hamilton matrix elements

$$\frac{dC_{\mathbf{m}}(\tau)}{d\tau} = \underbrace{-\left[\sum_{\mathbf{n}\neq\mathbf{m}} H_{\mathbf{mn}} C_{\mathbf{n}}(\tau)\right]}_{\text{spawning}} \underbrace{-(H_{\mathbf{mm}} - E_{\text{ref}} - E_S) C_{\mathbf{m}}(\tau)}_{\text{death/cloning}}. \tag{3.59}$$

Annihilation

In the final stage of each iteration, the newly spawned child walkers and surviving

---

[1] $\lfloor A \rfloor$ denotes the largest integer less than or equal to A.

parent walkers are combined. All pairs of walkers with opposite sign which reside on the same determinant annihilate each other and are removed from the simulation such that each determinant only retains walkers of a single sign. All walkers that survive this process form the new walker population which is propagated further in the next iteration.

3.3.3 Energy Estimators

FCIQMC provides two independent energy estimators: the shift, E_S, and the projected energy, E_{proj}. E_S has been introduced as part of the energy offset which according to Eq. 3.52 represents a measure of the energy of the system in the limit of a stationary solution. The shift assumes the role of a population control parameter which, ignoring statistical fluctuations, forces the total number of walkers N_w to remain constant, thereby allowing the system to reach a stationary solution. During an initial growth phase, E_S is fixed at a specified value, typically zero, (fixed-shift mode), after which the value of E_S is allowed to dynamically vary so as to keep N_w constant in τ (variable shift-mode). Its value is adjusted every A steps according to

$$E_S(\tau) = E_S(\tau - A\delta\tau) - \frac{\zeta}{A\delta\tau} \ln \frac{N_w(\tau)}{N_w(\tau - A\delta\tau)}, \tag{3.60}$$

where ζ is a damping parameter[222]. In this phase, $E_{\text{ref}} + E_S$ becomes a meaningful measure of the energy once the walker population has converged on the stationary ground state wavefunction.

An alternative, independent energy estimator is the projected energy E_{proj}, a non-variational mixed estimator, which is obtained by projecting the wavefunction onto a reference state, $|\mathbf{n}_{\text{ref}}\rangle$

$$\begin{aligned}
E_{\text{proj}}(\tau) &= \frac{\langle \mathbf{n}_{\text{ref}}|\hat{\mathcal{H}}|\Psi(\tau)\rangle}{\langle \mathbf{n}_{\text{ref}}|\Psi(\tau)\rangle} && (3.61)\\
&= \frac{\sum_{\mathbf{n}} C_{\mathbf{n}}(\tau)\,\langle \mathbf{n}_{\text{ref}}|\hat{\mathcal{H}}|\mathbf{n}\rangle}{\sum_{\mathbf{n}} C_{\mathbf{n}}(\tau)\,\langle \mathbf{n}_{\text{ref}}|\mathbf{n}\rangle} && (3.62)\\
&= \langle \mathbf{n}_{\text{ref}}|\hat{\mathcal{H}}|\mathbf{n}_{\text{ref}}\rangle + \sum_{\mathbf{n}\neq\mathbf{n}_{\text{ref}}} \langle \mathbf{n}_{\text{ref}}|\hat{\mathcal{H}}|\mathbf{n}\rangle\,\frac{C_{\mathbf{n}}(\tau)}{C_{\mathbf{n}_{\text{ref}}}(\tau)} && (3.63)\\
&= E_{\text{ref}} + \sum_{\mathbf{n}\neq\mathbf{n}_{\text{ref}}} \langle \mathbf{n}_{\text{ref}}|\hat{\mathcal{H}}|\mathbf{n}\rangle\,\frac{C_{\mathbf{n}}(\tau)}{C_{\mathbf{n}_{\text{ref}}}(\tau)} && (3.64)\\
&= E_{\text{ref}} + \sum_{\mathbf{n}\neq\mathbf{n}_{\text{ref}}} \langle \mathbf{n}_{\text{ref}}|\hat{\mathcal{H}}|\mathbf{n}\rangle\,\frac{N_{\mathbf{n}}(\tau)}{N_{\mathbf{n}_{\text{ref}}}(\tau)} && (3.65)
\end{aligned}$$

In the last line, the ratio of coefficients $\frac{C_{\mathbf{n}}(\tau)}{C_{\mathbf{n}_{\text{ref}}}(\tau)}$ has been equated to the ratio of walker populations $\frac{N_{\mathbf{n}}(\tau)}{N_{\mathbf{n}_{\text{ref}}}(\tau)}$ residing on those determinants, which is true in the long imaginary-time limit when the walker distribution is proportional to the ground state FCI wavefunction and $E_{\text{proj}}(\tau)$ equal to the FCI energy. In most circumstances, the reference state, $|\mathbf{n}_{\text{ref}}\rangle$, is defined to be the Hartree-Fock determinant, in which case E_{ref} is the HF energy. According to the Slater-Condon rules[85, 86], only the HF determinant and its doubly (and singly if another reference state is used and Brillouin's theorem[97, 98] does not apply) excited determinants contribute to $E_{\text{proj}}(\tau)$. The accuracy of the projected energy is rather sensitive to the relative error in the coefficient of the reference state and even diverges if $N_{\mathbf{n}_{\text{ref}}} = 0$. The error in $E_{\text{proj}}(\tau)$ is likely to be larger for systems where the reference determinant constitutes only a small fraction of the wavefunction, such as multireference systems. In these systems, instead of a single determinant, the wavefunction can be projected onto a trial wavefunction which is itself a linear combination of determinants[242]. These more sophisticated trial wavefunctions can significantly reduce the stochastic error in $E_{\text{proj}}(\tau)$[264, 248], but also increase the computational expense associated with the calculation of $E_{\text{proj}}(\tau)$ which may become prohibitively expensive.

The availability of these two independent energy estimators is of considerable value. Whilst the projected energy depends exclusively on the walker population at the reference state (or at determinants in the trial wavefunction) and its connected determinants, the shift derives from the dynamics of the entire occupied space. Agreement between these two distinct measures represents therefore a useful indicator of convergence in a calculation.

3.3.4 The Fermion Sign Problem and the Importance of Annihilation

Like all PMC methods FCIQMC needs to control the Fermion Sign problem which arises because repeated stochastic application of the projector causes the growth of an undesired state as the system evolves. In contrast to other PMC methods such as DMC, FCIQMC achieves this without introduction of approximations that are difficult to improve systematically and require a priori knowledge of the nodal structure of the wavefunction to be exact.

In part, this success is based on the use of the 2nd quantised basis of Slater determinants spanning the complete N-particle Hilbert space. Whilst a 1st quantised basis allows states of various symmetry which means that the dominant state of the projector is the physical bosonic ground state of the Hamiltonian and not its fermionic ground state, a 2nd quantised basis allows only states of the correct symmetry and noise from undesired non-fermionic states is thus prevented. However, working in a 2nd quantised basis does not solve the sign problem, as different paths between two states can contribute with opposite signs in which case they cancel and result in a total contribution of smaller absolute magnitude, just as they would in a deterministic calculation. Issues arise when contributions of opposite sign occur at different steps of the sampling process. Moreover, Ψ and $-\Psi$ are sampled with equal probability which further adds to the problem[51]. Yet, compared to a 1st quantised basis the intrinsically antisymmetric 2nd quantised basis reduces the severity of the sign problem[232]. The antisymmetrised basis not only introduces the possibility of internal cancellations but is also reduced in size by a factor of $N!$ which increases the probability for walkers of opposite signs to meet and cancel each other. Further, since states of symmetry other than fermionic are eliminated, a stable signal to noise ratio can be obtained in the limit of large walker populations. FCIQMC reaches exactly this limit with the introduction of the annihilation step which represents an efficient cancellation algorithm.

Although the annihilation process does not explicitly appear in the FCIQMC master equations in Eq. 3.40, it is nevertheless a key element to the control of the Fermion sign problem and the success of the algorithm. In the absence of annihilation the simulation fails to converge. Only in the presence of the annihilation step, the simulation is able to project out the ground state wavefunction with correct values for E_S and E_{proj} provided the total number of walkers in the simulation exceeds a system-dependent critical value. The annihilation step is also responsible for the pattern of walker growth in a typical FCIQMC calculation. In fixed-shift mode, where E_S is typically fixed at zero, the walker population initially grows exponentially. However, annihilation causes the walker growth to spontaneously halt and enter a plateau phase before the beginning of a second exponential growth phase. During the plateau phase the desired wavefunction emerges and its height therefore sets the system dependent minimum required walker number N_w for convergence (Figure 3.1).

This minimum walker number represents the minimum amount of sampling that is required for sufficient annihilation events to occur such that the Fermion sign problem is controlled and a stable signal to noise ratio is obtained. Like in all other PMC methods, noise arises from the growth of an undesired state and the severity of the sign problem is characterised by the difference in energy between the two competing states. Yet, unlike in a 1st quantised basis, where the undesired state is the physical bosonic ground state of the Hamiltonian, this need not be the case in a 2nd quantised basis.

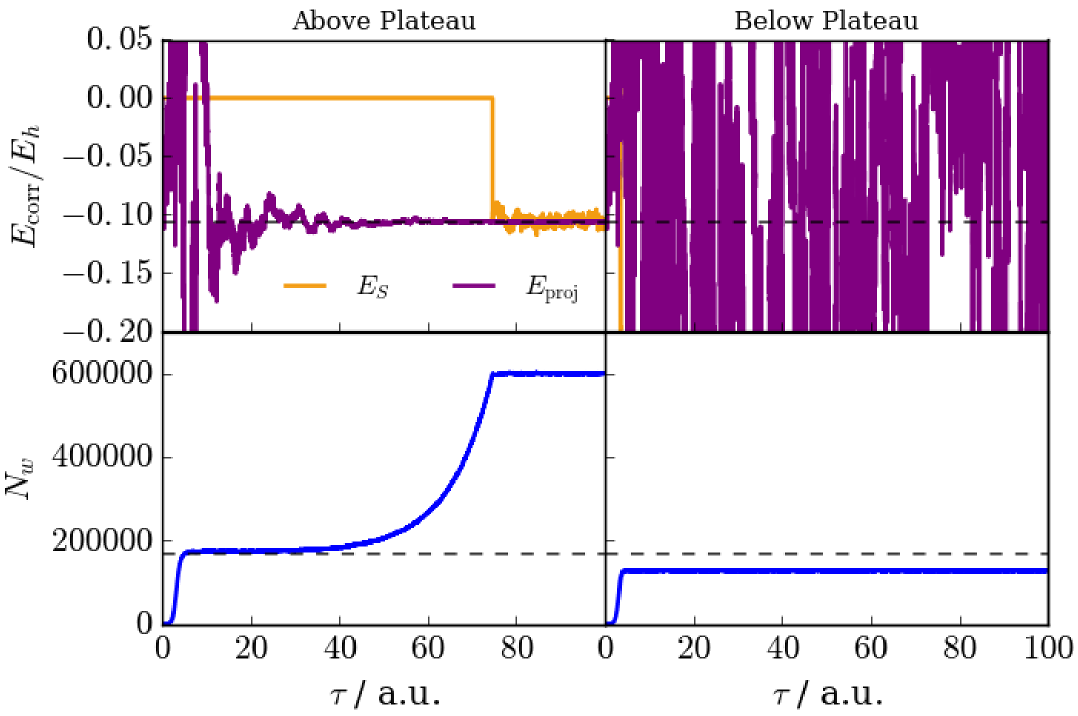

Fig. 3.1 An illustration of an FCIQMC calculation for the Be_2 molecule in a cc-pVTZ basis[265] with a bond length of 2.254Å. The $1\sigma_g^2 1\sigma_u^2$ core electrons are frozen. Both calculations use a time step of $\delta\tau = 10^{-3}$ and are initialised with a single walker at the RHF reference determinant. In the calculation shown on the left-hand side, N_w is allowed to exceed the annihilation plateau at $N_c = 168,000$ walkers. In this simulation both energy estimators converge onto the correlation energy of the system. In the calculation on the right-hand side the total walker population is stabilised (by allowing the shift E_S to vary) below the critical walker threshold. In this simulation no reliable estimate of the correlation energy can be obtained.

Instead, the undesired state represents the dominant state of the projector with all off-diagonal elements replaced by their absolute values which is the lowest eigenfunction of a matrix $\tilde{T}_{\mathbf{mn}} = H_{\mathbf{mn}}\delta_{\mathbf{mn}} - |H_{\mathbf{mn}} - H_{\mathbf{mn}}\delta_{\mathbf{mn}}|$[266]. The lowest eigenvalue of $\tilde{\mathbf{T}}$ is always lower than the lowest eigenvalue of the Hamiltonian $\mathbf{H}$, meaning that this undesired solution dominates in a regime without sufficient annihilation. The difference between the two eigenvalues of the competing states which characterises the severity of the sign problem is always smaller than or equal to the relevant difference in a 1st quantised basis, the energy gap between the fermionic and bosonic ground states. Introduction of cancellation events in the form of the annihilation step has been shown to inhibit specifically the growth of the undesired competing state and to give rise to the spontaneous plateau phase in the walker growth, allowing the true ground state wavefunction of the Hamiltonian to emerge.

3.3.5 The Initiator Approximation

Although the FCIQMC algorithm in its form described above represents a computational saving over more traditional diagonalisation techniques, its computational expense still needs to be reduced for the treatment of larger systems, ideally without a commensurate loss of accuracy. One of the most successful developments with this aim is the initiator approximation[226, 267] which introduces subtle modifications to the spawning step. These alterations significantly broaden the scope of FCIQMC by removing the plateau region from the simulation and reducing the associated minimum walker number required for convergence. This initiator adaptation of FCIQMC (i-FCIQMC) has been so successful that it is now routinely used as standard approach and all calculations presented in this thesis use the initiator adaptation i-FCIQMC, unless otherwise stated.

The alterations introduced by i-FCIQMC start by separating the occupied Slater determinants into two categories based on their instantaneous walker population relative to a predetermined parameter, N_a. Determinants with a walker population greater than this threshold, $|N_{\mathbf{n}}(\tau)| > N_a$, are classified as initiators while determinants with a walker population less than or equal to this threshold, $|N_{\mathbf{n}}(\tau)| \leq N_a$, are classified as non-initiators. The spaces of initiator and non-initiator determinants are dynamically updated throughout the simulation to reflect the changing populations on individual determinants. All walkers on initiator determinants attempt to die and spawn as normal and thus behave exactly as in FCIQMC. Walkers on non-initiator determinants also attempt to die as normal, but their spawning ability is restricted. In particular, if a walker on a non-initiator attempts to spawn onto a connected determinants that is vacant and the attempt is successful, the resulting child walker is still not allowed to survive but instead, is removed from the simulation. There is one exception from this restriction in the case of a so called 'double spawn' event wherein two (or more) walkers from non-initiator determinants successfully spawn child walkers of the same sign onto the same vacant determinant in one iteration. In these cases both child walkers are allowed to survive and propagate according to the same rules as all other walkers. Spawning from walkers on non-initiator determinants onto occupied determinants largely proceed as normal.[2]

These modifications to the algorithm aim to prevent the propagation of sign-incoherent noise. The initiator criteria are based on the assumptions that when considering determinants with a walker population in excess of N_a, more credence should be given to the sign information that it carries by giving it precedence in the spawning process and letting it propagate its information throughout the whole Hilbert space, and in particular, throughout new unexplored areas of the Hilbert space. On the contrary, determinants with small walker numbers below N_a carry less reliable sign information and are thus prevented from propagating their information onto vacant determinant in order to ensure that newly populated determinants are associated with the correct sign. As such, double spawn occurrences are also considered to be sign-coherent events, and the resultant walkers are therefore allowed to propagate, despite their parent walkers being located on low-weight non-initiator determinants. In addition to this sign-coherence argument, it is also thought that the imposed restrictions on the spawning process inhibit an initial rapid spread of walkers throughout the Hilbert space that is observed in full-scheme FCIQMC. This enhances the cancellation rate of oppositely signed walkers in the annihilation step in *i*-FCIQMC, in particular during the early stages of a simulation. In doing so, significant growth of the undesired state representing the lowest energy eigenfunction of $\tilde{\mathbf{T}}$[266] is impeded, thereby helping in controlling the sign problem and achieving a stable signal to noise ratio.

The initiator approximation has significantly extended the ability of FCIQMC to treat larger systems. The initiator rules prevent the propagation of noise arising from walkers spawned with the wrong sign which would otherwise have to be removed by annihilation events in the large walker limit. Suppressing this initial growth of sign-incoherent walkers removes the annihilation plateau from the dynamics of a simulation which is observed in the full-scheme version (Figure 3.2). The height of this annihilation plateau defines a restrictive minimum walker number N_w required for convergence. Since the computational expenditure scales approximately linearly with N_w, $\mathcal{O}[N_w]$,

---

[2] There are subtle but defined conventions in the case that simultaneous spawning events onto a single determinant originate from both initiator and non-initiator walkers and the resulting child walkers from different categories of determinants have different signs.

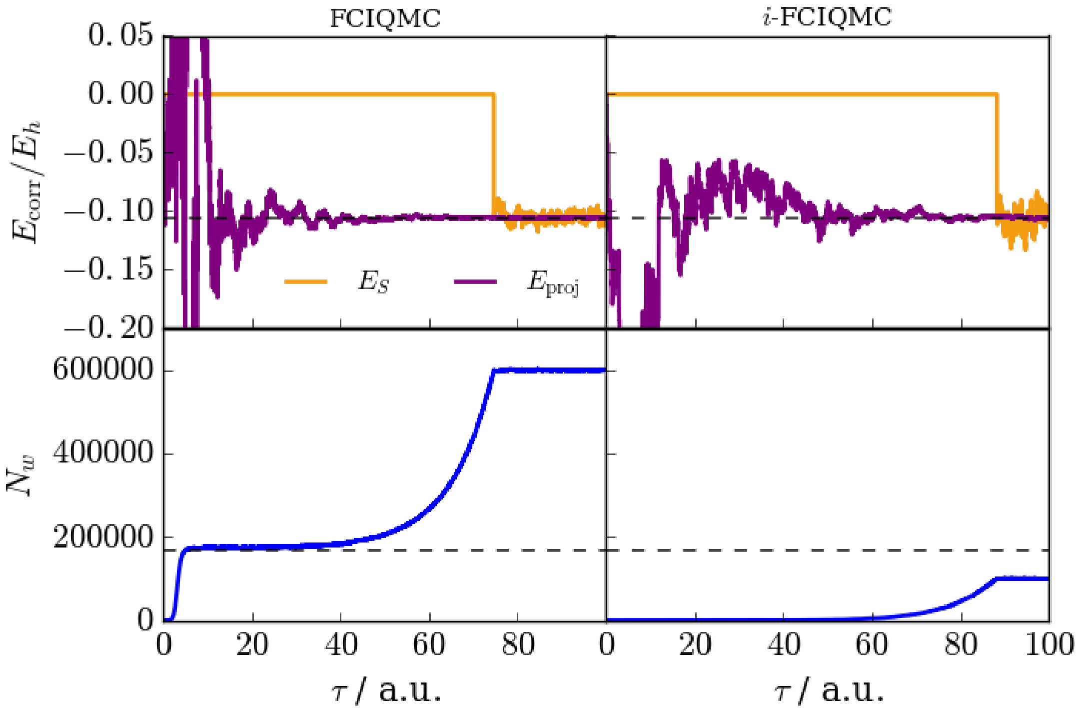

Fig. 3.2 A comparison of FCIQMC and i-FCIQMC calculations for the Be$_2$ molecule in a cc-pVTZ basis[265] with a bond length of 2.254Å. The $1\sigma_g^2 1\sigma_u^2$ core electrons are frozen. Both calculations use a time step of $\delta\tau = 10^{-3}$ and are initialised with a single walker at the RHF reference determinant. The FCIQMC simulation on the left-hand side displays the characteristic plateau behaviour in the growth of the total walker number N_w. This calculation requires $N_w = 600,000$ walkers for the energy estimates to converge onto the correlation energy of the system. In contrast, the i-FCIQMC simulation on the right-hand side with $N_a = 3$ converges onto the correct correlation energy even when the total walker number is stabilised at $N_w = 100,000$ below the critical walker threshold, $N_c = 168,000$, of conventional FCIQMC. The characteristic annihilation plateau is also removed from the i-FCIQMC simulation and i-FCIQMC thus provides a significant saving over FCIQMC.

the effort to overcome this barrier can be intractably expensive. Specifically, in some systems when the required walker number is comparable to the size of the full Hilbert space, FCIQMC was found to offer little benefit over conventional FCI techniques[52]. By removing the plateau phase, i-FCIQMC is able to converge onto the ground state wavefunction at substantially lower N_w than full-scheme FCIQMC[243]. Although the exact mechanism by which i-FCIQMC achieves remains unclear, it is thought that the combination of encouraging sign-coherent sampling of the Hilbert space and enhancing cancellation rates to prevent growth of the undesired competing state are the main factors. However, the success of i-FCIQMC comes at a cost, since the initiator restrictions on spawning events mean that i-FCIQMC samples a slightly different Hamiltonian in which some of the connecting off-diagonal elements are temporarily zeroed,

$$H'_{\mathbf{mn}}(\tau) = 0 \text{ if } \mathbf{n} \notin \{\text{initiators}\} \text{ and } N_{\mathbf{m}}(\tau) = 0. \tag{3.66}$$

This places restrictions on the instantaneous space accessible to the i-FCIQMC wavefunction, the extend of which depends on the number of initiators and walkers in the system. As the affected $H'_{\mathbf{mn}}(\tau)$ evolve with the distribution of walkers during the course of a simulations, these modifications do not generally act like a conventional truncation of space. Nonetheless, the temporary truncation of Hamiltonian matrix elements and available Hilbert space can introduce a systematic error. The result of this is that the measured shift or projected energy are not equal to the true energy of the system and this difference is defined to be the initiator error, ϵ_{init},

$$\epsilon_{\text{init}} = E_{\text{proj}} - E_{\text{exact}}. \tag{3.67}$$

Yet, this error is systematically controllable, tending to zero as $N_w \to \infty$. In this infinite walker limit, all determinants become occupied and thus eventually initiators which lifts the restrictions imposed by the initiator modifications and is equivalent to the full scheme FCIQMC algorithm. Similarly, in the limit that $N_a \to 0$ all occupied determinants act as initiators which again returns the full scheme algorithm. However, extrapolations to any of these limits are difficult, as the initiator error can be of either sign, as well as nonmonotonic, and in practice one or both of these limits must be explored in a number of simulations to ensure that any systematic error has been removed. A typical example is shown in Figure 3.3.

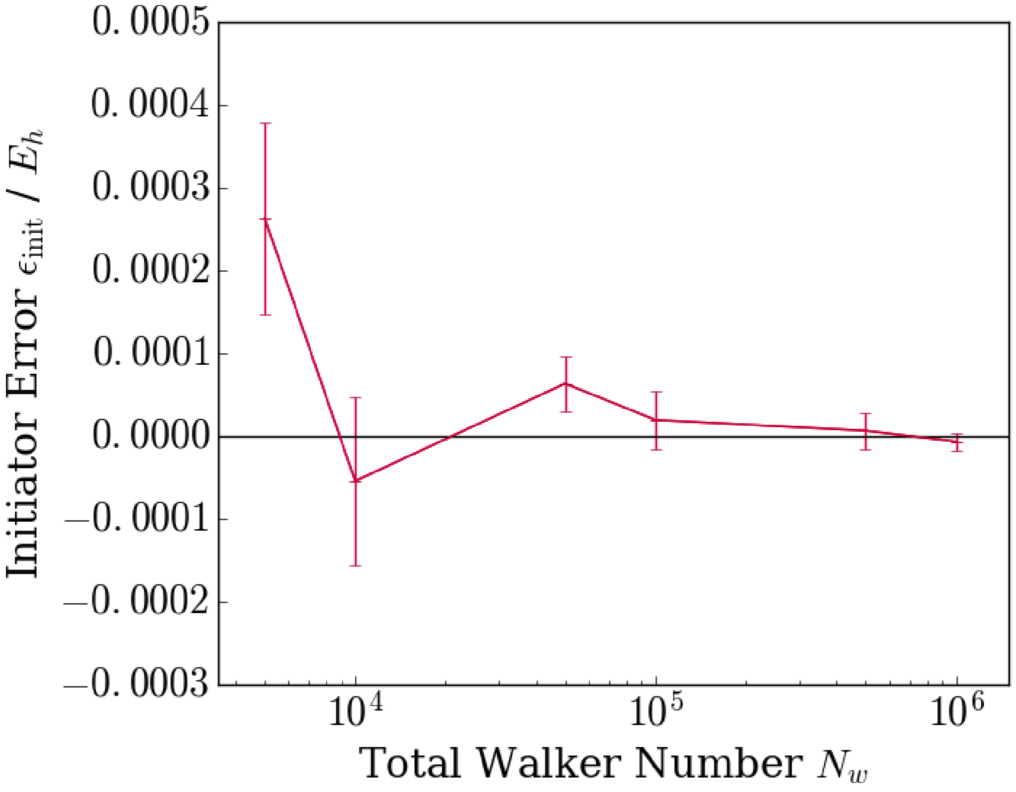

Fig. 3.3 Convergence of initiator error, $\epsilon_{\rm init}$, with respect to total walker number N_w for the Be_2 molecule in a cc-pVTZ basis[265] with a bond length of 2.254Å. The $1\sigma_g^2 1\sigma_u^2$ core electrons are frozen. Although for the majority of systems the energy seems to converge from above, a number of cases have been found where this is not the case[247, 245]. Stochastic errors have been obtained with a Flyvbjerg-Petersen blocking analysis[268].

3.3.6 Non-integer Real-weight Walkers

Although FCIQMC was originally developed with an ensemble of discrete integer weight walkers, it was found beneficial to introduce walkers with real non-integer weights[253, 269]. In the algorithm this is achieved by applying the spawning, death and annihilation process continuously, rather than discretely. In this context, continuously means that weights in spawning and death events are assigned in a continuous manner, omitting the additional stochastic process to convert the weight into an integer walker. Specifically, instead of spawning a walker of integer weight ±1 from $|\mathbf{n}\rangle$ to $|\mathbf{m}\rangle$ with probability $p_s(\mathbf{m}|\mathbf{n})$, a walker of weight p_s is spawned with probability 1. Similarly, a continuous death event on $|\mathbf{n}\rangle$ simply involves altering its walker population by $p_d(\mathbf{n})$ without the discretisation enforced in the integer walker algorithm. A complete definition of this non-integer algorithm requires a discretisation of the number of spawning attempts made from each determinant with real weight walkers. This number of spawning events is set to be a minimum of $\lfloor N_\mathbf{n} \rfloor$ with the possibility of one additional spawning attempt that is stochastically realised with a probability $N_\mathbf{n} - \lfloor N_\mathbf{n} \rfloor$ to ensure that the overall number of spawning events is still proportional to $N_\mathbf{n}$. Apart from these modifications, the remaining steps of the algorithm proceed largely in the same way as their integer counterparts.

The continuous version of the FCIQMC algorithm removes much of the random number generation in the code. At the same time, instantaneous fluctuations on each determinant are reduced by allowing changes to its population by small fractions of a walker, rather than by a whole walker at a time, which also leads to significant reductions in the stochastic error in estimates such as the projected energy. However, as continuous spawning events are automatically accepted, their number is substantially increased. Likewise, continuous death events of fractions of a walker can lead to many determinants being occupied by low-weight walkers. The costs in memory and simulation time associated with non-integer walkers can thus be significant and some means of stochastic compression of the low-weighted walkers is needed to avoid computational costs for these walkers which contribute little but would quickly span much of the Hilbert space. Three additional parameters are therefore introduced to control the computational expense of the continuous approach. First, only a subspace of the full Hilbert space is treated with non-integer walkers whilst the remainder is described in a discretised manner with integer walkers. The non-integer subspace is defined by a given number of particle-hole excitations from the reference determinant, determined by the cutoff parameter χ which is equal to the maximum excitation level. This still preserves to a large part the minimised fluctuations in the energy estimator as the most dominant contributions will be included in the non-integer subspace (or all contributions with a HF reference and $\chi \geq 2$) and creates a hierarchy of non-integer methods which offer different compromises between high resolution and computational cost. In addition, a minimum threshold value, κ, is introduced for a continuous spawning event. If $p_s > \kappa$, p_s walkers are spawned with probability 1 in a continuous process. If $p_s < \kappa$, κ walkers a spawned with probability $\frac{p_s}{\kappa}$ in a stochastic process, otherwise 0 walkers are spawned. This approach alleviates the disproportionate cost of low-weight walkers which incurs a substantial computational expense compared to their negligible impact on the simulation. While the death step requires no additional modification of this kind, the annihilation process needs further considerations and a minimum occupation threshold, N_{occ}, is defined. After the annihilation process is complete, the instantaneous population of each determinant, $N_{\mathbf{n}}$, is assessed with respect to this threshold. If $N_{\mathbf{n}} < N_{\text{occ}}$, its population is discretised to either N_{occ} with probability $\frac{N_{\mathbf{n}}}{N_{\text{occ}}}$ or 0 with probability $1 - \frac{N_{\mathbf{n}}}{N_{\text{occ}}}$. In doing so, it is ensured that determinants with low-weight walker populations do not proliferate.

It was observed that the description of at least some parts of the space in a continuous manner was universally beneficial mostly due to the reduction in stochastic noise[253].

3.3.7 The Semi-stochastic Adaption

A further notable development of FCIQMC which shall only be briefly mentioned is its semi-stochastic adaption [264, 248]. This approach takes advantage of the observation that for many system, a large proportion of the spectral weight of the ground state is concentrated on a relatively small part of the Hilbert space. The Hilbert space $\mathcal{H}_N$ is therefore divided into two subspaces, a deterministic subspace $\mathcal{D}$ and a stochastic subspace $\mathcal{S}$, such that $\mathcal{D} \cup \mathcal{S} = \mathcal{H}_N$ and $\mathcal{D} \cap \mathcal{S} = \emptyset$. Similarly, the linear projector expanded in the set of basis states $\{|\mathbf{n}\rangle\}$,

$$\hat{\mathcal{P}} = \hat{\mathcal{I}} - \delta\tau(\hat{\mathcal{H}} - E_S\hat{\mathcal{I}}) = \sum_{\mathbf{mn}} P_{\mathbf{mn}} |\mathbf{m}\rangle \langle\mathbf{n}| \,, \tag{3.68}$$

whose application is performed stochastically in (i)-FCIQMC, is partitioned into a deterministic projector $\hat{\mathcal{P}}^D$ and a stochastic complement $\hat{\mathcal{P}}^S$,

$$\hat{\mathcal{P}} = \hat{\mathcal{P}}^D + \hat{\mathcal{P}}^S, \tag{3.69}$$

where

$$P^D_{\mathbf{mn}} = \begin{cases} P_{\mathbf{mn}} & \text{if } \mathbf{m}, \mathbf{n} \in \mathcal{D} \\ 0 & \text{otherwise} \end{cases} . \tag{3.70}$$

Whereas $\hat{\mathcal{P}}^D$ is applied exactly, the application of $\hat{\mathcal{P}}^S$ is realised stochastically using the normal processes of FCIQMC. A good choice of states for the deterministic subspace should be of modest size whilst comprising an appreciable proportion of the ground state wavefunction. A number of techniques of making this choice have been proposed ranging from truncations based upon excitation level to iterative schemes that attempt to identify the highest weighted basis states in the wavefunction. Since a deterministic projection has no sign problem and no statistical error, the semi-stochastic approach reduces the severity of the sign problem and the amount of stochastic noise compared to the fully stochastic version[51].

3.4 Handling Stochastic Estimators

When using stochastic methods such as VMC or FCIQMC, estimates of quantities and their associated errors arising from statistical fluctuations need to be treated appropriately. Once a simulation has converged and equilibrated statistically significant data can be extracted in the form of statistical averages over the appropriate instantaneous values of estimators collected over a series of iterations. In this process, the problem of serial correlation in the data need to be addressed, whereby consecutive data points cannot be considered independent since the wavefunction at iteration $k+1$ is closely related to that at iteration k and new information is only obtained from data points which are separated by the correlation time. In order to treat these issues accurately and remove the serial correlation from the data, the reblocking analysis of Flyvbjerg and Petersen[268] is used which can be implemented in a computationally convenient and conceptionally simple algorithm. This method divides the set of data points $\{x_1, x_2, \ldots, x_n\}$ of n into blocks by averaging adjacent data points,

$$x'_i = \frac{1}{2}(x_{2i-1} + x_{2i}) \tag{3.71}$$

$$n' = \frac{1}{2}n, \tag{3.72}$$

and evaluating the mean m and variance σ^2 of the blocks. This blocking transformation is applied recursively so that the blocks contain 2^k data points after the k-th transformation. It can be shown that, under this blocking transformation

$$m' = m \tag{3.73}$$

$$\sigma^2(m') = \sigma^2(m) \tag{3.74}$$

$$\zeta_t' = \begin{cases} \frac{1}{2}\zeta_0 + \frac{1}{2}\zeta_1 & \text{if } t = 0 \\ \frac{1}{4}\zeta_{2t-1} + \frac{1}{2}\zeta_{2t} + \frac{1}{4}\zeta_{2t+1} & \text{if } t > 0 \end{cases}, \tag{3.75}$$

where ζ_t is the covariance between two data points separated by t steps. Further analysis shows that as the blocking transformations are repeatedly performed, the variance of the data set $\sigma^2(m)$ emerges, since

$$\sigma^2 \geq \frac{\zeta_0}{n} \tag{3.76}$$

and $\frac{\zeta_0}{n}$ increases every time a blocking operation is performed, unless $\zeta_1 = 0$, in which case $\frac{\zeta_0}{n}$ is invariant. During the reblocking process the variance initially increases until the serial correlation has been approximately removed from the data and a plateau is reached. From this point onwards the variance remains approximately constant with increasing block size but its error increases due to the small number of blocks. The quantity

$$\chi = \frac{\frac{1}{n}(\sum_{i=1}^{n} x_i^2) - \frac{1}{n^2}(\sum_{i=1}^{n} x_i)^2}{n-1} \tag{3.77}$$

acts as estimate for $\frac{\zeta_0}{n}$ during a calculation and its value is equal to the true variance of the data set when further blocking operations no longer change its value beyond minor fluctuations.

Chapter 4

Application of *i*-FCIQMC to Strongly Correlated Systems

Wavefunction-based methods represent the best approach for obtaining insight into the characteristics of a system and its most important microscopic properties since all observable properties that drive the physical behaviour of the system can be determined directly from the wavefunction. Owing to this high potential associated with the knowledge of the wavefunction, there is growing interest in wavefunction-based methods and their application to strongly correlated systems. Whilst in quantum chemical methods wavefunctions of strongly correlated molecular systems primarily build on restricted single-particle bases, the general approach in condensed matter physics is to start from qualitatively correct broken-symmetry solutions[3]. It is therefore important to investigate how the structure of a many-electron wavefunction of a prototypical strongly correlated system depends on the representation of the one-particle basis underlying the configuration space of the system. On the face it, such a question appears to be more of a mathematical rather than a physical nature: a unitary transformation of a basis cannot change the physical content of the wavefunction, any more than a rotation of a Cartesian system of coordinates changes the physical content of a tensorial quantity. Still, the choice of single-particle basis can impact the structure of the exact FCI expansion[270] of a many-body wavefunction in a dramatic and sometimes even counterintuitive manner. In order to shed more light on this question, the study in this chapter looks at a range of different basis sets: a broken-symmetry mean-field basis (UHF), a spin-restricted mean-field basis (RHF), as well as restricted and unrestricted natural orbitals which are known to give a compact FCI wavefunction[271–275].

4.1 Model Hamiltonians

Since reliable *ab-initio* methods encounter many difficulties, another traditional widely used theoretical approach is based on simplifying model Hamiltonians which take only a few relevant degrees of freedom into account. Reducing a full many-body Hamiltonian to the simplified model Hamiltonian still captures the physics of the relevant low-energy degrees of freedom, retains the essence of the physical phenomena and seems to better unravel the physical effects of strongly correlated electron systems.

4.1.1 The Hubbard Model

One of the most studied model system is the Hubbard Hamiltonian[33, 9] which is the simplest model of interacting electrons on a lattice

$$\hat{\mathcal{H}} = -t \sum_{\langle IJ \rangle, \sigma} a^{\dagger}_{I\sigma} a_{J\sigma} + U \sum_{I} n_{I\uparrow} n_{I\downarrow}. \tag{4.1}$$

This model associates one pair of opposite spin orbitals with each site I of the lattice. $a^{\dagger}_{I\sigma}$ and $a_{I\sigma}$ represent the second quantised fermionic creation and annihilation operators which create and annihilate an electron with spin σ in the orbital at lattice site I, while $n_{I\downarrow} = a^{\dagger}_{I\downarrow} a_{I\downarrow}$ denotes the number operator. The first summation runs over all nearest-neighbour pairs $\langle IJ \rangle$. The behaviour of the correlated electrons is controlled by just two fundamental parameters. Firstly, the hopping amplitude t describes the kinetic energy arising from the hopping of electrons between nearest-neighbour lattice sites. Secondly, the Hubbard repulsion coupling U represents the on-site Coulomb repulsion energy between two electrons residing at the same lattice site I. These two terms compete with each other since the kinetic energy favours mobility of the electrons whilst the electron-electron repulsion favours localisation of the electrons on different lattice sites. When the ratio $\frac{U}{t}$ is small, inter-site hopping of electrons leads to their complete delocalisation and band formation. If there is one electron per site, $n = \frac{N_{\text{el}}}{N} = 1$, the system will be a metal irrespective of how small the value of t is. Yet, if the distance between lattice sites is large and t correspondingly small (and $\frac{U}{t}$ large), the electrons prefer to remain localised with one particle per site in order to minimise the repulsion energy U. In a metallic state doubly occupied sites which increase the total energy of the system necessarily occur. However, for strong interactions $U > t$ (or rather if $U > W = 2zt$ where W denotes the band width and z the number of nearest-neighbours in the lattice geometry), creation of doubly occupied lattice sites is very unfavourable as this raises the energy by the Coulomb repulsion U and lowers the energy only by the kinetic energy $\sim t$. The system will therefore remain insulating with one electron per site, a state that is referred to as Mott insulator. Since the electrons in a Mott insulator are localised, localised spins or localised magnetic moments are simultaneously created[276]. Furthermore, the effective exchange interaction which represents the main mechanism of exchange in insulators, also known as superexchange, is antiferromagnetic in nature. This is a result of the tendency to gain kinetic energy due to the partial delocalisation which is only possible if spins of neighbouring sites are anti-parallel. Consequently, undoped Mott insulators with $n = 1$, $U >> t$ and simple lattices typically display an antiferromagnetic ordering of spins in the ground state. In general terms, the competition between the hopping parameter t and the on-site Coulomb repulsion energy U leads to the Mott-Hubbard metal-to-insulator transition, a metal-insulator transition that many strongly correlated systems at half filling undergo. As a function of the ratio $\frac{U}{t}$, the system undergoes several transitions of the charge and spin arrangements, as well as the dynamics at low temperatures. When a Mott insulator is doped, the doped electrons or holes can move through the material and the resulting state may become metallic. However, the strong correlations can make the metal anomalous. The motion of charge carriers is hindered by the antiferromagnetic order since the movement of the additional hole or electrons leaves behind a trail of wrong spins which in two or three dimensional systems can lead to confinement, that is the charge carrier remains close to its original position. It is therefore often favourable for the system to change the antiferromagnetic ordering to a ferromagnetic one which results in a loss of the superexchange interaction but also a gain in kinetic energy which more than compensates for the loss. This can result not only in a ferromagnetic, or paramagnetic, metal but also in more complicated magnetic orderings for smaller dopings such as canted antiferromagnetism, a magnetic spiral or in a phase separation whereby ferromagnetic droplets are enclosed in an antiferromagnetic matrix. This is a general trend that is also observed in more complicated circumstances: Mott insulating states often coexist with antiferromagnetic order whilst metallic states are typically associated with ferromagnetism. It is also thought that the magnetic degrees of freedom and electron correlation determine the nature of superconductivity in high-T_C cuprates and possibly in iron-based superconductors, although a detailed picture is still missing.

Although the simplifications introduced by model Hamiltonians compared to *ab-initio* systems are enormous, important insight can nevertheless be gained by studies of Hubbard model systems. In these studies the emphasis has been on two dimensions because it is claimed that the $2D$ Hubbard model retains all relevant physics for high-T_C superconductivity to occur. However, despite the simplicity of the model even simple properties such as the phase diagram of a strongly correlated electron system are difficult to calculate exactly. The competition between localisation and delocalisation, between hopping term t and Coulomb repulsion U, is thus at the very heart of the electronic many-body problem[277].

4.1.2 The three-band $(p-d)$ Hubbard Model

The single-band Hubbard model described in the previous section is, however, an over simplification when compounds are considered which, besides transition metal (TM) ions with their d electrons, comprise also other ions and electrons. Such compounds include transition metal oxides which contain not only correlated d electrons of the transition metal ion but also valence electrons of the s or p shells of elements such as O or F. In some cases an effective single-band model can be derived by projecting out electrons other than the transition metal d electrons and deriving effective values for the parameters which are determined by the interplay of all electrons in the system. In other cases, these electrons need to be included explicitly. Specifically, this is the case for perovskites in which the oxygen $2p$ levels are close in energy to that of the transition metal d electrons. In ideal materials, these perovskites are based on cubic lattices, where the transition metal ions are located in the centres of O_6 octahedra with oxygens sitting in between the transition metal ions so that the TM−O−TM angle is ideally 180°. In reality, distortions of this ideal structure occur in the form of tiling and rotation of the rigid MO_6 octahedra resulting in orthorhombic or rhombohedral structures, or in the presence of orbital degeneracy in the transition metal ions Jahn-Teller effects can lead to distortions, as well. Despite these possible distortions, the TM−O−TM angle is not far from the ideal case of 180°.

In materials such as perovskites, the important electrons which need to be included in model Hamiltonians are the transition metal d electrons and the p electrons of the ligands. The ligand p electrons have the strongest overlap with the metal d electrons and thus influence the properties of the materials strongest. In principle, the s electrons of the ligands could also be included but their inclusion rarely changes the qualitative picture. In cases of almost filled d-shells such as cuprates based on Cu^{2+} (d^9) ions, it is convenient to formulate the theoretical treatment not in terms of electrons but in terms of holes. In this hole picture, the Cu^{2+} state contains one d-hole whilst the filled oxygen O^{2-} $2p$ shells contain no holes. The simplest such theoretical model is the three-band, or $p-d$, Hubbard model introduced by Emery[278–280]. This minimal model describes the dynamics of holes in a copper oxide plane. The CuO_2 plane is modelled by a $3d_{x^2-y^2}$ orbital centred on the copper site and two O $2p_\sigma$ orbitals, a $2p_x$

on an oxygen atom displaced in the x-direction from the copper site and a $2p_y$ on the O-site displaced along the y-direction. The Hamiltonian comprises kinetic energy and hole interaction terms,

$$\hat{\mathcal{H}} = \sum_{i,\sigma}(\epsilon_d - \mu)d^{\dagger}_{i,\sigma}d_{i,\sigma} + \sum_{i\nu,\sigma}(\epsilon_{p_\nu} - \mu)p^{\dagger}_{i\nu,\sigma}p_{i\nu,\sigma} \tag{4.2}$$

$$+ \sum_{i,j,\nu,\sigma}(t_{i,j\nu}d^{\dagger}_{i,\sigma}p_{j\nu,\sigma} + h.c.) + \sum_{\substack{i,\nu,j,\kappa,\sigma\\ i\neq j}} t^{'}_{i\kappa,j\nu}p^{\dagger}_{i\kappa,\sigma}p_{j\nu,\sigma} \tag{4.3}$$

$$+ \sum_{i} U_d d^{\dagger}_{i,\uparrow}d_{i,\uparrow}d^{\dagger}_{i,\downarrow}d_{i,\downarrow} + \sum_{i,\nu} U_p p^{\dagger}_{i\nu,\uparrow}p_{i\nu,\uparrow}p^{\dagger}_{i\nu,\downarrow}p_{i\nu,\downarrow} \tag{4.4}$$

$$+ \sum_{\substack{i,j,\nu\\ \sigma,\sigma^{'},i\neq j}} U_{pd}d^{\dagger}_{i,\sigma}d_{i,\sigma}p^{\dagger}_{j\nu,\sigma'}p_{j\nu,\sigma'} \tag{4.5}$$

$$+ \sum_{\substack{i,\nu,j,\kappa,\\ \sigma\sigma^{``},i\neq j,\nu\neq\kappa}} U_{pp}p^{\dagger}_{i\nu,\sigma}p_{i\nu,\sigma}p^{\dagger}_{j\kappa,\sigma'}p_{j\kappa,\sigma'}, \tag{4.6}$$

where $d^{\dagger}_{i,\sigma}$ ($p^{\dagger}_{i\nu,\sigma}$) creates a hole with spin σ in the Cu $3d$ orbitals (O $2p_\nu$) at site i and $d_{i,\sigma}$ annihilates a hole with spin σ in the Cu $3d$ orbital (O $2p_\nu$) at site i. Furthermore, ϵ_d and $\epsilon_{px} = \epsilon_{py} = \epsilon_p$ represent the respective orbital energy levels and μ the chemical potential. Moreover, $t_{i,j\nu}$ and $t^{'}_{i\kappa,j\nu}$ describe nearest-neighbour hopping processes between the Cu $3d$ and the O $2p_{x/y}$ orbitals with the phase conventions shown in Figure 4.1[281]. While in this formulation, nearest-neighbour $2p_x - 2p_x$ ($2p_y - 2p_y$) hopping processes corresponding to $t^{'}_{i\kappa,j\nu}$ terms with $\kappa = \nu$ are included explicitly, other variants of the model without these terms also exist[282]. Local on-site repulsion interactions are taken into account by the U_d and U_p terms, whereas nearest-neighbour repulsion interactions are represented by U_{dp} and U_{pp}. The values chosen for the parameters (Table 4.1) were obtained with a constrained first-principles calculation for La_2CuO_4 by Hybertsen et al[283].

ϵ_d	ϵ_p	t_{pd}	t_{pp}	U_d	U_p	U_{pd}	U_{pp}
0.00	3.60	1.30	0.65	10.50	4.00	1.20	0.00

Table 4.1 Parameters (in eV) for the three-band Hubbard model obtained with a constrained first principles calculation for La_2CuO_4 by Hybertsen et al.[283]

Since the $p - d$ Hubbard model includes the oxygen p states explicitly, two types of charge excitation can principally appear in the system. Besides the $d - d$ transition known from the simple one-band Hubbard model, $d^n d^n \rightarrow d^{n+1}d^{n-1}$, excitations which

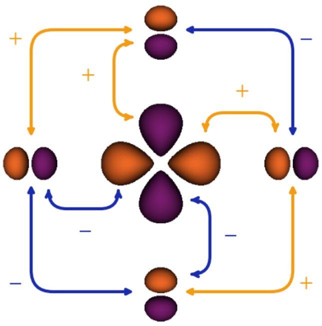

Fig. 4.1 Phase conventions for three-band $(p-d)$ Hubbard model.

transfer a hole from the transition metal ion to the $2p$ shell of O^{2-}, $d^n p^6 \rightarrow d^{n+1}p^5$, can also take place. Whilst the former $d-d$ transitions require an energy cost U_d, the Coulomb repulsion between two holes in the d shell, the latter $p-d$ transitions are associated with an energy cost, also known as the charge-transfer energy,

$$\Delta_{\mathrm{CT}} = \epsilon_p - \epsilon_d. \tag{4.7}$$

If two holes were to be created on the same oxygen site the Coulomb repulsion energy U_p should also be taken into account $\Delta_{\mathrm{CT}} = (\epsilon_p + U_p) - \epsilon_d$. In the simplest cases such as that of perovskites, direct $d-d$ hopping can be neglected. Instead the holes can hop from one transition metal ion to another via the oxygens in a two step process, $d_i^n p^6 d_j^n \rightarrow d_i^n p^5 d_j^{n+1} \rightarrow d_i^{n-1} p^6 d_j^{n+1}$. Since the intermediate state with an oxygen hole in this two step process incurs an excitation energy cost Δ_{CT}, an effective $d-d$ hopping $t_{dd}^{eff} = \frac{t_{pd}^2}{\Delta_{\mathrm{CT}}}$ results.

Similar to the case of the simple one-band Hubbard model, it can be shown that if the hopping t_{pd} is (much) smaller than both U_d and Δ_{CT}, the holes will remain localised at the their sites. The ground state of the material will thus be an insulator, like in the one-band Hubbard model, but the lowest charge-carrying excited states might be different, depending on the ratio of U_d and Δ_{CT}. A concept for the classification of such insulators was first proposed by Zaanen, Sawatsky and Allen and is also referred to as ZSA scheme[284]. Broadly speaking, the scheme distinguishes between two categories which both share an insulating ground state whereby the electrons are localised on the d states with corresponding localised magnetic moments and antiferromagnetic order, provided that $t_{pd} << \{\Delta_{\mathrm{CT}}, U_d\}$. This insulating state can be of two types: If $\Delta_{\mathrm{CT}} < U_d$, a charge-transfer insulator with $p-d$

transitions, $d^n p^6 \to d^{n+1} p^5$, as lowest energy excitations and an energy gap $E_g = \Delta_{\mathrm{CT}}$ results, whilst in the opposite case of $\Delta_{\mathrm{CT}} > U_d$, a Mott-Hubbard insulator with $d - d$ transitions, $d^n d^n \to d^{n+1} d^{n-1}$, as lowest energy excitations and an energy gap $E_g = U_d$ arises, yielding a schematic ZSA phase diagram[285, 276]. In both cases the magnetic properties of the materials are largely determined by the d states on the transition metal ions. Similarly, magnetic exchange interaction mostly involves hopping via intermediate oxygen. For materials with non-degenerate d levels and simple lattices with TM−O−TM ∼ 180°bond angle the exchange interaction will be antiferromagnetic in nature. However, whilst in Mott-Hubbard insulators the exchange interaction is dominated by the standard antiferromagnetic superexchange mechanism $d_i^n p^6 d_j^n \xrightarrow{1} d_i^n p^5 d_j^{n+1} \xrightarrow{2} d_i^{n-1} p^6 d_j^{n+1} \xrightarrow{3} d_i^n p^5 d_j^{n+1} \xrightarrow{4} d_i^n p^6 d_j^n$, in charge-transfer insulators another antiferromagnetic exchange process, the semicovalent exchange, dominates $d_i^n p^6 d_j^n \xrightarrow{1} d_i^n p^5 d_j^{n+1} \xrightarrow{2} d_i^{n+1} p^4 d_j^{n+1} \xrightarrow{3} d_i^{n+1} p^5 d_j^n \xrightarrow{4} d_i^n p^6 d_j^n$, which involves virtual excited states with two holes on oxygen and is therefore irrelevant in the Mott-Hubbard regime.

Most transition metal oxides belong to one of the two insulator categories and can be classified according to which regime of the ZSA phase diagram they are likely to fall into. In general, the charge-transfer energy Δ_{CT} decreases regularly across the $3d$ series from Ti to Cu. Similarly, it also decreases with increasing valency of the transition metal ion which becomes apparent from the values for Δ_{CT} obtained from spectroscopic data[286]. Early $3d$ transition metals have a relatively large Δ_{CT} so that their corresponding materials such as Ti or V oxides typically fall into the Mott-Hubbard insulator regime. When the $p - d$ hopping becomes large and the ratio $\frac{U_d}{t_{pd}}$ is reduced in this regime, the system will sooner or later undergo a Mott transition and a metallic state results. In contrast, heavy $3d$ transition metals usually belong to the charge-transfer insulator regime as $\Delta_{\mathrm{CT}} < U_d$. When the ratio $\frac{\Delta_{\mathrm{CT}}}{t_{pd}}$ is decreased in this regime, the picture is less clear[285]. In particular, interesting phenomena may appear for a small or even negative charge transfer energy[287] which can occur for late $3d$ transition metals with high valency like Fe^{4+} or Cu^{3+}. In these circumstances, the oxygen p bands acquire a certain number of holes since the transfer process $d^n p^6 \to d^{n+1} p^5$ leads to a gain in energy. (Strictly speaking, it should be noted that the energy levels are not single-particle energy levels of non-interacting electrons but also include effects of Coulomb repulsion interaction.) Hence, the real electronic configuration in these materials involve oxygen holes with configurations of the type $\mathrm{Fe}^{3+}\underline{\mathrm{L}}$ instead of Fe^{4+} and $\mathrm{Cu}^{2+}\underline{\mathrm{L}}$ instead of Cu^{3+} where $\underline{\mathrm{L}}$ denotes the ligand (here oxygen) hole. This phenomenon is also known as self-doping[288]: oxygen holes will spontaneously appear, even for nominally undoped, stoichiometric materials which can have a strong influence on many of their properties. Materials with small or negative charge-transfer energy gaps can thus display a variety of different states, specifically when U_d remains large. They may be metals (of a heavy-fermion type, as they still contain strongly correlated d-electrons coexisting with less correlated p-electrons of oxygen ($\frac{U_d}{t_{pd}}$ still $>> 1$)), or they may be insulators (probably resembling Kondo insulators). They may possess different magnetic properties, including ferromagnetism (CrO_2[288] and (La/Sr)CoO_3) or spontaneous charge disproportionation ($CaFeO_3$[289]) may occur. It is also thought that, although this is still an open question, the contribution of oxygen p holes is instrumental for the phenomenon of high-T_c superconductivity[290, 291] since these materials are mostly obtained by hole-doping of CuO_2-planes, as for example in the case of $La_{2-x}Sr_xCuO_4$ where the holes will predominantly go to oxygens and states such as Cu^{2+} (d^9) O^- (p^5) = $Cu^{2+}\underline{L}$ instead of Cu^{3+} will be created.

In some situations such as hole-doped cuprates, the basis of high-T_c superconductivity, the hybridisation of p and d states can lead to behaviour that resembles that of the simple one-band Hubbard model. The objects which appear in these cases are referred to as Zhang-Rice singlets[292]. The latter represent a bound singlet state of the type $d \uparrow p \downarrow - d \downarrow p \uparrow$ whereby the d-hole on the Cu^{2+} ion ($S = \frac{1}{2}$) and the p-hole of opposite spin delocalised over the surrounding four oxygens ($S = \frac{1}{2}$) hybridise. Coherence effects in the $p - d$ hybridisation ($t_{pd} \rightarrow t_{pd,coh.} = 2t_{pd}$) strongly enhances the binding energy of these singlets. In effect, when an undoped cuprate with Cu^{2+} (d^9,$S = \frac{1}{2}$) like La_2CuO_4 is doped with holes as in $La_{2-x}Sr_xCuO_4$[293], each hole first localises on the oxygen p states and then forms a singlet bound state with Cu^{2+}, corresponding to one singlet per doped hole similar to the states created when a simple one-band Hubbard model is doped with holes. Zhang and Rice[292] therefore concluded that for the ground and lowest excited state in typical high-T_C cuprates the $p - d$ model can be reduced to a simple non-degenerate one-band Hubbard model with the hole state replaced by a Zhang-Rice singlet state. To be precise, the situation cannot be described by a single-particle picture and the Coulomb repulsion between particles needs to be included. This will change some expressions and numerical values but the qualitative conclusion remain the same. Although some conflicting claims and controversies remain[294], the Zhang-Rice picture seems to be close to reality and is widely accepted.

4.2 Geometries and Cluster Sizes

Since reachable sizes of clusters are rather small it is important that their geometry is chosen appropriately and the correlation hole is properly described. In particular, for $2D$ lattices this is an essential question[167]. Apart from the obvious choices, Pythagorean lattices with $N = \lambda_x^2 + \lambda_y^2$[295] have significantly extended the available cluster geometries whilst at the same time keeping the periodic boundary conditions for $2D$ square lattices. Examples with an even number of lattice sites include $N = 8, 10, 16, 18, 20, \ldots$ and are shown in Figure 4.2. Although these cluster shapes are square, it has been observed that they are not always optimal with regard to the number of next nearest neighbours and further nearest neighbours. It has been claimed that slightly better results can be obtained with clusters with periodic boundary conditions and slightly deformed lattices[296, 297].

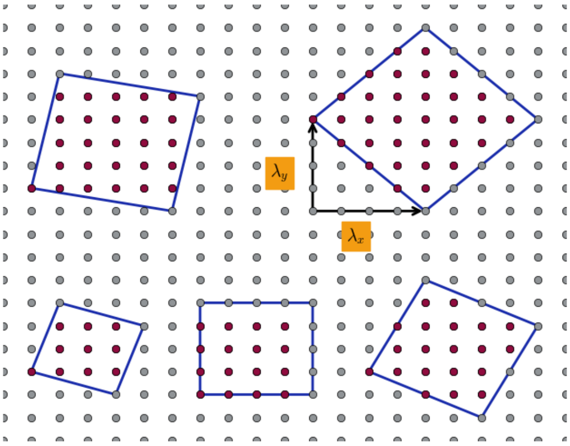

Fig. 4.2 Cluster sizes and geometries on a $2D$ square lattice.

In the following, results for the three-band Hubbard model on a tilted cluster with 10 CuO_2 unit cells are presented, populated by $N = 10$ holes which corresponds to an undoped system at half filling. The full Hilbert space of this system encompasses $\sim 20.3 \times 10^9$ configurations.

4.3 The three-band Hubbard Model in FCIQMC

Since i-FCIQMC provides access to the FCI wavefunction, that is the exact many-body wavefunction for a given one-particle basis set, it represents a high-accuracy method and is therefore the best and most accurate approach for studying the structure of many-body wavefunctions of prototypical strongly correlated systems. At the same time, due to its reduced computational cost, i-FCIQMC can treat systems which are much larger than those amenable to more traditional FCI techniques. As such, i-FCIQMC can handle larger periodic clusters than conventional FCI approaches which helps in reducing finite size and boundary errors. Additionally, a high-accuracy study for gaining an understanding of how the FCI representation of the wavefunction changes with the underlying single-particle basis set does not only enable conclusions about the structure of the exact wavefunction itself, but also about other wavefunction ansatzes and alternative more approximate wavefunction-based methods, as well as about suitable directions for their further development.

4.3.1 The Choice of Single-Particle Basis Sets

Since the FCI energy is invariant to unitary transformations of the underlying single-particle basis spanning the space, it is possible to freely choose a basis set amongst the huge variety of existing one-particle bases. The purpose of the study in this chapter is to investigate how this choice affects the resulting $C_{\mathbf{n}}$ coefficients in the FCI wavefunction expansion,

$$|\Psi_{\text{FCI}}\rangle = \sum_{\mathbf{n}} C_{\mathbf{n}} |\mathbf{n}\rangle \,, \tag{4.8}$$

where $|\mathbf{n}\rangle$ denotes the N-particle Slater determinant. While a good and fruitful choice of basis can lead to a compact and sparse FCI expansion of $|\Psi\rangle$ which is more amenable to treatment with configuration-based methods, a poor choice of basis can result in a highly multiconfigurational and extended wavefunction with many determinants contributing with significant weight. A natural measure for the sparsity of a wavefunction is the L_1 norm,

$$L_1 = \sum_{\mathbf{n}} |C_{\mathbf{n}}|. \tag{4.9}$$

Within (i)-FCIQMC this L_1 norm is quantified up to a normalisation constant by the total number of walkers $L_1 \propto N_w$. Consequently, in this i-FCIQMC study a representation of $|\Psi\rangle$ is sought in which the L_1 norm and level of complexity are small once the energy has converged to within small error bars. For this purpose, two widely available sources of single-particle spin orbitals are investigated, restricted and unrestricted Hartree-Fock spin orbitals (RHF, UHF) which are also compared with restricted and unrestricted natural orbitals (RNO, UNO). Although the latter require knowledge of the exact fully correlated wavefunction, they are known to yield rapidly converging FCI wavefunction expansion[271–275] and are therefore ideally suitable for comparisons and analyses.

In the independent-particle Hartree-Fock (HF) approximation, $|\Psi_{\mathrm{HF}}\rangle$ is written in the form of a single Slater determinant whose energy is variationally minimised with respect to unitary transformations of the single-particle states. As outlined in Chapter 2, this approach leads to a set of effective one-particle Schrödinger equations, the Roothaan-Hall[75] equations and Pople-Nesbet[76] equations, which are solved in a self-consistent manner to give the RHF and UHF spin orbitals, respectively. All RHF and UHF spin orbitals in this thesis have been obtained with a Fortran implementation of the Roothaan-Hall and Pople-Nesbet equations written by the author. In contrast to the HF single-particle states which derive from a mean-field wavefunction, the natural spin orbitals originate from the exact and fully correlated FCI wavefunction. Specifically, the eigenvectors which diagonalise the exact one-particle density matrix, $\gamma = \mathbf{U}\omega\mathbf{U}^\dagger$, are referred to as natural orbitals (NO) and their respective eigenvalues, ω_p, as NO occupation numbers. The reduced one- and two-body density matrices, whose elements are given by

$$\gamma^p_q = \langle\Psi|a^\dagger_p a_q|\Psi\rangle \tag{4.10}$$

$$\Gamma^{pq}_{rs} = \langle\Psi|a^\dagger_p a^\dagger_q a_s a_r|\Psi\rangle \qquad p > q,\ \ r > s, \tag{4.11}$$

and can be evaluated by sampling from the respective converged i-FCIQMC wavefunction within the dynamics of the FCIQMC algorithm[253]. This sampling process involves an independent replica approach so that the resulting sampled density matrices are unbiased and free from systematic errors (apart from those introduced by possible constraints imposed on the FCIQMC dynamics itself). Whereas restricted HF and NO spin orbitals, $\phi_{I,R}$, restrict the spatial distributions $\phi_I(\mathbf{r})$ to be the same for α and β spin parts,

$$\phi_{I,R} = \begin{cases} \phi_I(\mathbf{r})\alpha(\sigma), \\ \phi_I(\mathbf{r})\beta(\sigma), \end{cases} \qquad \phi_{I,U} = \begin{cases} \phi^\alpha_I(\mathbf{r})\alpha(\sigma), \\ \phi^\beta_I(\mathbf{r})\beta(\sigma), \end{cases} \tag{4.12}$$

unrestricted spin orbitals, $\phi_{I,U}$ relax this constraints, $\phi^\alpha_I(\mathbf{r}) \neq \phi^\beta_I(\mathbf{r})$[37].

The FCI wavefunction is not only an eigenfunction of the exact Hamiltonian ($\hat{\mathcal{H}}$) but also of operators which commute with the Hamiltonian such as the total ($\hat{\mathcal{S}}^2$) and projected ($\hat{\mathcal{S}}_z$) spin operators. However, approximate wavefunctions, like the UHF state, need not necessarily display the full symmetry of the exact wavefunction. Imposing symmetry constraints to fulfil this criterion can raise the energy of the state, a situation that is also known as symmetry dilemma[37, 298]. Thus, the RHF wavefunction is an eigenfunction of $\hat{\mathcal{S}}^2$ with $S = 0$ by virtue of being a closed-shell determinant of spin-restricted orbitals which is contrasted by its UHF counterpart which no longer represents an eigenstate of $\hat{\mathcal{S}}^2$.

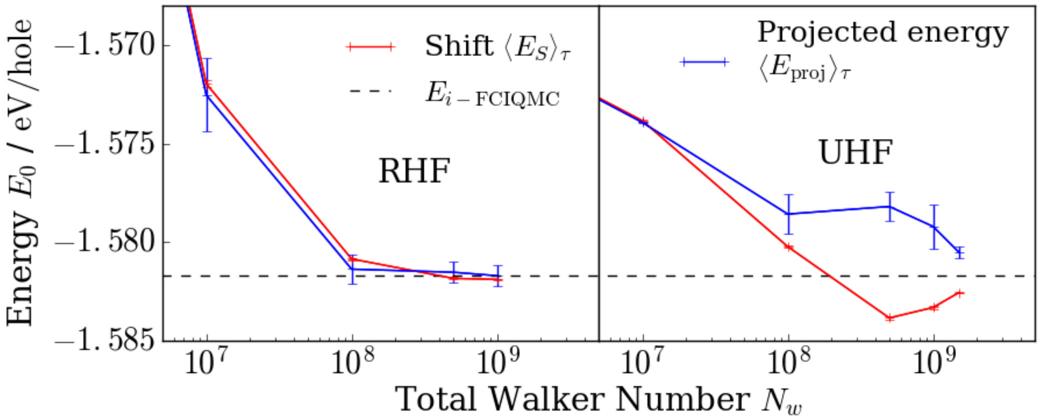

Fig. 4.3 The convergence of the ground state energy E_0 (eV/hole) of three-band Hubbard model with total walker number N_w in an i-FCIQMC simulations using RHF and UHF basis sets. The energy estimates and their stochastic errors have been obtained through a Flyvbjerg-Petersen reblocking analysis[268] of the shift E_S and projected energy E_{proj}.

4.3.2 An i-FCIQMC Study of the Many-Body Ground State Wavefunctions

Initially, convergence of the i-FCIQMC simulation to the FCI limit with respect to walker number N_w is established in order to remove the initiator error (Figure 4.3). Working with RHF orbitals means that the i-FCIQMC calculation appears to be well converged at a total walker number of $N_w = 1.0 \times 10^9$ give that for a tenfold growth in N_w from 1.0×10^8 to 1.0×10^9 in N_w the energy changes by < 0.4 meV which is on the order of statistical errors, thereby indicating that the initiator error has either been removed or is smaller than statistical errors. The resulting converged $|\Psi\rangle$ possesses an L_1 norm of $L_1 = 723.6$. In contrast, if the space is spanned by UHF spin orbitals the energy still changes significantly at $N_w = 1.5 \times 10^9$ and the simulation is far from convergence. Even the L_1 norm in this unconverged $|\Psi\rangle$ is with $L_1 = 1059.5$ already larger than in the RHF simulation. Additionally, while the RHF calculations display a well-behaved monotonic convergence to the FCI limit, UHF spin orbitals give rise to a non-monotonic convergence.

Wavefunction	$\lvert\Psi_{\mathrm{FCI}}\rangle$	$\lvert\Psi_{\mathrm{RHF}}\rangle$	$\lvert\Psi_{\mathrm{UHF}}\rangle$	$\lvert\Psi_{\mathrm{CAS}}\rangle$			
One-particle Basis	RHF/UHF	RHF	UHF	RHF	UHF	RNO	UNO
E_0	−1.5817(5)	−0.9521	−1.5291	−1.3399	−1.5341	−1.5586	−1.5587
E_{D}				−0.9521	−1.5291	−0.7636	−0.8350
p_{corr}				61.6	9.5	97.2	97.0
$\langle n_{\mathrm{Cu}}\rangle$	0.70	0.49	0.73	0.53	0.73	0.71	0.73
$\langle n_{\mathrm{O}}\rangle$	0.15	0.25	0.14	0.24	0.14	0.15	0.14
$\langle M^2\rangle$	0.118	0.000	0.113	0.056		0.130	
$\langle S^2\rangle$	0.00	0.00	4.37	0.00		0.00	

Table 4.2 Properties of the ground state wavefunctions for three-band Hubbard model. Ground state energies E_0(eV/hole), energy of the lowest-energy determinant E_{D}(eV/hole), percentage of correlation energy p_{corr}(%) captured by $\lvert\Psi_{\mathrm{CAS}}\rangle$, average hole densities per atom $\langle n_{\mathrm{A}}\rangle$ (holes/atom), staggered magnetisation $\langle M^2\rangle$, square magnitude of spin $\langle S^2\rangle$. Stochastic errors in the previous digit are presented in parentheses and were estimated with a Flyvbjerg-Petersen blocking analysis[268].

In order to shed some light on the reasons behind this profound difference, the i-FCIQMC, RHF and UHF ground states are examined. As far as the total ground state energy is concerned, the UHF approximation is able to capture ~ 97 % of the true i-FCIQMC ground state energy, whereas the RHF approximation only accounts for ~ 60 %. A similar picture arises when comparing the average hole densities per atom for the Cu, $\langle n_{\mathrm{Cu}}\rangle$, and O, $\langle n_{\mathrm{O}}\rangle$, atomic sites, defined as

$$\langle n_{\mathrm{A}}\rangle = \frac{1}{N_{\mathrm{A}}}\sum_{p\in\{\mathrm{A}\}}\gamma_p^p = \frac{1}{N_{\mathrm{A}}}\sum_{p\in\{\mathrm{A}\}}\langle\Psi|a_p^\dagger a_p|\Psi\rangle\,, \tag{4.13}$$

where the summation includes only those spin orbitals located on the respective N_{A} lattice sites that are associated with atoms of type A. Again, the distribution of hole density in the system as given by the i-FCIQMC wavefunction is much more closely approximated by the UHF wavefunction. Whilst $\lvert\Psi_{\mathrm{UHF}}\rangle$ only slightly overestimates the degree of ionicity in the system (by a few percentages, $\sim 4-6$ %, in $\langle n_{\mathrm{Cu/O}}\rangle$), $\lvert\Psi_{\mathrm{RHF}}\rangle$ largely overestimates the degree of covalency (by a significant percentage, $\sim 30-66$ %, in $\langle n_{\mathrm{Cu/O}}\rangle$).

Like previous studies of the three band Hubbard model[284, 4, 300–304], the exact i-FCIQMC ground state establishes an antiferromagnetic long-range order across the copper sites, as illustrated by the respective order parameter, the staggered magnetisation which can be obtained from the two-body density matrix of the wavefunction,

$$\langle M^2\rangle = \frac{1}{N_S}\sum_{ij}(-1)^{(x_i+y_i)+(x_j+y_j)}\langle\Psi_{\mathrm{FCI}}|\mathbf{S}_i\cdot\mathbf{S}_j|\Psi_{\mathrm{FCI}}\rangle\,, \tag{4.14}$$

where the summations over i and j run over all lattice sites with Cartesian coordinates (x_i, y_i) and spin operator $\mathbf{S}_i$ giving a total of N_S terms. Likewise, the local spin-spin

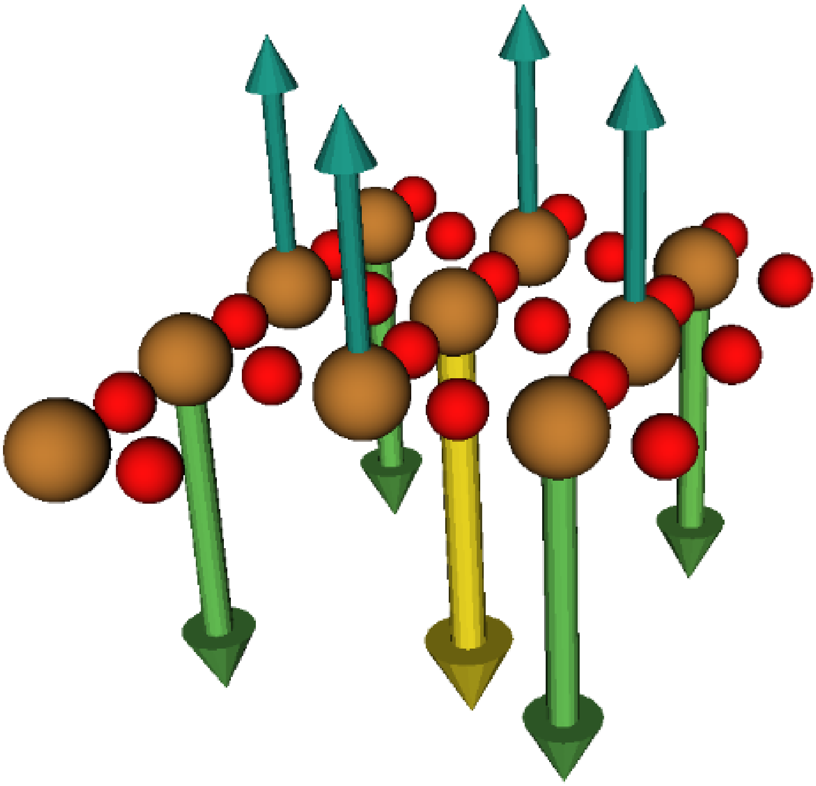

Fig. 4.4 The local spin-spin correlation function $\langle\Psi_{\mathrm{FCI}}|\mathbf{S}_i \cdot \mathbf{S}_j|\Psi_{\mathrm{FCI}}\rangle$ ($i = 1$ corresponds to the first left-most lattice site) from the i-FCIQMC ground state wavefunction. The spin-spin correlation function is obtained from the sampled two-body density matrix of the i-FCIQMC ground state wavefunction expressed in the metallic RHF single-particle basis. This spin-spin correlation function clearly displays the antiferromagnetic order of spins in the ground state as they arise from correlated two-body function rather than symmetry-breaking[299].

correlations in Figure 4.4 display the antiferromagnetic order of spins present in the *i*-FCIQMC ground state wavefunction expressed in the spin-restricted RHF single-particle basis. It is also worth pointing out that by evaluating the staggered magnetisation and the spin correlation function in this way from the two-body density matrix both are constructed from correlated two-body functions rather than from symmetry-breaking in the wavefunction. Again, UHF theory reproduces this antiferromagnetic phase closely by separating α and β spin orbitals on two copper sublattices while yielding identical band structures for both channels, and hence resulting in an insulating antiferromagnetic ground state. Since RHF cannot describe an antiferromagnetic order by construction, it gives rise to a metallic paramagnetic phase (Figure 4.5) where most orbitals are more or less delocalised over all lattice sites. However, the UHF wavefunction contains a significant amount of spin contamination, as illustrated by the huge difference in the squared magnitude of the spin $\langle S^2\rangle = \langle\Psi|\hat{\mathcal{S}}^2|\Psi\rangle$ between the UHF and *i*-FCIQMC states, and $|\Psi_{\text{RHF}}\rangle$ and $|\Psi_{\text{UHF}}\rangle$ constitute a clear example of the symmetry dilemma (Table 4.2). While the UHF basis provides a physically closer single-determinant description of the antiferromagnetic ground state, it breaks spin symmetry thereby introducing an inherent spin contamination. In contrast, the spin-symmetry-conserving RHF basis yields a qualitatively incorrect metallic ground state for the single-determinant description, but is still found to be a much more effective basis for correlated calculations within *i*-FCIQMC.

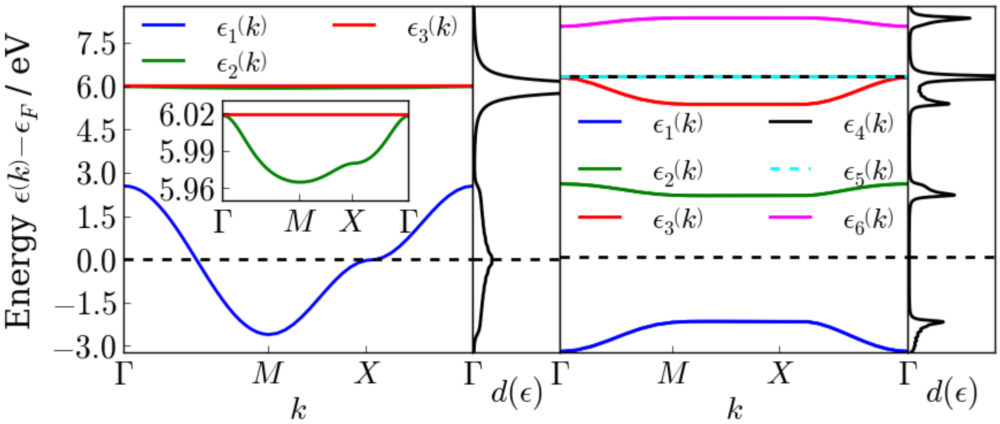

Fig. 4.5 The restricted (RHF) (left) and unrestricted (UHF) (right) Hartree-Fock band structures $\epsilon(k) - \epsilon_F$ (eV) and density of states $d(\epsilon)$ (a.u.) for the three-band Hubbard model. Whilst the RHF theory gives rise to a paramagnetic phase comprising opposite-spin two-particle channels, UHF theory yields an insulating antiferromagnetic ground state with single-particle spin channels.

4.3.3 Orbital Occupation Numbers and Correlation Entropy

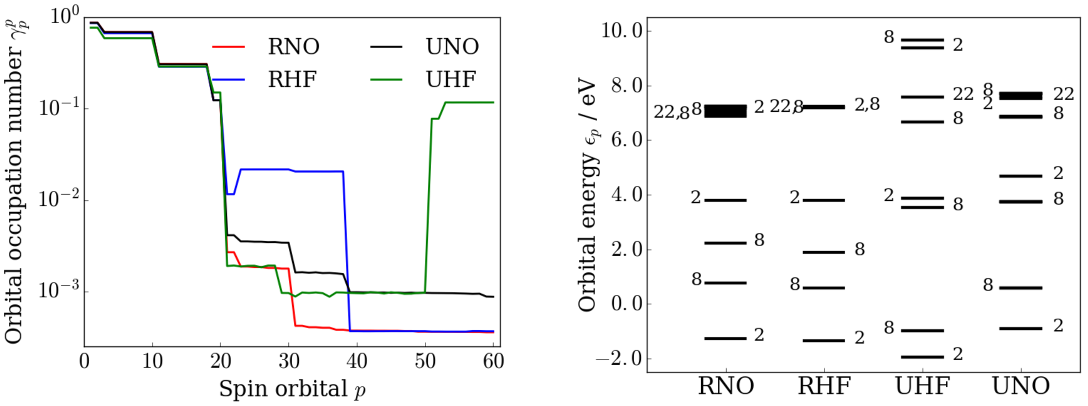

Fig. 4.6 The orbital occupation numbers γ_p^p (left) and mean-field orbital energies ϵ_p (diagonal elements of the mean-field generalised Fock matrix)[37, 305] for the restricted and unrestricted Hartree-Fock spin orbitals, as well as the restricted and unrestricted natural orbitals. In the diagram on the left the occupation numbers γ_p^p are ordered according to orbital energy for HF spin orbitals and according to the occupation numbers themselves for natural orbitals. In the orbital diagram on the right the numbers indicate degeneracies of the spin orbitals which are exact for HF orbitals and approximate for natural orbitals.

An indication regarding the nature of the difficulty introduced by the UHF basis can be obtained by considering the orbital occupation numbers γ_p^p and mean-field orbital energies ϵ_p (diagonal elements of the mean-field generalised Fock matrix)[37, 305] in the four basis sets (RHF, UHF, RNO and UNO) (Figure 4.6). While for the RHF basis the occupation numbers decay approximately monotonically with mean-field orbital energy ϵ_p, a sharp increase in γ_p^p is observed for the N highest UHF virtuals, which are also far higher in energy than those of any other basis (Figure 4.6). As far as the spatial distribution is concerned, these highest energy UHF virtuals correspond to spin-flipped counterparts of the occupied UHF orbitals. These spin-flipped versions can be obtained from their occupied analogues by changing sublattices for the orbital coefficients on copper atoms (Figure 4.7) which introduces significant anti-bonding character in the orbitals, thereby splitting the Hubbard bands far apart (Figure 4.5). It has been observed that in order to obtain rapidly converging CI expansions it is beneficial for orbitals which ought to correlate with each other to possess spatial distributions $\phi_I^\sigma(\mathbf{r})$ which have their greatest amplitudes concentrated in similar regions of space while simultaneously providing suitable nodal surfaces[95]. By breaking spin symmetry, UHF theory leads to a set of single-particle states characterised by localised $\phi_I^\sigma(\mathbf{r})$ which strongly differ in their spatial extent in the system (Figure 4.7). While this enables $|\Psi_{\mathrm{UHF}}\rangle$ to provide a qualitatively correct single-determinant description

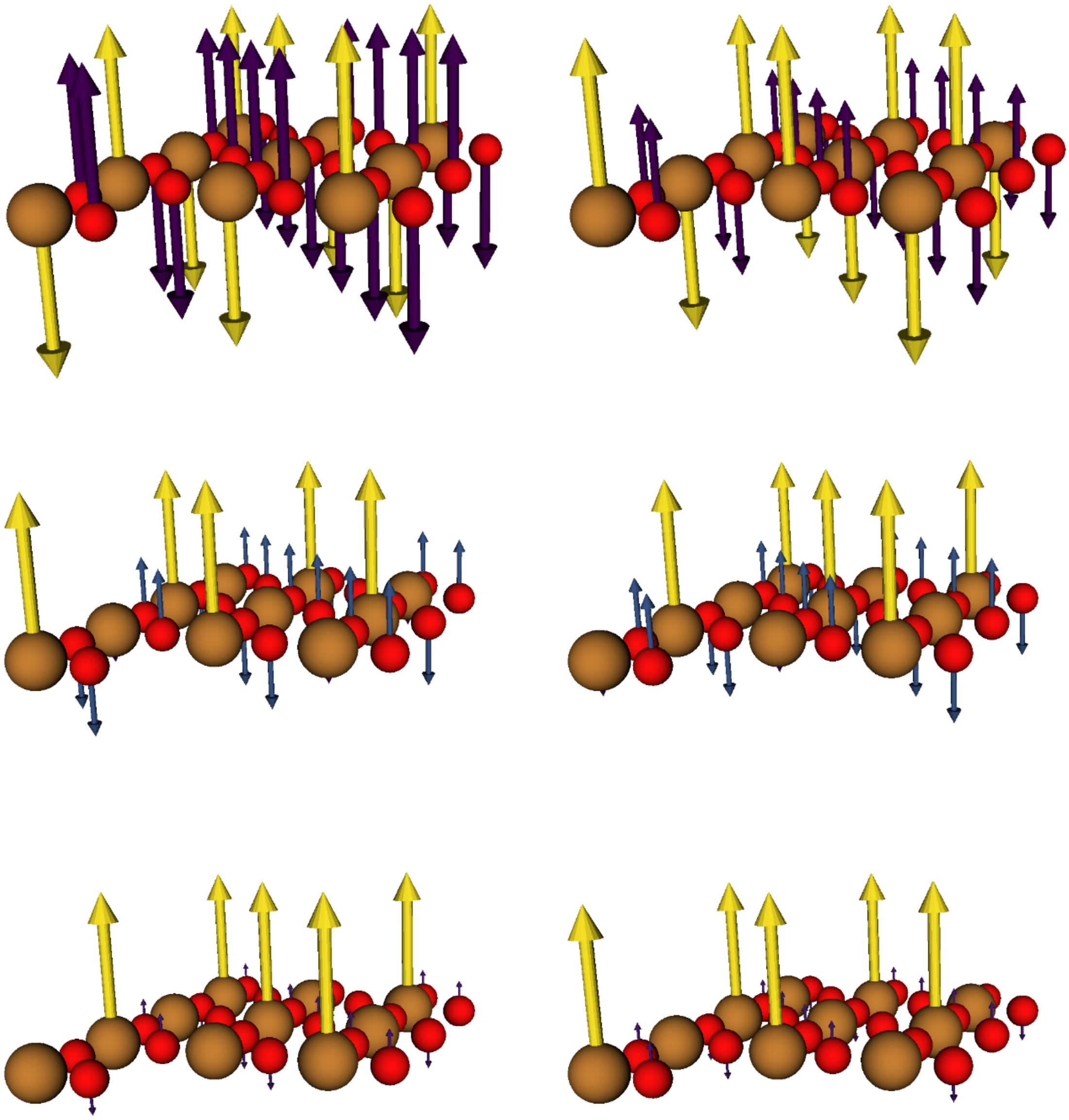

Fig. 4.7 Illustration of a selection of RHF and UHF spin orbitals for three-band $(p-d)$ Hubbard model which are used as basis sets. The arrows represent the sign and magnitude of the coefficients of the respective real space lattice basis orbital in the linear combination describing the illustrated RHF and UHF spin orbitals. The two graphs in the upper first row illustrate the lowest energy occupied RHF orbital (left) and a virtual RHF orbital (right) which represents the 21st and 22nd lowest energy spin orbitals of the RHF basis. The two pictures in the second row show the alpha (left) and beta (right) spin orbitals of the lowest energy occupied UHF orbital. Finally, the two graphs in lower third row display the alpha (left) and beta (right) virtual UHF spin orbitals representing the 51st and 52nd lowest energy UHF spin orbital. These are part of the set of N highest energy virtuals which seems to be crucial for the structure of $|\Psi\rangle$ when it is expressed in this UHF basis[299].

with antiferromagnetic long-range order, introducing correlations into $|\Psi_{\text{UHF}}\rangle$ requires very high energy orbitals. The highest and lowest energy UHF spin orbitals, which both share large γ_p^p and thus contribute significantly to the correlated wavefunction, need to correlate with each other in order to describe correlations in $|\Psi\rangle$ even though they are far apart from each other not only in terms of their mean-field energies but also with respect to their spatial extensions within this system. This then leads to a complex and extended CI expansion. In contrast, the metallic spin-restricted RHF orbitals are very delocalised and thus all exhibit similar spatial distributions $\phi_I(\mathbf{r})$, as well as closer mean-field orbital energies. This facilitates correlation of the single-particle states, thereby favouring a more rapidly converging CI expansion in comparison to UHF orbitals. In contrast to the spatial distribution of spin orbitals, the energy E_{ref} of the reference determinant, that is the determinant constructed from the N lowest energy spin orbitals, and its closeness to the true ground state energy seem not to represent any indicative measures, given that the reference determinants in both natural orbital basis sets are even higher in energy than the RHF determinant. In fact, minimising E_{ref} very aggressively, as in the UHF basis, rather seems to increase the difficulty of introducing correlation effects in the wavefunction. Instead, the energy range covered by the single-particle state appears to play a greater role. As such, since the RHF orbital energies cover a smaller energy range than their UHF counterparts, the determinants with significant amplitudes in $|\Psi\rangle$ are also concentrated within a smaller energy range. This seems to be an advantageous characteristic given that it is also shared by both NO bases which are known to yield less entangled representations of $|\Psi\rangle$[271, 275]. A quantitative measure of the configurational mixing present in the wavefunction representation is provided by the (Shannon-type) correlation entropy per hole[306] which is defined as

$$S_{\text{CE}} = -\frac{1}{N}\sum_p \gamma_p^p \ln \gamma_p^p. \tag{4.15}$$

For an uncorrelated wavefunction described by a single Slater determinant, the natural orbital occupation numbers are $\gamma_p^p = 1$ for spin orbitals contained in the determinant and $\gamma_p^p = 0$ otherwise and the correlation entropy thus vanishes $S_{\text{CE}} = 0$. Conversely, for a correlated N-particle CI wavefunction with $\sum_{\mathbf{n}} |C_{\mathbf{n}}|^2 = 1$ the configurational mixing of Slater determinants yields natural orbital occupation numbers between 0 and 1, $\gamma_p^p = \sum_{\mathbf{n}} |C_{\mathbf{n}}|^2 \Theta_{\mathbf{n}}(p)$, where $\Theta_{\mathbf{n}}(p) = 1$ if spin orbitals p is present in the determinant $|\mathbf{n}\rangle$ and 0 otherwise. Hence, the correlation entropy S_{CE} represents a measure of the configurational mixing of the correlated N-particle state $|\Psi\rangle$. With

$S_{\mathrm{CE}} = 0.6421$ for spin-restricted and $S_{\mathrm{CE}} = 0.6115$ for unrestricted natural orbitals, the entanglement in $|\Psi\rangle$ is smallest in NO bases. Whereas the UHF single-particle states give rise to the wavefunction with the largest configurational mixing ($S_{\mathrm{CE}} = 0.8846$), the metallic spin-symmetry-conserving RHF basis leads to a significantly less entangled $|\Psi\rangle$ with a smaller correlation entropy of $S_{\mathrm{CE}} = 0.7635$, even when describing an antiferromagnetic state which is strikingly physically different from the RHF ground state and to which the spin-symmetry-broken UHF single-determinant ground state is a far better approximation.

4.3.4 Subspace Diagonalisations and CI Expansions

Further insight into the different structure of the wavefunctions expressed in the four single-particle bases can be gained by examining the FCIQMC description of $|\Psi\rangle$ (Figure 4.8). As expected for a strongly correlated system, all wavefunctions are highly multiconfigurational with a large number of single- to N-fold particle-hole excitations of the reference with their amplitudes $|C_{\mathbf{n}}|$ decaying approximately exponentially with determinant energy $E_{\mathbf{n}}$. However, comparing RHF and UHF basis sets shows that the $|\Psi\rangle$ expansion is both sparser within the RHF space and more strongly weighted towards lower particle-hole excitations of the reference. Thus, when the wavefunction is expressed in the UHF basis, a plethora of 10-fold excitations contribute to $|\Psi\rangle$, the amplitudes of which are in most cases extremely difficult to account for in a treatment of electronic correlations. By contrast, when RHF, and even more so when RNO and UNO spin orbitals, are spanning the space, the wavefunction expansions are strongly weighted towards the low particle-hole excitations. In particular, the latter are more amenable to accurate treatment of correlations via a compact set of explicit configurations.

The extend of this amenability of the wavefunctions in the four different one-particle basis sets can be examined more closely with the help of simple subspace diagonalisation in a $(10, 10)$-CAS space, a complete active space in which 10 holes are distributed in 10 orbitals about the Fermi level[110], resulting in a Hilbert space of $63,504$ determinants. A further measure for this amenability is given by the percentage of correlation energy captured by $|\Psi_{\mathrm{CAS}}\rangle$, the ground state of these subspace diagonalisations.

$$p_{\mathrm{corr}} = \frac{E_0 - E_{\mathrm{ref}}}{E_{\mathrm{exact}} - E_D}, \tag{4.16}$$

where E_0 represents the ground state energy of $|\Psi_{\mathrm{CAS}}\rangle$, E_{ref} the energy of the reference determinant and E_{exact} the i-FCIQMC energy. Remarkably, $|\Psi_{\mathrm{FCI}}\rangle$ in the RHF basis

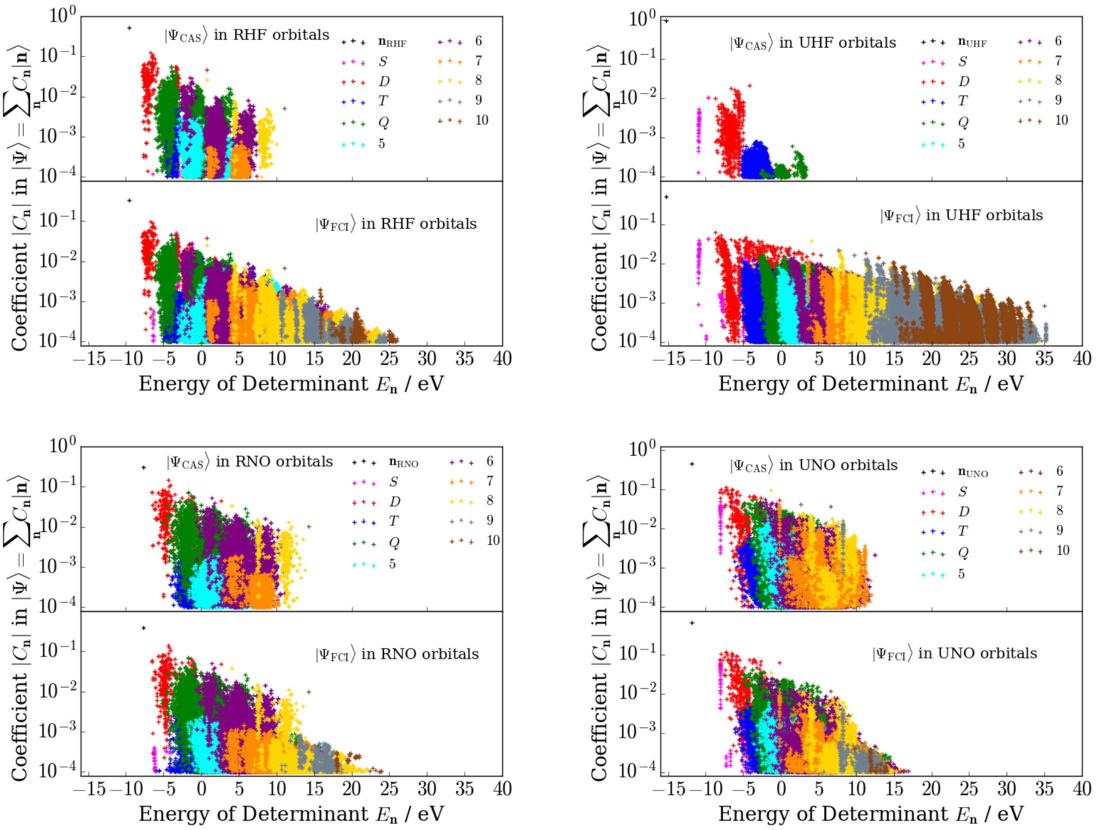

Fig. 4.8 The magnitude of CI coefficients $|C_{\mathbf{n}}| \geq 0.0001$ in the FCI expansion $|\Psi\rangle = \sum_{\mathbf{n}} C_{\mathbf{n}} |\mathbf{n}\rangle$ shown against the respective Slater determinant energy $E_{\mathbf{n}}$ for the restricted Hartree-Fock (RHF) (upper left), unrestricted Hartree-Fock (UHH) (upper right), restricted natural orbital (RNO) (lower left) and unrestricted natural orbital (UNO) (lower right) basis sets. In all four cases, the amplitudes of the Slater determinants in the full Hilbert space $|\Psi\rangle$ are depicted in the lower panels, whilst the $(10, 10)$-CAS space $|\Psi_{\mathrm{CAS}}\rangle$ are displayed in the top panels. The different colours distinguish between determinants based on their excitation level with respect to the reference determinant, that is between the x-fold excitations $(x \in \{1, 2, \ldots, N\})$ of the reference configuration.

can be well approximated by these simple CAS-subspace diagonalisations which achieve to account for 61.6 % of the true correlation energy. Likewise, this is also the case for restricted and unrestricted NO spanned spaces where $|\Psi_{\text{CAS}}\rangle$ captures the vast majority of the respective correlation energy ($p_{\text{corr}} \sim 97$ %), as well as the basic structure of $|\Psi\rangle$. However, in the UHF space barely any correlation energy at all is captured by this subspace, only a meagre $p_{\text{corr}} = 9.5$ %. This is a consequence of the fact that determinant weight is entirely absent from high particle-hole excitations when compared to $|\Psi\rangle$ despite the fact that many of these significant highly-excited determinants are in fact *included in the CAS space.* This suggests that orbitals outside the CAS space, especially the N highest-energy virtuals, are essential for establishing the basic structure of $|\Psi\rangle$ in the UHF basis.

4.3.5 Conclusions

These investigations of the strongly correlated three-band Hubbard model with i-FCIQMC show that the FCI wavefunction representations in different single-particle basis sets can profoundly differ in their amenability to accurate correlation treatments. Counterintuitively, the effectiveness of single-particle spaces for rapidly converging CI expansions is not necessarily paralleled by their ability to reproduce the physics of the system within a single-determinant description. Whilst the UHF determinant represents a qualitatively correct insulating antiferromagnet, imposing spin symmetry in the RHF basis gives a single-determinant wavefunction describing a qualitatively incorrect metal. Still, in this basis the FCI representation of $|\Psi\rangle$ is sparse, compact and converges rapidly with particle-hole excitations of the reference. The results therefore suggest that with an appropriate single-particle description, it may be possible to describe the many-body wavefunction of strongly correlated systems based on single-reference quantum chemical methods, which opens up a vast array of powerful many-body approaches for the study of such materials[307, 308].

For accurate studies of the physics and microscopic processes of real strongly correlated materials, extensions to larger cluster sizes are essential in order to control finite size and boundary errors and approach the thermodynamic limit[50, 309–311]. At the same time, this will also increase the computational expense associated with the simulations, even more so if *ab-initio* systems instead of Hubbard models are considered. In particular, the exponential growth of the Hilbert space with system size conceals exponential complexity in the linear FCI wavefunction ansatz and therefore poses a significant challenge for i-FCIQMC given that strongly correlated materials typically result in multiconfigurational wavefunctions. This formal exponential scaling of i-FCIQMC implies that larger cluster sizes can become intractable, even if an optimal single-particle basis set is chosen. Thus, in order to circumvent the challenge posed by the exponential scaling of the Hilbert space, the development of alternative wavefunction-based methods which bear a reduced scaling with system size is vital for the advancement to larger systems and appropriate cluster sizes of strongly correlated materials.

Chapter 5

A Projector Quantum Monte Carlo Method for Non-linear Wavefunctions

Conceptually, the description of quantum many-body states, which is central to understanding a wealth of complex emergent phenomena in condensed matter physics and quantum chemistry, is straightforward and well defined: with the Hamiltonian known, the exact solution is a linear superposition of all possible classical configurations of particles spanning the full Hilbert space. However, this conceals exponential complexity in the wavefunction which in general prohibits both the storage and manipulation of all of these linear coefficients.

From a methodological perspective, Quantum Monte Carlo methods provide one approach to deal with the exponentially large Hilbert space by sampling the space stochastically. For studies of the ground state of quantum systems, these broadly separate into two categories, Variational (VMC) and Projector (PMC) Quantum Monte Carlo approaches[193, 50] which are described in detail in Chapter 3. In the first, a compact, polynomial-complex approximate wavefunction ansatz is imposed, generally with a small number of variational parameters. State-of-the-art methods to optimise the wavefunction involve sampling and accumulating the gradient and hessian of the energy with respect to the parameters in the tangent space of the current wavefunction. This is done by projecting into and sampling from the exponential configurational space. Once a stochastic representation of these quantities is obtained, updates to the wavefunction parameters are found by a variety of iterative techniques until convergence of this non-linear parameterisation is achieved. By contrast, in PMC approaches an operator written as a decaying function of the Hamiltonian is continually applied to a stochastic representation of the full wavefunction. This projects out the higher energy components, leaving a stochastic sampling of the dominant, (generally ground state) eigenfunction. In particular, FCIQMC is a rather promising technique in this spirit which stochastically samples both the wavefunction and the propagator in Fock space[52, 247]. By exploiting sparsity inherent in the Hamiltonian, as well as in the wavefunction representations of many quantum systems essentially exact results can be obtained with only small fractions of the Hilbert space occupied at any one time. However, despite often admitting highly accurate solutions for systems far out of reach of many alternative approaches, as demonstrated by the application of the previous chapter, the method is formally exponentially scaling with system size, albeit often weakly.

In order to advance to larger and condensed phase systems whilst still building on the success of FCIQMC, one approach is to exploit the fact that electron correlation is, in general, inherently local, as well as the existence of area laws and thus the reduced amount of entanglement which effectively quantifies the relevant number of degrees of freedom. These facts not only imply that natural quantum many-body states live on a tiny submanifold of the exponentially large Hilbert space but also suggest that states within this relevant subspace may be faithfully described by efficient parameterisations which contain their scaling to polynomial cost, thereby circumventing the exponential scaling of the Hilbert space. Traditionally, these wavefunctions ansatzes inhabited the domain of Variation Quantum Monte Carlo approaches, such as the Linear Method and Stochastic Reconfiguration which represent state-of-the-art approaches for the optimisation of large numbers of parameters. In this chapter, a new Projector Quantum Monte Carlo approach is proposed which naturally admits polynomial complex wavefunction ansatzes by combining ideas from traditional Variational and Projector Quantum Monte Carlo approaches. At the same time, developments from the field of deep-learning neural networks are included to arrive at a new method which is able to handle and optimise arbitrary non-linear wavefunctions with large numbers of parameters.

5.1 Non-linear Projector Quantum Monte Carlo Method: Combining Variational and Projector Quantum Monte Carlo

The FCIQMC and some other PMC methods[51, 312] are simulated through stochastic dynamics given by

$$|\Psi_0\rangle = \lim_{k\to\infty} (\mathbf{1} - \tau(\hat{\mathcal{H}} - \hat{\mathcal{I}}E_0))^k \, |\psi^{(0)}\rangle \,, \tag{5.1}$$

with τ chosen to be sufficiently small, where $|\Psi_0\rangle$ is the ground state of the system, and E_0 is the self-consistently obtained ground state energy[52]. This can be considered both as a first-order approximation to imaginary-time dynamics as $e^{-\beta\hat{\mathcal{H}}}\,|\psi^{(0)}\rangle$, or as a power method to project out the dominant, lowest energy eigenvector of $\hat{\mathcal{H}}$[51]. Alternatively, a VMC perspective considers finding the variational minimum of the Ritz function,

$$\mathcal{R}[\Psi(Z_\sigma)] = \frac{\langle\Psi|\hat{\mathcal{H}}|\Psi\rangle}{\langle\Psi|\Psi\rangle}, \tag{5.2}$$

through optimisation of the wavefunction parameters $\{Z_\sigma\}$.

5.2 Derivation: Lagrangian Minimisation

These approaches can be shown to be analogous by considering the minimisation of a positive-definite Lagrangian

$$\mathcal{L}[\Psi(Z_\sigma)] = \langle\Psi|\hat{\mathcal{H}}|\Psi\rangle - E_0 \left(\langle\Psi|\hat{\mathcal{I}}|\Psi\rangle - A\right), \tag{5.3}$$

where normalisation (up to an arbitrary constant A) is enforced by a Lagrange multiplier, which at convergence is given by E_0. It is simple to show that the minimum of this functional is the same as that given by the Ritz functional (Appendix A). In order to find the wavefunction with the lowest energy, a simple gradient descent (GD)[313–315] minimisation of all variational parameters $\{Z_\sigma\}$ in Eq.5.3 with step size τ_k at iteration k is considered. Thus, for a particular parameter σ in the wavefunction this results in an equation which is equivalent to the finite difference approximation of imaginary time propagation,

$$
\begin{aligned}
Z_\sigma^{(k+1)} &= Z_\sigma^{(k)} - \tau_k \frac{\partial \mathcal{L}[\Psi^{(k)}(Z_\sigma^{(k)})]}{\partial Z_\sigma} && (5.4)\\
&= Z_\sigma^{(k)} - \tau_k \left[\langle \frac{\partial \Psi^{(k)}}{\partial Z_\sigma} | \hat{\mathcal{H}} | \Psi^{(k)} \rangle + \langle \Psi^{(k)} | \hat{\mathcal{H}} | \frac{\partial \Psi^{(k)}}{\partial Z_\sigma} \rangle \right. \\
&\quad \left. - E_0 \left(\langle \frac{\partial \Psi^{(k)}}{\partial Z_\sigma} | \hat{\mathcal{I}} | \Psi^{(k)} \rangle + \langle \Psi^{(k)} | \hat{\mathcal{I}} | \frac{\partial \Psi^{(k)}}{\partial Z_\sigma} \rangle \right) \right] && (5.5)\\
&= Z_\sigma^{(k)} - \tau_k \left[2 \langle \frac{\partial \Psi^{(k)}}{\partial Z_\sigma} | \hat{\mathcal{H}} | \Psi^{(k)} \rangle - 2E_0 \langle \frac{\partial \Psi^{(k)}}{\partial Z_\sigma} | \hat{\mathcal{I}} | \Psi^{(k)} \rangle \right] && (5.6)\\
&= Z_\sigma^{(k)} - \tau_k \langle \frac{\partial \Psi^{(k)}}{\partial Z_\sigma} | (\hat{\mathcal{H}} - E_0 \hat{\mathcal{I}}) | \Psi^{(k)} \rangle , && (5.7)
\end{aligned}
$$

where in the third line a real wavefunction and a real, symmetric Hamiltonian are assumed and in the forth line the factor of 2 is subsumed in the step size τ_k. Projecting the equations into the full Hilbert space of configurations $\{|\mathbf{m}\rangle\}$ using the resolution of the identity $\hat{\mathcal{I}} = \sum_{\mathbf{n}} |\mathbf{n}\rangle \langle \mathbf{n}|$, the equations

$$
\begin{aligned}
Z_\sigma^{(k+1)} &= Z_\sigma^{(k)} - \tau_k \langle \frac{\partial \Psi^{(k)}}{\partial Z_\sigma} | (\hat{\mathcal{H}} - E^{(k)} \hat{\mathcal{I}}) | \Psi^{(k)} \rangle && (5.8)\\
&= Z_\sigma^{(k)} - \tau_k \sum_{\mathbf{mn}} \langle \frac{\partial \Psi^{(k)}}{\partial Z_\sigma} | \mathbf{m} \rangle \langle \mathbf{m} | (\hat{\mathcal{H}} - E^{(k)} \hat{\mathcal{I}}) | \mathbf{n} \rangle \langle \mathbf{n} | \Psi^{(k)} \rangle && (5.9)\\
&= Z_\sigma^{(k)} - \tau_k \sum_{\mathbf{mn}} \langle \frac{\partial \Psi^{(k)}}{\partial Z_\sigma} | \mathbf{m} \rangle \left(\langle \mathbf{m} | \hat{\mathcal{H}} | \mathbf{n} \rangle - E^{(k)} \langle \mathbf{m} | \hat{\mathcal{I}} | \mathbf{n} \rangle \right) \langle \mathbf{n} | \Psi^{(k)} \rangle && (5.10)\\
&= Z_\sigma^{(k)} - \tau_k \sum_{\mathbf{mn}} \langle \frac{\partial \Psi^{(k)}}{\partial Z_\sigma} | \mathbf{m} \rangle \left(H_{\mathbf{mn}} - E^{(k)} \delta_{\mathbf{mn}} \right) \langle \mathbf{n} | \Psi^{(k)} \rangle , && (5.11)
\end{aligned}
$$

are obtained where the Lagrange multiplier E_0 is replaced by the energy $E^{(k)}$ of the wavefunction at iteration k which at convergence is equal to E_0. Similar equations can simply be derived for complex wavefunctions and hermitian Hamiltonians. This approach is very versatile and applicable to any wavefunction ansatz for which the respective derivatives exist. If the chosen wavefunction is an expansion of linearly independent configurations, then this will return exactly the 'imaginary-time' dynamics of Eq. 5.1 and the FCIQMC master equations, demonstrating the deep connection between imaginary-time propagation, gradient descent and the power method[315].

Working in the 2nd quantised basis comes with the benefit of a diagonally dominant and sparse Hamiltonian matrix. Furthermore, since the Hamiltonian is a two-body operator, non-zero matrix elements, $H_{\mathbf{mn}} = \langle \mathbf{m} | \hat{\mathcal{H}} | \mathbf{n} \rangle$, connect only configurations which are at most two particle-substitutions of each other ($\sim \mathcal{O}[N^2M^2+NM]$). Despite the compact nature of the gradient full GD becomes unfeasible for large systems, since its computational cost per iteration scales linearly with the size of the exponentially growing Hilbert space. In order to go beyond system sizes tractable with a deterministic gradient descent, a stochastic approach is pursued instead. In keeping with FCIQMC, the summations over configurations are replaced by random samples of both the wavefunction and Hamiltonian connections.

By replacing the deterministically evaluated gradient with its stochastic estimate the resulting iteration cost is independent of the size of the Hilbert space which renders this stochastic gradient descent (SGD) approach inherently suitable for large scale systems. A further major advantage of stochastic gradient descent over its deterministic counterpart is that its stochastic fluctuations enable it to jump between basins of minima. This reduces the probability of the optimisation getting trapped in one of the abundantly present local minima which is one of the key challenges faced by minimisations of non-linear functions[316] and thus aids convergence towards the global minimum, or at least a better local minimum with smaller error. (Dauphin et al.[317] argue that these encountered convergence difficulties are in fact not caused by local minima but rather by saddle points which are points on the surface where one dimension slopes up and another one slopes down. These saddle points are usually surrounded by a plateau of the same error where the gradient is close to zero in all directions which makes it extremely difficult for SGD to escape and thus drastically slows down convergence.)

5.3 Sampling of the Lagrangian Gradient

A key insight due to Robbins and Monro[318] was that for first order methods such as gradient descent, the gradient does not have to be evaluated exactly to ensure convergence towards the optimal solution. Provided that these methods use sufficiently small step sizes and that the gradient estimate is unbiased, the error introduced by the gradient approximation will be lifted on appropriate averaging. The stochastically evaluated gradient of the Lagrangian for the optimisation of the wavefunction parameters at iteration k is written as

$$\frac{\partial \mathcal{L}[\Psi^{(k)}(Z_\sigma^{(k)})]}{\partial Z_\sigma} = \sum_{\mathbf{mn}} \langle \frac{\partial \Psi^{(k)}}{\partial Z_\sigma} |\mathbf{m}\rangle \left(H_{\mathbf{mn}} - E^{(k)}\delta_{\mathbf{mn}}\right) \langle \mathbf{n}|\Psi^{(k)}\rangle \, , \tag{5.12}$$

where σ refers to a particular parameter in the wavefunction, $\{\mathbf{m}, \mathbf{n}\}$ to a many-body determinant in the configuration space, and $E^{(k)}$ to the current sampled energy as given by the density matrices and described in Section 5.7 further below. Minimising the statistical fluctuations in the stochastic sampling of this quantity is key to the success and robustness of the algorithm. The quantities σ, $\mathbf{n}$ and $\mathbf{m} \neq \mathbf{n}$ are all selected stochastically to ensure that no summation over quantities which explicitly scale with the system size are considered. The sole exception from this is the 'diagonal' contribution of $\mathbf{m} = \mathbf{n}$ which is considered explicitly for each sample of $\mathbf{n}$. Thus, the sum over $\{\mathbf{n}\}$ is stochastically sampled via a Metropolis Markov chain, to evaluate a stochastic representation of the wavefunction[51, 199, 200]. Similarly, a small selecton of configurations, $\{\mathbf{m}\}$, are sampled from the set of non-zero connections via $H_{\mathbf{mn}}$ in the manner of FCIQMC, and unbiasing for the probability with a computed normalised generation probability[261, 263]. Furthermore, the derivatives $\langle \frac{\partial \Psi^{(k)}}{\partial Z_\sigma} | \mathbf{m} \rangle$ can be efficiently evaluated from the respective wavefunction amplitudes $\langle \Psi^{(k)} | \mathbf{m} \rangle$. Further technical details on the sampling of this gradient are outlined in the following subsections.

Markov Chain Sampling

The selection of $\mathbf{n}$ is given by a Markov chain sampling of the many-body states yielding a stochastic representation of the wavefunction $\Psi^{(k)}$. It is chosen to sample according to the probability distribution

$$P_{\text{markov}}(\mathbf{n}; \Psi^{(k)}) = \frac{|\langle \mathbf{n} | \Psi^{(k)} \rangle|^2}{\sum_{\mathbf{n}'} |\langle \mathbf{n}' | \Psi^{(k)} \rangle|^2} = \frac{|\langle \mathbf{n} | \Psi^{(k)} \rangle|^2}{\mathcal{N}[|\Psi^{(k)}|^2]}. \tag{5.13}$$

where $\mathcal{N}[|\Psi^{(k)}|^2] = \sum_{\mathbf{n}'} |\langle \mathbf{n}' | \Psi^{(k)} \rangle|^2$ represents the normalisation constant of the probability distribution. Other distributions for instance sampling according to the modulus of the wavefunction are possible and may be preferable in some instances[51]. By requiring the probability distribution to depend on $\Psi^{(k)}$, $P_{\text{markov}}(\mathbf{n}; \Psi^{(k)})$ follows the evolution of $\Psi^{(k)}$ and there is thus no bias originating from the choice of a (fixed) guiding wavefunction. Due to the difficulty of calculating the normalisation of Eq.5.13 the sampling of the set of N_{samples} configurations $\mathbf{n}$ is performed via a Metropolis-Hastings algorithm[199, 200], which does not require explicit calculation of the normalisation constant $\mathcal{N}[|\Psi^{(k)}|^2]$, an unfeasibly expensive operation. Instead, the algorithm generates configurations $\{\mathbf{n}_i\}$ in the Markov chain by proposing a move from $\mathbf{n}_i$ to $\mathbf{n}'_i$ with probability $T(\mathbf{n}'_i \leftarrow \mathbf{n}_i)$. The move is then accepted (i.e. $\mathbf{n}_{i+1} = \mathbf{n}'_i$) with probability

$$A(\mathbf{n}'_i \leftarrow \mathbf{n}_i) = \min\left[1, \frac{T(\mathbf{n}_i \leftarrow \mathbf{n}'{}_i) P_{\text{markov}}(\mathbf{n}'_i; \Psi^{(k)})}{T(\mathbf{n}'_i \leftarrow \mathbf{n}_i) P_{\text{markov}}(\mathbf{n}_i; \Psi^{(k)})}\right], \tag{5.14}$$

and otherwise rejected (i.e. $\mathbf{n}_{i+1} = \mathbf{n}_i$). For the proposal of moves along the Markov chain only up to double electron substitutions are considered which allows for high acceptance ratios, thereby greatly improving the efficiency of the Markov chain sampling[319].

Traditional Fock-space VMC calculations generally perform an exact summation over the possible values of $\{\mathbf{m}\}$ and update all $\{\sigma\}$ parameters in the wavefunction. In the limit of this exact summation, a zero-variance estimator for the gradient is possible in the case that the wavefunction $\Psi^{(k)}$ represents an exact eigenstate of the Hamiltonian[51, 198]. However, in systems with a general two-body interaction, this gives rise to an $\mathcal{O}[N^4]$ step per evaluation of the gradient for a given $\mathbf{n}$. Instead, the zero-variance principle is sacrificed and the set of Hamiltonian connections of $\mathbf{n}$ is sampled via a stochastic algorithm to avoid this high cost. Hence, a small number (N_s) of configurations ($\{\mathbf{m}\}$) are generated with an efficient algorithm, according to a normalised probability for each connection, $P_{\text{gen}}(\mathbf{m}|\mathbf{n}; \hat{\mathcal{H}})$, which can depend on the Hamiltonian under consideration. Finally a single wavefunction parameter, σ is chosen to be updated in the algorithm, again with a normalised probability distribution.

The evaluation of the gradient term for each sample of $\mathbf{n}$, and for stochastic sampling of σ and N_s off-diagonal terms with $\mathbf{m} \neq \mathbf{n}$, can then be written as

$$\left.\frac{\partial \mathcal{L}[\Psi^{(k)}(Z_\sigma^{(k)})]}{\partial Z_\sigma}\right|_{\text{offdiag}} = \left\langle \frac{\langle \frac{\partial \Psi^{(k)}}{\partial Z_\sigma} | \mathbf{m} \rangle \, H_{\mathbf{mn}} \, \langle \mathbf{n} | \Psi^{(k)} \rangle}{N_s P_{\text{gen}}(\mathbf{m}|\mathbf{n}; \hat{\mathcal{H}}) P(\mathbf{n}; \Psi^{(k)})} \right\rangle_{P(\mathbf{n};\Psi^{(k)})} \tag{5.15}$$

where the outer brackets imply that the sampling of $\mathbf{n}$ is performed according to the distribution given in Eq.5.13. Diagonal terms, where $\mathbf{m} = \mathbf{n}$ are sampled deterministically due to the generally diagonally dominant nature of the Hamiltonian and contribute for every sample of $\mathbf{n}$ as

$$\left.\frac{\partial \mathcal{L}[\Psi^{(k)}(Z_\sigma^{(k)})]}{\partial Z_\sigma}\right|_{\text{diag}} = \left\langle \frac{\langle \frac{\partial \Psi^{(k)}}{\partial Z_\sigma} | \mathbf{n} \rangle \, (H_{\mathbf{nn}} - E^{(k)}) \, \langle \mathbf{n} | \Psi^{(k)} \rangle}{P(\mathbf{n}; \Psi^{(k)})} \right\rangle_{P(\mathbf{n};\Psi^{(k)})}. \tag{5.16}$$

Combination of both contributions

$$\frac{\partial \mathcal{L}[\Psi^{(k)}(Z_\sigma^{(k)})]}{\partial Z_\sigma} = \left.\frac{\partial \mathcal{L}[\Psi^{(k)}(Z_\sigma^{(k)})]}{\partial Z_\sigma}\right|_{\text{diag}} + \left.\frac{\partial \mathcal{L}[\Psi^{(k)}(Z_\sigma^{(k)})]}{\partial Z_\sigma}\right|_{\text{offdiag}} \tag{5.17}$$

then results in the final estimate of the gradient.

Sampling of Connected Configurations: Excitation Generation

A key to the efficiency of the algorithm is the choice of sampling distribution for $P_{\text{gen}}(\mathbf{m}|\mathbf{n};\hat{\mathcal{H}})$. The ideal distribution would sample each $\mathbf{m}$ according to a probability of $P_{\text{gen}}(\mathbf{m}|\mathbf{n};\hat{\mathcal{H}}) = \frac{|H_{\mathbf{mn}}|(1-\delta_{\mathbf{mn}})}{\sum_{\mathbf{m}'\neq\mathbf{n}}|H_{\mathbf{m}'\mathbf{n}}|}$, however, the cost of computing the denominator for this distribution returns the algorithm to $\mathcal{O}[N^4]$ complexity. Instead, this normalised distribution is approximated without requiring prohibitive computational cost. For lattice models like the Hubbard model, only $\mathcal{O}[N]$ excitations exist, all of the same magnitude (apart from minor exception arising for particular boundary conditions), which allows for a random, uniform choice amongst the possibilities. For *ab-initio* Hamiltonians, the distribution and magnitude of non-zero matrix elements, $H_{\mathbf{mn}}$, is more complex and covers a wider range, and the quality of the results is more sensitive to the choice of distribution of excitation sampled.

Progress in this direction has recently been achieved with the ‘heat-bath’ sampling of Holmes et. al.[263], however, the memory cost of this approach precludes its use for large applications. Instead, borrowing techniques of ‘excitation generation’ from the FCIQMC algorithm, the excitations are considered as separable ‘single’ and ‘double’ excitations depending on whether one or two electrons change occupation, and the probabilities are split into products of normalised conditional probabilities for each orbital substitution[261]. In the context of FCIQMC the sampling process for the set of off-diagonal Hamiltonian connections $H_{\mathbf{mn}}$ ($\mathbf{m}\neq\mathbf{n}$) between two configurations $\{\mathbf{m};\mathbf{n}\}$ in the Hilbert space is referred to as excitation generation[261, 262], a terminology that arises since $\mathbf{m}$ can be constructed by vacating occupied states / spin orbitals (particles ij) in $\mathbf{n}$, and filling unoccupied states / spin orbitals (holes ab) in $\mathbf{n}$. With the Hamiltonian being a two-body operator, non-zero Hamiltonian matrix elements $H_{\mathbf{mn}}$ connect only configurations which are at most two-particle substitutions ($\sim \mathcal{O}[N^2M^2+NM]$) of each other. The excitation generation algorithm therefore considers the excitations as separate ‘single’ ($i \to a$, $\mathbf{m}=\mathbf{n}_i^a$) and ‘double’ ($ij \to ab$, $\mathbf{m}=\mathbf{n}_{ij}^{ab}$) excitations, depending on whether one or two electrons change occupations

$$|\mathbf{n}\rangle \to |\mathbf{m}\rangle \tag{5.18}$$

$$|n_1,\ldots,1_i,\ldots,0_a,\ldots,n_M\rangle \to |n_1,\ldots,0_i,\ldots,1_a,\ldots,n_M\rangle = |\mathbf{n}_i^a\rangle \tag{5.19}$$

$$|n_1,\ldots,1_i,1_j,\ldots,0_a,0_b,\ldots,n_M\rangle \to |n_1,\ldots,0_i,0_j,\ldots,1_a,1_b,\ldots,n_M\rangle = |\mathbf{n}_{ij}^{ab}\rangle\,, \tag{5.20}$$

and the probabilities are split into products of normalised conditional probabilities for each orbital substitution[261]. In addition, the concept of conditional probabilities is further extended so that the spin orbitals involved in the substitution are required to satisfy particular conditions. In this respect, a number of probabilities are introduced, such as whether to generate a single, p_{sing}, or double, $p_{\text{doub}} = 1 - p_{\text{sing}}$, excitation, or in the case of a double excitation, whether a parallel, p_{para}, or opposite, $p_{\text{opp}} = 1 - p_{\text{para}}$, spin electron pair is involved. Thus, instead of sampling from the ideal but prohibitively expensive distribution $P_{\text{gen}}(\mathbf{m}|\mathbf{n}; \hat{\mathcal{H}}) = \frac{|H_{\mathbf{mn}}|(1-\delta_{\mathbf{mn}})}{\sum_{\mathbf{m}' \neq \mathbf{n}} |H_{\mathbf{m}'\mathbf{n}}|}$, the generation probabilities are factorised such that the probability for generating a single excitation is written as

$$P_{\text{gen}}(\mathbf{n}_i^a|\mathbf{n}; \hat{\mathcal{H}}) = p(a|i)p(i)p_{\text{sing}}, \tag{5.21}$$

whilst the double excitation probabilities for low and high spin pairs are given by

$$P_{\text{gen}}(\mathbf{n}_{ij}^{ab}|\mathbf{n}; \hat{\mathcal{H}}) = p(ab|ij)p(ij)p_{\text{opp}}p_{\text{doub}} \tag{5.22}$$

$$P_{\text{gen}}(\mathbf{n}_{ij}^{ab}|\mathbf{n}; \hat{\mathcal{H}}) = p(ab|ij)p(ij)p_{\text{para}}p_{\text{doub}}. \tag{5.23}$$

$p(i)$ represents the probability of selecting particle i and $p(a|i)$ denotes the probability of choosing hole a given that particle i has been picked. By analogy, $p(ij)$ describes the probability of choosing the pair of particles ij and $p(ab|ij)$ represents the probability of selecting the pair of holes ab on the condition that particles ij have already been chosen. Whilst it is perfectly valid to use uniform distributions for these selections processes, the algorithm will become very inefficient, as the number of single and double excitations scales as $\sim \mathcal{O}[N^2M^2 + NM]$ and many $\mathbf{m}$ with zero or small magnitude $H_{\mathbf{mn}}$ will therefore be generated. An efficient approach thus requires more sophisticated choices for the probabilities such that $P_{\text{gen}}(\mathbf{m}|\mathbf{n}; \hat{\mathcal{H}})$ approximates the distribution of $H_{\mathbf{mn}}$ more closely.

For model systems such as the Hubbard model in the lattice-space basis this is straightforward, since only $\mathcal{O}[N]$ excitations with non-zero $H_{\mathbf{mn}}$ exist, all of the same magnitude (apart from some minor exceptions for systems with open or anti-periodic boundary conditions), which allows for a random, uniform choice amongst the possibilities. As such, the set of excitations available for sampling of $\mathbf{m}$ is restricted to those single excitations $\mathbf{m} = \mathbf{n}_i^a$ which satisfy the condition that a is a hole of the correct spin residing on a lattice site that is a nearest-neighbour to the lattice site of particle i, $a \in \{h_{a\leftarrow i}\}$. The appropriate probabilities are thus given by

$$p_{\text{sing}} = 1 \tag{5.24}$$

$$p(i) = \frac{1}{N_i} \tag{5.25}$$

$$p(a|i) = \begin{cases} \frac{1}{N_{h_a(i)}} & \text{if } a \in \{h_{a\leftarrow i}\} \\ 0 & \text{otherwise} \end{cases}, \tag{5.26}$$

where N_i and $N_{h_a(i)}$ denote the number of available particles and holes satisfying the restriction, respectively. In the algorithm, realisation of these distributions can be implemented by constructing appropriate lists of allowed particles and holes in $\mathcal{O}[NN_{\text{dim}}]$ time prior to the sampling process, (where N_{dim} is the dimensionality of the lattice).

However, for *ab-initio* Hamiltonians, the distribution and magnitude of non-zero matrix elements, $H_{\mathbf{mn}}$, is more complex and covers a wider range, and the quality of the results is more sensitive to the choice of distribution of excitations sampled. Progress in this direction has been made with the sampling of Smart et al.[262] which optimises the individual probabilities by basing them on subsets of the exact Hamiltonian matrix elements, as well as approximations to them using the Cauchy-Schwartz inequality on the magnitude of the two-electron matrix elements between orbitals. Their choice of probability distributions is designed to approximate the ideal distribution $P_{\text{gen}}(\mathbf{m}|\mathbf{n};\hat{\mathcal{H}}) = \frac{|H_{\mathbf{mn}}|(1-\delta_{\mathbf{mn}})}{\sum_{\mathbf{m}'\neq\mathbf{n}}|H_{\mathbf{m}'\mathbf{n}}|}$ as closely as possible without requiring its prohibitive computational cost. In order to reduce the complexity of the resulting algorithm, the particles involved in any type of excitation are uniformly sampled from the set of allowed particles or particle pairs, thereby implying that the individual probabilities are given by

$$p(i) = \frac{1}{N} \tag{5.27}$$

$$p(ij) = p(i) \times p(j) = \frac{1}{N_\alpha} \times \frac{1}{N_\beta} \tag{5.28}$$

$$p(ij) = \frac{1}{\binom{N_\alpha}{2} + \binom{N_\beta}{2}}, \tag{5.29}$$

for single, opposite and parallel spin pair double excitations, respectively. In return, the probability distributions that the holes of excitations are sampled from are designed to best approximate the ideal distribution which involves the Hamiltonian matrix elements $H_{\mathbf{mn}}$. For single excitations $\mathbf{m} = \mathbf{n}_i^a$, there is no simple approximation which is close enough to the Hamiltonian matrix element $H_{\mathbf{n}_i^a\mathbf{n}} = \langle i|\hat{h}|a\rangle + \sum_j[\langle ij|aj\rangle - \langle ij|ja\rangle]$ and the full matrix element therefore forms the basis for the probability distribution according to which hole a is sampled

$$p(a|i) = \frac{|\,\langle\mathbf{n}_i^a|\hat{\mathcal{H}}|\mathbf{n}\rangle\,|}{\sum_{h\in\sigma\mathbf{n}}|\,\langle\mathbf{n}_i^h|\hat{\mathcal{H}}|\mathbf{n}\rangle\,|}. \tag{5.30}$$

The notation in the denominator means that the sum runs over all holes h in $\mathbf{n}$ with the same spin σ as particle i, thereby requiring an order $\mathcal{O}[MN]$ operation. Although this is relatively expensive, in fact the single most expensive part of the excitation generation algorithm, the gains in efficiency with this probability distribution still outweigh the computational cost compared to uniform distributions or approximate distributions which do not resemble the ideal distribution closely enough. In contrast, when considering two-particle substitutions $\mathbf{m} = \mathbf{n}_{ij}^{ab}$ of $\mathbf{n}$, whose matrix elements are given by $H_{\mathbf{n}_{ij}^{ab}\mathbf{n}} = \langle ij|ab\rangle - \langle ij|ba\rangle$, good approximations in lieu of the exact $H_{\mathbf{n}_{ij}^{ab}\mathbf{n}}$ are required since implementations of sampling processes from distributions of exact $H_{\mathbf{n}_{ij}^{ab}\mathbf{n}}$ are too expensive. The Cauchy-Schwarz inequality provides a route towards obtaining these faithful approximations. In particular, if the two picked particles have opposite spins, the exchange term is zero, $\langle ij|ba\rangle = 0$ and a strict upper bound to the matrix element can be formulated with the Cauchy-Schwarz inequality,

$$\langle ij|ab\rangle \leq \sqrt{\langle ii|aa\rangle\,\langle jj|bb\rangle}. \tag{5.31}$$

This product form suggests that instead of picking a pair of holes holes a and b are chosen independently, $p(ab|ij) = p(a|ij)p(b|ij)$, from the distributions

$$p(a|ij) = \frac{\sqrt{\langle ii|aa\rangle}}{\sum_{h\in\sigma\mathbf{n}}\sqrt{\langle ii|hh\rangle}} \tag{5.32}$$

$$p(b|ij) = \frac{\sqrt{\langle jj|bb\rangle}}{\sum_{h\in\sigma\mathbf{n}}\sqrt{\langle jj|hh\rangle}}. \tag{5.33}$$

If instead a parallel spin pair ij is considered, the exchange term is non-zero and a factorised Cauchy-Schwarz based upper bound to the difference provides a much less tight upper bound to the exact matrix element

$$|\,\langle ij|ab\rangle - \langle ij|ba\rangle\,| \leq |\sqrt{\langle ii|aa\rangle} + \sqrt{\langle jj|aa\rangle}| \times |\sqrt{\langle ii|bb\rangle} + \sqrt{\langle jj|bb\rangle}|. \tag{5.34}$$

This suggests that holes are sampled from the probability distributions

$$p(a|ij) = \frac{\sqrt{\langle ii|aa\rangle} + \sqrt{\langle jj|aa\rangle}}{\sum_{h\in\sigma\mathbf{n}} \sqrt{\langle ii|hh\rangle} + \sqrt{\langle jj|hh\rangle}} \tag{5.35}$$

$$p(b|a,ij) = \frac{\sqrt{\langle ii|bb\rangle} + \sqrt{\langle jj|bb\rangle}}{\sum_{h\in\sigma\mathbf{n},h\neq a} \sqrt{\langle ii|bb\rangle} + \sqrt{\langle jj|bb\rangle}}, \tag{5.36}$$

where it should be noted that the sum over h in the denominator of $p(b|a,ij)$ excludes the term $h = a$ to ensure that hole a is not reselected. As noted above, the Cauchy-Schwarz upper bound obtained is particularly poor for double excitations with the same spin. Some of this can be regained by sacrificing the strict upper bound to the matrix element provided by the Cauchy-Schwarz inequality. Instead, only the first hole a is selected according to the distribution $p(a|ij)$ and the second hole b is sampled from a different probability distribution based on the exact Hamiltonian matrix elements $H_{\mathbf{n}_{ij}^{ab}\mathbf{n}}$

$$p(b|a,ij) = \frac{\sqrt{\langle ij|ab\rangle - \langle ij|ba\rangle}}{\sum_{h\in\sigma\mathbf{n},h\neq a} \sqrt{\langle ij|ah\rangle - \langle ij|ha\rangle}}. \tag{5.37}$$

As such, this scheme better represents the cancellation of coulomb and exchange term in the matrix element and is thus expected to provide a better approximation to $H_{\mathbf{n}_{ij}^{ab}\mathbf{n}}$. This approach was found to lead to a much higher efficiency, specifically, in systems dominated by local interactions where the cancellation of terms assumes a greater importance. Irrespective of which distribution is used, the associated computational cost remains the same since all of them involve $\mathcal{O}[M]$ operations. In addition, since both particles share the same spin, the two holes can be chosen in either order which has to be taken into account when computing the probability $p(ab|ij) = p(b|a,ij)p(a|ij) + p(a|b,ij)p(b|ij)$. Taking all these things together, the complete expressions for the generation probabilities can be formulated as

$$P_{\text{gen}}(\mathbf{n}_i^a|\mathbf{n};\hat{\mathcal{H}}) = p(a|i)p(i)p_{\text{sing}} \tag{5.38}$$

$$p(i) = \frac{1}{N} \tag{5.39}$$

$$p(a|i) = \frac{|\langle\mathbf{n}_i^a|\hat{\mathcal{H}}|\mathbf{n}\rangle|}{\sum_{h\in\sigma\mathbf{n}} |\langle\mathbf{n}_i^h|\hat{\mathcal{H}}|\mathbf{n}\rangle|}, \tag{5.40}$$

for single excitations,

$$
\begin{aligned}
P_{\text{gen}}(\mathbf{n}_{ij}^{ab}|\mathbf{n};\hat{\mathcal{H}}) &= p(ab|ij)p(ij)p_{\text{opp}}p_{\text{doub}} && (5.41)\\
&= p(a|ij)p(b|ij)p(ij)p_{\text{opp}}p_{\text{doub}} && (5.42)\\
p(ij) &= p(i)\times p(j) = \frac{1}{N_\alpha}\times\frac{1}{N_\beta} && (5.43)\\
p(a|ij) &= \frac{\sqrt{\langle ii|aa\rangle}}{\sum_{h\in\sigma\mathbf{n}}\sqrt{\langle ii|hh\rangle}} && (5.44)\\
p(b|ij) &= \frac{\sqrt{\langle jj|bb\rangle}}{\sum_{h\in\sigma\mathbf{n}}\sqrt{\langle jj|hh\rangle}}, && (5.45)
\end{aligned}
$$

for opposite spin pair and

$$
\begin{aligned}
P_{\text{gen}}(\mathbf{n}_{ij}^{ab}|\mathbf{n};\hat{\mathcal{H}}) &= p(ab|ij)p(ij)p_{\text{para}}p_{\text{doub}} && (5.46)\\
&= [p(b|a,ij)p(a|ij)+p(a|b,ij)p(b|ij)]p(ij)p_{\text{para}}p_{\text{doub}} && (5.47)\\
p(ij) &= \frac{1}{\binom{N_\alpha}{2}+\binom{N_\beta}{2}} && (5.48)\\
p(a|ij) &= \frac{\sqrt{\langle ii|aa\rangle}+\sqrt{\langle jj|aa\rangle}}{\sum_{h\in\sigma\mathbf{n}}\sqrt{\langle ii|hh\rangle}+\sqrt{\langle jj|hh\rangle}} && (5.49)\\
p(b|a,ij) &= \frac{\sqrt{\langle ij|ab\rangle-\langle ij|ba\rangle}}{\sum_{h\in\sigma\mathbf{n},h\neq a}\sqrt{\langle ij|ah\rangle-\langle ij|ha\rangle}}, && (5.50)
\end{aligned}
$$

for parallel spin pair double excitations. Algorithmically, sampling from these probability distribution can be realised by computation and inversion of the respective cumulative distribution function (CDF)[262]. Additionally, in order to further enhance the efficiency of the algorithm, the probabilities p_{sing}, p_{doub}, p_{opp} and p_{same} are dynamically updated during the course of a simulation so as to favour preferential selection of excitations with large magnitude $H_{\mathbf{mn}}$. Whilst initial values for these parameters are computed using the relative number of excitations, better values can be obtained by requiring that

$$\max\left[\frac{|H_{\mathbf{n}_i^a\mathbf{n}}|}{P_{\text{gen}}(\mathbf{n}_i^a|\mathbf{n};\hat{\mathcal{H}})}\right]_{\text{sing}} = \max\left[\frac{|H_{\mathbf{n}_{ij}^{ab}\mathbf{n}}|}{P_{\text{gen}}(\mathbf{n}_{ij}^{ab}|\mathbf{n};\hat{\mathcal{H}})}\right]_{\text{doub}} \tag{5.51}$$

$$\max\left[\frac{|H_{\mathbf{n}_{ij}^{ab}\mathbf{n}}|}{P_{\text{gen}}(\mathbf{n}_{ij}^{ab}|\mathbf{n};\hat{\mathcal{H}})}\right]_{\text{opp}} = \max\left[\frac{|H_{\mathbf{n}_{ij}^{ab}\mathbf{n}}|}{P_{\text{gen}}(\mathbf{n}_{ij}^{ab}|\mathbf{n};\hat{\mathcal{H}})}\right]_{\text{same}}, \tag{5.52}$$

where the notation $\max\left[\frac{|H_{\mathbf{n}_{ij}^{ab}\mathbf{n}}|}{P_{\text{gen}}(\mathbf{n}_{ij}^{ab}|\mathbf{n};\hat{\mathcal{H}})}\right]_{\text{doub}}$ stands for the maximum value attained by the ratio of matrix element and corresponding generation probability for single excitations and by analogy for the other types of excitations.

Selection of Wavefunction Parameter

Finally, the choice of wavefunction parameter, σ, to update is made uniformly from the set of variables which contribute to the amplitude in configuration $\mathbf{m}$. If a wavefunction ansatz comprises two or more major components, e.g. a Correlator Product State contribution and reference state Slater determinant (as detailed in Chapter 6), a probability is introduced with respect to the prior decision to which of these principal wavefunction components the set of parameters that σ is chosen from belongs. This probability may either be fixed at a particular value or dynamically adjusted by requiring that the L_1-norm of the gradient with respect to the parameters of the first wavefunction component (e.g. the Correlator Product State part) is approximately equal to the L_1-norm of the gradient with respect to the parameters belonging to the second major component (e.g. the reference state Slater determinant). However, the precise value of this probability was not observed to make a profound difference and an update procedure with equal probability for both sets of parameters was found to generally perform well. Investigations were also carried out using more sophisticated probability distributions for the choice of σ based on the values of the parameters or the derivatives with respect to the parameters. However, all of these schemes were found to be less effective due to the increased computational cost associated with construction of the probability distributions and uniform selection of σ proved to be the most efficient approach.

5.4 Momentum Methods: Nesterov's Accelerated Gradient Descent

However, similar stochastic gradient descent (SGD) approaches have been considered before with little success for large numbers of variables, due to the slow (linear) convergence of the parameters as $\mathcal{O}\left(\frac{1}{k} + \frac{\sigma}{\sqrt{k}}\right)$ where σ is the variance in the gradient and k the number of iterations[313]. Improving on this to obtain the convergence rate of state-of-the-art quasi-second order methods involves advances in SGD methods, used in the field of deep learning algorithms of neural networks[320–322]. Analogously, these networks represent a flexible non-linear function with parameters to be optimised via minimisation of a cost function, often achieved via SGD schemes similar to the one in Eq. 5.4[323, 324].

A major role in slowing down the convergence of SGD minimisation is played by ravines which typically occur around minima. Within these ravines the gradient is small in the direction pointing towards the minimum and large in undesired directions. As a consequence, SGD strongly oscillates around the slope of the ravine whilst progressing only hesitantly towards to bottom of the minimum[325].

A classical technique for accelerating SGD is the momentum method[326] whereby the addition of a 'momentum' implies that the update depends on not just the current iterate, but retains a memory of previous iterations. Classical momentum approaches employ the following pairs of equation

$$X_\sigma^{(k+1)} = \mu X_\sigma^{(k)} - \tau_k \frac{\partial \mathcal{L}[\Psi^{(k)}(Z_\sigma^{(k)})]}{\partial Z_\sigma} \tag{5.53}$$

$$Z_\sigma^{(k+1)} = Z_\sigma^{(k)} + X_\sigma^{(k+1)}, \tag{5.54}$$

where the intermediate $X_\sigma^{(k+1)}$ is introduced as update for the final wavefunction parameter $Z_\sigma^{(k+1)}$. μ is a momentum constant (or equally $1-\mu$ can be regarded as friction constant) which controls over how many iterations the gradient information persists. Propagation thus results in the accumulation of velocity in directions of low curvature and persistent decrease in energy, thereby accelerating the update in directions of low curvature over multiple iterations. At the same time, by combining gradients with opposite signs pointing along the same direction oscillations in directions of high curvature but gradients with changing directions are damped, thereby reducing updates for directions whose gradients frequently change directions. (In this sense, a physical analogy to ball rolling down a hill can be drawn.) As a result, propagation of the momentum equations leads to a faster convergence and reduced oscillations, formally accelerating the convergence rate to a second-order $\mathcal{O}\left(\frac{1}{k^2}+\frac{\sigma}{\sqrt{k}}\right)$.

A better version of the momentum method can be formulated as Nesterov's accelerated gradient descent[327], whereby the sequence $\lambda_0 = 0$, $\lambda_k = \frac{1}{2}+\frac{1}{2}\sqrt{1+4\lambda_{k-1}^2}$, $\gamma_k = \frac{1-\lambda_k}{\lambda_{k+1}}$ is defined and starting at an initial point $Z_\sigma^{(1)} = Y_\sigma^{(1)}$, the algorithm stochastically iterates the equations[328],

$$Y_\sigma^{(k+1)} = Z_\sigma^{(k)} - \tau_k \frac{\partial \mathcal{L}[\Psi^{(k)}(Z_\sigma^{(k)})]}{\partial Z_\sigma} \tag{5.55}$$

$$Z_\sigma^{(k+1)} = (1-\gamma_k) Y_\sigma^{(k+1)} + \gamma_k Y_\sigma^{(k)}, \tag{5.56}$$

for $k \geq 1$. The analogies and differences between classical momentum methods and Nesterov's accelerated gradient descent can be more clearly seen by defining $X_\sigma^{(k+1)} = Y_\sigma^{(k+1)} - Y_\sigma^{(k)}$ and $\mu_k = -\gamma_k$ and rewriting the equations of Nesterov's approach as[329]

$$X_\sigma^{(k+1)} = \mu_k X_\sigma^{(k)} - \tau_k \frac{\partial \mathcal{L}[\Psi^{(k)}(Z_\sigma^{(k)} + \mu_k X_\sigma^{(k)})]}{\partial Z_\sigma} \tag{5.57}$$

$$Z_\sigma^{(k+1)} = Z_\sigma^{(k)} + X_\sigma^{(k+1)}. \tag{5.58}$$

Ignoring the proposed schedule for γ_k, the key difference between classical momentum and Nesterov's accelerated gradient descent approaches is that classical momentum methods first compute the gradient before applying the velocity, whilst Nesterov's accelerated gradient descent method computes the gradient after doing so[330].

This anticipatory update allows Nesterov's accelerated gradient descent to move in a quicker and more responsive way[331], letting it behave more stably than classical momentum methods in many iterations. To illustrate this point, the situation is considered where the addition of the momentum term $\mu_k X_\sigma^{(k)}$ undesirably increases the energy (Figure 5.1). In Nesterov's accelerated gradient descent, the gradient is computed at $Z_\sigma^{(k)} + \mu_k X_\sigma^{(k)}$, and if $Z_\sigma^{(k)} + \mu_k X_\sigma^{(k)}$ is indeed a higher energy, the gradient $\frac{\partial \mathcal{L}[\Psi^{(k)}(Z_\sigma^{(k)}+\mu_k X_\sigma^{(k)})]}{\partial Z_\sigma}$ will point more strongly downwards in energy than the gradient $\frac{\partial \mathcal{L}[\Psi^{(k)}(Z_\sigma^{(k)})]}{\partial Z_\sigma}$ computed at $Z_\sigma^{(k)}$ (which is used in classical momentum methods), thereby providing a better and more timely correction. Whilst each iteration of Nesterov's approach might only be slightly more effective than classical momentum techniques, the combined effect means that Nesterov's accelerated gradient descent performs significantly better in many situations. Whilst this is not necessarily always the case, it was generally observed to perform better or at least equally well as standard momentum techniques in the proposed optimisation and is therefore used in this optimisation.

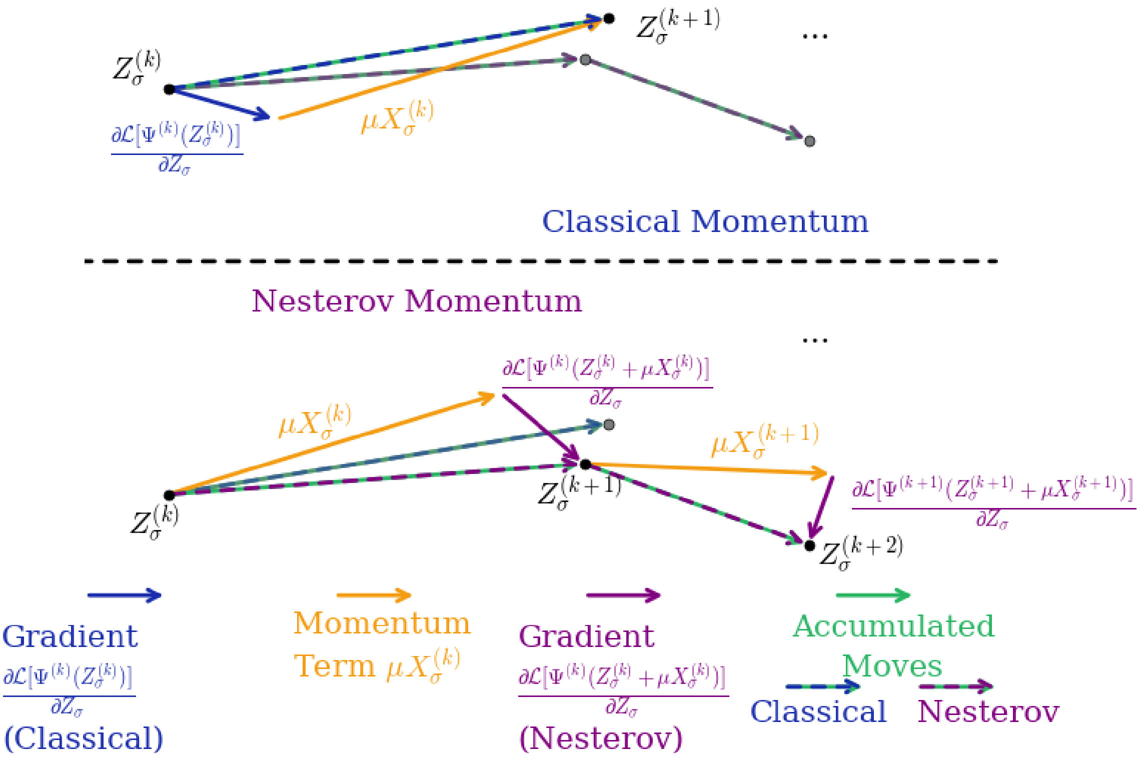

Fig. 5.1 Comparison of steps taken in Classical Momentum Methods (top) and Nesterov's Accelerated Gradient Descent (bottom).

Due to the addition of the momentum term Nesterov's scheme is no longer monotone and as such there is no requirement that each iteration will decrease the energy and instabilities can be observed[332, 333]. To mitigate this behaviour, some restarting schemes have been proposed[333, 334], but their restarting criteria are difficult to realise in stochastic approaches. Instead, in this approach it has also been found beneficial to include a damping for the momentum, d, as $\gamma_k \to \gamma_k e^{-\frac{1}{d}(k-1)}$. With a suitably chosen parameter the rate of convergence of the optimisation should not be hindered, since this is dominated in the latter stages by the $\frac{\sigma}{\sqrt{k}}$ term for both accelerated and conventional gradient descent[331, 329].

5.5 Matrix Polynomials - Closing a Circle of Connections

Mathematically, on a more general and abstract level, projections, such as the stochastic projection onto eigenstates of the Hamiltonian as described in Eq. 5.8, are given by a monic polynomial of the propagator of degree k[335–338], such that

$$\Psi^{(k)} = p_A^k(\mathbf{A})\Psi^{(0)}, \tag{5.59}$$

where $p_A^k(\mathbf{A})$ represents a monic polynomial of the matrix $\mathbf{A}$ belonging to the linear space $\mathcal{P}_k$ of polynomials of degree at most k. More specifically, expanding $\Psi^{(0)} = \sum_{i=0}^{n-1} c_i\Psi_i$ in the spectral basis of $\mathbf{A}$ with eigenpairs (λ_i, Ψ_i) ordered accordingly $|\lambda_0| \geq |\lambda_1| \geq \ldots \geq |\lambda_{n-1}|$, the projection leads to

$$\begin{aligned}\Psi^{(k)} &= p_A^k(\mathbf{A})\Psi^{(0)} &(5.60)\\ &= \sum_{i=0}^{n-1} p_A^k(\lambda_i)c_i\Psi_i &(5.61)\\ &= p_A^k(\lambda_0)c_0\Psi_0 + \sum_{i=1}^{n-1} p_A^k(\lambda_i)c_i\Psi_i. &(5.62)\end{aligned}$$

If the dominant eigenpair (λ_0, Ψ_0) is desired, the component $p_A^k(\lambda_0)c_0$ should be much larger than all other components $p_A^k(\lambda_i)c_i$, $\forall i > 0$. Within this requirement, the polynomial p_A^k should ideally be rescaled such that $p_A^k(\lambda_0) = 1$ and

$$\Psi^{(k)} = c_0\Psi_0 + \sum_{i=1}^{n-1} \frac{p_A^k(\lambda_i)}{p_A^k(\lambda_0)} c_i\Psi_i, \tag{5.63}$$

while $|p_A^k(\lambda_0)| > |p_A^k(\lambda_i)|\ \forall i > 0$ and $c_0 \neq 0$ are necessary conditions to project onto the dominant eigenpair.

The most basic matrix polynomial which fulfills these requirements is $P_A^k(\mathbf{A}) = b_k\mathbf{A}^k$ with b_k being an arbitrary constant. This matrix polynomial is not only constructed during iterations of the power method[335, 337],

$$
\begin{aligned}
\Psi^{(k)} &= b_k \mathbf{A}^k \mathbf{\Psi}^{(0)} && (5.64)\\
&= b_k \left(c_0 \lambda_0^k \Psi_0 + \sum_{i=1}^{n-1} c_i \lambda_i^k \Psi_i \right) && (5.65)\\
&= b_k \lambda_0^k \left(c_0 \Psi_0 + \sum_{i=1}^{n-1} c_i \frac{\lambda_i^k}{\lambda_0^k} \Psi_i \right), && (5.66)
\end{aligned}
$$

which filters out the dominant eigenstate $\mathbf{\Psi}_0$ and leads to a decay of contributions of all other states provided that $c_0 \neq 0$, but also during those of the Projector Quantum Monte Carlo method FCIQMC which uses the linear projector $\hat{\mathcal{P}}_{\text{linear}} = \hat{\mathcal{I}} - \tau(\hat{\mathcal{H}} - E_0 \hat{\mathcal{I}})$. Likewise, successive iterations of the basic (S)GD method whose iterations are

$$
\begin{aligned}
\Psi^{(k+1)} &= \Psi^{(k)} - \tau \frac{\partial \mathcal{L}[\Psi^{(k)}]}{\partial \Psi} && (5.67)\\
&= (\mathbf{I} - \tau(\mathbf{H} - E_0 \mathbf{I}))^k \Psi^{(0)} && (5.68)\\
&= \left(-\tau \left(\mathbf{H} - \left(E_0 + \frac{1}{\tau} \right) \mathbf{I} \right) \right)^k \Psi^{(0)} && (5.69)\\
&= \mathbf{A}^k \Psi^{(0)} && (5.70)
\end{aligned}
$$

computes this polynomial with $\mathbf{A} = (\mathbf{I} - \tau(\mathbf{H} - E_0\mathbf{I})) = (-\tau(\mathbf{H} - (E_0 + \frac{1}{\tau})\mathbf{I}))$. The matrix $\mathbf{A}$ can be identified with the matrix representation of the linear projector $\hat{\mathcal{P}}_{\text{linear}}$ applied in FCIQMC. Essentially, both approaches, FCIQMC and (S)GD, amount to a shifted power method, thereby highlighting the deep connections between the methods (in the limit of an exact wavefunction ansatz) which are all equivalent in their realisation of the simple polynomial $P_A^k(\mathbf{A}) = b_k \mathbf{A}^k$. A major drawback of this matrix polynomial is that the decay rate for contributions from unwanted eigenpairs depends on the separation of eigenvalues. Specifically, the power method attains convergence rates of $|\mathbf{\Psi}^{(k)} - \mathbf{\Psi}_0| = \mathcal{O}\left(\frac{|\lambda_1|^k}{|\lambda_0|^k}\right)$ and $|\lambda^{(k)} - \lambda_0| = \mathcal{O}\left(\frac{|\lambda_1|^{2k}}{|\lambda_0|^{2k}}\right)$. In general, convergence rates for this set of methods can be extremely slow, in particular, if the two dominant eigenvalues are close to each other. The use of a shift, as employed in the projector approaches, may then help to either separate the desired eigenvalue from the remaining spectrum or to suppress components of close eigenvalues. Yet, this requires a priori knowledge of the eigenvalues which is not available in practice.

A more sophisticated approach is taken by a number of methods which are commonly referred to as polynomial ‘filtering’ or ‘acceleration’ techniques. They accelerate convergence by designing a polynomial $p_A^k(\mathbf{A})$, ideally the minimal polynomial, a matrix polynomial of smallest degree $k \leq n$ (where n represents the dimension of the matrix $\mathbf{A}$) such that $m_A^k(\mathbf{A}) = 0$, which enhances components form desired regions of the spectrum and suppresses those from unwanted regions[335]. For best convergence onto the dominant eigenpair (λ_0, Ψ_0), a polynomial $p_A^k(\mathbf{A})$ is required with $p_A^k(\lambda_0) = 1$ and whose maximum absolute value over all λ_i with $i > 0$ is the smallest possible (Figure 5.2). However, as the eigenvalues λ_i are generally unknown, the problem is reformulated. Thus, relying on ideas from approximation theory, a polynomial approximation to a continuous scalar function is sought whose value at the desired eigenvalue λ_0 of the propagator is 1 and whose maximum absolute value in a range $[a, b]$ covering the rest of the spectrum containing all remaining eigenvalues λ_i is minimised

$$\min_{p_A^k \in \mathcal{P}_k, p_A^k(\lambda_0)=1} \max_{t \in [a,b]} |p_A^k(t)|, \tag{5.71}$$

where $\mathcal{P}_k$ is the linear space of polynomials of degree k. Analytically, the optimal polynomial for this approximation problem is the shifted and scaled Chebyshev polynomial of the first kind of degree k[335, 338]

$$C_A^k(t(x)) = \frac{\bar{C}_A^k(t(x))}{\bar{C}_A^k(t(\lambda_0))} \tag{5.72}$$

with

$$\bar{C}_A^k(t) = \cos[k \cos^{-1}(t)] \text{ for } -1 \leq t \leq 1, \tag{5.73}$$

and $t(x)$ providing a simple linear transformation

$$t(x) = \frac{2x - (a+b)}{b-a} \tag{5.74}$$

to shift and scale the Chebyshev polynomials which are only defined over the range $[-1, 1]$ to any finite range $[a, b]$. Additionally, these shifted and scaled Chebyshev polynomials $C_A^k(\mathbf{A})$ represent a set of orthogonal polynomials satisfying a three term recurrence

$$C_A^{k+1}(\mathbf{A}) = 2\mathbf{A}C_A^k(\mathbf{A}) - C_A^{k-1}(\mathbf{A}), \tag{5.75}$$

with initial conditions $C_A^0(\mathbf{A}) = \mathbf{I}$ and $C_A^1(\mathbf{A}) = \mathbf{A}$. This recurrence relation renders them perfectly suitable for an enhanced projection process in the form $\Psi^{(k)} = C_A^k(\mathbf{A})\Psi^{(0)}$ which typically converges much faster than the power method or equivalent first-order optimisation (Figure 5.2). The success of the Lanczos approach as a second-order optimisation, as well as other deterministic projections can also be rationalised in this fashion by considering similar matrix polynomial approximations to the projection[339, 340].

By analogy to Krylov space methods, convergence of GD can also be enhanced by extracting information from the state vectors $\Psi^{(k-1)}$ of the previous $k-1$ iterations. This becomes apparent by considering the residual after k GD iterations $\Psi^{(k)} - \Psi_{\text{opt}} = \mathbf{A}^k(\Psi^{(0)} - \Psi_{\text{opt}})$ (where Ψ_{opt} denotes the optimal state vector) and combining the state vectors $\Psi^{(k)}$ linearly using coefficients a_k which results in[338]

$$\begin{aligned} \sum_{k=0}^{i} a_k \Psi^{(k)} &= \sum_{k=0}^{i} a_k \mathbf{A}^k (\Psi^{(0)} - \Psi_{\text{opt}}) + \sum_{k=0}^{i} a_k \Psi_{\text{opt}} && (5.76) \\ &= p_A^k(\mathbf{A})(\Psi^{(0)} - \Psi_{\text{opt}}) + p_I^k(\mathbf{I})\Psi_{\text{opt}}. && (5.77) \end{aligned}$$

Consequently, if $p_I^k(\mathbf{I}) = \mathbf{I}$ is enforced, the value

$$\min \| p_A^k(\mathbf{A})(\Psi^{(0)} - \Psi_{\text{opt}}) \|_2 \tag{5.78}$$

needs to be minimised to obtain the best approximation to Ψ_{opt}. Nesterov's accelerated GD achieves this by iterating the equations in 5.55 which in matrix form reads as

$$\begin{aligned} \Omega^{(k+1)} &= \Psi^{(k)} - \tau \frac{\partial \mathcal{L}[\Psi^{(k)}]}{\partial \Psi} && (5.79) \\ \Psi^{(k+1)} &= (1 - \gamma_k)\Omega^{(k+1)} + \gamma_k \Omega^{(k)}. && (5.80) \end{aligned}$$

This projection process iteratively builds a polynomial $N_A^k(\mathbf{A})$ which satisfies $\Omega^{(0)} - \Omega_{\text{opt}} = N_A^k(\mathbf{A})(\Psi^{(0)} - \Psi_{\text{opt}})$. This implicitly constructed polynomial $N_A^k(\mathbf{A})$ can be conveniently expressed as a three term recurrence relation[338]

$$N_A^k(\mathbf{A}) = \mathbf{A}\left[(1 - \gamma_{k-1})N_A^{k-1}(\mathbf{A}) + \gamma_{k-1}N^{k-2}(\mathbf{A})\right] \tag{5.81}$$

with initial conditions $N_A^0(\mathbf{A}) = \mathbf{I}$ and $N_A^1(\mathbf{A}) = \mathbf{A}$. Whilst not being exactly equal to the Chebyshev polynomial the polynomial $N_A^k(\mathbf{A})$ of Nesterov's accelerated approach is similar to the Chebyshev polynomial and also satisfies $N_I^k = \mathbf{I}$ for all k. This means that it filters out contributions of Ψ_{opt} and suppresses those of undesired states more efficiently than the simple (S)GD approach, thereby accelerating convergence of the projection. A schematic illustration of the differences in efficiency of the projection processes onto the desired state resulting from the various employed polynomials of the propagator can be seen in Figure 5.2.

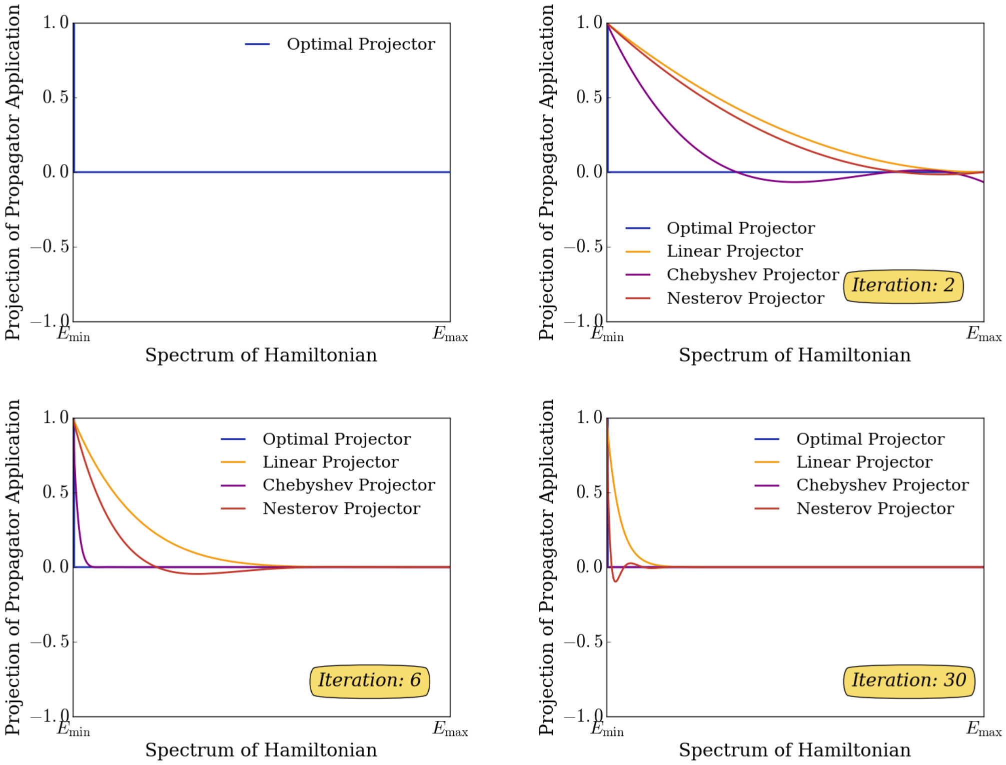

Fig. 5.2 Comparison of projections of propagators onto the desired eigenvalue E_{min} of the Hamiltonian. The projections resulting from repeated application of the Linear Projector (SGD, FCIQMC, Power Method) constructing the simple polynomial $\mathbf{A}^k$, of the Chebyshev Projector employing Chebyshev polynomials $C^k(\mathbf{A})$ and of the Nesterov Projector (Nesterov's Accelerated Gradient Descent) implicitly constructing the polynomials $N^k(\mathbf{A})$ are compared to the Optimal Projector.

5.6 Step Size Adaptation: RMSprop

The remaining arbitrariness concerns the step size (or 'learning rate') τ_k, which is not only crucial for the efficiency of the optimisation but also affects its accuracy. Whilst decreasing the step size generally improves robustness and accuracy, it slows convergence and increases autocorrelation time[324, 323]. On the contrary, if too large a τ_k is chosen, the optimisation continually overshoots the minimum and oscillates around it, thereby resulting in poor accuracy, and again slow convergence, or even divergences. A variety of different schemes, such as Adagrad[341], Adadelta[342], RMSprop[330, 343] and Adam[344] to name just a few, have been proposed in order to avoid the use of fixed step sizes and try to address these issues. Amongst these, it was found numerically that optimal convergence and accuracy within the accelerated SGD approach described above is achieved with a deep-learning technique denoted RMSprop[330, 343], an adaptive step size method which dynamically estimates an individual and independent $\tau^{(k)}_{Z_\sigma}$ for each parameter. This gives

$$\tau^{(k)}_{Z_\sigma} = \frac{\eta}{\mathrm{RMS}[g_{Z_\sigma}]^{(k)}}, \tag{5.82}$$

where η is a tuned global parameter for all variables, and $\mathrm{RMS}[g_{Z_\sigma}]^{(k)}$ represents the root mean square (RMS) of previous gradients for the variable up to the current iteration,

$$\mathrm{RMS}[g_{Z_\sigma}]^{(k)} = \sqrt{\mathrm{E}[g^2_{Z_\sigma}]^{(k)} + \epsilon}, \tag{5.83}$$

evaluated by accumulating an exponentially decaying average of the squared gradients of the Lagrangian, g_{Z_σ},

$$\mathrm{E}[g^2_{Z_\sigma}]^{(k)} = \rho \mathrm{E}[g^2_{Z_\sigma}]^{(k-1)} + (1-\rho) g^{2(k)}_{Z_\sigma}. \tag{5.84}$$

The small constant ϵ is added to better condition the denominator and ρ represents a decay constant. The use of the exponentially weighted average in the denominator instead of a simple accumulating sum which is employed in other adaptation schemes such as Adagrad[341] avoids a continually decreasing step size which, even though being beneficial from an accuracy point of view, eventually shrinks to zero and thus stops the optimisation. This dynamically adaptive, parameter-specific step-size, acts much like a preconditioner for the system, and allows the optimisation to take larger steps for those parameters with small gradients, and vice versa. This ensures robustness of the algorithm to large sudden gradients due to the stochastic nature of the gradient evaluation[342].

5.7 Wavefunction Properties

In addition, the dynamics of the outlined Projector Quantum Monte Carlo method also provide a straightforward route to unbiased computation of the two-body reduced density matrix (2-RDM)[345, 253], a rank-4 tensor in the basis of spin orbitals,

$$\Gamma_{pq,rs} = \langle \Psi | a^\dagger_p a^\dagger_q a_s a_r | \Psi \rangle \qquad p > q, r > s, \tag{5.85}$$

from which the 1-body reduced density matrix (1-RDM)

$$\gamma_{pq} = \langle \Psi | a_p^\dagger a_q | \Psi \rangle = \frac{2}{N-1} \sum_a \Gamma_{pa,qa}, \tag{5.86}$$

can be traced out with the factor of $\frac{2}{N-1}$ arising from the normalisation of the 1-RDM and 2-RDM to N and $\frac{N(N-1)}{2}$, respectively. As such, the reduced density matrix represents a highly compact representation of the relevant information in the N-electron wavefunction, allowing for the computation of pure expectation values. By evaluating the trace of the relevant 1- and 2-body operator $\hat{Q}$ with the 2-RDM

$$\langle Q \rangle = \mathrm{Tr}[\Gamma \hat{Q}], \tag{5.87}$$

arbitrary 1- and 2-body static properties can be found[37]. This includes the energy,

$$E_{\mathrm{RDM}} = \sum_{pq} h_{pq} \gamma_{pq} + \sum_{p>q,r>s} (g_{pqrs} - g_{pqsr}) \Gamma_{pq,rs} + E_{\mathrm{nuc}}, \tag{5.88}$$

(with h_{pq}, g_{pqrs} and E_{nuc} as defined in Section 2.2.2 of Chapter 2), spin, magnetic properties and many more. In particular, the self-consistently determined energy $E^{(k)}$ appearing in the gradient in Eq. 5.12 is evaluated each iteration anew from the sampled energy as given by the density matrix $E^{(k)} = E^{(k)}_{\mathrm{RDM}}$, rather than from the local energy as it is commonly done in traditional VMC methods.

In sampling the 2-RDM a similar approach to the one developed in FCIQMC[253, 269, 267] is employed which projects the 2-RDM into the full Hilbert space of configurations $\{|\mathbf{m}\rangle\}$,

$$\Gamma_{pq,rs} = \sum_{\mathbf{mn}} \langle \Psi^{(k)} | \mathbf{m} \rangle \langle \mathbf{m} | a_p^\dagger a_q^\dagger a_s a_r | \mathbf{n} \rangle \langle \mathbf{n} | \Psi^{(k)} \rangle \,. \tag{5.89}$$

Within this formulation, it is obvious that a matrix element is non-zero only when the configurations $\mathbf{m}$ and $\mathbf{n}$ are at most two-particle substitutions of each other, or put another way, when $\mathbf{m}$ is at most a double excitation of $\mathbf{n}$. As such, the existing sampling processes of the Lagrangian gradient that occur throughout the dynamics of the stochastic projection already provide all the necessary machinery required to sample the 2-RDM. Thus, entirely analogous to the sampling of the gradient, the sum over $\mathbf{m}$ in Eq. 5.89 is stochastically evaluated by the Metropolis Markov chain. Similarly, the off-diagonal terms in the sum over $\mathbf{m}$ are replaced by a small selection of configurations sampled within the excitation generation process whilst the diagonal term $\mathbf{n} = \mathbf{m}$ is included deterministically for each sample in the Markov chain. It should be noted that for an unbiased 2-RDM from which properties other than the energy are evaluated uniform probability distributions for the orbital selections in the excitation generation process need to be used[261] to guarantee that all contributions of the 2-RDM can in principal be selected in the sampling procedure. Otherwise sampling difficulties can arise if two configurations with significant amplitude weight are only connected by a very small Hamiltonian matrix element, their contribution to the RDM may be sampled poorly, or even omitted entirely. Furthermore, both wavefunction amplitudes $\left\{\langle\Psi^{(k)}|\mathbf{m}\rangle, \langle\mathbf{n}|\Psi^{(k)}\rangle\right\}$ have already been evaluated for the calculation of the Lagrangian gradient. As a result, stochastic evaluation of the reduced density matrix contribution for each sample $\mathbf{n}$, and for stochastic sampling of $\mathbf{m} \neq \mathbf{n}$ can then be formulated as

$$\Gamma_{pq,rs,\text{offdiag}} = \left\langle \frac{\langle\Psi^{(k)}|\mathbf{m}\rangle \langle\mathbf{n}|\Psi^{(k)}\rangle}{N_s P_{\text{gen}}(\mathbf{m}|\mathbf{n}) P(\mathbf{n};\Psi^{(k)})} \right\rangle_{P(\mathbf{n};\Psi^{(k)})} \tag{5.90}$$

where the outer brackets imply that the sampling of $\mathbf{n}$ is performed according to the distribution given in Eq.5.13. Diagonal terms, where $\mathbf{m} = \mathbf{n}$, are sampled deterministically and contribute for every sample of $\mathbf{n}$ as

$$\Gamma_{pq,rs,\text{diag}} = \left\langle \frac{\langle\Psi^{(k)}|\mathbf{n}\rangle \langle\mathbf{n}|\Psi^{(k)}\rangle}{P(\mathbf{n};\Psi^{(k)})} \right\rangle_{P(\mathbf{n};\Psi^{(k)})}. \tag{5.91}$$

Combination of both estimates

$$\Gamma_{pq,rs} = \Gamma_{pq,rs,\text{diag}} + \Gamma_{pq,rs,\text{offdiag}} \tag{5.92}$$

then leads to the complete density matrix. At the end of the sampling process, the 2-RDM is normalised to ensure that it satisfies the trace relation

$$\sum_{pq} \Gamma_{pq,pq} = \frac{N(N-1)}{2}, \tag{5.93}$$

whilst the one-body RDM can be integrated out if desired. Simultaneously, hermiticity $\Gamma_{pq,rs} = \Gamma_{rs,pq}$ is enforced in the two-body reduced density matrix by averaging the related pairs of elements, allowing for evaluation of a hermiticity error $\frac{\Gamma_{pq,rs}-\Gamma_{rs,pq}}{2}$ for each pair of off-diagonal elements whose maximum and mean value act as indicators for the sampling quality and convergence of the RDM[269].

This sampling approach allows for an efficient stochastic evaluation of the 2-RDM during the dynamics of the SGD algorithm with little additional computational cost.

Part of this computational expenditure is caused by the increase in memory requirement for storage of the 2-body reduced density matrix which scales as $\mathcal{O}[\left(\frac{M(M-1)}{2}\right)^2]$. The remaining computational costs are largely associated with identification and update of the density matrix elements to which each pair of determinants contributes. These processes involve $\mathcal{O}[N^2]$ operations for diagonal terms, and $\mathcal{O}[N]$ or $\mathcal{O}[1]$ operations for off-diagonal terms with single- or double excitations, respectively.

Care must be taken when evaluating stochastic estimators of non-linear functions of expectation values such as the 2-body reduced density matrix and properties obtained from it so as not to introduce a bias in the estimator. In general, for an unbiased estimator the expectation value over the probability distribution of the wavefunction should satisfy (up to a normalisation constant)

$$\mathrm{E}\left[\left\langle \frac{\Psi^{(k)}}{P(\Psi^{(k)})} \right\rangle_{P(\Psi^{(k)})}\right] = \Psi^{(k)}, \tag{5.94}$$

where $\left\langle \frac{\Psi^{(k)}}{P(\Psi^{(k)})} \right\rangle_{\Psi^{(k)})}$ denotes sampling of the exact wavefunction $\Psi^{(k)}$ according to the probability distribution $P(\Psi^{(k)})$. Yet, for any function $f(\Psi^{(k)})$ that is nonlinear in $\Psi^{(k)}$,

$$\mathrm{E}\left[f\left(\left\langle \frac{\Psi^{(k)}}{P(\Psi^{(k)})} \right\rangle_{P(\Psi^{(k)})}\right)\right] \neq f\left(\mathrm{E}\left[\left\langle \frac{\Psi^{(k)}}{P(\Psi^{(k)})} \right\rangle_{P(\Psi^{(k)})}\right]\right) \tag{5.95}$$

holds, which implies that estimating $f(\Psi^{(k)})$ by $\mathrm{E}\left[f\left(\left\langle \frac{\Psi^{(k)}}{P(\Psi^{(k)})} \right\rangle_{P(\Psi^{(k)})}\right)\right]$ will introduce a bias[346, 347]. This bias was present when reduced density matrices were sampled in FCIQMC[269, 253], since the appropriate contributions $\mathrm{E}\left[\left\langle \frac{\langle \Psi^{(k)}|\mathbf{m}\rangle}{P(\Psi^{(k)})} \right\rangle_{P(\Psi^{(k)})}\right]$ $\times\, \mathrm{E}\left[\left\langle \frac{\langle \mathbf{n}|\Psi^{(k)}\rangle}{P(\Psi^{(k)})} \right\rangle_{P(\Psi^{(k)})}\right]$ are in fact approximated by $\mathrm{E}\left[\left\langle \frac{\langle \Psi^{(k)}|\mathbf{m}\rangle\langle \mathbf{n}|\Psi^{(k)}\rangle}{P(\Psi^{(k)})} \right\rangle_{P(\Psi^{(k)})}\right]$ which neglects the (non-zero) covariance between the amplitudes and thus results in biased sampling even if the $\mathrm{E}\left[\left\langle \frac{\langle \mathbf{n}|\Psi^{(k)}\rangle}{P(\Psi^{(k)})} \right\rangle_{P(\Psi^{(k)})}\right]$ themselves are unbiased. The main source of potential error is therefore the fact that the two amplitudes contributing to the density matrix elements are correlated with the dominant error arising from diagonal terms where the instantaneous amplitude projections are perfectly correlated and where the error is of a single sign thereby removing the possibility of fortuitous cancellation of errors. To guarantee unbiased sampling of the density matrices, FCIQMC uses a replica sampling approach whereby two completely independent walker populations (replicas) are propagated simultaneously such that the amplitudes are uncorrelated between them[260, 269, 253], allowing for independent estimates of $\mathrm{E}\left[\left\langle \frac{\langle \Psi^{(k)}|\mathbf{m}\rangle}{P(\Psi^{(k)})}\right\rangle_{P(\Psi^{(k)})}\right] \times \mathrm{E}\left[\left\langle \frac{\langle \mathbf{n}|\Psi^{(k)}\rangle}{P(\Psi^{(k)})}\right\rangle_{P(\Psi^{(k)})}\right]$ as $\mathrm{E}\left[\left\langle \frac{\langle \Psi^{(k)}_{(1)}|\mathbf{m}\rangle\langle \mathbf{n}|\Psi^{(k)}_{(2)}\rangle}{P(\Psi^{(k)})}\right\rangle_{P(\Psi^{(k)})}\right]$ or $\mathrm{E}\left[\left\langle \frac{\langle \Psi^{(k)}_{(2)}|\mathbf{m}\rangle\langle \mathbf{n}|\Psi^{(k)}_{(1)}\rangle}{P(\Psi^{(k)})}\right\rangle_{P(\Psi^{(k)})}\right]$ or the appropriate average of both, where the notation $\langle \Psi^{(k)}_{(1)}|\mathbf{m}\rangle$ denotes the wavefunction amplitude $\langle \Psi^{(k)}|\mathbf{m}\rangle$ of replica 1. In the 2-RDM sampling procedure outlined above a similar replica approach is employed to a limited extend. In general, because of the non-linearity of the wavefunction many solutions with the same energy will exist. As a consequence, independent replicas will usually converge to different minima with the same energy and as such, the replica approach used in FCIQMC cannot be employed while the parameters in a polynomial complex wavefunction ansatz are still optimised. Instead, contributions to the energy $E^{(k)}_{\mathrm{RDM}}$ and the gradient $\frac{\partial \mathcal{L}[\Psi^{(k)}(Z^{(k)}_{\sigma})]}{\partial Z_{\sigma}}$ are simply evaluated from a single replica. Investigations were made as to whether approaches involving two replicas for sampling of the gradient and / or energy improved optimisation behaviour. However, all approaches were found to lead to divergences due to the multitude of different wavefunctions with the same energy. Once a single replica wavefunction is converged upon the 2-RDM can be sampled by initialising two replicas from the converged wavefunction, propagating them completely independently and sampling contributions to the 2-RDM and $E^{(k)}_{\mathrm{RDM}}$ using amplitudes from both replicas. This technique will remove as much of the correlation between the wavefunction amplitudes as possible although the possibility exists that a small degree of correlation still remains giving the same initial starting wavefunction for the two replicas. Similarly, concerns may be raised that a sampling of $E^{(k)}_{\mathrm{RDM}}$ and $\frac{\partial \mathcal{L}[\Psi^{(k)}(Z^{(k)}_{\sigma})]}{\partial Z_{\sigma}}$ may be biased during the wavefunction optimisation when both amplitudes in the contribution originate from the same replica and thus introduce an error in the optimisation. However, given the results to follow in the next chapter, it seems that this bias is smaller than the stochastic error in the sampling. In fact, no such error has so far been observed in practice and the RDM energy obtained from one replica was usually found to be in agreement with that obtained using two replica. A similar situation arose in an excited state approach within FCIQMC[249] where analogously concerns about a similar potential sampling bias were raised. Yet, as in this SGD approach no such bias was observed in practice despite its theoretical presence.

5.8 A Technical Point: Wavefunction Normalisation, Step Sizes and Parameter Updates

A technical yet important point regarding the efficiency of the optimisation is the dependence of estimators and parameter updates on the generally unknown normalisation of the wavefunction $\mathcal{N}[|\Psi^{(k)}|^2]$. In particular, updating the parameters alters the normalisation of the wavefunction such that the parameter changes may no longer be the optimal ones. In state-of-the-art VMC wavefunction optimisations this factor was found to profoundly affect the efficiency of the optimisation[217, 215] and therefore also needs consideration in this SGD approach. All energy expressions used in this SGD approach scale as $(\mathcal{N}[|\Psi^{(k)}|^2])^0$ as they ought to. By sampling the unnormalised two-body reduced density matrix from the wavefunction and then explicitly normalising from the trace relation, there is thus no issue introduced by any change in the normalisation of the wavefunction. Similarly, $P(\mathbf{n}, \Psi^{(k)})$ in Eq. 5.13 is a normalised distribution and therefore scales as $(\mathcal{N}[|\Psi^{(k)}|^2])^0$. However, the equations for the Lagrangian in Eq. 5.15 and 5.16 include a global dependence on the normalisation of the wavefunction. A change in the normalisation of the wavefunction therefore affects the effective magnitude of the update in each iteration, thereby resulting in a new effective step size, $\tau_{Z_\sigma}^{(k)'}$, in a non-trivial manner, through the magnitude of both $\mathcal{N}[|\Psi^{(k)}|^2]$, as well as $\langle \frac{\partial \Psi^{(k)}}{\partial Z_\sigma}|$ and $|\Psi^{(k)}\rangle$. In the case of a fixed step size, the dynamics of the non-linear optimisation will not be invariant to this change which is in contrast to FCIQMC with its linear ansatz where the magnitude of changes to the wavefunction would vary linearly with the L_1 norm of $\Psi^{(k)}$. The dependence of the resultant effective step size on the normalisation of the wavefunction will change with both the parameterisation and the probability distribution used to sample the wavefunction in Eq. 5.13. However, for an exact parameterisation and sampling, the gradient vector will necessarily vanish as the solution is converged upon, thereby mitigating the norm dependence in the effective step size.

It is worth considering the ramifications of the dependence of the parameter changes on the $\mathcal{N}[|\Psi^{(k)}|^2]$ and their relationship to other approaches in literature. In general, controlling the norm of parameter updates for non-linear wavefunctions is a difficult task for state-of-the-art VMC methods like Stochastic Reconfiguration or the Linear Method, as well. In these approaches, the update is rescaled, damped or a line search is performed to search for the optimal changes in parameters[215, 211]. These measures are not feasible for this SGD approach as they require an explicit projection into the tangent subspace of the wavefunction, a step that is avoided at all times in the

SGD optimisation. Yet, in practical applications, the implementation avoids potential problems for two reasons. Firstly, due to the shifting of the Hamiltonian by the current estimate of the energy only small changes in the normalisation of the wavefunction occur for all calculations attempted, even far from convergence. Secondly, the dynamical parameter-specific step size adjustment also mitigates many of the effects of the norm dependence of the effective step size. Specifically, by considering parameter-specific information from gradients of previous iterations and introducing an inverse dependence on these gradients into the individual step sizes the norm dependence is mitigated and a stable and efficient optimisation is achieved. For this reason, the $\mathcal{N}[|\Psi^{(k)}|^2]$ term in Eq. 5.15 and 5.16 are not explicitly considered in the algorithm, and its effect on the formal convergence rate is small[323].

5.9 Comparison to State-of-the-art VMC Methods

The stochastic gradient descent (SGD) of the Lagrangian described above results in an iteration cost that is independent of the size of the Hilbert space and thus renders this method inherently suitable for large scale systems like other Quantum Monte Carlo approaches. Yet, it also admits a number of advantages over state-of-the-art VMC optimisation[215, 348, 213], such as the avoidance of the construction of matrices in the tangent space of the wavefunction, whose sampling and manipulation becomes a bottleneck for large numbers of parameters. Krylov subspace techniques have been proposed to circumvent this by projecting down to more manageable space[208]. Yet, ill-conditioning can limit the efficiency of this approach although recent developments of the Linear Method attempt to address its memory bottleneck[349]. Furthermore, diagonalisation of the randomly sampled matrices required in some optimisations can lead to biases in the final parameters[248, 350]. Moreover, the SGD approach bears similarities with the Stochastic Reconfiguration method (SR)[348, 213], which can also be considered an imaginary time propagation that differs from steepest descent in its definition of the metric in parameter space for the updates[212]. Due to this, SR requires projection of the equations into the fixed tangent space of the current wavefunction and stabilisation of the resultant matrix equations[213]. However, the proposed matrix-free stochastic application of Eq. 5.4 describes a quasi-continuous optimisation, where the error bar at convergence represents both the stochastic error in the sampling, and the variation in the wavefunction as it is sampled. In addition, the dynamics of the optimisation also provide access to the two-body reduced density, and thus arbitrary 1- and 2-body static properties of the wavefunction as outlined above with little additional computational cost. Hence, these static properties including spin and magnetic properties, as well as the energy, are evaluated from the sampled density matrix, rather than from the local energy as it is commonly the case in traditional VMC approaches. Furthermore, Quantum Monte Carlo methods working in first quantised basis of electron coordinates usually evaluate density matrices by sampling either from a grid or a suitable probability distribution within the configuration space which tends to be more expensive, in particular when considering a 2-RDM expressed in non-localised basis functions[345].

Chapter 6

Applications of the Projector Quantum Monte Carlo Method for Non-linear Wavefunctions to Correlator Product State Wavefunctions

In this chapter, a number of applications of the Projector Quantum Monte Carlo method for non-linear wavefunctions are presented which demonstrate the ability of this approach to optimise arbitrary non-linear wavefunction ansatzes for quantum many-body systems, as well as its ability to evaluate the static properties of these wavefunction from their sampled two-body reduced density matrix. These wavefunctions are sought for a multitude of systems, ranging from lattice Hubbard models to *ab-initio* systems in one- and two-dimensions

In order to advance to larger condensed phase systems than those amenable to FCI techniques and circumvent the exponential scaling of the full Hilbert space, one approach for designing an efficient and compact wavefunction ansatz is to exploit the fact that electron correlation is, in general, inherently local. Two-point correlation functions (away from criticality) will decay exponentially with distance, whilst the screening of the Coulomb interaction in bulk systems will result in local entanglement of nearby electrons, with distant electrons behaving increasingly independently[132]. The existence of this locality of electron correlation, as well as the existence of area laws, and thereby the reduced amount of entanglement which effectively quantifies the relevant number of degrees of freedom, suggests that quantum many-body states of strongly-correlated materials may be faithfully described by an efficient parameterisation. This concept lies at the heart of powerful numerical algorithms such as the density-matrix renormalisation group approach (DMRG)[56, 143, 144] and its higher-dimensional analogues[55] in the realm of Tensor Network States (TNS). A further quantum many-body state ansatz which exploits locality to formally contain the scaling to polynomial cost is an ansatz in the form of Correlator Product States (CPS)[351–356], which explicitly correlate plaquettes of neighbouring degrees of freedom. Related wavefunctions are also referred to as entangled plaquette states[357–359] or complete graph tensor networks[360, 361]) to stress their connection to higher-dimension generalisations of matrix product states[362]. In this sense, the CPS ansatz, which can also be regarded as a class of Tensor Network States, has been introduced to extend DMRG to higher dimensions whilst avoiding the computational cost of other higher dimensional TNS algorithms. Whereas TNS introduce auxiliary degrees of freedom in order to introduce correlations between physical degrees of freedom, CPS correlate the physical degrees of freedom explicitly. The CPS ansatz is extremely versatile, the form and size of correlators can be chosen to best represent the properties of the system, which also makes the wavefunction systematically improvable. A mapping between some types of CPS and TNS and vice versa can be established, however, each parameterisation form will always only represent a subset of the states that it is mapped onto[351, 363]. Like TNS, CPS with local correlators satisfy an area law thereby suggesting that they should be well suited for systems with finite correlation length. On the contrary, CPS with long-ranged correlators are area law violating. Obeying a volume law, they are able to describe an even higher degree of entanglement and are thus suitable for parameterising states of critical systems[351, 364].

Previously, the variational parameters of these CPS wavefunction have been optimised with a number of approaches, some of which are of deterministic nature[352, 363], whilst most of them use Variational Monte Carlo (VMC) approaches[357, 364, 208]. In particular, VMC methods such as the Linear Method and Stochastic Reconfiguration enabled the optimisation of large numbers of parameters. The results presented in this chapter, demonstrate that the Projector Quantum Monte Carlo method proposed in the previous Chapter is able to optimise and handle CPS wavefunctions with much larger numbers of variational parameters then previous VMC optimisations.

6.1 The Correlator Product State Wavefunction Ansatz

The exact eigenstate of the non-relativistic time-independent electronic Schrödinger equation for an N-particle system in a discrete basis of M one-particle states assumes the form of an FCI wavefunction ansatz, as in FCIQMC,

$$|\Psi_{\mathrm{FCI}}\rangle = \sum_{n_1 n_2 \ldots n_M}^{q} X_{\mathbf{n}} |n_1 n_2 \ldots n_M\rangle = \sum_{\mathbf{n}} X_{\mathbf{n}} |\mathbf{n}\rangle , \tag{6.1}$$

where $X_{\mathbf{n}}$ denotes the expansion coefficient of the occupation number vector $|\mathbf{n}\rangle$. The first sum runs over the dimension q of the local Hilbert space of the single-particle basis states $\{|n_i\rangle\} = \{|1\rangle, |0\rangle\}$ and is restricted to those occupation vectors satisfying $\sum_i^M n_i = N$. Since each occupation vector is formed as a direct product of states in the local Hilbert space $|\mathbf{n}\rangle = |n_1 n_2 \ldots n_M\rangle = |n_1\rangle \otimes |n_2\rangle \otimes \ldots \otimes |n_M\rangle$, the size of the complete N-particle Hilbert space, and hence, of the number of variational parameters in the FCI wavefunction scales exponentially with system size[37].

Although the exactness of the FCI wavefunction for a given basis represents a huge advantage, its exponential scaling makes it prohibitively expensive in practice, particularly for large systems, and efficient and more compact parameterisations of the wavefunction such as correlator product states are needed. An integral part of the CPS ansatz is the concept of a correlator which directly encodes correlations between single-particle states. In general, the CPS ansatz defines 'correlators' as diagonal operators which directly encode the entanglements within sets of single-particle states as[351, 352, 357]

$$\hat{C}_\lambda = \sum_{\mathbf{n}_\lambda} C_{\mathbf{n}_\lambda} \hat{P}_{\mathbf{n}_\lambda}, \tag{6.2}$$

where $\hat{P}_{\mathbf{n}_\lambda} = |\mathbf{n}_\lambda\rangle \langle \mathbf{n}_\lambda|$ is the projection operator for the single many-body state $\mathbf{n}_\lambda$ in the set of all many-body Fock states $\{\mathbf{n}_\lambda\}$ in the correlator λ with correlator amplitudes $\{C_{\mathbf{n}_\lambda}\}$. The CPS wavefunction is then written as multi-linear product of correlator operators acting on a chosen reference state[351, 365]

$$|\Psi_{\mathrm{CPS}}\rangle = \prod_\lambda \hat{C}_\lambda |\Phi\rangle . \tag{6.3}$$

Possible choices for the reference state include the uniform reference

$$|\Phi_{\mathrm{U}}\rangle = \sum_{\mathbf{n}} |\mathbf{n}\rangle \,, \tag{6.4}$$

an equally weighted sum of all occupation number vectors which may be chosen to satisfy symmetry constraints, as well as an Antisymmetrised Geminal Power (AGP) wavefunctions[5, 366, 212]

$$|\Phi_{\mathrm{AGP}}\rangle = \exp(\hat{F})\,|0\rangle \,, \tag{6.5}$$

where the pairing operator $\hat{F}$ creates a linear combination of all possible singlet pairings of one-particle states $\hat{F} = \sum_{i,j=1}^{\frac{M}{2}} f_{ij} a^{\dagger}_{i\uparrow} a^{\dagger}_{j\downarrow}$. Similarly, further states which can act as reference state are a generalisation of the AGP wavefunction, the Pfaffian pairing wavefunction[367–369]

$$|\Phi_{\mathrm{PF}}\rangle = \exp(\hat{G})\,|0\rangle \,, \tag{6.6}$$

defined in terms of a generalised pairing operator $\hat{G} = \sum_{i=1}^{M} \sum_{j=i+1}^{M} g_{ij} a^{\dagger}_{i} a^{\dagger}_{j}$ that creates linear combinations of all singlet and triplet pairings. Alternatively, a single Slater determinant can act as reference state

$$|\Phi_{\mathrm{D}}\rangle = \prod_{i=1}^{N} \left(\sum_{j=1}^{M} \Theta_{ij} a^{\dagger}_{j} \right) |0\rangle \,, \tag{6.7}$$

where $|0\rangle$ is the vacuum state, $a^{\dagger}_{j}$ represents the creation operator for the jth one-particle state of the basis set and $\boldsymbol{\Theta}$ denotes the matrix of coefficients whose ith row defines the coefficient of the ith state[365, 65]. The CPS wavefunction thus provides a product approximation to the FCI wavefunction which for a single Slater determinant reference state, as it will be used often throughout this work, is of the explicit form

$$|\Psi_{\mathrm{CPS}}\rangle = \sum_{\mathbf{n}} \prod_{\lambda} C^{(\mathbf{n})}_{\lambda} |\mathbf{n}\rangle \langle \mathbf{n}| \prod_{i=1}^{N} \left(\sum_{j=1}^{M} \Theta_{ij} a^{\dagger}_{j} \right) |0\rangle \,, \tag{6.8}$$

where $\prod_{\lambda} C^{(\mathbf{n})}_{\lambda}$ denotes the set of correlator amplitudes which give rise to the global occupation defined in $|\mathbf{n}\rangle$. It can be shown that a number of different phases and wavefunctions can be expressed in this form, including resonating valence bond (RVB) and Laughlin wavefunctions[351]. As the number of degrees of freedom in the system grows, the complexity of the wavefunction grows only linearly. Additionally, this choice of low-rank factorisation of the wavefunction is systematically improvable in the limit of increasing correlator sizes as this recovers longer-ranged entanglement effects and increases the number of variables in the wavefunction parameterisation. In the limit of one large correlator covering all single-particle states in the system, the exact FCI wavefunction is recovered[351, 352] and the CPS wavefunction is thus systematically improvable to exactness.

6.2 Wavefunction Amplitudes and Derivatives

Projecting the CPS wavefunction into the complete Hilbert space of configurations $\{\mathbf{n}\}$, the wavefunction amplitudes are given by

$$\langle \mathbf{n} | \Psi_{\mathrm{CPS}} \rangle = \langle \mathbf{n} | \prod_{\lambda} \hat{C}_{\lambda} | \mathbf{n} \rangle \, \langle \mathbf{n} | \Phi \rangle \, . \tag{6.9}$$

Whilst the correlator part of the CPS wavefunction makes a contribution of

$$\langle \mathbf{n} | \prod_{\lambda} \hat{C}_{\lambda} | \mathbf{n} \rangle = \langle \mathbf{n} | \prod_{\lambda}^{N_{\mathrm{corr}}} \hat{C}_{\lambda}^{(\mathbf{n})} | \mathbf{n} \rangle \, , \tag{6.10}$$

where $\hat{C}_{\lambda}^{(\mathbf{n})}$ denotes the set of correlator amplitudes contributing to $|\mathbf{n}\rangle$ and N_{corr} the number of correlators, the explicit form of the reference state contribution depends on the nature of $|\Phi\rangle$. For a uniform reference state, its contribution to the wavefunction amplitude is

$$\langle \mathbf{n} | \Phi_{\mathrm{U}} \rangle = \sum_{\mathbf{m}} \langle \mathbf{n} | \mathbf{m} \rangle = \delta_{\mathbf{nm}}, \tag{6.11}$$

while a single Slater determinant reference state results in a determinant of orbital coefficients

$$\langle \mathbf{n} | \Phi_{\mathrm{D}} \rangle = \langle \mathbf{n} | \prod_{i=1}^{N} \left(\sum_{j=1}^{M} \Theta_{ij} a_j^{\dagger} \right) | 0 \rangle \, , \tag{6.12}$$

where $\boldsymbol{\Theta}$ represents the matrix defining the orbitals in the reference Slater determinant. Similarly, in the case of an AGP reference state its respective component of the projection onto the configuration is a determinant of the pairing matrix

$$\langle \mathbf{n} | \Phi_{\mathrm{AGP}} \rangle = \frac{1}{\left(\frac{N}{2}\right)!} \langle \mathbf{n} | \left(\sum_{i,j=1}^{\frac{M}{2}} f_{ij} a^{\dagger}_{i\uparrow} a^{\dagger}_{j\downarrow} \right)^{\frac{N}{2}} |0\rangle \,, \tag{6.13}$$

where $\mathbf{f}$ represents the symmetric pairing matrix ($f_{ij} = -f_{ji}$) describing the coefficients of all possible singlets in the linear combination. For a general pairing function acting as reference state the contribution is given by a pfaffian of the occupied pairing matrix

$$\langle \mathbf{n} | \Phi_{\mathrm{PF}} \rangle = \frac{1}{\left(\frac{N}{2}\right)!} \langle \mathbf{n} | \left(\sum_{i=1}^{M} \sum_{j=i+1}^{M} g_{ij} a^{\dagger}_{i} a^{\dagger}_{j} \right)^{\frac{N}{2}} |0\rangle \tag{6.14}$$

with $\mathbf{g}$ describing the occupied pairing matrix ($g_{ij} = -g_{ji}$) holding the coefficients of all possible singlets and triplets in the linear combination.

Whereas the correlator part of the wavefunction amplitudes can be computed in $\mathcal{O}[N_{\mathrm{corr}}]$ time, the determinant and pfaffian of the reference states both require an $\mathcal{O}[N^3]$ operation. Fast updates of the determinant based on the Sherman-Morrison formula reduce the scaling of the computation of the determinant overlap down to $\mathcal{O}[N^2]$, while the correlator amplitudes for a local update can similarly scale as $\mathcal{O}[1]$.

Derivatives with respect to the wavefunction parameters Z_σ can be computed as

$$\langle \mathbf{n} | \frac{\partial \Psi_{\mathrm{CPS}}}{\partial C_\sigma} \rangle = \frac{1}{C_\sigma} \langle \mathbf{n} | \Psi_{\mathrm{CPS}} \rangle \tag{6.15}$$

$$\langle \mathbf{n} | \frac{\partial \Psi_{\mathrm{CPS}}}{\partial \Theta_{ij}} \rangle = \left(\Theta^{-1} \right)_{ji} \langle \mathbf{n} | \Psi_{\mathrm{CPS}} \rangle \tag{6.16}$$

$$\langle \mathbf{n} | \frac{\partial \Psi_{\mathrm{CPS}}}{\partial f_{ij}} \rangle = \left(f^{-1} \right)_{ji} \langle \mathbf{n} | \Psi_{\mathrm{CPS}} \rangle \tag{6.17}$$

$$\langle \mathbf{n} | \frac{\partial \Psi_{\mathrm{CPS}}}{\partial g_{ij}} \rangle = \frac{1}{2} \left(g^{-1} \right)_{ji} \langle \mathbf{n} | \Psi_{\mathrm{CPS}} \rangle \,, \tag{6.18}$$

which are thus obtainable from the respective wavefunction amplitudes $\langle \mathbf{n} | \Psi_{\mathrm{CPS}} \rangle$ in $\mathcal{O}[1]$ time.

6.3 2D Hubbard Model

A first example of the ability of the Projector Quantum Monte Carlo approach to converge wavefunctions with many parameters is given by the treatment of a 98-site

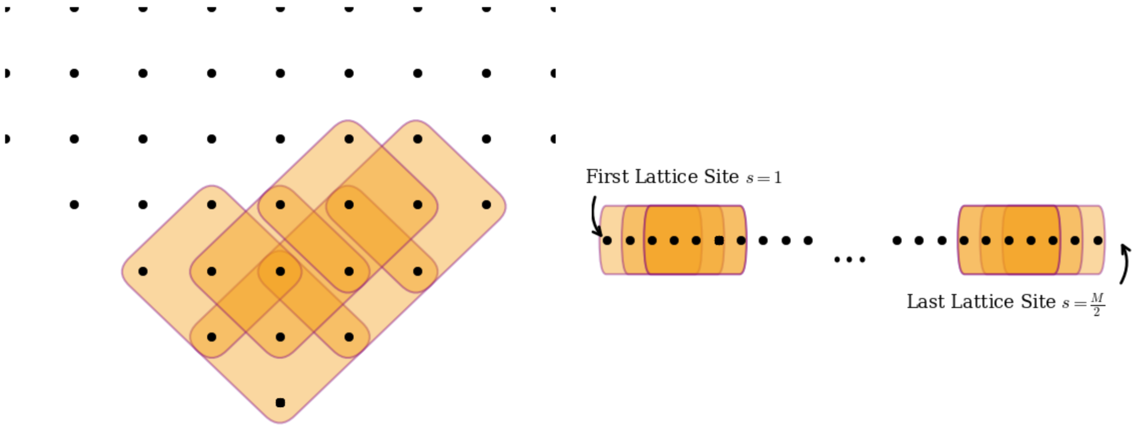

Fig. 6.1 Illustration of correlators. On the left hand-side, the independent, overlapping five-site correlator plaquettes are shown as they are used in the CPS wavefunction parameterisation for the $2D$ 98-site Hubbard Model on a square lattice. One such correlator plaquette is centred at each lattice site, giving a total of 98 correlators building the CPS wavefunction. For lattice sites at the boundaries, the correlators are tiled around the 98-site cluster in accordance with the periodic boundary conditions. The graph on the right-hand side illustrates the independent, overlapping 5-site line correlators one of which is anchored at each lattice site. The one exception from this arises in the case of open boundary conditions where the final last lattice sites are not associated with a correlator. In other words, for n-site line correlators employed for a $1D$ system with $\frac{M}{2}$ lattices sites and open boundary conditions all lattice sites apart from the last $n-1$ lattice sites are associated with one line correlators and the CPS wavefunction of the system is parameterised with $\frac{M}{2}-(n-1)$ independent line correlators. These line correlators are employed for CPS wavefunctions describing states in the $1D$ linear Hubbard model, as well as the linear H_{50} chain.

Method	E_{total}	E_{corr}	P_{corr}
RHF	0.351374	0.0	0.0
PMC+CPS	−0.505443(3)	−0.856817(3)	97.9
GFMC	−0.52370(1)	−0.87507(1)	100.0

Table 6.1 $2D$ Hubbard model: 98-site tilted cluster on a square lattice at half-filling with $\frac{U}{t} = 8$ and periodic boundary conditions. The total ground state energy E_{total}, and correlation energy E_{corr} per site (both in E_h) were obtained using Restricted Hartree-Fock (RHF) theory, Greens-function Monte Carlo (GFMC) methods and the developed Projector Quantum Monte Carlo approach in combination with a CPS wavefunction (PMC+CPS) with five-site tilted square correlators and an unrestricted reference Slater determinant. $P_{\text{corr}} = \frac{E_{\text{corr}}(\text{approach})}{E_{\text{corr}}(\text{GFMC})}$ (in %) denotes the percentage of GFMC correlation energy, E_{corr}(GFMC), captured by the other approaches. The numbers in parentheses represents the error in the previous digit. Stochastic errors for PMC+CPS have been obtained through a Flyvbjerg-Petersen blocking analysis[268]. The GFMC energy is taken from Ref.[370].

tilted 2D Hubbard model at half-filling, with $\frac{U}{t} = 8$ and periodic boundary conditions. As CPS wavefunction in this study, independent, overlapping five-site correlators centred on every site in the lattice were chosen to correlate with nearest neighbours, allowing up to ten-electron short-ranged correlations to be directly captured, as well as long range correlation and symmetry-breaking through coupling between the overlapping correlators and the optimisation of the Slater determinant. The lattice and tiling of these correlator plaquettes is depicted in Figure 6.1. Accurate results for this system are given by Greens-function Monte Carlo (GFMC)[370] methods. The optimised CPS wavefunction captures 97.9% of this correlation energy (Table 6.1), with the remaining likely to be due to the lack of direct long-range two-body correlation. However, this parameterisation still requires the simultaneous optimisation of over 10^5 parameters, specifically 109, 950 parameters, beyond the capabilities of most VMC implementations. Figure 6.2 displays the convergence of the CPS wavefunction for the simple SGD scheme and the accelerated scheme with Nesterov acceleration and RMSProp step size adaptation which demonstrates a striking advance in the rate of convergence afforded by the accelerated scheme. The inset in Figure 6.2 illustrates fluctuations in both the statistical sampling of the expectation values and in the variations of the wavefunction parameters. It is likely that the remaining, or at least part of the remaining 2.1% of the GFMC correlation energy, can be accounted for by including long-range two-site correlators, larger-sized correlator plaquettes or a better reference state such as an AGP or general pairing function.

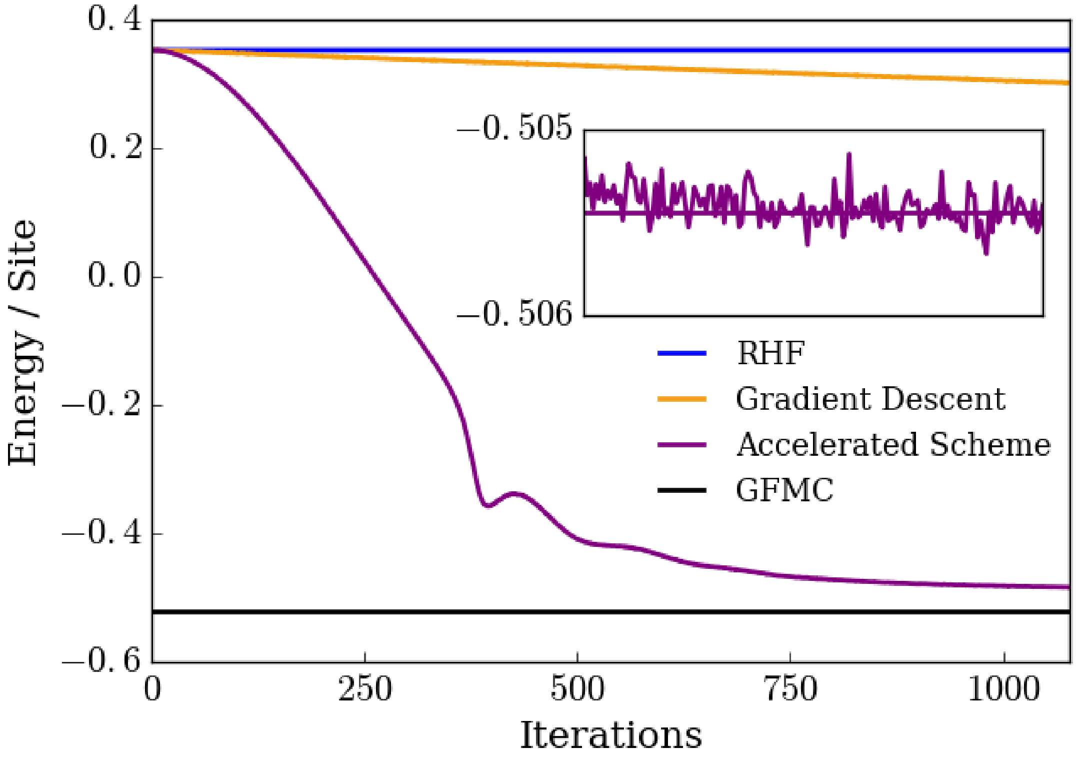

Fig. 6.2 Convergence of CPS wavefunction with $\mathcal{O}[10^5]$ parameters for the $2D$ 98-site Hubbard model on a square lattice at half-filling with $\frac{U}{t} = 8$. The differences in the convergences rates of the Stochastic Gradient Descent (SGD) and the accelerated scheme are apparent. As outlined in the previous chapter, the accelerated scheme combines Nesterov's accelerated gradient descent with the RMSprop algorithms for dynamical step size adjustments. The GFMC energy is taken from Ref.[370]. The inset illustrates both the statistical sampling of expectation values and in the variations of the parameters.

6.4 1D Hubbard Model

To study the systematic improvability of the CPS ansatz, a 1D 1×22-site Hubbard model is considered such that benchmark data can be found from the Density Matrix Renormalisation Group (DMRG), which can be made numerically exact for this 1D system[352]. Results at half-filling and $U = 4t$ with open boundary conditions are presented in Figure 6.3 and Table 6.2 while the independent, overlapping line correlators used in this study are depicted in Figure 6.1. For a CPS wavefunction of three-site overlapping correlators and a fixed, non-interacting reference, the SGD approach finds a variationally lower result than previously published for an identical wavefunction parameterisation via Linear Method optimisation[352]. This might be due to the bias arising from the non-linear operations (diagonalisation) of random variables present in these alternate algorithms[248, 350]. Furthermore, this system is used to investigate how increasing the size of the correlators (three-site ($\hat{C}_3$), five-site ($\hat{C}_5$) and seven-site ($\hat{C}_7$) line correlators) in order to directly capture longer-ranged many-body correlations, as well as optimising spin-polarised (Φ_{UHF}) or non-collinear (Φ_{GHF}) Slater determinants rather than a paramagnetic orbital component (Φ_{RHF}) affects the quality of the wavefunction. The increased flexibility of this democratic wavefunction gives rise to systematic convergence towards DMRG with very small error bars, despite requiring over quarter of a million variables. In particular, the total number of simultaneously optimised parameters in Ψ_{CPS} ranges from $1,280$ (three-site line correlators with fixed RHF Slater determinant) to $263,112$ (seven-site line correlators with optimised non-collinear Slater determinant). Examining the convergence towards the DMRG limit more closely reveals two factors: Firstly, with increasing correlator size more of the longer-ranged many-body correlations are described directly which, as expected, increases the accuracy of the CPS wavefunction. Yet, once the correlators span a number of lattice sites that is comparable to the correlation length of the system the gain in accuracy resulting from a further enlargement of the correlators in relation to the associated increase in computational expenditure decreases and convergence to the exact DMRG limit becomes successively more expensive as the latter is approached. Similarly, augmenting the variational flexibility of the reference Slater determinant leads to a smaller rise in accuracy of Ψ_{CPS} with increasing correlator size, as more of the longer-ranged correlations can now be described directly by the correlators and need not be accounted for by the reference state.

In addition, the two-body density matrices are sampled from the converged wavefunctions and a range of wavefunctions properties are evaluated from the former. These

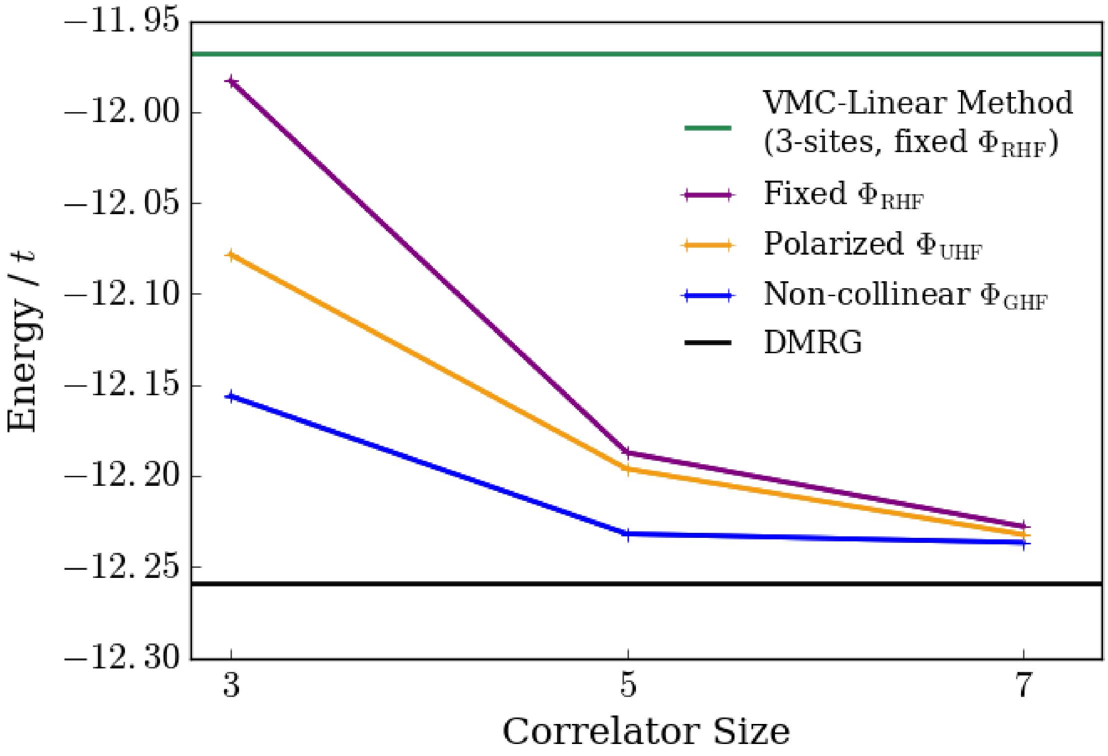

Fig. 6.3 Convergence of energy of CPS wavefunctions with increased flexibility for the $1D$ 1×22 Hubbard model at half-filling with $U = 4t$. The CPS energy converges towards the DMRG energy is the number of parameters and thus the flexibility in the wavefunction is increased. VMC Linear Method and DMRG energies are taken from Ref. [352].

properties include the RDM energy

$$E_{\text{RDM}} = \text{Tr}[\Gamma\hat{\mathcal{H}}] = \sum_{pq} h_{pq}\gamma_{pq} + \sum_{p>q,r>s}(g_{pqrs} - g_{pqsr})\Gamma_{pq,rs} + E_{\text{nuc}}, \tag{6.19}$$

(with h_{pq}, g_{pqrs} and E_{nuc} as defined in Section 2.2.2 of Chapter 2), to demonstrate that this estimator sampled from two replicas is in agreement with the energy estimated during convergence which is sampled from just one replica. Likewise, the total squared magnitude of the spin, $\hat{\mathcal{S}}^2 = \hat{\mathcal{S}} \cdot \hat{\mathcal{S}}$, is computed[37, 57]

$$\begin{aligned} S^2 = S(S+1) &= \text{Tr}[\Gamma\hat{\mathcal{S}}^2] && (6.20)\\ &= \frac{1}{4}\sum_{PQ}[\Gamma_{P\alpha Q\alpha,P\alpha Q\alpha} + \Gamma_{P\beta Q\beta,P\beta Q\beta}] - \frac{1}{4}\sum_{PQ}\Gamma_{P\alpha Q\beta,P\alpha Q\beta} && (6.21)\\ &\quad - \frac{1}{4}\sum_{PQ}\Gamma_{P\beta Q\alpha,P\beta Q\alpha} - \sum_{PQ}\Gamma_{P\alpha Q\beta,Q\alpha P\beta} + \frac{3}{4}N_\alpha + \frac{3}{4}N_\beta, && (6.22)\end{aligned}$$

where P_α refers to the α spin orbital with spatial index P. The value of S^2 can also be taken as a measure for the accuracy of the wavefunction given that the exact wavefunction has $S^2 = 0$. Moreover, further properties are evaluated such as the double occupancy, $\hat{\mathcal{D}} = \frac{1}{N_{\text{lat}}}\sum_I n_{I\uparrow}n_{I\downarrow} = \frac{1}{N_{\text{lat}}}\sum_I a^\dagger_{I\uparrow}a^\dagger_{I\downarrow}a_{I\downarrow}a_{I\uparrow}$,

$$D = \text{Tr}[\Gamma\hat{\mathcal{D}}] = \frac{1}{N_{\text{lat}}}\sum_I \Gamma_{I\uparrow I\downarrow,I\uparrow I\downarrow}, \tag{6.23}$$

where the sum over I includes all N_{lat} lattice sites, as well as the correlation entropy per electron

$$S_{\text{CE}} = -\text{Tr}[\gamma\ln\gamma] = -\frac{1}{N}\sum_p \gamma^p_p \ln\gamma^p_p, \tag{6.24}$$

with γ^p_p being the occupation numbers of the one-body RDM γ that is integrated out from the 2-RDM. A last quantity which is evaluated from the density matrix is the anti-ferromagnetic order parameter, the staggered magnetisation, which is defined according to

$$M^2 = \frac{1}{N^2_{\text{lat}}}\sum_{IJ}(-1)^{(x_I+y_I)+(x_J+y_I)}\left\langle\Psi|\hat{\mathcal{S}}_I \cdot \hat{\mathcal{S}}_J|\Psi\right\rangle, \tag{6.25}$$

where the summations over I and J run over all N_{lat} lattice sites and x_I and y_I represent the x- and y-coordinate of the position of the lattice site I. The total spin operator

$\hat{\mathcal{S}} = \hat{\mathcal{S}}_\mathbf{x} + \hat{\mathcal{S}}_\mathbf{y} + \hat{\mathcal{S}}_\mathbf{z}$ comprises three Cartesian components which are given by

$$\hat{\mathcal{S}}_\mathbf{x} = \frac{1}{2}\sum_P (a^\dagger_{P\alpha} a_{P\beta} + a^\dagger_{P\beta} a_{P\alpha}) \tag{6.26}$$

$$\hat{\mathcal{S}}_\mathbf{y} = \frac{1}{2i}\sum_P (a^\dagger_{P\alpha} a_{P\beta} - a^\dagger_{P\beta} a_{P\alpha}) \tag{6.27}$$

$$\hat{\mathcal{S}}_\mathbf{z} = \frac{1}{2}\sum_P (a^\dagger_{P\alpha} a_{P\alpha} + a^\dagger_{P\beta} a_{P\beta}) \tag{6.28}$$

with $\hat{\mathcal{S}}_z = \frac{1}{2}(N_\alpha - N_\beta) = M_z$.

The results for the properties evaluated from the sampled two-body density matrix of the differently parameterised wavefunctions are presented in Table 6.2. Firstly, a good agreement within error bars is observed between the RDM energy E_{RDM} sampled with one replica during the convergence of the wavefunction and E_{RDM} evaluated from the density matrix sampled with two replicas. This agreement demonstrates that a bias which can potentially arise when E_{RDM} is sampled from just one replica cannot be observed, seems to be negligible, or at least, smaller than stochastic errors and does not cause any issues. Secondly, the increased accuracy of Ψ_{CPS} with successively larger correlators becomes apparent in the values of S^2 which for any given reference state converge towards the correct value $S^2 = 0$ of the exact wavefunction with increasing correlator size. However, for any given correlator size, whilst increasing the flexibility of the reference state lowers and improves the CPS energy, the accuracy of Ψ_{CPS} does not necessarily improves in the same manner. This becomes obvious when considering the S^2 values of different reference states for a fixed correlator size which shows the rise in spin contamination in Ψ_{CPS} as the number of simultaneously optimised variables in the reference state is raised when going from Φ_{RHF} to Φ_{GHF}.

		Total Ground State Energy			RDM Properties			
$\lvert\Psi_{\mathrm{CPS}}\rangle$	N_{var}	E_{CPS}	P_{CPS}	E_{RDM}	S^2	M^2	D	S_{CE}
$\hat{C}_3\,\lvert\Phi_{\mathrm{RHF}}\rangle$	1280	−11.98302(5)	97.7	−11.982683	0.569250	0.093333	0.098274	7.810853
$\hat{C}_3\,\lvert\Phi_{\mathrm{UHF}}\rangle$	1764	−12.0785(2)	98.5	−12.078699	0.859770	0.090578	0.097759	7.409758
$\hat{C}_3\,\lvert\Phi_{\mathrm{GHF}}\rangle$	2248	−12.1562(2)	99.2	−12.157271	0.207711	0.095843	0.097799	8.834799
$\hat{C}_5\,\lvert\Phi_{\mathrm{RHF}}\rangle$	18432	−12.18720(2)	99.4	−12.186753	0.003052	0.091709	0.096725	8.971220
$\hat{C}_5\,\lvert\Phi_{\mathrm{UHF}}\rangle$	18916	−12.1962(1)	99.5	−12.195981	0.014278	0.086440	0.096763	8.887227
$\hat{C}_5\,\lvert\Phi_{\mathrm{GHF}}\rangle$	19400	−12.2319(2)	99.8	−12.231588	0.034608	0.094762	0.097059	8.968472
$\hat{C}_7\,\lvert\Phi_{\mathrm{RHF}}\rangle$	262144	−12.22782(9)	99.7	−12.228038	0.008617	0.091558	0.096904	8.959519
$\hat{C}_7\,\lvert\Phi_{\mathrm{UHF}}\rangle$	262628	−12.2323(3)	99.8	−12.233850	0.007314	0.090469	0.096930	8.948812
$\hat{C}_7\,\lvert\Phi_{\mathrm{GHF}}\rangle$	263112	−12.23677(9)	99.8	−12.237546	0.022978	0.095207	0.097127	8.956856

Table 6.2 $1D$ Hubbard model: 1×22 chain at half-filling with $\frac{U}{t} = 4$ and open boundary conditions. While the RHF ground state energy for this system is $E_{\mathrm{RHF}} = -5.307287E_h$, the DMRG energy is $E_{\mathrm{DMRG}} = -12.259082E_h$ (The DMRG energy is taken from Ref. [352]). A range of CPS wavefunctions $\lvert\Psi_{\mathrm{CPS}}\rangle$ were optimised for this system with the Projector Quantum Monte Carlo approach for non-linear wavefunctions. Optimised $\lvert\Psi_{\mathrm{CPS}}\rangle$ use 3-site ($\hat{C}_3$), 5-site ($\hat{C}_5$) and 7-site ($\hat{C}_7$) overlapping line correlators each in combination with either a fixed RHF ($\lvert\Phi_{\mathrm{RHF}}\rangle$), optimised unrestricted ($\lvert\Phi_{\mathrm{UHF}}\rangle$) or optimised non-collinear ($\lvert\Phi_{\mathrm{GHF}}\rangle$) reference Slater determinant, giving a total number of N_{var} optimised parameters in each case. E_{CPS} denotes their total ground state energies (in E_h) and $P_{CPS} = \frac{E_{\mathrm{CPS}}}{E_{\mathrm{DMRG}}}$ (in %) the percentage of DMRG energy captured by $\lvert\Psi_{\mathrm{CPS}}\rangle$. Quantities evaluated from the sampled RDM for $\lvert\Psi_{\mathrm{CPS}}\rangle$ include total energy obtained from RDM E_{RDM}, square magnitude of spin S^2, staggered magnetisation M^2, double occupancy D and entanglement entropy S_{CE}. All quantities are given in atomic units. Stochastic errors in the previous digits are presented in parentheses and were estimated with a Flyvbjerg-Petersen blocking analysis[268]. An estimate of the stochastic error associated with RDM properties is more difficult to obtain, but an idea can be gained by considering the difference between the theoretical and calculated value of S^2, as well as the maximum absolute error in Hermiticity and the sum of all absolute errors in Hermiticity, which are typically ~ 0.002 and ~ 4.0, respectively, in these calculations.

6.5 Linear H_{50} Chain

Ab-initio systems can also be treated in the same vein by stochastically sampling from both the configuration space of the wavefunction and from its $\mathcal{O}[N^4]$ connected configurations in Eq. 5.12, which are now far larger than found in the Hubbard model due to long-range interactions. As an example, the symmetric dissociation of H_{50} (in a STO-6G minimal basis[371]) is considered which represents a molecular model for strongly-correlated systems and a non-trivial benchmark system[372] at the same time. This system has been treated not only with conventional quantum chemistry methods such as Coupled Cluster (CC) but also with strongly-correlated approaches including DMFT and other embedding methods[373, 307, 374–376], due to the availability of numerically exact DMRG values for comparison[372]. Whilst CC methods encounter convergence difficulties at stretched bond-lengths beyond $2.0a_0$, a well known and documented fundamental problem in CC theory[372], strongly-correlated approaches can treat all bond lengths. The CPS wavefunction is parameterised with 5-atom overlapping correlators, and both a fixed unpolarised, or stochastically optimised unrestricted reference determinant, leading to a total of $47,104$ or $49,604$ simultaneously optimised variables. The results obtained with this Ψ_{CPS} are comparable or in some cases even better in their accuracy and closeness to DMRG results than approaches designed to treat strongly-correlated electrons as can be seen in the comparison in Table 6.3. At stretched bond lengths, nearly all of the DMRG correlation energy is captured (99.7%), as the correlation length spans few atoms, and on-site repulsion dominates (Figure 6.4). However, as the bond length decreases, a successively smaller percentage of the DMRG correlation energy is captured, as the entanglement of the electrons span larger numbers of atoms, which can also be seen in the larger bond dimension required of DMRG at these geometries[372]. Despite this, the correlation energy is so small at these lengths, that the maximum error in the total energy is only 1.1 kcal/mol per atom across all bond lengths.

		Correlation Energy									
								$\hat{C}_5 \vert\Phi_{\mathrm{RHF}}\rangle$		$\hat{C}_5 \vert\Phi_{\mathrm{UHF}}\rangle$	
R	E_{RHF}	E_{MP2}	E_{CCSD}	$E_{\mathrm{CCSD(T)}}$	E_{CPMFT}	$E_{\mathrm{CPMFT}(\kappa\mathrm{TPSSc})}$	E_{DMRG}	E_{CPS}	P_{corr}	E_{CPS}	P_{corr}
1.0	−16.86488	−0.36145	−0.40729	−0.41739			−0.41919	−0.3426(8)	81.7	−0.3451(4)	82.3
1.2	−22.46127	−0.40183	−0.47011	−0.48330			−0.48638	−0.4057(5)	83.4	−0.4075(2)	83.8
1.4	−25.02976	−0.44473	−0.54303	−0.55936			−0.56402	−0.4815(3)	85.4	−0.4829(7)	85.6
1.6	−26.06225	−0.49188	−0.63118	−0.65089			−0.65719	−0.5708(2)	86.9	−0.5721(1)	87.1
1.8	−26.26598	−0.54550	−0.74167	−0.76547	−0.21112	−1.38431	−0.77267	−0.6833(1)	88.4	−0.6853(1)	88.7
2.0	−26.00820	−0.60789	−0.88329	−0.91270			−0.91789	−0.8298(2)	90.4	−0.8307(2)	90.5
2.4	−24.83576	−0.76883	–	–			−1.32481	−1.2646(2)	95.5	−1.26603(6)	95.6
2.8	−23.36081	−0.99530	–	–			−1.91399	−1.86978(9)	97.7	−1.87091(4)	97.7
3.2	−21.89633	−1.30778	–	–			−2.67195	−2.64409(6)	99.0	−2.64503(2)	99.0
3.6	−20.57429	−1.72332	–	–			−3.52848	−3.51225(4)	99.5	−3.51295(3)	99.6
4.2	−18.95595	−2.55899	–	–			−4.79376	−4.77699(4)	99.7	−4.77792(2)	99.7

Table 6.3 Symmetric dissociation of H_{50}: For a range of bond lengths R (in a_0) for a linear chain of 50 H atoms in a STO-6G basis two types of CPS wavefunctions $|\Psi_{\mathrm{CPS}}\rangle$ are optimised with the Projector Quantum Monte Carlo approach for non-linear wavefunctions and their CPS correlation energies E_{CPS} are compared to correlation energies obtained with alternative high-level methods. $|\Psi_{\mathrm{CPS}}\rangle$ is parameterised with 5-site ($\hat{C}_5$) line correlators each in combination with either a fixed, unpolarised RHF ($|\Phi_{\mathrm{RHF}}\rangle$) or an optimised unrestricted ($|\Phi_{\mathrm{UHF}}\rangle$) reference Slater determinant. While E_{RHF} denotes the total RHF energy $P_{\mathrm{corr}} = \frac{E_{\mathrm{CPS}}}{E_{\mathrm{DMRG}}}$ (in %) represents the percentage of DMRG correlation energy captured by $|\Psi_{\mathrm{CPS}}\rangle$. All energies are given in E_h. Stochastic errors in the previous digits are presented in parentheses and were obtained with a Flyvbjerg-Petersen blocking analysis[268]. Energies from high-level correlated quantum chemical methods of Møller-Plesset perturbation theory (MP2), E_{MP2}, coupled-cluster up to double excitations (CCSD), E_{CCSD}, and with perturbative triple excitations (CCSD(T)), $E_{\mathrm{CCSD(T)}}$, as well as from numerically exact DMRG, E_{DMRG}, are taken from Ref. [372]. Whilst CPMFT (constrained-pairing mean-field theory) and CPMFT(κ TPSSc) can treat all bond lengths, energies are only available for a bond length of $R = 1.8a_0$ from Ref. [373].

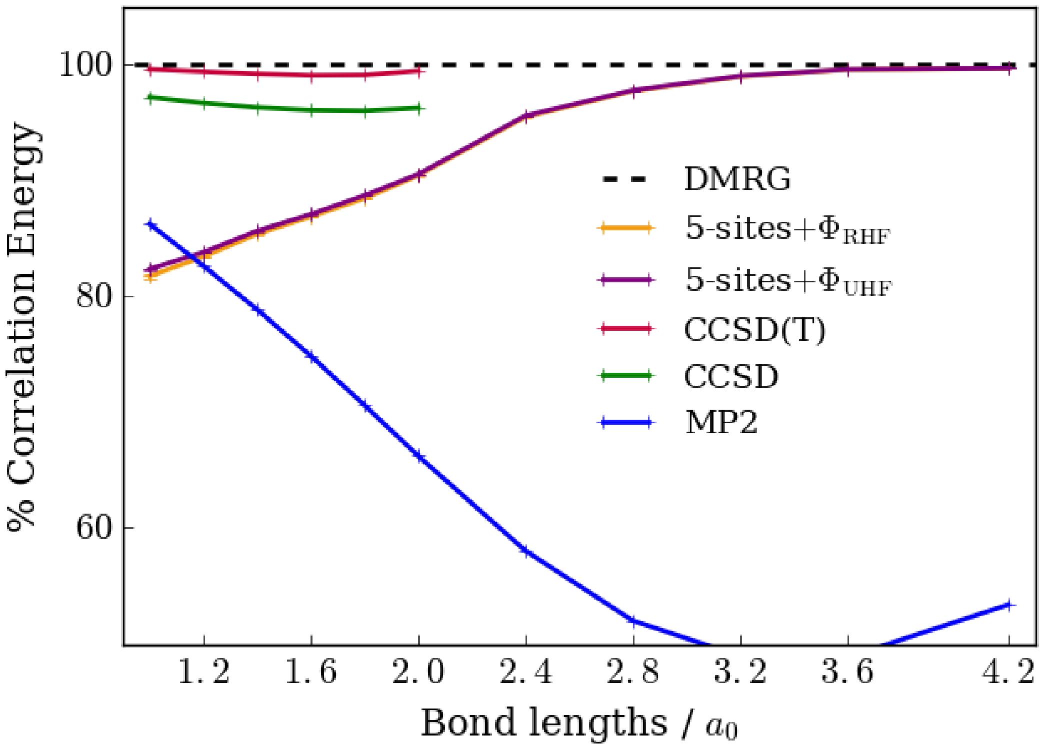

Fig. 6.4 The percentage of DMRG correlation energy captured by the CPS wavefunction for the symmetric dissociation of a linear chain of 50 H atoms in a STO-6G basis. The CPS wavefunction is parameterised with 5-atom overlapping correlators, and both a fixed unpolarised, or stochastically optimised unrestricted reference determinant. Numerically exact DMRG, as well as high-level correlated quantum chemical methods of Møller-Plesset perturbation theory (MP2), coupled-cluster up to double excitations (CCSD) and with perturbative triple excitations (CCSD(T)) are also included with values taken from Ref. [372]. The largest deviation in the total energy compared to DMRG across all bond lengths is 1.1kcal/mol per atom.

6.6 Graphene Sheet

Fully periodic localised orbitals can also be used to construct a Fock space in which to form a CPS wavefunction, and here an infinitely periodic graphene sheet with 4 × 4 k-point sampling[377] is considered. From a double-zeta periodic Gaussian basis one localised, translationally invariant $2p_z$ orbital centred on each carbon atom is chosen. Overlapping correlators consisting of the atoms on each hexagonal six-membered ring can then be constructed (Figure 6.5), and the full Hamiltonian projected into this low-energy space, including a potential from the core electrons at the Hartree-Fock level[255]. A generalised reference determinant is then stochastically optimised along with the correlators, giving a wavefunction parameterisation of $67,584$ parameters – the largest, or at least one of the largest numbers of non-linear parameters for an *ab-initio* system to date. This is equivalent to a quantum chemical calculation of a complete active space of 32 orbitals, which is beyond that which could be treated by conventional techniques. This spans the dominant strong correlation effects, but precludes high-energy many-body dynamic correlation and screening.

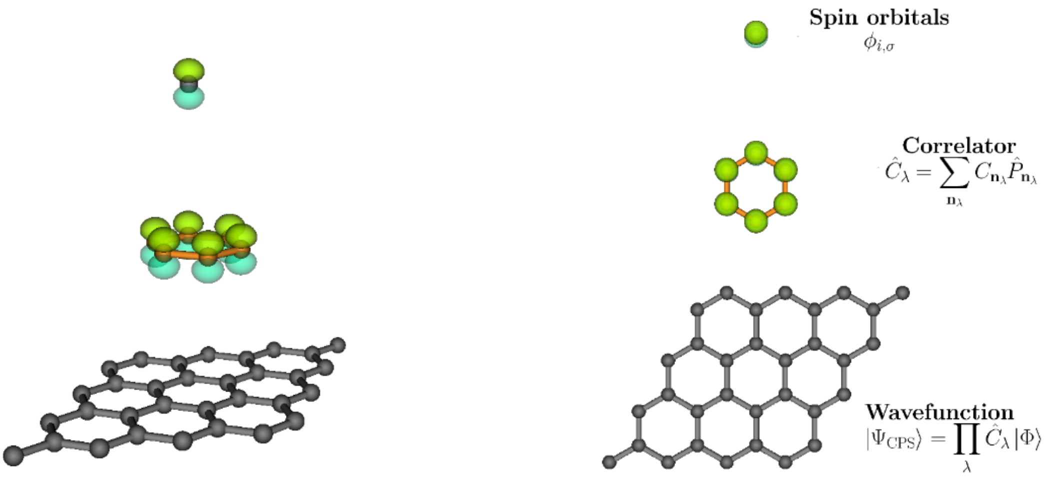

Fig. 6.5 Illustration of correlators and CPS wavefunction for graphene sheet used for both the $S = 0$ ground state and the $S = 1$ excited state[299]. This CPS wavefunction is parameterised with overlapping correlators covering hexagonal six-membered rings and a generalised Slater determinant as reference state.

This graphene sheet serves as an example that not only ground states but also excited states are accessible with this SGD approach. By restricting the spin quantum number S the first excited state with $S = 1$ becomes accessible and the spin gap, the difference in energy between the $S = 0$ and the $S = 1$ state, can be computed. For the CPS wavefunction the spin gap evaluates to $0.18147 \pm 0.00012\mathrm{E_h}$, which is slightly smaller than at the Hartree-Fock level of theory $0.182661\mathrm{E_h}$. Thus, correlation effects stabilise the $S = 1$ state to a slightly larger extend than the $S = 0$ ground state. Table 6.4 summarises all evaluated properties of the wavefunctions of both states which are defined as above, apart from the staggered magnetisation, which for a hexagonal lattice is defined according to

$$M^2 = \frac{1}{N_{\text{lat}}^2} \sum_{IJ} (-1)^{n_I} (-1)^{n_J} \langle \Psi | \hat{\mathcal{S}}_I \cdot \hat{\mathcal{S}}_J | \Psi \rangle \,, \tag{6.29}$$

where the sign factor $(-1)^{n_I}$ assumes a value of -1 ($n_I = 1$) if the lattice site I belongs to sublattice A and 1 ($n_I = 2$) if it belongs to sublattice B.

	Total Energies		
S state	$E_{\text{RHF/UHF}}$	E_{CPS}	E_{RDM}
$S = 0$	−104.211436	−104.48575(12)	−104.485398
$S = 1$	−104.028775	−104.304276(15)	−104.304271
$E_{S=1} - E_{S=0}$	0.182661	0.18147(12)	0.181127

	RDM Properties				
S state	E_{RDM}	S^2	M^2	D	S_{CE}
$S = 0$	−104.485398	0.013560	0.033896	0.206018	3.261103
$S = 1$	−104.304271	2.024314	0.032950	0.200342	3.424658

Table 6.4 4×4 graphene sheet: Total energies of the $S = 0$ and $S = 1$ states were obtained with Hartree-Fock theory $E_{\text{RHF/UHF}}$ (RHF for $S = 0$ and UHF for $S = 1$ state). E_{CPS} represents to total energies of the states described by a CPS wavefunction with overlapping, six-membered ring correlators and a generalised reference determinant optimised with the Projector Quantum Monte Carlo method for non-linear wavefunctions. The spin gap $E_{S=1} - E_{S=0}$ is thus evaluated at different levels of theory. All energies are given in E_h. Quantities evaluated from the sampled RDM for $|\Psi_{\text{CPS}}\rangle$ for both states include total energy obtained from RDM E_{RDM}, square magnitude of spin S^2, staggered magnetisation M^2, double occupancy D and entanglement entropy S_{CE}. All quantities are given in atomic units. Stochastic errors in the previous digits are presented in parentheses and were estimated with a Flyvbjerg-Petersen blocking analysis[268]. An estimate of the stochastic error associated with RDM properties is more difficult to obtain, but an idea can be gained by considering the difference between the theoretical and calculated value of S^2, as well as the maximum absolute error in Hermiticity and the sum of all absolute errors in Hermiticity, which are typically ∼ 0.0007 and ∼ 40.0, respectively, in these calculations.

Furthermore, from the two-body sampled density matrix, the spin correlation function

$$\langle\Psi|\hat{\mathcal{S}}_I \cdot \hat{\mathcal{S}}_J|\Psi\rangle\,, \tag{6.30}$$

can be evaluated to analyse the extent to which spin fluctuations among the π/π^*-bands around the Fermi level affect the magnetic order of the system. The spin correlation functions are constructed from two-point functions, rather than from symmetry-breaking in the wavefunction, and show a rapid decay of anti-ferromagnetic correlations which only substantially affect nearest neighbours as shown in Figure 6.6.

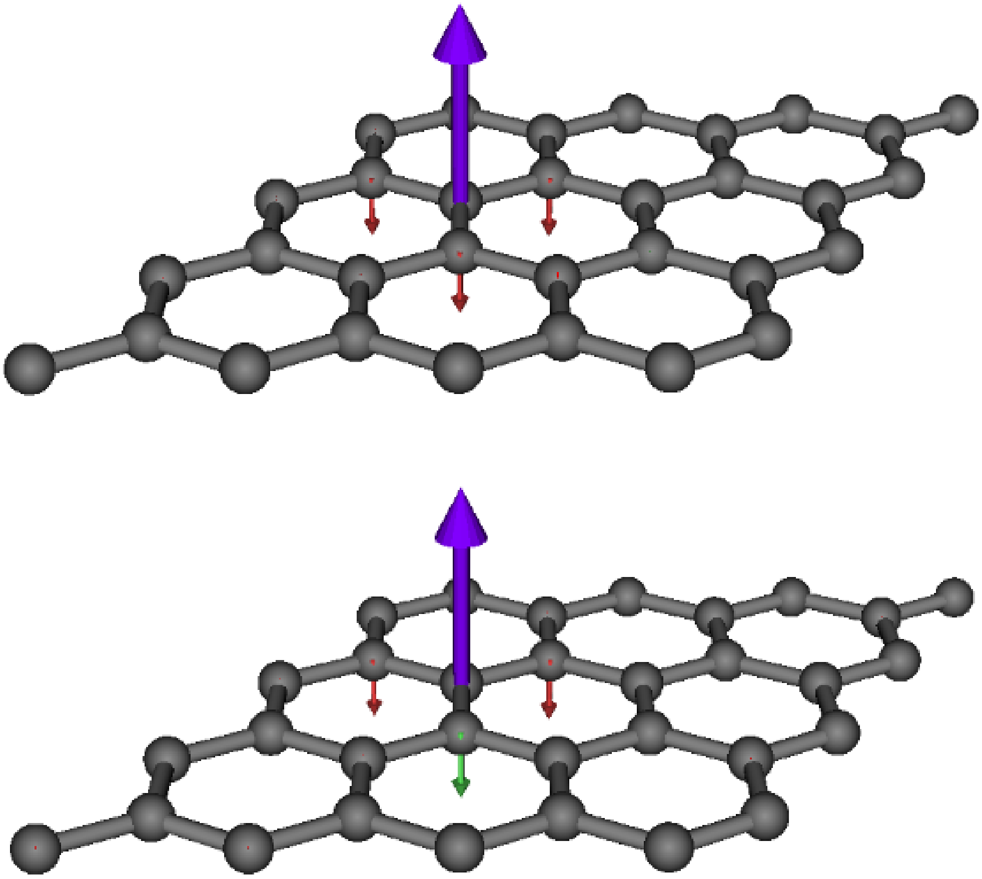

Fig. 6.6 Spin correlation functions for $\langle\Psi|\hat{\mathcal{S}}_I \cdot \hat{\mathcal{S}}_J|\Psi\rangle$ for graphene sheet for the $S = 0$ ground state (top) and the $S = 1$ excited state (bottom)[299]. The spin correlations are obtained from two-body reduced density matrices which are samples from the converged CPS wavefunctions.

6.7 Conclusions

The applications presented in this chapter demonstrate the capability of this stochastic accelerated projector approach to handle and optimise arbitrary non-linear wavefunctions of quantum many-body systems. The large numbers of simultaneously optimised parameters in the wavefunctions greatly exceeds those accessible to alternative formulations of Variational Quantum Monte Carlo optimisations. Systematically improvable Fock-space wavefunctions have thus been found for both lattice Hubbard models and *ab-initio* systems, as well as one- and two-body static properties of these wavefunctions. At the same time, the proposed Projector Quantum Monte Carlo method for non-linear wavefunction ansatzes blurrs the line between traditional Variational and Projector Quantum Monte Carlo approaches.

Chapter 7

Projector Quantum Monte Carlo Method for Tensor Network States

Many natural quantum many-body states live on a tiny submanifold of the exponentially large Hilbert space. This ‘natural corner of the Hilbert space’ derives from the locality of interactions, implying that these physical states obey area laws for entanglement (or show only small violations thereof)[132, 55, 53, 54] (as detailed in Chapter 2). Progress in quantum information theory has lead to a better understanding of entanglement in quantum many-body states and enabled the formulation of efficient parameterisations which directly target this relevant subspace of the Hilbert space: Tensor Network States (TNS). By efficiently describing the structure of quantum correlations and capturing the entanglement in low-energy states of a system, they satisfy area laws by construction and are thus able to approximate physical states to a high level of accuracy with a number of parameters that grows only polynomial with system size whilst still retaining systematic improvability towards exactness[55, 53, 54]. Amongst the large variety of tensor networks Matrix Product States (MPS)[170], the underlying variational ansatz of the DMRG approach, have been extremely successful in one-dimensional systems[136, 148]. However, the extension of their success to higher dimensions has proved more difficult due to their one-dimensional encoding of correlations. In recent years, Projected Entangled Pair States (PEPS)[53, 55, 54, 142, 155], the natural generalisation of MPS to higher dimension, have emerged as a potential promising alternative. This has been demonstrated by accurate results obtained for many quantum systems including the $t-J$[378], the Hubbard model[189] and frustrated spin systems[379].

However, in contrast to MPS, contraction of a PEPS network, as it is necessary for the extraction of information from a state vector, is a computationally hard problem in the complexity class $\sharp P$[160] and approximate contraction schemes need to be resorted to. Despite these developments, PEPS are still much harder to handle computationally than their one-dimensional analogues due to the increased exponent in their polynomial scaling with system size[55, 53, 54]. Even more so, an efficient optimisation of the variational parameters in a PEPS which give the best approximation to ground states has remained profoundly more challenging than for MPS. Since this involves a highly non-linear minimisation of the energy expectation value, state-of-the-art PEPS optimisations employ imaginary time evolution which projects an initial trial state onto the ground state $|\psi_0\rangle = \lim_{\tau\to\infty} e^{-\tau\hat{\mathcal{H}}}\,|\psi\rangle$[158, 161, 179]. The limit $\tau \to \infty$ is approached with a Trotter-Suzuki decomposition by applying sufficiently small time steps. To arrive at an efficient algorithm with tractable cost, the PEPS bond dimensions have to be truncated in an approximate way after each time step. This truncation can be realised with a range of differing techniques each of which provides a different compromise between accuracy and computational cost such as the full[158, 179], the variational[55] or the simple[161] update scheme. Whilst the full update approach which takes into account the complete environment as provided by the full PEPS wavefunction represents the most accurate procedure, even though it is not guaranteed to result in the globally optimal truncation, it is also the computationally most expensive one[158, 179]. In contrast, the simple update scheme sacrifices part of this accuracy by using simple approximations to the environment which can be evaluated at a much reduced computational cost[161]. Yet, at both ends of the scale the optimisation can become inefficient: whereas the computational cost of the full update scheme is often too demanding, the approximate local environment of the simple update is often a crude oversimplification of the quantum correlations. Because of these difficulties it is unclear whether these state-of-the-art approaches succeed in obtaining the optimal state of a given variational PEPS parameterisation which has also sparked the proposal of alternative optimisation approaches based on the variational principle[380] or gradient methods[381].

As an alternative to circumvent the challenges described above, this chapter proposes an optimisation of TNS with the Projector Quantum Monte Carlo method for non-linear wavefunctions described in Chapter 5. Being formulated in a very general manner, this approach is applicable to any arbitrary wavefunction ansatz for which the gradient of the energy functional with respect to the wavefunction parameters exists. For practical implementations, it is also vital that projections of the wavefunction parameterisations onto configurations in the Hilbert space, as well as projections of the respective energy derivatives onto the same configurations, are efficiently computable. For this reason a novel approach for evaluating tensor network contractions stochastically is also developed in this chapter which in combination with the Projector Quantum Monte Carlo method enables the efficient optimisation of tensor network state wavefunctions. It is worth noting that the considerations outlined in this chapter are in principle also applicable to many of the existing TNS categories and appropriate equations can be straightforwardly derived. However, the main focus of this chapter are PEPS and MPS, and for brevity and clarity any equations are formulated in terms of PEPS and MPS wavefunctions only.

7.1 The Computational Challenge of PEPS Wavefunctions - Can It Be Tackled Stochastically ?

Before detailing the rigorous mathematical foundations of the tensor notwork state optimisation developed in this chapter, it is worth giving a more intuitive and broad picture of the challenge encountered in dealing with PEPS wavefunctions and the proposed approach to tackle it by returning to the graphical description of a PEPS wavefunction introduced in Chapter 2 (Figure 7.1). Optimisations, or even just the extraction of information, from a PEPS state require contraction of the tensor network which can conceptually be split in two nested contractions: firstly, a contraction of the physical indices (represented by the red filled circles in the graphical depiction) and secondly, a contraction of the auxiliary indices (embodied by the blue circles and lines in the graph). Exact evaluation of these contractions is prohibitively expensive for PEPS wavefunctions and state-of-the-art PEPS calculations therefore perform these contractions deterministically, but in an approximate manner. This chapter proposes an alternative approach which instead of deterministically contracting the network, samples the contraction. This stochastic network contraction will also be coupled to a stochastic optimisation of the variational parameters in the PEPS state using the Projector Quantum Monte Carlo method for non-linear wavefunctions which has been outlined in Chapter 5. Essentially, this results in two nested stochastic processes: The outer stochastic process realises the contraction of physical indices with a Metropolis Markov chain just in the same way as it is outlined in Chapter 5 and used in the applications of Chapter 6. Within this, the inner stochastic process evaluates the contraction over auxiliary indices to obtain stochastic estimates for the projections of wavefunction amplitudes and derivatives onto configurations in the full Hilbert space which are required within the Markov chain sampling of the outer sampling procedure for physical indices. In order to aid the stochastic contraction and avoid it suffering from the negative sign problem, the tensor elements are constrained to be positive. Additional multiplication by a reference state such as a Slater determinant or a general pairing function introduces a nodal structure in the PEPS wavefunction. Simultaneous optimisation of the variational parameters in this state means that the optimal nodal structure available within the functional form of the reference state is obtained.

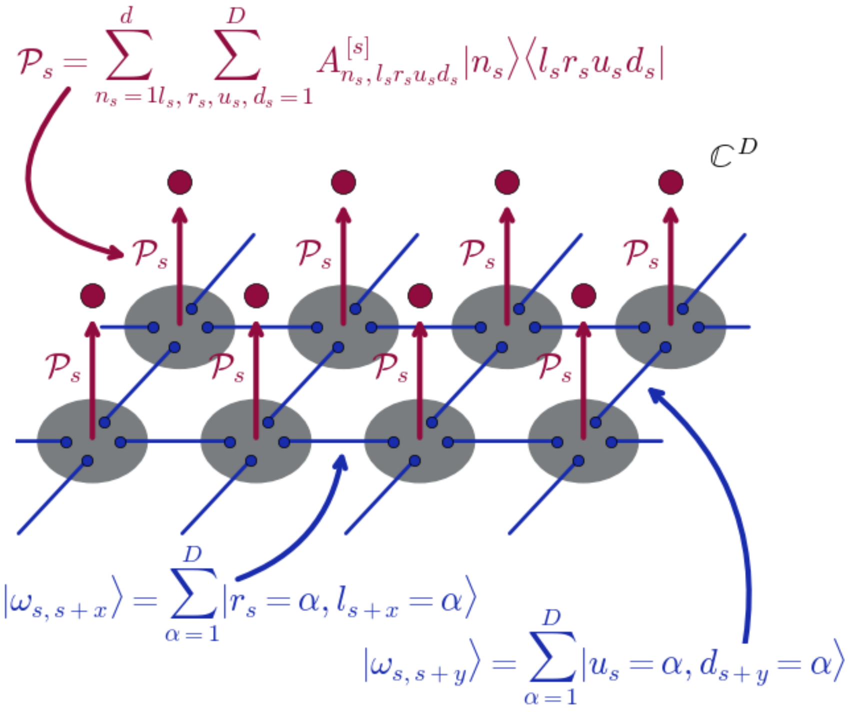

Fig. 7.1 Illustration of a PEPS network. As detailed in Chapter 2, each lattice site is associated with four virtual subsystems (blue filled circles). Each such virtual subsystem is placed in a maximally entangled product state, $|\omega_{s,s+x}\rangle$ and $|\omega_{s,s+y}\rangle$, (blue lines) with the corresponding virtual subsystem of the adjacent lattice site. At each lattice site s, linear maps $\mathcal{P}_s$ are applied which project from the local Hilbert space of the four virtual subsystems to the Hilbert space of the physical lattice site s (red filled circles). Conceptually, contraction of the PEPS network can be split in two nested contractions: a contraction of the physical indices represented by the red filled circles (sums over n_s) and a contraction of the auxiliary indices represented by the blue filled circles and lines (sums over D).

7.2 The PEPS and MPS Wavefunction Ansatz

The rigorous mathematical formulation of the PEPS wavefunction in Figure 7.1 has been derived and explained in detail in Chapter 2. Thus, for a lattice with $\frac{M}{2}$ sites each of which comprises a local Hilbert space of dimension $\mathbb{C}^d$, a general PEPS state vector in the full Hilbert space $\mathcal{H} = (\mathbb{C}^d)^{\otimes \frac{M}{2}}$ can be written as[55, 53, 54]

$$
\begin{aligned}
|\Psi_{\text{PEPS}}\rangle &= \left(\bigotimes_{s=1}^{\frac{M}{2}} \mathcal{P}_s \right) \left(\bigotimes_{s=1}^{\frac{M}{2}} \left(\bigotimes_{i=1}^{p-1} |\omega_{s,i}\rangle \right) \right) && (7.1) \\
&= \sum_{n_1 n_2 \ldots n_{\frac{M}{2}}} \mathcal{F}(A^{[1]}_{n_1} A^{[2]}_{n_2} \ldots A^{[\frac{M}{2}]}_{n_{\frac{M}{2}}}) \, |n_1 n_2 \ldots n_{\frac{M}{2}}\rangle \, , && (7.2)
\end{aligned}
$$

where $A^{[s]}_{n_s}$ denotes the rank-p tensor at lattice site s whose local configuration is n_s. The rank p of the tensor is usually equal to the number of nearest-neighbours of the lattice site s and the function $\mathcal{F}(\ldots)$ represents the contractions of tensors $A^{[s]}_{n_s}$ whose explicit form depends on the rank p of the tensors, as well as the dimension and shape of the lattice. As explained in Chapter 2, for one dimensional systems, this formulation recovers an MPS

$$
\begin{aligned}
|\Psi_{\text{MPS}}\rangle &= \left(\bigotimes_{s=1}^{\frac{M}{2}} \mathcal{P}_s \right) \left(\bigotimes_{s=1}^{\frac{M}{2}} |\omega_{s,s+1}\rangle \right) && (7.3) \\
&= \sum_{n_1 n_2 \ldots n_{\frac{M}{2}}} \mathcal{F}(f(A^{[1]}_{n_1}) f(A^{[2]}_{n_2}) \ldots f(A^{[\frac{M}{2}]}_{n_{\frac{M}{2}}})) \, |n_1 n_2 \ldots n_{\frac{M}{2}}\rangle \, . && (7.4)
\end{aligned}
$$

This well known and widely used ansatz is slightly extended in order to aid the stochastic evaluation of the tensor network contraction. Hence, the fully generalised wavefunction parameterisation can be expressed as

$$
\begin{aligned}
|\Psi_{\text{PEPS}}\rangle &= \left[\left(\bigotimes_{s=1}^{\frac{M}{2}} \mathcal{P}_s \right) \left(\bigotimes_{s=1}^{\frac{M}{2}} \left(\bigotimes_{i=1}^{p-1} |\omega_{s,i}\rangle \right) \right) \right] |\Phi\rangle && (7.5) \\
&= \sum_{n_1 n_2 \ldots n_{\frac{M}{2}}} \mathcal{F}(f(A^{[1]}_{n_1}) f(A^{[2]}_{n_2}) \ldots f(A^{[\frac{M}{2}]}_{n_{\frac{M}{2}}})) \, |n_1 n_2 \ldots n_{\frac{M}{2}}\rangle \langle n_1 n_2 \ldots n_{\frac{M}{2}} | \Phi\rangle \, , && (7.6)
\end{aligned}
$$

where the PEPS is multiplied by a reference state $|\Phi\rangle$. Similar to the CPS wavefunction parameterisation in Chapter 6, the uniform reference $|\Phi_{\text{U}}\rangle$, a Slater determinant $|\Phi_{\text{D}}\rangle$, an AGP $|\Phi_{\text{AGP}}\rangle$ or a general pairing wavefunction $|\Phi_{\text{PF}}\rangle$ can act as reference state. Their contributions to wavefunction amplitudes are all given in Section 6.2 of the previous chapter. Moreover, $f(\ldots)$ represents a function of the tensor elements, such as $f(x) = x^2$, $f(x) = |x|$, $f(x) = e^x$ etc. These two extensions of the wavefunction ansatz are introduced in order to prevent the sampling approach for the tensor network contraction from suffering from the negative sign problem. Whereas the functions $f(\ldots)$ serve the purpose of constraining the tensor elements to be positive, the reference state $|\Phi\rangle$ reintroduces a nodal structure into $|\Psi_{\text{PEPS}}\rangle$. In the limit of a uniform reference $|\Phi_{\text{U}}\rangle$ as reference state and the function $f(x) = x$, the original wavefunction ansatz of Eq.7.1 is recovered. By analogy, for one-dimensional systems the generalised wavefunction ansatz based on MPS can be written as

$$|\Psi_{\text{MPS}}\rangle = \left[\left(\bigotimes_{s=1}^{\frac{M}{2}} \mathcal{P}_s\right)\left(\bigotimes_{s=1}^{\frac{M}{2}} |\omega_{s,s+1}\rangle\right)\right]|\Phi\rangle\,, \tag{7.7}$$

$$= \sum_{n_1 n_2 \ldots n_{\frac{M}{2}}} \mathcal{F}(f(A^{[1]}_{n_1}) f(A^{[2]}_{n_2}) \ldots f(A^{[\frac{M}{2}]}_{n_{\frac{M}{2}}}))\, |n_1 n_2 \ldots n_{\frac{M}{2}}\rangle \langle n_1 n_2 \ldots n_{\frac{M}{2}}|\Phi\rangle\,. \tag{7.8}$$

7.3 Wavefunction Amplitudes and Derivatives

Hence, projecting the $|\Psi_{\text{PEPS}}\rangle$ of Eq. 7.5 into the full Hilbert space of configurations $\{|\mathbf{n}\rangle\} = \left\{|n_1 n_2 \ldots n_{\frac{M}{2}}\rangle\right\}$, the wavefunction amplitudes are given by

$$\langle \mathbf{n}|\Psi_{\text{PEPS}}\rangle = \langle \mathbf{n}|\mathcal{F}(f(A^{[1]}_{n_1}) f(A^{[2]}_{n_2}) \ldots f(A^{[\frac{M}{2}]}_{n_{\frac{M}{2}}}))|\mathbf{n}\rangle \langle \mathbf{n}|\Phi\rangle\,. \tag{7.9}$$

For an MPS, the function $\mathcal{F}$ representing the contraction over auxiliary indices involves rank-2 tensors of dimensions $D_\alpha, D_\beta, \ldots$ such that

$$\langle \mathbf{n}|\Psi_{\text{MPS,obc}}\rangle = \langle \mathbf{n}| \sum_{\alpha\beta\ldots\lambda=1}^{D_\alpha D_\beta \ldots D_\lambda} f(A^{[1]}_{n_1;\alpha}) f(A^{[2]}_{n_2;\alpha\beta}) \ldots f(A^{[\frac{M}{2}]}_{n_{\frac{M}{2}};\lambda})|\mathbf{n}\rangle \langle \mathbf{n}|\Phi\rangle \tag{7.10}$$

$$\langle \mathbf{n}|\Psi_{\text{MPS,pbc}}\rangle = \langle \mathbf{n}| \sum_{\alpha\beta\gamma\ldots\omega=1}^{D_\alpha D_\beta D_\gamma \ldots D_\omega} f(A^{[1]}_{n_1;\omega\alpha}) f(A^{[2]}_{n_2;\alpha\beta}) \ldots f(A^{[\frac{M}{2}]}_{n_{\frac{M}{2}};\lambda\omega})|\mathbf{n}\rangle \langle \mathbf{n}|\Phi\rangle\,, \tag{7.11}$$

for open and periodic boundary conditions, respectively. By analogy, for a PEPS on a 2D square lattice, the wavefunction amplitudes can be written as contraction of rank-4 tensors of dimensions $D_\alpha, D_\beta, \ldots$

$$\langle \mathbf{n}|\Psi_{\text{PEPS}}\rangle = \langle \mathbf{n}| \sum_{\alpha\beta\gamma\delta\ldots\omega=1}^{D_\alpha D_\beta D_\gamma D_\delta \ldots D_\omega} f(A^{[1]}_{n_1;\alpha\beta\gamma\omega}) f(A^{[2]}_{n_2;\delta\alpha\lambda\eta}) \ldots f(A^{[\frac{M}{2}]}_{n_{\frac{M}{2}};\chi\zeta\omega\nu})|\mathbf{n}\rangle \langle \mathbf{n}|\Phi\rangle\,. \tag{7.12}$$

From these, the appropriate derivatives of the wavefunction amplitudes with respect to a particular element of a tensor such as $A^{[2]}_{n_2;ij}$ can be evaluated as

$$\langle \mathbf{n}|\frac{\partial \Psi_{\text{MPS,obc}}}{\partial A^{[2]}_{n_2;ij}}\rangle = \langle \mathbf{n}| \sum_{\alpha\beta\ldots\lambda=1}^{D_\alpha D_\beta \ldots D_\lambda} f(A^{[1]}_{n_1;\alpha}) \frac{\partial f(A^{[2]}_{n_2;\alpha\beta})}{\partial A^{[2]}_{n_2;ij}} \delta_{i\alpha}\delta_{j\beta}\ldots f(A^{[\frac{M}{2}]}_{n_{\frac{M}{2}};\lambda})|\mathbf{n}\rangle \langle \mathbf{n}|\Phi\rangle \tag{7.13}$$

$$\langle \mathbf{n}|\frac{\partial \Psi_{\text{MPS,pbc}}}{\partial A^{[2]}_{n_2;ij}}\rangle = \langle \mathbf{n}| \sum_{\alpha\beta\gamma\ldots\omega=1}^{D_\alpha D_\beta D_\gamma \ldots D_\omega} f(A^{[1]}_{n_1;\omega\alpha}) \frac{\partial f(A^{[2]}_{n_2;\alpha\beta})}{\partial A^{[2]}_{n_2;ij}} \delta_{i\alpha}\delta_{j\beta}\ldots f(A^{[\frac{M}{2}]}_{n_{\frac{M}{2}};\lambda\omega})|\mathbf{n}\rangle \langle \mathbf{n}|\Phi\rangle \,, \tag{7.14}$$

in the case of open and periodic boundary MPS. Likewise, the derivative of a PEPS projection with respect to a particular tensor element $A^{[2]}_{n_2;ijkl}$ can be formulated as

$$\langle \mathbf{n}|\frac{\partial \Psi_{\text{PEPS}}}{\partial A^{[2]}_{n_2;ijkl}}\rangle \tag{7.15}$$

$$= \langle \mathbf{n}| \sum_{\alpha\beta\gamma\delta\ldots\omega=1}^{D_\alpha D_\beta D_\gamma D_\delta \ldots D_\omega} f(A^{[1]}_{n_1;\alpha\beta\gamma\omega}) \frac{\partial f(A^{[2]}_{n_2;\delta\alpha\lambda\eta})}{\partial A^{[2]}_{n_2;ijkl}} \delta_{i\delta}\delta_{j\alpha}\delta_{k\lambda}\delta_{l\eta}\ldots f(A^{[\frac{M}{2}]}_{n_{\frac{M}{2}};\chi\zeta\omega\nu})|\mathbf{n}\rangle \langle \mathbf{n}|\Phi\rangle \,. \tag{7.16}$$

Similar expressions for wavefunction amplitudes and derivatives of PEPS states living on lattices with other geometries, shapes and dimensionalities can be straightforwardly derived. Furthermore, appropriate derivatives with respect to the parameters of the reference state $|\Phi\rangle$ are given by the expressions in Section 6.2 of Chapter 6.

In the case of MPS, the contractions involved in the projections amount to a series of simple matrix-vector (open boundary conditions) or matrix-matrix (periodic boundary conditions) multiplications which can be computed efficiently. On the contrary, PEPS contraction involves rank-4 tensors whose exact contraction is prohibitively expensive. State-of-the-art PEPS simulations therefore rely on approximate contraction schemes. Yet, these still incur a much worse scaling with bond dimension D than their exact MPS counterparts.

7.4 A Sampling Approach for Wavefunction Amplitudes and Derivatives

Similar to the Projector Quantum Monte Carlo method proposed in this thesis, previous approaches have also combined PEPS contraction and Monte Carlo sampling[382–384] by replacing sums over physical indices which arise during the evaluation of expectation values by random samples. These techniques have allowed for the use of larger values of D with the same computational resources[383, 382, 384]. Still, since even approximate contraction schemes for PEPS projections $\langle \mathbf{n}|\Psi_{\text{PEPS}}\rangle$ incur significant computational expenditures, a new approach is proposed in this section which employs Monte Carlo sampling for the contraction of auxiliary indices. Thus, in addition to sampling of the physical indices and nested within this first sampling process, the explicit sums over all N_{auxinds} auxiliary indices $\alpha, \beta, \ldots$ in the PEPS projections

$$\begin{aligned}
\langle \mathbf{n}|\Psi_{\text{PEPS}}\rangle &= S_{\mathbf{n}} \langle \mathbf{n}|\Phi\rangle && (7.17)\\
&= \langle \mathbf{n}| \sum_{\alpha\beta\gamma\delta\ldots\omega=1}^{D_\alpha D_\beta D_\gamma D_\delta \ldots D_\omega} f(A^{[1]}_{n_1;\alpha\beta\gamma\omega}) f(A^{[2]}_{n_2;\delta\alpha\lambda\eta}) \ldots f(A^{[\frac{M}{2}]}_{n_{\frac{M}{2}};\chi\zeta\omega\nu}) |\mathbf{n}\rangle \langle \mathbf{n}|\Phi\rangle && (7.18)\\
\langle \mathbf{n}| \frac{\partial \Psi_{\text{PEPS}}}{\partial A^{[2]}_{n_2;ijkl}}\rangle &= S^{'}_{\mathbf{n};n_2;ijkl} \langle \mathbf{n}|\Phi\rangle && (7.19)\\
&= \langle \mathbf{n}| \sum_{\alpha\beta\gamma\delta\ldots\omega=1}^{D_\alpha D_\beta D_\gamma D_\delta \ldots D_\omega} f(A^{[1]}_{n_1;\alpha\beta\gamma\omega}) \frac{\partial f(A^{[2]}_{n_2;\delta\alpha\lambda\eta})}{\partial A^{[2]}_{n_2;ijkl}} \delta_{i\delta}\delta_{j\alpha}\delta_{k\lambda}\delta_{l\eta} \ldots f(A^{[\frac{M}{2}]}_{n_{\frac{M}{2}};\chi\zeta\omega\nu}) |\mathbf{n}\rangle \langle \mathbf{n}|\Phi\rangle \,, && (7.20)
\end{aligned}$$

are also evaluated stochastically by drawing a few randomly sampled terms. For a practical implementation of this sampling approach, all terms arising in the sum need to be positive as otherwise the sampling approach is prone to suffer from the negative sign problem. This restriction can be straightforwardly imposed with the help of the functions $f(\ldots)$, such as $f(x) = e^x$, $f(x) = x^2$, $f(x) = |x|$, …, which have been introduced for this sole purpose of restraining the individual tensor elements to be positive. $|\Psi_{\text{PEPS}}\rangle$ then retains a sign structure by multiplication by the reference state $|\Phi\rangle$ which, likewise, has been included solely for this purpose of providing the nodal structure of the wavefunction. Similar to the CPS wavefunction optimisation in Chapter 6, the reference state is optimised simultaneously such that the optimal nodal structure available within its functional constraint is obtained at convergence. For brevity and clarity, any equations below are given for PEPS on a 2D square lattice, but similar expressions can be derived for PEPS in other dimensions and lattice shapes with a different contraction function $\mathcal{F}$ such as MPS.

Instead of explicitly enumerating all terms appearing in the sum $S_{\mathbf{n}}$, a number of $N_{\text{TNS,samples}}$ terms are randomly chosen instead. Each single product term of this sampling process is picked by randomly selecting a particular value for each of the N_{auxinds} auxiliary indices and unbiasing for the probability of the occurrence of this event

$$
\begin{aligned}
S_{\mathbf{n}} &= \sum_{\alpha\beta\gamma\delta\ldots\omega=1}^{D_\alpha D_\beta D_\gamma D_\delta \ldots D_\omega} f(A^{[1]}_{n_1;\alpha\beta\gamma\omega}) f(A^{[2]}_{n_2;\delta\alpha\lambda\eta}) \ldots f(A^{[\frac{M}{2}]}_{n_{\frac{M}{2}};\chi\zeta\omega\nu}) && (7.21)\\
&\equiv \frac{1}{N_{\text{TNS,samples}}} \sum_{z}^{N_{\text{TNS,samples}}} \left\langle \frac{f(A^{[1]}_{n_1;abco}) f(A^{[2]}_{n_2;daef}) \ldots f(A^{[\frac{M}{2}]}_{n_{\frac{M}{2}};ghio})}{p_\alpha^{n_1 n_2}(a) p_\beta^{n_1 n_3}(b) \ldots p_\omega^{n_1 n_{M/2}}(o)} \right\rangle_{P_{\alpha\beta\ldots\omega}(z)} && (7.22)\\
&= \frac{1}{N_{\text{TNS,samples}}} \sum_{z}^{N_{\text{TNS,samples}}} \frac{T_{\alpha\beta\ldots\omega}(z)}{P_{\alpha\beta\ldots\omega}(z)}, && (7.23)
\end{aligned}
$$

where a term $T_{\alpha\beta\ldots\omega}(z)$ and its respective probability $P_{\alpha\beta\ldots\omega}(z)$ are given by

$$
\begin{aligned}
T_{\alpha\beta\ldots\omega}(z) &= f(A^{[1]}_{n_1;abco}) f(A^{[2]}_{n_2;daef}) \ldots f(A^{[\frac{M}{2}]}_{n_{\frac{M}{2}};ghio}) && (7.24)\\
P_{\alpha\beta\ldots\omega}(z) &= p_\alpha^{n_1 n_2}(a) p_\beta^{n_1 n_3}(b) \ldots p_\omega^{n_1 n_{M/2}}(o). && (7.25)
\end{aligned}
$$

In this notation, Greek letters $\alpha, \beta, \gamma, \ldots$ refer to auxiliary indices and Roman letters $a, b, c, \ldots$ to the particular values which are chosen for each auxiliary index, that is a denotes the particular value which has been picked for the auxiliary index α. All these picked values for the auxiliary indices are then collectively combined into one single index z. $p_\alpha^{n_1 n_2}(a)$ represents the normalised probability distribution from which the value a is sampled for auxiliary index α which connects lattice sites 1 and 2 with occupations n_1 and n_2 in their local Hilbert spaces of size d. There exists a relatively large freedom in the choice for $p_\alpha^{n_1 n_2}(a)$ provided that it satisfies the necessary constraint that there remains a finite probability of picking each non-zero tensor element. The functional form for these probability distributions is thus chosen such that it enables preferential selection of the most dominant terms whilst still being efficiently calculable. A good comprise was found to be

$$
p_\alpha^{n_1 n_2}(a) = \frac{1}{N_{\text{norm}}} \left(\sum_{\beta\gamma\omega} f(A^{[1]}_{n_1;a\beta\gamma\omega}) \right) \times \left(\sum_{\delta\lambda\eta} f(A^{[2]}_{n_2;\delta a\lambda\eta}) \right), \qquad (7.26)
$$

where N_{norm} is a normalisation constant.

Similar to the wavefunction amplitudes, the derivative of a PEPS projection with respect to a particular rank-4 tensor $A^{[2]}_{n_2}$ is also sampled by stochastically choosing $N_{\text{TNS,samples}}$ terms in the manner described above and accumulating them in the appropriate elements of the rank-4 tensor $S'_{\mathbf{n};n_2}$ holding all derivatives with respect to

$A^{[2]}_{n_2}$, such that a particular element $S'_{\mathbf{n};n_2,ijkl}$ is given by

$$S'_{\mathbf{n};n_2,ijkl} = \sum_{\alpha\beta\gamma\delta\ldots\omega=1}^{D_\alpha D_\beta D_\gamma D_\delta\ldots D_\omega} f(A^{[1]}_{n_1;\alpha\beta\gamma\omega})\frac{\partial f(A^{[2]}_{n_2;\delta\alpha\lambda\eta})}{\partial A^{[2]}_{n_2;ijkl}}\delta_{i\delta}\delta_{j\alpha}\delta_{k\lambda}\delta_{l\eta}\ldots f(A^{[\frac{M}{2}]}_{n_{\frac{M}{2}};\chi\zeta\omega\nu}) \tag{7.27}$$

$$\equiv \frac{1}{N_{\text{TNS,samples}}}\sum_{z}^{N_{\text{TNS,samples}}}\left\langle\frac{f(A^{[1]}_{n_1;abco})\frac{f(A^{[2]}_{n_2;daef})}{\partial A^{[2]}_{n_2;ijkl}}\delta_{id}\delta_{ja}\delta_{ke}\delta_{lf}\ldots f(A^{[\frac{M}{2}]}_{n_{\frac{M}{2}};ghio})}{p^{n_1n_2}_{\alpha}(a)p^{n_1n_3}_{\beta}(b)\ldots p^{n_1n_{M/2}}_{\omega}(o)}\right\rangle_{P_{\alpha\beta\ldots\omega}(z)} \tag{7.28}$$

$$= \frac{1}{N_{\text{TNS,samples}}}\sum_{z}^{N_{\text{TNS,samples}}}\frac{T'_{n_2;ijkl;\alpha\beta\ldots\omega}(z)}{P_{\alpha\beta\ldots\omega}(z)}, \tag{7.29}$$

with $T'_{n_2;ijkl;\alpha\beta\ldots\omega}(z)$ defined as

$$T'_{n_2;ijkl;\alpha\beta\ldots\omega}(z) = f(A^{[1]}_{n_1;abco})\frac{f(A^{[2]}_{n_2;daef})}{\partial A^{[2]}_{n_2;ijkl}}\delta_{id}\delta_{ja}\delta_{ke}\delta_{lf}\ldots f(A^{[\frac{M}{2}]}_{n_{\frac{M}{2}};ghio}). \tag{7.30}$$

In the algorithm, the distributions $p^{n_1n_2}_{\alpha}$ are all computed at the beginning of each iteration with $\mathcal{O}[d^2N_{\text{auxinds}}D]$ operations such that they follow the changes in tensor elements. Following this, sampling from these distributions can be efficiently realised in $\mathcal{O}[1]$ time with the Alias method and the computation of one TNS projection onto a Hilbert space configuration, as well as the evaluation of its derivatives with respect to a single tensor, therefore requires $\mathcal{O}[N_{\text{TNS,samples}}N_{\text{auxinds}}]$ operations.

7.5 Investigation of TNS Projection Sampling Approach

Prior to optimisations of arbitrary TNS wavefunctions with the proposed Projector Quantum Monte Carlo approach in combination with the previously outlined sampling approach for the TNS projections, an investigation of the convergence behaviour of the TNS projection sampling approach is necessary to demonstrate that the latter is able to yield faithful and accurate stochastic estimates of the gradient and energy at a tractable computational cost. MPS naturally lend themselves for such a rigorous study as their exact contraction can be evaluated efficiently, thereby granting access to exact benchmark results. For this purpose, a $1D$ 1×8 Hubbard model at half-filling and $\frac{U}{t}=2$ and $\frac{U}{t}=8$ with open boundary conditions is considered which represents a non-trivial benchmark system that is still small enough to allow for deterministic evaluation of the energy, as well as for a deterministic gradient descent optimisation of the wavefunction. The investigated MPS wavefunctions are parameterised with a general pairing function as reference state and rank-3 tensors (rank-2 at the boundaries) (one physical and two (one at the boundaries) auxiliary indices) with a bond dimension of $D = 10$. Evaluation of the TNS projections onto configurations therefore requires contractions over auxiliary indices whose exact computation involves $N_{\text{terms}} = 10,000,000$. In the following, energies are evaluated for MPS wavefunctions with a fixed set of parameters which have either been chosen randomly or obtained by a deterministic optimisation and the convergence of the stochastic estimates with respect towards the number of samples for the auxiliary, N_{aux}, and physical, N_{phys}, indices towards the true deterministic values are studied.

Hence, in a first instance, the convergence of the energy estimate with respect to the amount of sampling for auxiliary indices only is investigated. While the TNS projections onto configurations are sampled, the contraction of the physical indices is realised deterministically as represented by the full sum over all configurations $\{\mathbf{n}, \mathbf{m}\}$ in the Hilbert space

$$E_{\text{TNS}} = \frac{\sum_{\mathbf{mn}} \langle \Psi_{\text{TNS}} | \mathbf{m} \rangle \, H_{\mathbf{mn}} \, \langle \mathbf{n} | \Psi_{\text{TNS}} \rangle}{\sum_{\mathbf{n}} \langle \Psi_{\text{TNS}} | \mathbf{n} \rangle \, \langle \mathbf{n} | \Psi_{\text{TNS}} \rangle} = \frac{\sum_{\mathbf{mn}} S_{\mathbf{m}} \, \langle \Phi | \mathbf{m} \rangle \, H_{\mathbf{mn}} \, \langle \mathbf{n} | \Phi \rangle \, S_{\mathbf{n}}}{\sum_{\mathbf{n}} S_{\mathbf{n}} \, \langle \Phi | \mathbf{n} \rangle \, \langle \mathbf{n} | \Phi \rangle \, S_{\mathbf{n}}}. \tag{7.31}$$

It should be stressed that for each single occurrence of a particular configuration appearing in the sums over $\mathbf{n}$ and $\mathbf{m}$ a separate and independent stochastic estimate of the TNS projection $S_{\mathbf{n}/\mathbf{m}}$ is sampled. In particular, this includes diagonal terms of the form $S_{\mathbf{n}} \, \langle \Phi | \mathbf{n} \rangle \, H_{\mathbf{nn}} \, \langle \mathbf{n} | \Phi \rangle \, S_{\mathbf{n}}$ and $S_{\mathbf{n}} \, \langle \Phi | \mathbf{n} \rangle \, \langle \mathbf{n} | \Phi \rangle \, S_{\mathbf{n}}$ where two independent estimates of $S_{\mathbf{n}}$ are calculated, one for the bra and one for the ket state. This repeated independent estimation of the sampled quantities $S_{\mathbf{n}}$ is vital to ensure that no bias arising from a repeated use of the same stochastic estimate with the same associated error is introduced in the stochastic energy estimate. Unfortunately, the normalisation in the energy estimate in Eq. 7.31 can introduce a potential unavoidable bias since the $(\sum_{\mathbf{n}} S_{\mathbf{n}} \, \langle \Phi | \mathbf{n} \rangle \, \langle \mathbf{n} | \Phi \rangle \, S_{\mathbf{n}})^{-1}$ factor represents a non-linear function of the sampled quantities $S_{\mathbf{n}}$.

The convergences in Figure 7.2 illustrate that already at a moderate number of samples for the auxiliary indices ($N_{\text{aux}} \approx 100$), which represents a tiny fraction of the total number of terms in the contraction sum ($\frac{N_{\text{aux}}}{N_{\text{terms}}} \approx 1 \times 10^{-6}$), the errors in the energy estimates is less than one percent in almost all cases. As expected, increasing N_{aux} results in a general trend towards the deterministic value and agreement within error bars in most cases. This behaviour is more pronounced for wavefunctions with

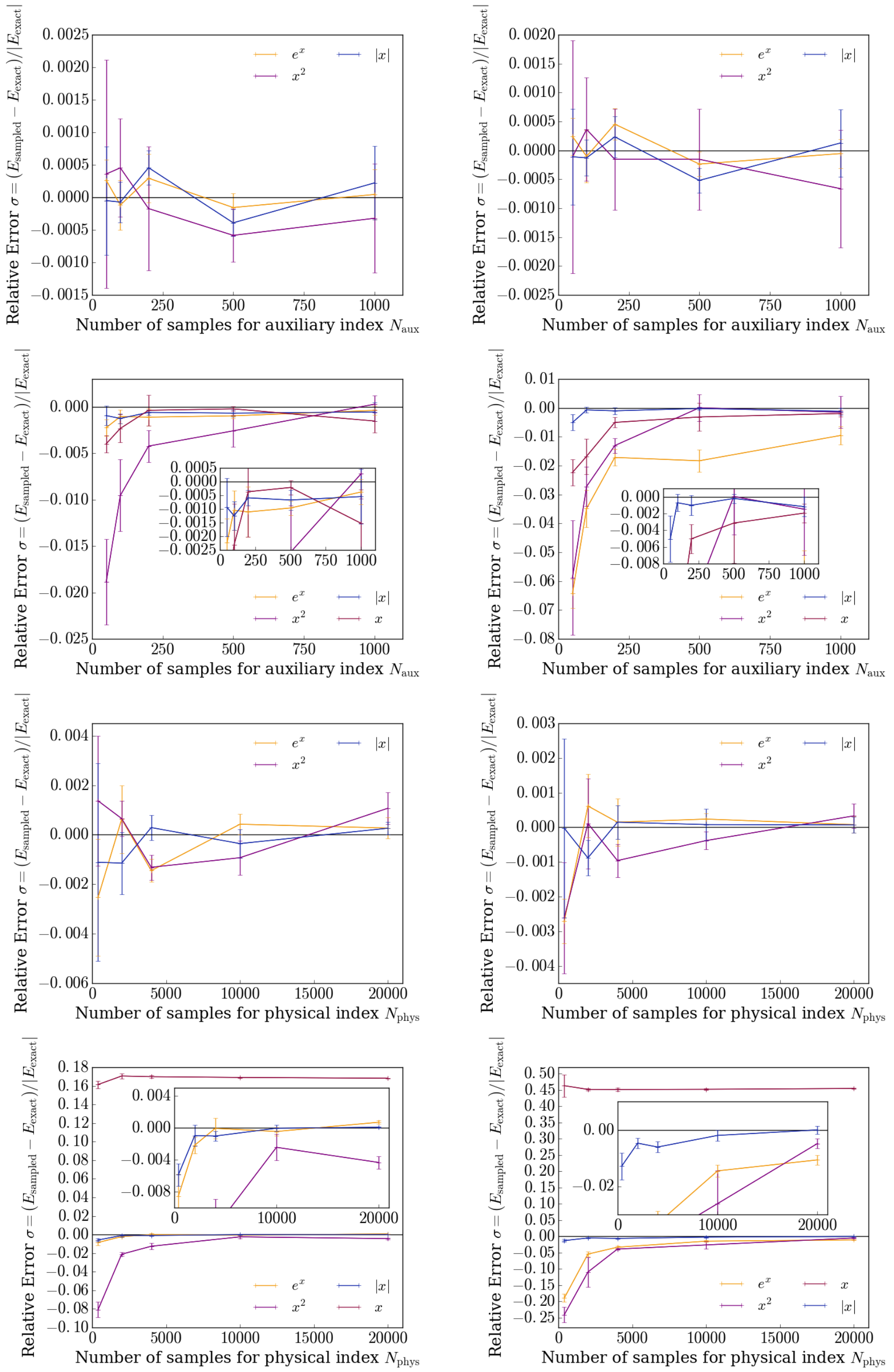

Fig. 7.2 Convergence of stochastic energy estimates with the number of samples. The considered system is a $1D$ 1×8 Hubbard model at half-filling with open boundary conditions and $\frac{U}{t} = 2$ (left column) and $\frac{U}{t} = 8$ (right column). The wavefunction is parameterised with a general pairing function as reference state and a matrix product state with bond dimension $D = 10$. Whilst the first and third row consider a wavefunction with random parameter values, the second and last row treat a wavefunction with optimal parameters which have been obtained with a completely deterministic optimisation. The top four graphs display the convergences of the stochastic energy estimate with the number of samples for the auxiliary indices N_{aux} while the sum over physical indices is evaluated deterministically (Eq. 7.31). The four graphs on the bottom show the convergence of the stochastic energy estimate in Eq. 7.34 with the number of samples for the physical indices for $N_{\text{aux}} = 100$. All eight graphs compare the convergence behaviour for different functional forms of $f(x)$.

optimal parameters where the error in the estimate tends to be larger than for random values. Moreover, for optimal wavefunction parameters a tendency of the energy estimates to converge from below onto the exact energy is observed. This is most likely an appearance of the potential bias introduced by the division of the sampled normalisation. At the same time, convergences for the three functional forms $f(x) = e^x$, $f(x) = x^2$ and $f(x) = |x|$ as possible choices for the restriction function $f(\ldots)$ are compared. These clearly demonstrate that the most efficient function is $f(x) = |x|$ given that for the same number of samples the error is typically smaller, even by an order of magnitude in the case of optimal wavefunction parameters.

Moreover, the convergence of the stochastic energy estimates towards its deterministic analogue is investigated when in addition to the contraction of auxiliary indices the contraction of physical indices is also sampled using the techniques outlined in Section 5.3 and 5.7 of Chapter 5. Thus, the energy is estimated with two nested stochastic processes whereby the outer sampling procedure involves a Metropolis Markov chain comprising N_{phys} samples of $\mathbf{n}$. Each sampled configuration $\mathbf{n}$ contributes a small sampled selection of N_s off-diagonal terms with $\mathbf{m} \neq \mathbf{n}$,

$$E_{\text{TNS,off-diag}} = \left\langle \frac{\langle \Psi^{(k)} | \mathbf{m} \rangle \, H_{\mathbf{mn}} \, \langle \mathbf{n} | \Psi^{(k)} \rangle}{N_s P_{\text{gen}}(\mathbf{m}|\mathbf{n}; \hat{\mathcal{H}}) P(\mathbf{n}; \Psi^{(k)})} \right\rangle_{P(\mathbf{n};\Psi^{(k)})} \tag{7.32}$$

where the outer brackets imply that the sampling of $\mathbf{n}$ is performed according to the distribution given in Eq.5.13, as well as a diagonal term $\mathbf{m} = \mathbf{n}$ which is included deterministically and contributes

$$E_{\text{TNS,diag}} = \left\langle \frac{\langle \Psi^{(k)} | \mathbf{n} \rangle \, H_{\mathbf{nn}} \, \langle \mathbf{n} | \Psi^{(k)} \rangle}{P(\mathbf{n}; \Psi^{(k)})} \right\rangle_{P(\mathbf{n};\Psi^{(k)})}, \tag{7.33}$$

to the complete estimate of the energy.

$$E_{\text{TNS}} = E_{\text{TNS,diag}} + E_{\text{TNS,offdiag}}. \tag{7.34}$$

Again, two independent estimates are sampled for the bra and the ket state to remove as much of a potential bias as possible. Unfortunately, three potential sources for the introduction of a bias in the estimate still remain in this sampling procedure. Firstly, due to the choice of probability distribution in Eq.5.13 unbiasing by the probability $P(\mathbf{n}; \Psi^{(k)})$ involves computation of $\frac{1}{\langle \mathbf{n} | \Psi^{(k)} \rangle}$ for the off-diagonal contributions which can potentially introduce a bias given that $\frac{1}{S_{\mathbf{n}}}$ represents a non-linear function of the sampled quantity $S_{\mathbf{n}}$. However, since this bias is only present in the off-diagonal terms and the diagonal terms tend to dominate the estimate, this potential bias is likely to be small. Secondly, within the Markov chain sampling process whenever a move from the configuration $\mathbf{n}_i$ to a new configuration is proposed and rejected, no new estimate of the TNS projection $S_{\mathbf{n}_i}$ is sampled but the old estimate is reused instead. Many investigations were undertaken in order to arrive at an approach which involves newly sampled independent estimates for each sampled $\mathbf{n}$ and proposed move along the Markov chain. All of these were found to introduce too much stochastic noise, leading to very unstable algorithms, and therefore do not provide a viable route forward. Yet, provided that the acceptance rate of the Markov chain is high enough all sampled configurations will be revisited, most likely several times, with different independently sampled estimates which thus still allows for independent stochastic estimates to represent the TNS projections for the same configuration, thereby helping in mitigating this potential bias. Furthermore, another potential source for introduction of a potential bias is the evaluation of the acceptance ratio $\frac{\langle \mathbf{n}_i^{'}|\Psi^{(k)}\rangle}{\langle \mathbf{n}_i|\Psi^{(k)}\rangle}$ itself. Again, this involves with its $\frac{1}{S_{\mathbf{n}_i}}$ component a non-linear function of the sampled quantity $S_{\mathbf{n}_i}$ and can thus potentially lead to a bias in the decision whether to accept or reject the proposed move which implies that the distribution which is actually sampled with the Markov chain includes a non-linear bias. Similar challenges arising from the use of stochastic estimates within a Metropolis Markov chain have also been observed in other contexts[385]. It has been investigated whether one of the many proposed schemes for evaluation of a (first-order) correction of the bias in the ratio estimator can aid the situation and remove at least part of the bias. However, these were all found to perform worse and the only viable approach to reduce this potential bias is the limit of a sufficiently large number of samples. Fortunately, the potential biases in the ratios represent $\mathcal{O}(\frac{1}{N})$ biases where N denotes the number of samples[347]. This means that they will asymptotically tend to zero as the limit of an infinite number of samples is approached. In general, there are cases where a biased estimator may be preferred to an unbiased estimator if the mean square error of the former is less than the variance of the latter[386]. In these cases the (small) bias of the estimator is compensated by the small mean square error such that the biased estimator still represents a more efficient one. The sampling procedure described above seems to be such a situation where in the limit of a sufficiently large number of samples the bias is controlled and the reduced mean square error implies that the biased estimator is still more efficient than its unbiased analogue.

Initially, the convergence behaviour of this stochastic estimate is also compared for the three functional forms $f(x) = e^x$, $f(x) = x^2$ and $f(x) = |x|$ as possible choices

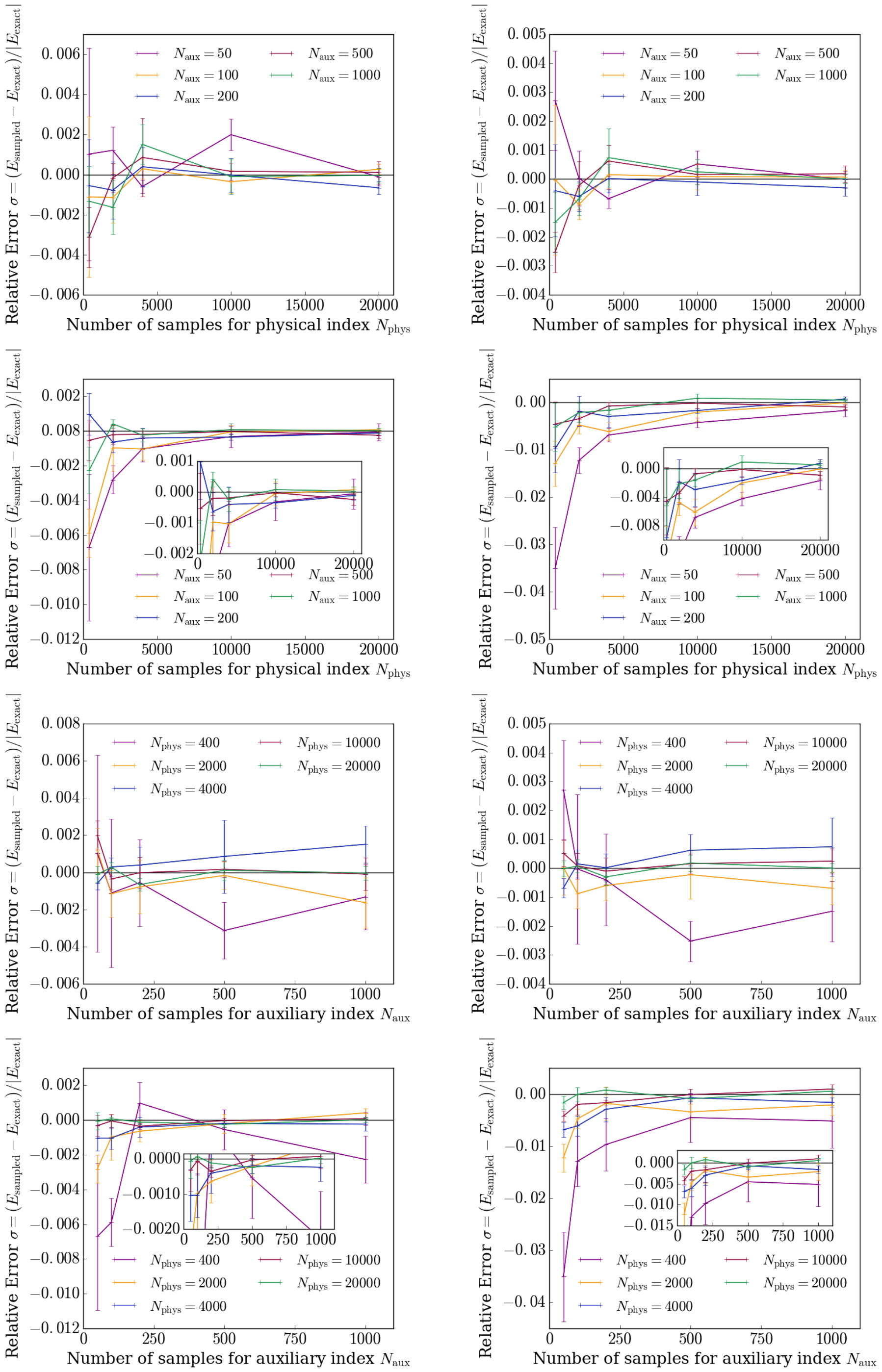

Fig. 7.3 Convergence of stochastic energy estimates with the number of samples for auxiliary and physical indices. The considered system is a $1D$ 1×8 Hubbard model at half-filling with open boundary conditions and $\frac{U}{t} = 2$ (left column) and $\frac{U}{t} = 8$ (right column). The wavefunction is parameterised with a general pairing function as reference state and a matrix product state with bond dimension $D = 10$. Whilst the first and third row consider a wavefunction with random parameter values, the second and last row treat a wavefunction with optimal parameters which have been obtained with a completely deterministic optimisation. All eight graphs consider the stochastic energy estimate in Eq. 7.34 which stochastically evaluates the sum over auxiliary indices with N_{aux} random samples and the sum over physical indices with N_{phys} samples.

for $f(\ldots)$. As with the previous estimate, the functional form $f(x) = |x|$ is again found to be the most effective one with errors which are often smaller than for the others, even by an order of magnitude in the case of optimal parameters (Figure 7.2). For completeness, stochastic estimates for optimal wavefunction parameters are also included in Figure 7.2 for the function $f(x) = x$ which means that the tensor elements can be of either sign. The observed errors, in particular the large errors in the estimate of 7.34 which employs two nested stochastic processes, are a clear manifestation of the negative sign problem and demonstrate the necessity to constrain the tensor elements to be positive. Thus, all calculations considered in the following impose this constraint with the function $f(x) = |x|$. As can be seen in the convergence profiles in Figure 7.3, the stochastic estimates converge towards the deterministic value with increasing number of samples for N_{aux} and N_{phys} until agreement within the estimated error bars is reached in most cases. Even for the least amount of sampling the errors in the estimates are smaller than five percent and relatively rapidly drop below one percent already at small number of samples ($N_{\text{aux}} \approx 100$ and $N_{\text{phys}} \approx 2,000$). In general, in order to achieve a given error in the energy estimates, increasing the number of samples for the physical indices allows for the use of a smaller value for N_{aux} and vice versa. Good choices for N_{aux} and N_{phys} therefore depend on each other. When a wavefunction with random parameters is considered, the energy estimates in the convergence profiles oscillate around their deterministic counterpart and the potential biases mentioned above appear to be smaller than the stochastic noise associated with the estimates. However, when a wavefunction with optimal parameter values is considered, the stochastic estimates exhibit a tendency to converge from below onto the exact energy. One explanation for this observation is that the above mentioned biases become noticeable. In general, the acceptance ratio for optimal wavefunction parameters is significantly smaller than for arbitrary values. As a consequence, the configurations are most likely not revisited enough to reduce the bias arising from repeated use of the same estimate of $S_{\mathbf{n}}$ along the Markov chain below stochastic errors. Still, the stochastic estimates converge onto their deterministic analogue and in the limit of a sufficient amount of sampling of N_{aux} and N_{phys} the biases seem to be controllable. It should be noted that even though many efforts are taken to remove as much as possible of any potential biases in the estimates, non-linear biases still remain which cannot be removed exactly. Even the individual tensor elements are correlated, and therefore through the multiplication of several of them for a particular TNS projection, a biased distribution for the TNS projection will result which might also explain the tendency of the estimates to converge from below. Irrespective of the detailed explanations for the obtained convergence behaviours, all observations indicate that with increasing number of samples for the physical and auxiliary indices, the stochastic estimates relatively rapidly converge towards the correct value such that at relatively small number of samples for N_{aux} and N_{phys} potential biases seem to be controllable and stochastic estimates with small errors obtainable.

7.6 Applications for MPS and PEPS Wavefunctions

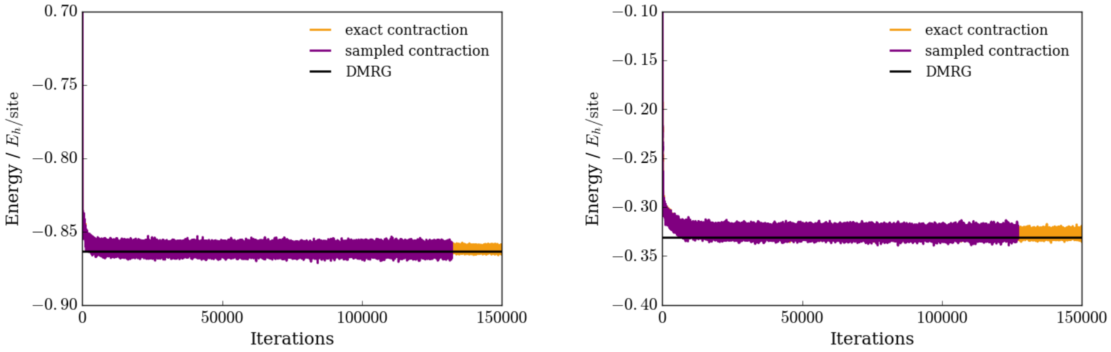

Fig. 7.4 The convergence of the ground state energy with number of iterations for the $1D$ 1×10 Hubbard model at half-filling with periodic boundary conditions and $\frac{U}{t} = 2$ (left) or $\frac{U}{t} = 8$ (right). The wavefunctions are parameterised with matrix product states of bond dimensions $D = 4$ in combination with a general pairing function. DMRG values have been obtained with a bond dimension of $D = 1000$ and are converged with respect to bond dimension. Whilst the optimisation with 'exact contraction' evaluates the contraction of auxiliary indices deterministically and only samples the contraction of physical indices, the optimisation with 'sampled contraction' samples the contraction of auxiliary indices nested within the stochastic sampling of physical indices. These calculations illustrate that with an appropriate amount of sampling wavefunction optimisations employing stochastic and exact network contraction are able to result in wavefunctions which are very close in energy.

In a first series of applications, the ability of the sampling approach for the tensor network contractions to optimise the wavefunction parameters within the framework of the Projector Quantum Monte Carlo method proposed in this thesis is assessed with applications to a range of $1D$ Hubbard models. With exact tensor network contractions being tractable for the MPS wavefunctions $|\Psi_{\text{MPS,pbc}}\rangle$ of these system, benchmark results from optimisations employing exact network contractions are available which allows for a rigorous assessment of the effects of the stochastic evaluation of the tensor network contraction on the wavefunction optimisation. The considered $1D$ $1 \times \frac{M}{2}$ Hubbard models include chains with $\frac{M}{2} = 10$, $\frac{M}{2} = 14$ and $\frac{M}{2} = 22$ lattice sites, all at half-filling with periodic boundary conditions and $\frac{U}{t} = 2$ or $\frac{U}{t} = 8$. The wavefunctions are parameterised with matrix product states of bond dimension $D = 2$

and $D = 4$ comprising $\frac{M}{2}$ independent, simultaneously optimised rank-3 tensors which are combined with a simultaneously optimised general pairing function as reference state.

1 × 10 Hubbard model

$\frac{U}{t}$	E_{DMRG}	$E_{\text{TNS}}(D=2)$		P_{TNS}	$E_{\text{TNS}}(D=4)$		P_{TNS}
		exact	sampled		exact	sampled	
2	-0.86384157	$-0.86211(1)$	$-0.86201(3)$	99.8	$-0.862221(8)$	$-0.86230(1)$	99.8
8	-0.33149967	$-0.3243(2)$	$-0.32214(7)$	97.8	$-0.32767(6)$	$-0.3249(2)$	98.8

1 × 14 Hubbard model

$\frac{U}{t}$	E_{DMRG}	$E_{\text{TNS}}(D=2)$		P_{TNS}
		exact	sampled	
2	-0.85388192	$-0.851697(4)$	$-0.85149(5)$	99.7
8	-0.32950733	$-0.32003(2)$	$-0.32023(5)$	97.1

1 × 22 Hubbard model

$\frac{U}{t}$	E_{DMRG}	$E_{\text{TNS}}(D=2)$		P_{TNS}
		exact	sampled	
2	-0.84790465	$-0.842108(9)$	$-0.841890(2)$	99.3
8	-0.32832582	$-0.31757(3)$	$-0.31471(3)$	96.7

Table 7.1 Ground state energies per site E_{TNS} for $1D$ 1×10, 1×14 and 1×22 Hubbard model for MPS wavefunctions parameterised according to Eq. 7.7 with bond dimensions of $D = 2$ and $D = 4$ whose variational parameters have been obtained with the Projector Quantum Monte Carlo method whereby the MPS contraction of auxiliary indices is either sampled ('sampled') or evaluated deterministically ('exact'). E_{DMRG} denotes the DMRG energy for the system ($D = 1000$). $P_{\text{TNS}} = \frac{E_{\text{TNS}}}{E_{\text{DMRG}}}$ (%) represents the percentage of E_{DMRG} captured by $|\Psi_{\text{MPS,pbc}}\rangle$ where E_{TNS} is estimated using exact network contraction. Differences in the Projector Quantum Monte Carlo energies between optimisations involving exact and stochastic contraction of the auxiliary indices tend to increase for larger system sizes and bond dimensions and are most likely due to the non-linear biases of the sampling approaches which cannot be remove. Furthermore, exact agreement with DMRG values is in general not expected for a number of reasons detailed in the text. All energies are given in E_h/site. The numbers in parentheses represent the stochastic error in the previous digit as obtained through a Flyvbjerg-Petersen reblocking analysis[268].

As a first observation, the results in Table 7.1 demonstrate that already at small values of D, the parameterised $|\Psi_{\text{MPS,pbc}}\rangle$ are able to capture the vast majority of the total DMRG energy ($\sim 99.0\%$ in many cases). Part of this success of the Projector Quantum Monte Carlo energies, E_{TNS}, and their closeness to DMRG values is due to the optimised pairing function acting as reference state which is usually able to account for a large part of the correlation energy and thus allows for the use of small values of D whilst still yielding energies close the the infinite D limit of DMRG. However, it is worth pointing out that the results obtained with the Projector Quantum Monte Carlo method for non-linear wavefunctions are in general not expected to agree exactly with DMRG values for a number of reasons. Firstly, DMRG rigorously conserves all symmetries and quantum numbers, whereas the Projector Quantum Monte Carlo optimisation explicitly breaks symmetries and non-zero projections onto section of the Hilbert space with other (e.g. spin) quantum numbers and symmetries typically remain. Secondly, by constraining the nodal structure of $|\Psi_{\mathrm{MPS,pbc}}\rangle$ to the variational flexibility affordable by the reference state, a 'fixed-node' error will in general be introduced apart from those cases where the nodal structure of the reference state recovers the nodal structure of the exact wavefunction. In most situations small values of D are then sufficient to reach the wavefunction with the variational lowest energy available within the given parameterisation. In contrast, DMRG energies are converged with respect to bond dimension D in which limit they can be considered to be numerically exact.

Moreover, the convergences displayed in Figure 7.4 demonstrate that the Projector Quantum Monte Carlo optimisation for non-linear wavefunctions is able to converge onto wavefunctions whose energies largely agree with DMRG results irrespective of whether just one single stochastic process for sampling of the physical indices is employed or whether two nested stochastic processes sample both the contraction of physical and auxiliary indices. Unfortunately, when comparing Projector Quantum Monte Carlo energies in Table 7.1 obtained with exact deterministic (one stochastic process) and sampled (two nested stochastic processes) contraction of auxiliary indices small differences persist which tend to become more pronounced when either system sizes, bond dimensions or both increase. These deviations are most likely due to the unavoidable biases in the TNS sampling approach which have been detailed in the previous section. Yet, given the smallness of the difference for small systems and values of D, this is another indication that the biases can be controlled in the limit of sufficient sampling.

In principle, the number of samples for stochastic contraction of the auxiliary indices, N_{aux}, as well as for stochastic contraction of the physical indices, N_{phys}, which are required for efficient wavefunction optimisations grows with the bond dimension D of the tensors and system size. In the initial stages of the optimisation, relatively small number of samples are sufficient (e.g. $N_{\mathrm{aux}} \sim 100$ and a total of $N_{\mathrm{phys}} \sim 4 \times 10^6$ distributed across several processors) for all considered system sizes and bond dimensions. As the optimisation progresses these typically have to be raised gradually to achieve a higher accuracy with the maximum number of samples now depending on system size and bond dimension ($N_{\text{aux}} \sim 200$ and $N_{\text{phy}} \sim 16 \times 10^6$ for the 1×14 Hubbard model with $D = 2$). However, a precise scaling of N_{aux} and N_{phys} with bond dimension and system size is more difficult to arrive at since the appropriate values depend on each other, as well as on the step size of the optimisation and the value of $\frac{U}{t}$. It should be pointed out that in order to ensure converged results, the optimisations aimed to substantially oversample, which results in small error bars in the calculated quantities. Since reducing error bars in this approach by an order of magnitude represents two orders of magnitude more computational effort, results close to convergence can already be obtained with substantially fewer number of samples. In terms of reducing stochastic errors, one of the dominant factors is the sampling of the gradient. Since the N_{aux} samples used to stochastically evaluate the derivatives with respect to a whole tensor $S^{'}_{\mathbf{n};n_s}$, the actual number of samples which contribute to the estimate of the derivative of a single element $S^{'}_{\mathbf{n};n_s,ijkl}$ is smaller, e.g. by approximately a factor of $\sim \frac{1}{D^4}$ for rank-4 tensors of dimension D (assuming approximately uniform selection of the elements of $S^{'}_{\mathbf{n};n_s}$ for simplicity). Whilst this approach increases the stochastic errors of the derivatives, it ensures that each element $S^{'}_{\mathbf{n};n_s,ijkl}$ is estimated independently from all other elements in $S^{'}_{\mathbf{n};n_s}$. If the elements of $S^{'}_{\mathbf{n};n_s}$ were not estimated independently, correlations in between them will be significantly enhanced which will lead to considerable biases. Additionally, the random selection of elements of $S^{'}_{\mathbf{n};n_2}$ also aids in breaking the symmetry of the individual tensor elements in the optimisation.

Having established that sampling the tensor network also allows for efficient optimisation of the wavefunction parameters within the framework of the Projector Quantum Monte Carlo method proposed in this thesis, the approach is applied to PEPS wavefunctions, the main aim of this chapter. Thus, a two-dimensional 4×4 Hubbard model on a square lattice at half-filling is considered with periodic boundary conditions and $\frac{U}{t} = 2$ or $\frac{U}{t} = 4$. For these systems benchmark results from the Auxiliary Field Quantum Monte Carlo method (AFQMC) are available[387] which can be considered numerically exact at half-filling. While the nodal structure of the PEPS wavefunction $|\Psi_{\text{PEPS}}\rangle$ is provided by an optimised general pairing function acting as reference state, further correlations are captured by the independent, simultaneously optimised rank-5 tensors of the PEPS state (one physical index and four auxiliary indices). At a bond dimension of $D = 2$, the error in the total ground state energy per site of $|\Psi_{\text{PEPS}}\rangle$ is only $\sim 1.0\%$ for both values of $\frac{U}{t}$.

4 × 4 Hubbard model			
$\frac{U}{t}$	E_{AFQMC}	$E_{\text{PEPS}}(D=2)$	P_{PEPS}
2	$-1.1265(4)$	$-1.11812(5)$	99.3
4	$-0.8510(4)$	$-0.84228(2)$	98.9

Table 7.2 Ground state energy per site E_{PEPS} for $2D$ 4×4 Hubbard model on a square lattice at half-filling with periodic boundary conditions and $\frac{U}{t}=2$ or $\frac{U}{t}=4$. The PEPS wavefunctions are parameterised according to Eq. 7.5 with a bond dimension of $D=2$ and a general pairing function acting as reference state. The wavefunction parameters have been optimised with the Projector Quantum Monte Carlo method coupled to stochastic evaluation of the PEPS contraction. E_{AFQMC} represents Auxiliary Field Quantum Monte Carlo (AFQMC) energies which can be considered to be numerically exact at half-filling. $P_{\text{PEPS}} = \frac{E_{\text{PEPS}}}{E_{\text{AFQMC}}}$ (%) denotes the percentage of E_{AFQMC} captured by $|\Psi_{\text{PEPS}}\rangle$. All energies are given in E_h/site. The numbers in parentheses represent the stochastic error in the previous digit as obtained through a Flyvbjerg-Petersen reblocking analysis[268]. The AFQMC energies are taken from Ref.[387].

7.7 Conclusions

In this chapter, a sampling approach for stochastic evaluation of the contraction of tensor networks has been proposed as alternative to approximate deterministic contraction schemes that state-of-the-art PEPS optimisation methods rely on. This sampling method is able to yield stochastic estimates which are close to results obtained with exact tensor network contraction. Some potential and unavoidable sources of biases still remain but these can be controlled in the limit of sufficient sampling. Within the framework of the Projector Quantum Monte Carlo approach detailed in the previous chapters, this sampling approach allows for the efficient stochastic optimisation of the variational parameters in a wavefunction with energies close to those values exact contraction results. In future, an improvement in the efficiency of the sampling approach or additional development for a better control of the potential sources of biases would benefit this sampling approach, in particular when it is applied to larger system sizes. Further applications to wavefunction parameterised with higher bond dimensions D, as well as treatments of larger system sizes, might then also allow for extrapolations to the infinite D and thermodynamic limit[189].

Chapter 8

Concluding Remarks and Continuing Directions

In this thesis, a novel Projector Quantum Monte Carlo method for non-linear wavefunction ansatzes has been developed and successfully applied to a range of challenging strongly correlated systems. The formulation of this new approach has been partially inspired by a prior application of the Full Configuration Interaction Quantum Monte Carlo (FCIQMC) method to a prototypical strongly correlated system. FCIQMC repeatedly and stochastically applies a projector onto an initial trial wavefunction parameterised as linear expansion in the basis of Slater determinants spanning the full Hilbert space of a system. Whilst stochastic application of the propagator takes advantage of the sparse and diagonally dominant nature of the Hamiltonian in Fock space, sparsity inherent in the wavefunction is exploited by an ensemble of walkers which provides a stochastic coarse-grained description of the wavefunction. As such, FCIQMC represents a stochastic realisation of the Power Method, allowing access to essentially exact results for systems far out of reach of many traditional diagonalisation approaches.

FCIQMC therefore naturally lends itself as a suitable method for obtaining benchmark results and investigating the nature of the exact wavefunction. As a first investigation in this spirit, an FCIQMC study of a prototypical and highly non-trivial strongly correlated system, the three-band $(p-d)$ Hubbard model, was conducted. The main focus of this study was the FCI wavefunction representation expressed in different single-particle basis sets and their amenability to accurate correlation treatments. The investigated one-particle bases included the widely available restricted (RHF) and unrestricted (UHF) Hartree-Fock spin orbitals which were compared with restricted (RNO) and unrestricted (UNO) natural orbitals. The latter are known to yield compact FCI expansions whose coefficients decay rapidly with increasing particle-hole excitations of the reference Slater determinant.

Counterintuitively, it was found in this investigation that the ability of single-particle basis sets to reproduce the physics of a system within a single-determinant description is not necessarily an indicator for their ability to give rise to rapidly converging CI expansions. Instead, it was observed that whilst a UHF determinant describes a qualitatively correct insulating antiferromagnet as ground state, imposing spin symmetry in the RHF basis provides a qualitatively incorrect metal as RHF determinant. Still, in the latter basis, and even more so in both natural orbital bases, the FCI expansion of the many-body wavefunction is sparser and converges rapidly with particle-hole excitations of the reference determinant. These findings are of particular interest for approaches in condensed matter physics. Whilst these typically start from qualitatively correct symmetry-broken solutions, the findings of this FCIQMC study indicate that these may not always be the optimal starting points and that approaches building on symmetry conserving basis sets may be more successful. In addition, the results of this investigation suggest that single-reference quantum chemical methods in combination with an appropriate single-particle descriptions may be able to treat many-body wavefunctions of strongly correlated systems. This is of great importance for the development of these single-reference approaches and their applications to strongly correlated materials which have so far been found to pose non-trivial challenges for these methodologies.

Despite these findings, the challenge of an exponentially growing Hilbert space still remains, implying that for highly multi-reference wavefunctions, as they typically occur for strongly correlated materials, the FCI expansion will become intractable for large systems even when expressed in an optimal single-particle basis. Thus, if progress to larger system sizes is to be made, more compact wavefunction ansatzes need to be considered which scale polynomially rather than exponentially with system size, ideally whilst still building on the success of FCIQMC. This has lead to the development of a novel Projector Quantum Monte Carlo approach through reformulation of the projected imaginary time evolution of FCIQMC in terms of a Lagrangian minimisation. This naturally admits wavefunction ansatzes with polynomial complexity which have more traditionally inhabited the realm of Variational Quantum Monte Carlo approaches. At the same time, it highlights the deep connection between imaginary time evolution, the power method and (stochastic) gradient descent. However, similar approaches have previously had little success given the slow convergence rate of stochastic gradient descent. Improvements on this have been made by advances in the field of deep learning algorithms and neural networks. Two of these have been incorporated in the proposed Projector Quantum Monte Carlo method resulting in a modification of the propagator of the wavefunction dynamics. As a first advancement, Nesterov's accelerated approach has been included which belongs to the class of 'momentum' methods. Within these techniques the update of variational parameters retains a memory of previous updates thereby formally accelerating convergence rates to second order. The second improvement has been the incorporation of RMSprop which is a scheme to automatically and independently estimate an individual optimal step size for each individual variational parameter. This has increased the robustness of the optimisation, as well as accelerated its convergence by taking larger steps for parameters with small gradients and vice versa. Combining all these methods has lead to a new Projector Quantum Monte Carlo approach which represents a very versatile and general, as well as highly efficient optimisation of arbitrary non-linear wavefunction ansatzes of quantum many-body systems with large numbers of parameters.

Following the exposition of the method, it has been combined with a number of efficient and highly accurate wavefunction ansatzes. The first of these is a parameterisation referred to as Correlator Product States (CPS), a form of Tensor Network States whose complexity grows polynomially with system size. This CPS ansatz represents a versatile approach which, at the same time, is systematically improvable to the exact FCI limit. The capabilities of the proposed accelerated Projector Quantum Monte Carlo approach has thus been demonstrated by optimising wavefunctions of this CPS parameterisation for a number of strongly correlated systems. These applications include one and two dimensional Hubbard models, as well as *ab-initio* systems. The latter begin with the highly non-trivial benchmark system of the symmetric dissociation of H_{50} for whose stretching total energies have been obtained with chemical accuracy and culminate in a fully periodic *ab-initio* graphene sheet. In addition to optimisation of wavefunction parameters, the same dynamics also allow for sampling of the reduced one- and two-body density matrices, thereby granting access to one- and two-body static properties of the investigated systems.

In a further series of applications, the developed Projector Quantum Monte Carlo method has been applied to another wavefunction ansatz, Projected Entangled Pair States (PEPS), also a class of Tensor Network States and the natural generalisation of the extremely successful Matrix Product States (MPS) to higher dimensions. Whilst PEPS wavefunctions are known to yield accurate approximations to ground states, efficient optimisation of their variational parameters still poses a significant challenge. This is partly rooted in the large computational cost associated with exact contraction of a PEPS network when information in the form of expectation values and correlation functions is extracted from the wavefunction. Even though approximate contraction schemes improve on this, they are still relatively expensive. A new approach has therefore been proposed in this thesis which, instead of performing the contraction deterministically, relies on Monte Carlo sampling to obtain a stochastic estimate of the contraction by sampling a sufficient number of terms appearing in the sum. With this stochastic contraction approach, applications of the Projector Quantum Monte Carlo method for MPS and PEPS wavefunctions have been realised for a number of Hubbard models providing results close to exact energies. In the future, this approach would benefit from improvements in the Monte Carlo sampling scheme for the PEPS contractions in the sense that fewer number of samples will lead to a more accurate estimate.

The ability of the proposed Projector Quantum Monte Carlo method for non-linear wavefunctions to treat wavefunctions with polynomial complexity allows for the consideration of systems which are intractable for exact but exponentially complex wavefunction ansatzes, as illustrated by the many successful applications presented in this thesis. It has been demonstrated in this thesis that this novel approach can handle and efficiently optimise large numbers of parameters, greatly exceeding those which are amenable to state-of-the-art VMC methods where only recent developments have made progress at extending these numbers[349]. Moreover, this optimisation approach is very versatile and general and can be applied to arbitrary wavefunction ansatzes provided that the projections of wavefunction amplitudes, as well as the derivatives of the Lagrangian with respect to the variational parameters, onto configurations in the full Hilbert space are efficiently computable.

Thus, further ansatzes which might be considered include wavefunctions parameterised as artificial neural networks which have already been successfully applied to spin models with state-of-the-art VMC approaches[388]. In addition to applications with other wavefunction ansatzes, continuing developments can also extend the scope of the Projector Quantum Monte Carlo method. A possible direction for these developments involves the use of symmetry. So far, the Projector Quantum Monte Carlo has not made any use of symmetry but instead has explicitly broken symmetry. Thus, as an extension, symmetry may be directly enforced in order to reduce the number of independent variational parameters which allows for the treatment of even larger systems. Additionally, by imposing a specified symmetry excited states with a symmetry different to the ground state can also be converged upon. Another route to excited states might be via orthogonalisation against the ground state as it has been introduced in FCIQMC[249].

In conclusion, the Projector Quantum Monte Carlo method formulated in this thesis has been demonstrated to provide a powerful and promising novel method for efficient optimisation of the variational parameters in arbitrary non-linear wavefunction ansatzes. The presented results have clearly illustrated the ability of this approach to handle large numbers of variational parameters which greatly exceed those amenable to alternative Variational Quantum Monte Carlo techniques. Moreover, the employed non-linear wavefunction ansatzes represent efficient and accurate approximate parameterisations. At the same time, they grow only polynomially with system size and thus allow for the treatment of much larger systems than those which are amenable to the exact wavefunction ansatz of diagonalisation approaches. Like other wavefunction-based methodologies, this proposed Projector Quantum Monte Carlo approach possesses two major advantages over DFT-based approaches which have dominated electronic structure calculations, so far. Firstly, typical approximations involved in the wavefunction parameterisation are controlled and systematically improvable toward exactness. In addition, many-body wavefunction descriptions of physical systems grant access to all of its properties and therefore represent one of the best frameworks to gain deeper insight into the mechanics of quantum many-body systems,

Appendix A

Comparison of Lagrangian and Ritz Functional Derivatives

For an arbitrary wavefunction ansatz $\Psi(Z_\sigma)$ based on variational parameters $\{Z_\sigma\}$ the positive-definite Lagrangian is given by

$$\mathcal{L}[\Psi(Z_\sigma)] = \langle\Psi|\hat{\mathcal{H}}|\Psi\rangle - E_0\left(\langle\Psi|\hat{\mathcal{I}}|\Psi\rangle - A\right), \tag{A.1}$$

where normalisation of the wavefunction $\Psi(Z_\sigma)$ (up to an arbitrary constant A) is enforced by a Lagrange multiplier which at convergence is equal to the self-consistently determined ground state energy E_0. As outlined in Chapter 5, the derivative of this Lagrangian with respect to any of the wavefunction parameters, Z_σ, can be written as

$$\begin{aligned}
\frac{\partial\mathcal{L}[\Psi(Z_\sigma)]}{\partial Z_\sigma} &= \langle\frac{\partial\Psi}{\partial Z_\sigma}|\hat{\mathcal{H}}|\Psi\rangle + \langle\Psi|\hat{\mathcal{H}}|\frac{\partial\Psi}{\partial Z_\sigma}\rangle && \text{(A.2)}\\
&. - E_0\left(\langle\frac{\partial\Psi}{\partial Z_\sigma}|\hat{\mathcal{I}}|\Psi\rangle + \langle\Psi|\hat{\mathcal{I}}|\frac{\partial\Psi}{\partial Z_\sigma}\rangle\right) && \text{(A.3)}\\
&= 2\,\langle\frac{\partial\Psi}{\partial Z_\sigma}|\hat{\mathcal{H}}|\Psi\rangle - 2E_0\,\langle\frac{\partial\Psi}{\partial Z_\sigma}|\hat{\mathcal{I}}|\Psi\rangle && \text{(A.4)}\\
&= 2\,\langle\frac{\partial\Psi}{\partial Z_\sigma}|(\hat{\mathcal{H}} - E_0\hat{\mathcal{I}})|\Psi\rangle\,, && \text{(A.5)}
\end{aligned}$$

where in the third line a real wavefunction and a real, symmetric Hamiltonian are assumed.

Furthermore, when considering the same wavefunction parameterisation $\Psi(Z_\sigma)$, the Ritz functional is defined as

$$\mathcal{R}[\Psi(Z_\sigma)] = \frac{\langle\Psi|\hat{\mathcal{H}}|\Psi\rangle}{\langle\Psi|\Psi\rangle}, \tag{A.6}$$

and its derivative with respect to any of the wavefunction parameters, Z_σ, is given by

$$\begin{aligned}
\frac{\partial\mathcal{R}[\Psi(Z_\sigma)]}{\partial Z_\sigma} &= \frac{2\,\langle\frac{\partial\Psi}{\partial Z_\sigma}|\hat{\mathcal{H}}|\Psi\rangle}{\langle\Psi|\Psi\rangle} - \frac{2\,\langle\Psi|\hat{\mathcal{H}}|\Psi\rangle\,\langle\frac{\partial\Psi}{\partial Z_\sigma}|\Psi\rangle}{(\langle\Psi|\Psi\rangle)^2} &\quad (\text{A.7})\\
&= \frac{2}{\langle\Psi|\Psi\rangle}\left(\langle\frac{\partial\Psi}{\partial Z_\sigma}|\hat{\mathcal{H}}|\Psi\rangle - \frac{\langle\Psi|\hat{\mathcal{H}}|\Psi\rangle\,\langle\frac{\partial\Psi}{\partial Z_\sigma}|\Psi\rangle}{\langle\Psi|\Psi\rangle}\right) &\quad (\text{A.8})\\
&= \frac{2}{\langle\Psi|\Psi\rangle}\left(\langle\frac{\partial\Psi}{\partial Z_\sigma}|\hat{\mathcal{H}}|\Psi\rangle - \mathcal{R}[\Psi(Z_\sigma)]\,\langle\frac{\partial\Psi}{\partial Z_\sigma}|\Psi\rangle\right), &\quad (\text{A.9})
\end{aligned}$$

where again a real wavefunction and a real, symmetric Hamiltonian are assumed.

A comparison of the Lagrangian and Ritz functional derivative leads to the conclusion that both are equivalent if the following two conditions are satisfied: that is if $\langle\Psi|\Psi\rangle = 1$ and $\mathcal{R}[\Psi(Z_\sigma)] = E_0$. These conditions are met by the Projector Quantum Monte Carlo method detailed in Chapter 5. Firstly, since the gradient employed in this approach is sampled with the probability distribution of Eq. 5.13 in Chapter 5, normalisation is implicitly imposed such that $\langle\Psi|\Psi\rangle = 1$ is ensured. Secondly, during the course of an optimisation the value of E_0 is explicitly set to the energy of the wavefunction which is given by $\mathcal{R}[\Psi(Z_\sigma)]$, such that the second condition $\mathcal{R}[\Psi(Z_\sigma)] = E_0$ is fulfilled, as well.

References

[1] J. G. Bednorz and K. A. Müller. Possible high T_c superconductivity in the Ba−La−Cu−O system. *Zeitschrift für Physik B Condensed Matter*, 64(2):189–193, 1986.

[2] J. G. Bednorz and K. A. Müller. Perovskite-type oxides—the new approach to high-T_c superconductivity. *Reviews of Modern Physics*, 60:585–600, Jul 1988.

[3] Adolfo Avella and Ferdinando Mancini. *Strongly Correlated Systems: Theoretical Methods*, volume 171 of *Springer Series in Solid-State Sciences*. Springer Science & Business Media, 2011.

[4] E. Dagotto. Correlated electrons in high-temperature superconductors. *Reviews of Modern Physics*, 66:763–840, Jul 1994.

[5] P. W. Anderson. The resonating valence bond state in La_2CuO_4 and superconductivity. *Science*, 235:1196–1198, March 1987.

[6] E. Dagotto. Complexity in Strongly Correlated Electronic Systems. *Science*, 309(5732):257–262, 2005.

[7] E. Dagotto and Y. Tokura. Strongly Correlated Electronic Materials: Present and Future. *MRS Bulletin*, 33(11):1037–1045, 11 2008.

[8] Evgeny Y. Tsymbal. *Multifunctional oxide heterostructures*. Oxford University Press, 2012.

[9] M. Imada, A. Fujimori, and Y. Tokura. Metal-insulator transitions. *Reviews of Modern Physics*, 70:1039–1263, Oct 1998.

[10] A. Georges, G. Kotliar, W. Krauth, and M. J. Rozenberg. Dynamical mean-field theory of strongly correlated fermion systems and the limit of infinite dimensions. *Reviews of Modern Physics*, 68:13–125, Jan 1996.

[11] Th. Pruschke, M. Jarrell, and J.K. Freericks. Anomalous normal-state properties of high-T_c superconductors: intrinsic properties of strongly correlated electron systems? *Advances in Physics*, 44(2):187–210, 1995.

[12] Y. Kamihara, T. Watanabe, M. Hirano, and H. Hosono. Iron-Based Layered Superconductor $La[O_{1-x}F_x]FeAs$ ($x = 0.05 - 0.12$) with $T_c = 26$ K. *Journal of the American Chemical Society*, 130(11):3296–3297, 2008. PMID: 18293989.

[13] H. Jiang. First-principles approaches for strongly correlated materials: A theoretical chemistry perspective. *International Journal of Quantum Chemistry*, 115(11):722–730, 2015.

[14] G. Kotliar and S. Y. Savrasov. *Model Hamiltonians and First Principles Electronic Structure Calculations*, page 259–301. Springer Netherlands, Dordrecht, 2001.

[15] J. Paier, C. Penschke, and J. Sauer. Oxygen Defects and Surface Chemistry of Ceria: Quantum Chemical Studies Compared to Experiment. *Chemical Reviews*, 113(6):3949–3985, 2013. PMID: 23651311.

[16] J. P. Malrieu, R. Caballol, C. J. Calzado, C. de Graaf, and N. Guihéry. Magnetic Interactions in Molecules and Highly Correlated Materials: Physical Content, Analytical Derivation, and Rigorous Extraction of Magnetic Hamiltonians. *Chemical Reviews*, 114(1):429–492, 2014. PMID: 24102410.

[17] Y. S. Meng and M. E. Arroyo-de Dompablo. First principles computational materials design for energy storage materials in lithium ion batteries. *Energy & Environmental Science*, 2:589–609, 2009.

[18] E. Schrödinger. Quantisierung als Eigenwertproblem. *Annalen der Physik*, 385(13):437–490, 1926.

[19] W. Pauli. Über den Zusammenhang des Abschlusses der Elektronengruppen im Atom mit der Komplexstruktur der Spektren. *Zeitschrift für Physik*, 31(1):765–783, 1925.

[20] G. E. Uhlenbeck and S. Goudsmit. Ersetzung der Hypothese vom unmechanischen Zwang durch eine Forderung bezüglich des inneren Verhaltens jedes einzelnen Elektrons. *Die Naturwissenschaften*, 13(47):953–954, 1925.

[21] W. Heisenberg. Mehrkörperproblem und Resonanz in der Quantenmechanik. *Zeitschrift für Physik*, 38(6):411–426, 1926.

[22] E. Schrödinger. An undulatory theory of the mechanics of atoms and molecules. *Physical Review*, 28:1049–1070, Dec 1926.

[23] P. A. M. Dirac. Quantum Mechanics of Many-Electron Systems. *Proceedings of the Royal Society of London A: Mathematical, Physical and Engineering Sciences*, 123(792):714–733, 1929.

[24] P. Hohenberg and W. Kohn. Inhomogeneous electron gas. *Physical Review*, 136:B864–B871, Nov 1964.

[25] W. Kohn and L. J. Sham. Self-consistent equations including exchange and correlation effects. *Physical Review*, 140:A1133–A1138, Nov 1965.

[26] K. Terakura, T. Oguchi, A. R. Williams, and J. Kübler. Band theory of insulating transition-metal monoxides: Band-structure calculations. *Physical Review B*, 30:4734–4747, Oct 1984.

[27] W. E. Pickett. Electronic structure of the high-temperature oxide superconductors. *Reviews of Modern Physics*, 61:433–512, Apr 1989.

[28] G. Zwicknagl. Quasi-particles in heavy fermion systems. *Advances in Physics*, 41(3):203–302, 1992.

[29] V. I. Anisimov, J. Zaanen, and O. K. Andersen. Band theory and mott insulators: Hubbard u instead of stoner i. *Physical Review B*, 44:943–954, Jul 1991.

[30] A. Svane and O. Gunnarsson. Transition-metal oxides in the self-interaction–corrected density-functional formalism. *Physical Review Letters*, 65:1148–1151, Aug 1990.

[31] K. Held, I. A. Nekrasov, N. Blümer, V. I. Anisimov, and D. Vollhardt. Realistic modeling of strongly correlated electron systems: An introduction to the LDA+DMFT approach. *International Journal of Modern Physics B*, 15(19n20):2611–2625, 2001.

[32] Th. Maier, M. Jarrell, Th. Pruschke, and M. H. Hettler. Quantum cluster theories. *Reviews of Modern Physics*, 77:1027–1080, Oct 2005.

[33] J. Hubbard. Electron correlations in narrow energy bands. *Proceedings of the Royal Society of London. Series A, Mathematical and Physical Sciences*, 276(1365):238–257, 1963.

[34] F. Gebhard. *The Mott Metal-Insulator Transition: Models and Methods*. Springer Tracts in Modern Physics. Springer Berlin Heidelberg, 1997.

[35] M. M. Korshunov, V. A. Gavrichkov, S. G. Ovchinnikov, I. A. Nekrasov, Z. V. Pchelkina, and V. I. Anisimov. Hybrid LDA and generalized tight-binding method for electronic structure calculations of strongly correlated electron systems. *Physical Review B*, 72:165104, Oct 2005.

[36] Peter Fulde. *Electron correlations in molecules and solids*. Springer series in solid-state sciences. Springer-Verlag, 1991.

[37] Trygve Helgaker, Poul Jørgensen, and Jeppe Olsen. *Molecular Electronic-Structure Theory*. Wiley, 2014.

[38] P. Fulde. Wavefunction methods in electronic-structure theory of solids. *Advances in Physics*, 51(3):909–948, 2002.

[39] Ch. Riplinger, B. Sandhoefer, A. Hansen, and F. Neese. Natural triple excitations in local coupled cluster calculations with pair natural orbitals. *The Journal of Chemical Physics*, 139(13):134101, 2013.

[40] W. Kohn. Nobel lecture: Electronic structure of matter—wave functions and density functionals. *Reviews of Modern Physics*, 71:1253–1266, Oct 1999.

[41] Fulde P. Wavefunction-based electronic-structure calculations for solids. *Nature Physics*, 12(2):106–107, Feb 2016.

[42] G. Stollhoff and P. Fulde. On the computation of electronic correlation energies within the local approach. *The Journal of Chemical Physics*, 73(9):4548–4561, 1980.

[43] P. Pulay. Localizability of dynamic electron correlation. *Chemical Physics Letters*, 100(2):151–154, 1983.

[44] L. Hozoi, U. Birkenheuer, H. Stoll, and P. Fulde. Spin-state transition and spin-polaron physics in cobalt oxide perovskites: ab initio approach based on quantum chemical methods. *New Journal of Physics*, 11(2):023023, 2009.

[45] H. Stoll. Correlation energy of diamond. *Physical Review B*, 46:6700–6704, Sep 1992.

[46] H. Stoll, B. Paulus, and P. Fulde. On the accuracy of correlation-energy expansions in terms of local increments. *The Journal of Chemical Physics*, 123(14):144108, 2005.

[47] K. Doll, M. Dolg, P. Fulde, and H. Stoll. Quantum chemical approach to cohesive properties of NiO. *Physical Review B*, 55:10282–10288, Apr 1997.

[48] K. Rościszewski, K. Doll, B. Paulus, P. Fulde, and H. Stoll. Ground-state properties of rutile: Electron-correlation effects. *Physical Review B*, 57:14667–14672, Jun 1998.

[49] E. Voloshina and B. Paulus. Influence of electronic correlations on the ground-state properties of cerium dioxide. *The Journal of Chemical Physics*, 124(23):234711, 2006.

[50] W. M. C. Foulkes, L. Mitas, R. J. Needs, and G. Rajagopal. Quantum monte carlo simulations of solids. *Reviews of Modern Physics*, 73:33–83, Jan 2001.

[51] C. J. Umrigar. Observations on variational and projector Monte Carlo methods. *The Journal of Chemical Physics*, 143(16):164105, 2015.

[52] G. H. Booth, A. J. W. Thom, and A. Alavi. Fermion Monte Carlo without fixed nodes: A game of life, death, and annihilation in Slater determinant space. *The Journal of Chemical Physics*, 131(5):054106, 2009.

[53] J. Eisert. Entanglement and tensor network states. *ArXiv e-prints*, August 2013.

[54] Orús R. A practical introduction to tensor networks: Matrix product states and projected entangled pair states. *Annals of Physics*, 349:117–158, oct 2014.

[55] F. Verstraete, V. Murg, and J.I. Cirac. Matrix product states, projected entangled pair states, and variational renormalization group methods for quantum spin systems. *Advances in Physics*, 57(2):143–224, 2008.

[56] S. R. White. Density matrix formulation for quantum renormalization groups. *Physical Review Letters*, 69:2863–2866, Nov 1992.

[57] Attila Szabo and Neil S. Ostlund. *Modern Quantum Chemistry: Introduction to Advanced Electronic Structure Theory.* Dover Publications, New York, 1996.

[58] M. Born and R. Oppenheimer. Zur Quantentheorie der Molekeln. *Annalen der Physik*, 389(20):457–484, 1927.

[59] G. A. Worth and L. S. Cederbaum. Beyond Born-Oppenheimer: Molecular Dynamics Through a Conical Intersection. *Annual Review of Physical Chemistry*, 55(1):127–158, 2004. PMID: 15117250.

[60] T. Azumi and K. Matsuzaki. What does the term "Vibronic Coupling” mean? *Photochemistry and Photobiology*, 25(3):315–326, 1977.

[61] M. Fierz. Über die relativistische Theorie kräftefreier Teilchen mit beliebigem Spin. *Helvetica Physica Acta*, 12(3), 1939.

[62] W. Pauli. The Connection Between Spin and Statistics. *Physical Review*, 58:716–722, Oct 1940.

[63] P. A. M. Dirac. On the Theory of Quantum Mechanics. *Proceedings of the Royal Society of London A: Mathematical, Physical and Engineering Sciences*, 112(762):661–677, 1926.

[64] Michela Massimi. *Pauli's Exclusion Principle: The Origin and Validation of a Scientific Principle.* Cambridge University Press, 2005.

[65] J. C. Slater. The Theory of Complex Spectra. *Physical Review*, 34:1293–1322, Nov 1929.

[66] P. A. M. Dirac. The Quantum Theory of the Emission and Absorption of Radiation. *Proceedings of the Royal Society of London A: Mathematical, Physical and Engineering Sciences*, 114(767):243–265, 1927.

[67] V. Fock. Konfigurationsraum und zweite Quantelung. *Zeitschrift für Physik*, 75(9):622–647, 1932.

[68] Alexander L. Fetter and John Dirk Walecka. *Quantum Theory of Many-particle Systems.* Dover Publications, 2003.

[69] Felix Alexandrovich Berezin. *The method of second quantization.* Pure and applied physics. A series of monographs and textbooks. Academic Press, 1966.

[70] Wolfgang Nolting. *Grundkurs Theoretische Physik 5/2: Quantenmechanik - Methoden und Anwendungen.* Springer-Lehrbuch. Springer, 2015.

[71] Vladimir Aleksandrovich Fock. *V. A. Fock - Selected Works: Quantum Mechanics and Quantum Field Theory.* Chapman & Hall/CRC, Boca Raton, Fla, 2004.

[72] V. Fock. Näherungsmethode zur Lösung des quantenmechanischen Mehrkörperproblems. *Zeitschrift für Physik*, 61(1):126–148, 1930.

[73] D. R. Hartree. The wave mechanics of an atom with a non-coulomb central field. part i. theory and methods. In *Mathematical Proceedings of the Cambridge Philosophical Society*, volume 24, pages 89–110. Cambridge University Press, 1928.

[74] D. R. Hartree, W. Hartree, and B. Swirles. Self-consistent field, including exchange and superposition of configurations, with some results for oxygen. *Philosophical Transactions of the Royal Socity of London. Series A, Mathematical and Physical Sciences*, 238(790):229–247, 1940.

[75] C. C. J. Roothaan. New developments in molecular orbital theory. *Reviews of Modern Physics*, 23(2):69–89, 1951.

[76] J.A. Pople and R.-K. Nesbet. Self-consistent orbitals for radicals. *The Journal of Chemical Physics*, 22(3):571–572, 1954.

[77] E. A. Hylleraas. The Schrödinger Two-Electron Atomic Problem. In P.-O. Löwdin, editor, , volume 1 of *Advances in Quantum Chemistry*, page 1–33. Academic Press, 1964.

[78] T. Kato. On the eigenfunctions of many-particle systems in quantum mechanics. *Communications on Pure and Applied Mathematics*, 10(2):151–177, 1957.

[79] R. T. Pack and W. B. Brown. Cusp Conditions for Molecular Wavefunctions. *The Journal of Chemical Physics*, 45(2):556–559, 1966.

[80] D. P. Tew, W. Klopper, and T. Helgaker. Electron correlation: The many-body problem at the heart of chemistry. *Journal of Computational Chemistry*, 28(8):1307–1320, 2007.

[81] W. Kutzelnigg and W. Klopper. Wave functions with terms linear in the inter-electronic coordinates to take care of the correlation cusp. i. general theory. *The Journal of Chemical Physics*, 94(3):1985–2001, 1991.

[82] J. K. L. MacDonald. Successive approximations by the rayleigh-ritz variation method. *Physical Review*, 43:830–833, May 1933.

[83] S. F. Boys. Electronic Wave Functions. I. A General Method of Calculation for the Stationary States of Any Molecular System. *Proceedings of the Royal Society of London A: Mathematical, Physical and Engineering Sciences*, 200(1063):542–554, 1950.

[84] N. C. Handy. Multi-root configuration interaction calculations. *Chemical Physics Letters*, 74(2):280–283, 1980.

[85] J. C. Slater. Molecular energy levels and valence bonds. *Physical Review*, 38:1109–1144, Sep 1931.

[86] E. U. Condon. The theory of complex spectra. *Physical Review*, 36:1121–1133, Oct 1930.

[87] C. Lanczos. An iteration method for the solution of the eigenvalue problem of linear differential and integral operators. *Journal of Research of the National Bureau of Standards*, 45:225–282, 1950.

[88] R.-K. Nesbet. Algorithm for diagonalization of large matrices. *The Journal of Chemical Physics*, 43(1):311–312, 1965.

[89] E. R. Davidson. The iterative calculation of a few of the lowest eigenvalues and corresponding eigenvectors of large real-symmetric matrices. *Journal of Computational Physics*, 17(1):87–94, 1975.

[90] B. Roos. A new method for large-scale CI calculations. *Chemical Physics Letters*, 15(2):153–159, 1972.

[91] E. Rossi, G. L. Bendazzoli, S. Evangelisti, and D. Maynau. A full-configuration benchmark for the N_2 molecule. *Chemical Physics Letters*, 310(5–6):530–536, 1999.

[92] Chr. Møller and M. S. Plesset. Note on an approximation treatment for many-electron systems. *Physical Review*, 46:618–622, Oct 1934.

[93] M. Head-Gordon. Quantum chemistry and molecular processes. *The Journal of Physical Chemistry*, 100(31):13213–13225, 1996.

[94] M. L. Leininger, W. D. Allen, H. F. Schaefer III, and C. D. Sherrill. Is Møller-Plesset perturbation theory a convergent ab initio method? *The Journal of Chemical Physics*, 112(21):9213–9222, 2000.

[95] Isaiah Shavitt. *The Method of Configuration Interaction*, page 189–275. Springer US, Boston, MA, 1977.

[96] R. E. Watson. Approximate wave functions for atomic Be. *Physical Review*, 119:170–177, Jul 1960.

[97] L. Brillouin. La méthode du champs self-consistent. *Actualités Scientifiques et Industrielles*, 71, 1933.

[98] L. Brillouin. Les champs self-consistents de hartree et du fock. *Actualités Scientifiques et Industrielles*, 159, 1934.

[99] J. Olsen, P. Jo, H. Koch, A. Balkova, R. J. Bartlett, et al. Full configuration–interaction and state of the art correlation calculations on water in a valence double-zeta basis with polarization functions. *The Journal of Chemical Physics*, 104(20):8007–8015, 1996.

[100] R. J. Bartlett. Many-body perturbation theory and coupled cluster theory for electron correlation in molecules. *Annual Review of Physical Chemistry*, 32(1):359–401, 1981.

[101] Stephen R. Langhoff and Ernest R. Davidson. Configuration interaction calculations on the nitrogen molecule. *International Journal of Quantum Chemistry*, 8(1):61–72, 1974.

[102] F. Coester. Bound states of a many-particle system. *Nuclear Physics*, 7:421–424, August 1958.

[103] F. Coester and H. Kümmel. Short-range correlations in nuclear wave functions. *Nuclear Physics*, 17:477–485, July 1960.

[104] J. Čížek. On the Correlation Problem in Atomic and Molecular Systems. Calculation of Wavefunction Components in Ursell-Type Expansion Using Quantum-Field Theoretical Methods. *The Journal of Chemical Physics*, 45:4256–4266, December 1966.

[105] J. Cizek and J. Paldus. Coupled Cluster Approach. *Physica Scripta*, 21(3-4):251, 1980.

[106] R. J. Bartlett and M. Musiał. Coupled-cluster theory in quantum chemistry. *Reviews of Modern Physics*, 79:291–352, Feb 2007.

[107] G. E. Scuseria and T. J. Lee. Comparison of coupled-cluster methods which include the effects of connected triple excitations. *The Journal of Chemical Physics*, 93(8):5851–5855, 1990.

[108] T. Helgaker, T. A. Ruden, P. Jørgensen, J. Olsen, and W. Klopper. A priori calculation of molecular properties to chemical accuracy. *Journal of Physical Organic Chemistry*, 17(11):913–933, 2004.

[109] H.-J. Werner and P. J. Knowles. A second order multiconfiguration scf procedure with optimum convergence. *The Journal of Chemical Physics*, 82(11):5053–5063, 1985.

[110] B. O. Roos, P. R. Taylor, and P. E.M. Siegbahn. A complete active space SCF method (CASSCF) using a density matrix formulated super-CI approach. *Chemical Physics*, 48(2):157–173, 1980.

[111] P. E. M. Siegbahn, J. Almlöf, A. Heiberg, and B. O. Roos. The complete active space SCF (CASSCF) method in a newton–raphson formulation with application to the HNO molecule. *The Journal of Chemical Physics*, 74(4):2384–2396, 1981.

[112] B. O. Roos. The complete active space SCF method in a fock-matrix-based super-CI formulation. *International Journal of Quantum Chemistry*, 18(S14):175–189, 1980.

[113] J. Olsen. The casscf method: A perspective and commentary. *International Journal of Quantum Chemistry*, 111(13):3267–3272, 2011.

[114] P. A. Malmqvist, A. Rendell, and B. O. Roos. The restricted active space self-consistent-field method, implemented with a split graph unitary group approach. *The Journal of Physical Chemistry*, 94(14):5477–5482, 1990.

[115] K. Andersson, P. A. Malmqvist, B. O. Roos, A. J. Sadlej, and K. Wolinski. Second-order perturbation theory with a casscf reference function. *The Journal of Physical Chemistry*, 94(14):5483–5488, 1990.

[116] K. Andersson, P. Malmqvist, and B. O. Roos. Second-order perturbation theory with a complete active space self-consistent field reference function. *The Journal of Chemical Physics*, 96(2):1218–1226, 1992.

[117] H.-J. Werner and P. J. Knowles. An efficient internally contracted multiconfiguration–reference configuration interaction method. *The Journal of Chemical Physics*, 89(9):5803–5814, 1988.

[118] R. J. Buenker and S. D. Peyerimhoff. Individualized configuration selection in CI calculations with subsequent energy extrapolation. *Theoretica Chimica Acta*, 35(1):33–58, 1974.

[119] H.-J. Werner and E.-A. Reinsch. The self-consistent electron pairs method for multiconfiguration reference state functions. *The Journal of Chemical Physics*, 76(6):3144–3156, 1982.

[120] P. E. M. Siegbahn. Generalizations of the direct CI method based on the graphical unitary group approach. I. Single replacements from a complete CI root function of any spin, first order wave functions. *The Journal of Chemical Physics*, 70(12):5391–5397, 1979.

[121] P. E. M. Siegbahn. Generalizations of the direct CI method based on the graphical unitary group approach. II. Single and double replacements from any set of reference configurations. *The Journal of Chemical Physics*, 72(3):1647–1656, 1980.

[122] B. R. Brooks and H. F. Schaefer III. The graphical unitary group approach to the electron correlation problem. Methods and preliminary applications. *The Journal of Chemical Physics*, 70(11):5092–5106, 1979.

[123] P. E. M. Siegbahn. Current status of the multiconfiguration-configuration interaction (MC-CI) method as applied to molecules containing transition-metal atoms. *Faraday Symposia of the Chemical Society*, 19:97–107, 1984.

[124] N. Oliphant and L. Adamowicz. The implementation of the multireference coupled-cluster method based on the single-reference formalism. *The Journal of Chemical Physics*, 96(5):3739–3744, 1992.

[125] L. Z. Stolarczyk. Complete active space coupled-cluster method. Extension of single-reference coupled-cluster method using the CASSCF wavefunction. *Chemical Physics Letters*, 217(1–2):1–6, 1994.

[126] T. Yanai and G. K.-L. Chan. Canonical transformation theory for multireference problems. *The Journal of Chemical Physics*, 124(19):194106, 2006.

[127] R. M. Dickson and A. D. Becke. Reaction barrier heights from an exact-exchange-based density-functional correlation model. *The Journal of Chemical Physics*, 123(11):111101, 2005.

[128] M. Troyer and U.-J. Wiese. Computational complexity and fundamental limitations to fermionic quantum monte carlo simulations. *Physical Review Letters*, 94:170201, May 2005.

[129] J. von Neumann. Thermodynamik quantenmechanischer gesamtheiten. *Nachrichten von der Gesellschaft der Wissenschaften zu Göttingen, Mathematisch-Physikalische Klasse*, 1927:273–291, 1927.

[130] John von Neumann. *Mathematische Grundlagen der Quantenmechanik.* Springer, 1932.

[131] C. H. Bennett, D. P. DiVincenzo, J. A. Smolin, and W. K. Wootters. Mixed-state entanglement and quantum error correction. *Physical Review A*, 54:3824–3851, Nov 1996.

[132] J. Eisert, M. Cramer, and M. B. Plenio. Colloquium. *Reviews of Modern Physics*, 82:277–306, Feb 2010.

[133] M. B. Plenio, J. Eisert, J. Dreißig, and M. Cramer. Entropy, entanglement, and area: Analytical results for harmonic lattice systems. *Physical Review Letters*, 94:060503, Feb 2005.

[134] F. G. S. L. Brandão and M. Horodecki. An area law for entanglement from exponential decay of correlations. *Nature Physics*, 9(11):721–726, nov 2013.

[135] F. G. S. L. Brandão and M. Horodecki. Exponential Decay of Correlations Implies Area Law. *Communications in Mathematical Physics*, 333(2):761–798, 2015.

[136] M. B. Hastings. An area law for one-dimensional quantum systems. *Journal of Statistical Mechanics: Theory and Experiment*, 2007(08):P08024, 2007.

[137] I. Arad, Z. Landau, and U. Vazirani. Improved one-dimensional area law for frustration-free systems. *Physical Review B*, 85:195145, May 2012.

[138] I. Arad, A. Kitaev, Z. Landau, and U. Vazirani. An area law and sub-exponential algorithm for 1D systems. *ArXiv e-prints*, January 2013.

[139] K. Van Acoleyen, M. Mariën, and F. Verstraete. Entanglement rates and area laws. *Physical Review Letters*, 111:170501, Oct 2013.

[140] G. Vidal, J. I. Latorre, E. Rico, and A. Kitaev. Entanglement in quantum critical phenomena. *Physical Review Letters*, 90:227902, Jun 2003.

[141] Y. Ge and J. Eisert. Area laws and efficient descriptions of quantum many-body states. *New Journal of Physics*, 18(8):083026, 2016.

[142] N. Schuch. Condensed Matter Applications of Entanglement Theory. *ArXiv e-prints*, June 2013.

[143] S. R. White and R. L. Martin. Ab initio quantum chemistry using the density matrix renormalization group. *The Journal of Chemical Physics*, 110(9):4127–4130, 1999.

[144] U. Schollwöck. The density-matrix renormalization group in the age of matrix product states. *Annals of Physics*, 326(1):96–192, 2011. January 2011 Special Issue.

[145] N. Schuch, M. M. Wolf, F. Verstraete, and J. I. Cirac. Entropy scaling and simulability by matrix product states. *Physical Review Letters*, 100:030504, Jan 2008.

[146] Ingemar Bengtsson and Karol Ży̆czkowskui. *Geometry of Quantum States: An Introduction to Quantum Entanglement.* Cambridge University Press, Cambridge, paperback ed. edition, 2010.

[147] T. B. Wahl. Tensor network states for the description of quantum many-body systems. *ArXiv e-prints*, September 2015.

[148] F. Verstraete, M. M. Wolf, D. Perez-Garcia, and J. I. Cirac. Criticality, the area law, and the computational power of projected entangled pair states. *Physical Review Letters*, 96:220601, Jun 2006.

[149] A. Rényi et al. On measures of entropy and information. In *Proceedings of the fourth Berkeley symposium on mathematical statistics and probability*, volume 1, pages 547–561, 1961.

[150] F. Verstraete and J. I. Cirac. Matrix product states represent ground states faithfully. *Physical Review B*, 73:094423, Mar 2006.

[151] Z. Landau, U. Vazirani, and T. Vidick. A polynomial time algorithm for the ground state of one-dimensional gapped local Hamiltonians. *Nature Physics*, 11(7):566–569, jul 2015.

[152] S. Wouters and D. Van Neck. The density matrix renormalization group for ab initio quantum chemistry. *The European Physical Journal D*, 68(9):272, 2014.

[153] U. Schollwöck. The density-matrix renormalization group. *Reviews of Modern Physics*, 77:259–315, Apr 2005.

[154] G. Vidal. Class of quantum many-body states that can be efficiently simulated. *Physical Review Letters*, 101:110501, Sep 2008.

[155] F. Verstraete and J. I. Cirac. Renormalization algorithms for Quantum-Many Body Systems in two and higher dimensions. *eprint arXiv:cond-mat/0407066*, July 2004.

[156] M. B. Hastings. Solving gapped hamiltonians locally. *Physical Review B*, 73:085115, Feb 2006.

[157] M. B. Hastings. Entropy and entanglement in quantum ground states. *Physical Review B*, 76:035114, Jul 2007.

[158] J. Jordan, R. Orús, G. Vidal, F. Verstraete, and J. I. Cirac. Classical simulation of infinite-size quantum lattice systems in two spatial dimensions. *Physical Review Letters*, 101:250602, Dec 2008.

[159] A. Molnar, N. Schuch, F. Verstraete, and J. I. Cirac. Approximating gibbs states of local hamiltonians efficiently with projected entangled pair states. *Physical Review B*, 91:045138, Jan 2015.

[160] N. Schuch, M. M. Wolf, F. Verstraete, and J. I. Cirac. Computational complexity of projected entangled pair states. *Physical Review Letters*, 98:140506, Apr 2007.

[161] H. C. Jiang, Z. Y. Weng, and T. Xiang. Accurate determination of tensor network state of quantum lattice models in two dimensions. *Physical Review Letters*, 101:090603, Aug 2008.

[162] Z.-C. Gu, M. Levin, and X.-G. Wen. Tensor-entanglement renormalization group approach as a unified method for symmetry breaking and topological phase transitions. *Physical Review B*, 78:205116, Nov 2008.

[163] Z. Y. Xie, H. C. Jiang, Q. N. Chen, Z. Y. Weng, and T. Xiang. Second renormalization of tensor-network states. *Physical Review Letters*, 103:160601, Oct 2009.

[164] J. Eisert. Computational difficulty of global variations in the density matrix renormalization group. *Physical Review Letters*, 97:260501, Dec 2006.

[165] N. Schuch, I. Cirac, and F. Verstraete. Computational difficulty of finding matrix product ground states. *Physical Review Letters*, 100:250501, Jun 2008.

[166] S. R. White. Density-matrix algorithms for quantum renormalization groups. *Physical Review B*, 48:10345–10356, Oct 1993.

[167] Adolfo Avella and Ferdinando Mancini. *Strongly Correlated Systems: Numerical Methods*, volume 176 of *Springer Series in Solid-State Sciences*. Springer Science & Business Media, 2013.

[168] S. Östlund and S. Rommer. Thermodynamic limit of density matrix renormalization. *Physical Review Letters*, 75:3537–3540, Nov 1995.

[169] S. Rommer and S. Östlund. Class of ansatz wave functions for one-dimensional spin systems and their relation to the density matrix renormalization group. *Physical Review B*, 55:2164–2181, Jan 1997.

[170] D. Perez-Garcia, F. Verstraete, M. M. Wolf, and J. I. Cirac. Matrix product state representations. *Quantum Information & Computation*, 7(5):401–430, July 2007.

[171] L. Tagliacozzo, G. Evenbly, and G. Vidal. Simulation of two-dimensional quantum systems using a tree tensor network that exploits the entropic area law. *Physical Review B*, 80:235127, Dec 2009.

[172] V. Murg, F. Verstraete, Ö. Legeza, and R. M. Noack. Simulating strongly correlated quantum systems with tree tensor networks. *Physical Review B*, 82:205105, Nov 2010.

[173] G. Vidal. Entanglement renormalization. *Physical Review Letters*, 99:220405, Nov 2007.

[174] G. Vidal. Efficient simulation of one-dimensional quantum many-body systems. *Physical Review Letters*, 93:040502, Jul 2004.

[175] A. J. Daley, C. Kollath, U. Schollwöck, and G. Vidal. Time-dependent density-matrix renormalization-group using adaptive effective Hilbert spaces. *Journal of Statistical Mechanics: Theory and Experiment*, 2004(04):P04005, 2004.

[176] S. R. White and A. E. Feiguin. Real-time evolution using the density matrix renormalization group. *Physical Review Letters*, 93:076401, Aug 2004.

[177] J. Haegeman, J. I. Cirac, T. J. Osborne, I. Pižorn, H. Verschelde, and F. Verstraete. Time-dependent variational principle for quantum lattices. *Physical Review Letters*, 107:070601, Aug 2011.

[178] R. Hübener, V. Nebendahl, and W. Dür. Concatenated tensor network states. *New Journal of Physics*, 12(2):025004, 2010.

[179] H. N. Phien, J. A. Bengua, H. D. Tuan, P. Corboz, and R. Orús. Infinite projected entangled pair states algorithm improved: Fast full update and gauge fixing. *Physical Review B*, 92:035142, Jul 2015.

[180] F. Verstraete, J. J. García-Ripoll, and J. I. Cirac. Matrix product density operators: Simulation of finite-temperature and dissipative systems. *Physical Review Letters*, 93:207204, Nov 2004.

[181] T. Fukuhara, A. Kantian, M. Endres, M. Cheneau, P. Schausz, S. Hild, D. Bellem, U. Schollwöck, T. Giamarchi, C. Gross, I. Bloch, and S. Kuhr. Quantum dynamics of a mobile spin impurity. *Nature Physics*, 9(4):235–241, apr 2013. 10.1038/nphys2561.

[182] R. Orús and G. Vidal. Simulation of two-dimensional quantum systems on an infinite lattice revisited: Corner transfer matrix for tensor contraction. *Physical Review B*, 80:094403, Sep 2009.

[183] G. M. Crosswhite, A. C. Doherty, and G. Vidal. Applying matrix product operators to model systems with long-range interactions. *Physical Review B*, 78:035116, Jul 2008.

[184] I. P. McCulloch. Infinite size density matrix renormalization group, revisited. *ArXiv e-prints*, April 2008.

[185] R. Orús and G. Vidal. Infinite time-evolving block decimation algorithm beyond unitary evolution. *Physical Review B*, 78:155117, Oct 2008.

[186] Ö. Legeza and G. Fáth. Accuracy of the density-matrix renormalization-group method. *Physical Review B*, 53:14349–14358, Jun 1996.

[187] Ö. Legeza, J. Röder, and B. A. Hess. Controlling the accuracy of the density-matrix renormalization-group method: The dynamical block state selection approach. *Physical Review B*, 67:125114, Mar 2003.

[188] G. K.-L. Chan and M. Head-Gordon. Highly correlated calculations with a polynomial cost algorithm: A study of the density matrix renormalization group. *The Journal of Chemical Physics*, 116(11):4462–4476, 2002.

[189] P. Corboz. Improved energy extrapolation with infinite projected entangled-pair states applied to the two-dimensional hubbard model. *Physical Review B*, 93:045116, Jan 2016.

[190] S. Liang and H. Pang. Approximate diagonalization using the density matrix renormalization-group method: A two-dimensional-systems perspective. *Physical Review B*, 49:9214–9217, Apr 1994.

[191] E.M. Stoudenmire and S. R. White. Studying Two-Dimensional Systems with the Density Matrix Renormalization Group. *Annual Review of Condensed Matter Physics*, 3(1):111–128, 2012.

[192] W. L. McMillan. Ground state of liquid He^4. *Physical Review*, 138:A442–A451, Apr 1965.

[193] M. Peter Nightingale and Cyrus J. Umrigar. *Quantum Monte Carlo methods in physics and chemistry*, volume 525 of *NATO ASI Series C*. Springer Science & Business Media, 1998.

[194] Malvin H. Kalos and Paula A. Whitlock. *Monte Carlo Methods*. Wiley-VCH Verlag GmbH, 2007.

[195] J. Kolorenč and L. Mitas. Applications of quantum Monte Carlo methods in condensed systems. *Reports on Progress in Physics*, 74(2):026502, 2011.

[196] J. R. Trail. Heavy-tailed random error in quantum monte carlo. *Physical Review E*, 77:016703, Jan 2008.

[197] J. R. Trail. Alternative sampling for variational quantum monte carlo. *Physical Review E*, 77:016704, Jan 2008.

[198] J. R. Trail and R. Maezono. Optimum and efficient sampling for variational quantum Monte Carlo. *The Journal of Chemical Physics*, 133(17):174120, 2010.

[199] N. Metropolis, A. W. Rosenbluth, M. N. Rosenbluth, A. H. Teller, and E. Teller. Equation of State Calculations by Fast Computing Machines. *The Journal of Chemical Physics*, 21(6):1087–1092, 1953.

[200] W. K. Hastings. Monte Carlo sampling methods using Markov chains and their applications. *Biometrika*, 57:97–109, 1970.

[201] R. Assaraf and M. Caffarel. Zero-variance zero-bias principle for observables in quantum Monte Carlo: Application to forces. *The Journal of Chemical Physics*, 119(20):10536–10552, 2003.

[202] R. Jastrow. Many-body problem with strong forces. *Physical Review*, 98:1479–1484, Jun 1955.

[203] N. D. Drummond, P. López Ríos, A. Ma, J. R. Trail, G. G. Spink, M. D. Towler, and R. J. Needs. Quantum Monte Carlo study of the Ne atom and the Ne^+ ion. *The Journal of Chemical Physics*, 124(22):224104, 2006.

[204] C. J. Umrigar, K. G. Wilson, and J. W. Wilkins. Optimized trial wave functions for quantum monte carlo calculations. *Physical Review Letters*, 60:1719–1722, Apr 1988.

[205] C. J. Umrigar and C. Filippi. Energy and variance optimization of many-body wave functions. *Physical Review Letters*, 94:150201, Apr 2005.

[206] P. R. C. Kent, R. J. Needs, and G. Rajagopal. Monte carlo energy and variance-minimization techniques for optimizing many-body wave functions. *Physical Review B*, 59:12344–12351, May 1999.

[207] C. Filippi and C. J. Umrigar. Multiconfiguration wave functions for quantum Monte Carlo calculations of first-row diatomic molecules. *The Journal of Chemical Physics*, 105(1):213–226, 1996.

[208] E. Neuscamman, C. J. Umrigar, and G. K.-L. Chan. Optimizing large parameter sets in variational quantum monte carlo. *Physical Review B*, 85:045103, Jan 2012.

[209] S. Sorella. Green function monte carlo with stochastic reconfiguration. *Physical Review Letters*, 80:4558–4561, May 1998.

[210] S. Sorella and L. Capriotti. Green function monte carlo with stochastic reconfiguration: An effective remedy for the sign problem. *Physical Review B*, 61:2599–2612, Jan 2000.

[211] S. Sorella. Generalized lanczos algorithm for variational quantum monte carlo. *Physical Review B*, 64:024512, Jun 2001.

[212] M. Casula, C. Attaccalite, and S. Sorella. Correlated geminal wave function for molecules: An efficient resonating valence bond approach. *The Journal of Chemical Physics*, 121(15):7110–7126, 2004.

[213] S. Sorella, M. Casula, and D. Rocca. Weak binding between two aromatic rings: Feeling the van der Waals attraction by quantum Monte Carlo methods. *The Journal of Chemical Physics*, 127(1):014105, 2007.

[214] M. P. Nightingale and V. Melik-Alaverdian. Optimization of ground- and excited-state wave functions and van der waals clusters. *Physical Review Letters*, 87:043401, Jul 2001.

[215] J. Toulouse and C. J. Umrigar. Optimization of quantum Monte Carlo wave functions by energy minimization. *The Journal of Chemical Physics*, 126(8):084102, 2007.

[216] J. Toulouse and C. J. Umrigar. Full optimization of Jastrow–Slater wave functions with application to the first-row atoms and homonuclear diatomic molecules. *The Journal of Chemical Physics*, 128(17):174101, 2008.

[217] C. J. Umrigar, J. Toulouse, C. Filippi, S. Sorella, and R. G. Hennig. Alleviation of the fermion-sign problem by optimization of many-body wave functions. *Physical Review Letters*, 98:110201, Mar 2007.

[218] J. B. Anderson. Quantum chemistry by random walk. H ^2P, H_3^+ D_{3h} $^1A_1'$, H_2 $^3\Sigma_u^+$, H_4 $^1\Sigma_g^+$, Be ^1S. *The Journal of Chemical Physics*, 65(10):4121–4127, 1976.

[219] R.C. Grimm and R.G. Storer. Monte-Carlo solution of Schrödinger's equation. *Journal of Computational Physics*, 7(1):134–156, 1971.

[220] D. M. Ceperley and B. J. Alder. Ground state of the electron gas by a stochastic method. *Physical Review Letters*, 45:566–569, Aug 1980.

[221] P. J. Reynolds, D. M. Ceperley, B. J. Alder, and William A. L. Jr. Fixed-node quantum Monte Carlo for moleculesa) b). *The Journal of Chemical Physics*, 77(11):5593–5603, 1982.

[222] C. J. Umrigar, M. P. Nightingale, and K. J. Runge. A diffusion Monte Carlo algorithm with very small time-step errors. *The Journal of Chemical Physics*, 99(4):2865–2890, 1993.

[223] M. H. Kalos. Monte carlo calculations of the ground state of three- and four-body nuclei. *Physical Review*, 128:1791–1795, Nov 1962.

[224] M. H. Kalos, D. Levesque, and L. Verlet. Helium at zero temperature with hard-sphere and other forces. *Physical Review A*, 9:2178–2195, May 1974.

[225] Kurt Binder. Monte carlo methods in statistical physics (topics in current physics 7), 1979.

[226] D. Cleland, G. H. Booth, and A. Alavi. Communications: Survival of the fittest: Accelerating convergence in full configuration-interaction quantum Monte Carlo. *The Journal of Chemical Physics*, 132(4):041103, 2010.

[227] S. Zhang and H. Krakauer. Quantum monte carlo method using phase-free random walks with slater determinants. *Physical Review Letters*, 90:136401, Apr 2003.

[228] M. Suzuki. Relationship between d-Dimensional Quantal Spin Systems and (d+1)-Dimensional Ising Systems: Equivalence, Critical Exponents and Systematic Approximants of the Partition Function and Spin Correlations. *Progress of Theoretical Physics*, 56(5):1454–1469, 1976.

[229] J. Hubbard. Calculation of partition functions. *Physical Review Letters*, 3:77–78, Jul 1959.

[230] G. Sugiyama and S.E. Koonin. Auxiliary field Monte-Carlo for quantum many-body ground states. *Annals of Physics*, 168(1):1–26, 1986.

[231] W. A. Al-Saidi, S. Zhang, and H. Krakauer. Auxiliary-field quantum Monte Carlo calculations of molecular systems with a Gaussian basis. *The Journal of Chemical Physics*, 124(22):224101, 2006.

[232] M. H. Kolodrubetz, J. S. Spencer, B. K. Clark, and W. M.C. Foulkes. The effect of quantization on the full configuration interaction quantum Monte Carlo sign problem. *The Journal of Chemical Physics*, 138(2):024110, 2013.

[233] K. E. Schmidt and M. H. Kalos. *Few- and Many-Fermion Problems*, page 125–143. Springer Berlin Heidelberg, Berlin, Heidelberg, 1987.

[234] D. F. B. ten Haaf, H. J. M. van Bemmel, J. M. J. van Leeuwen, W. van Saarloos, and D. M. Ceperley. Proof for an upper bound in fixed-node monte carlo for lattice fermions. *Physical Review B*, 51:13039–13045, May 1995.

[235] Y. Kwon, D. M. Ceperley, and R. M. Martin. Effects of three-body and backflow correlations in the two-dimensional electron gas. *Physical Review B*, 48:12037–12046, Oct 1993.

[236] P. López Ríos, A. Ma, N. D. Drummond, M. D. Towler, and R. J. Needs. Inhomogeneous backflow transformations in quantum monte carlo calculations. *Physical Review E*, 74:066701, Dec 2006.

[237] D. M. Ceperley and B. J. Alder. Quantum Monte Carlo for molecules: Green's function and nodal release. *The Journal of Chemical Physics*, 81(12):5833–5844, 1984.

[238] Z. Bačić, M. Kennedy-Mandziuk, J. W. Moskowitz, and K. E. Schmidt. He_2Cl_2 and He_3Cl_2 van der Waals clusters: A quantum Monte Carlo study. *The Journal of Chemical Physics*, 97(9):6472–6480, 1992.

[239] P. Seth, P. López Ríos, and R. J. Needs. Quantum Monte Carlo study of the first-row atoms and ions. *The Journal of Chemical Physics*, 134(8):084105, 2011.

[240] G. H. Booth. *A novel Quantum Monte Carlo method for molecular systems.* Phd thesis, University of Cambridge, 2010.

[241] G. H. Booth and A. Alavi. Approaching chemical accuracy using full configuration-interaction quantum Monte Carlo: A study of ionization potentials. *The Journal of Chemical Physics*, 132(17):174104, 2010.

[242] G. H. Booth, D. Cleland, A. J. W. Thom, and A. Alavi. Breaking the carbon dimer: The challenges of multiple bond dissociation with full configuration interaction quantum Monte Carlo methods. *The Journal of Chemical Physics*, 135(8):084104, 2011.

[243] D. M. Cleland, G. H. Booth, and A. Alavi. A study of electron affinities using the initiator approach to full configuration interaction quantum Monte Carlo. *The Journal of Chemical Physics*, 134(2):024112, 2011.

[244] R. E. Thomas, G. H. Booth, and A. Alavi. Accurate *Ab Initio* calculation of ionization potentials of the first-row transition metals with the configuration-interaction quantum monte carlo technique. *Physical Review Letters*, 114:033001, Jan 2015.

[245] J. J. Shepherd, G. H. Booth, and A. Alavi. Investigation of the full configuration interaction quantum Monte Carlo method using homogeneous electron gas models. *The Journal of Chemical Physics*, 136(24):244101, 2012.

[246] J. J. Shepherd, G. E. Scuseria, and J. S. Spencer. Sign problem in full configuration interaction quantum monte carlo: Linear and sublinear representation regimes for the exact wave function. *Physical Review B*, 90:155130, Oct 2014.

[247] Booth G. H., Grüneis A., Kresse G., and Alavi A. Towards an exact description of electronic wavefunctions in real solids. *Nature*, 493(7432):365–370, jan 2013. 10.1038/nature11770.

[248] N. S. Blunt, A. Alavi, and G. H. Booth. Krylov-projected quantum monte carlo method. *Physical Review Letters*, 115:050603, Jul 2015.

[249] N. S. Blunt, S. D. Smart, G. H. Booth, and A. Alavi. An excited-state approach within full configuration interaction quantum Monte Carlo. *The Journal of Chemical Physics*, 143(13):134117, 2015.

[250] G. H. Booth and G. K.-L. Chan. Communication: Excited states, dynamic correlation functions and spectral properties from full configuration interaction quantum Monte Carlo. *The Journal of Chemical Physics*, 137(19):191102, 2012.

[251] S. Ten-no. Stochastic determination of effective Hamiltonian for the full configuration interaction solution of quasi-degenerate electronic states. *The Journal of Chemical Physics*, 138(16):164126, 2013.

[252] A. Humeniuk and R. Mitrić. Excited states from quantum Monte Carlo in the basis of Slater determinants. *The Journal of Chemical Physics*, 141(19):194104, 2014.

[253] C. Overy, G. H. Booth, N. S. Blunt, J. J. Shepherd, D. Cleland, and A. Alavi. Unbiased reduced density matrices and electronic properties from full configuration interaction quantum Monte Carlo. *The Journal of Chemical Physics*, 141(24):244117, 2014.

[254] R. E. Thomas, D. Opalka, C. Overy, P. J. Knowles, A. Alavi, and G. H. Booth. Analytic nuclear forces and molecular properties from full configuration interaction quantum Monte Carlo. *The Journal of Chemical Physics*, 143(5):054108, 2015.

[255] R. E. Thomas, Q. Sun, A. Alavi, and G. H. Booth. Stochastic Multiconfigurational Self-Consistent Field Theory. *Journal of Chemical Theory and Computation*, 11(11):5316–5325, 2015.

[256] G. Li Manni, S. D. Smart, and A. Alavi. Combining the Complete Active Space Self-Consistent Field Method and the Full Configuration Interaction Quantum Monte Carlo within a Super-CI Framework, with Application to Challenging Metal-Porphyrins. *Journal of Chemical Theory and Computation*, 12(3):1245–1258, 2016. PMID: 26808894.

[257] G. H. Booth, D. Cleland, A. Alavi, and D. P. Tew. An explicitly correlated approach to basis set incompleteness in full configuration interaction quantum Monte Carlo. *The Journal of Chemical Physics*, 137(16):164112, 2012.

[258] J. A. F. Kersten, G. H. Booth, and A. Alavi. Assessment of multireference approaches to explicitly correlated full configuration interaction quantum Monte Carlo. *The Journal of Chemical Physics*, 145(5):054117, 2016.

[259] A. J. W. Thom. Stochastic coupled cluster theory. *Physical Review Letters*, 105:263004, Dec 2010.

[260] N. S. Blunt, T. W. Rogers, J. S. Spencer, and W. M. C. Foulkes. Density-matrix quantum monte carlo method. *Physical Review B*, 89:245124, Jun 2014.

[261] G. H. Booth, S. D. Smart, and A. Alavi. Linear-scaling and parallelisable algorithms for stochastic quantum chemistry. *Molecular Physics*, 112(14):1855–1869, 2014.

[262] G. H. Booth, S. D. Smart, and A. Alavi. (unpublished).

[263] A. A. Holmes, H. J. Changlani, and C. J. Umrigar. Efficient Heat-Bath Sampling in Fock Space. *Journal of Chemical Theory and Computation*, 12(4):1561–1571, 2016. PMID: 26959242.

[264] F. R. Petruzielo, A. A. Holmes, Hitesh J. Changlani, M. P. Nightingale, and C. J. Umrigar. Semistochastic projector monte carlo method. *Physical Review Letters*, 109:230201, Dec 2012.

[265] T. H. Dunning Jr. Gaussian basis sets for use in correlated molecular calculations. I. The atoms boron through neon and hydrogen. *The Journal of Chemical Physics*, 90(2):1007–1023, 1989.

[266] J. S. Spencer, N. S. Blunt, and W. M.C. Foulkes. The sign problem and population dynamics in the full configuration interaction quantum Monte Carlo method. *The Journal of Chemical Physics*, 136(5):054110, 2012.

[267] D. Cleland. *The initiator full configuration interaction quantum monte car lo method: development and applications to molecular systems.* Phd thesis, University of Cambridge, 2012.

[268] H. Flyvbjerg and H. G. Petersen. Error estimates on averages of correlated data. *The Journal of Chemical Physics*, 91(1):461–466, 1989.

[269] C. Overy. *Reduced Density Matrices and Stochastic Quantum Monte Carlo.* Phd thesis, University of Cambridge, 2014.

[270] P.J. Knowles and N.C. Handy. A new determinant-based full configuration interaction method. *Chemical Physics Letters*, 111(4–5):315–321, 1984.

[271] E. R. Davidson. Properties and uses of natural orbitals. *Reviews of Modern Physics*, 44:451–464, Jul 1972.

[272] C. W. Bauschlicher and P. R. Taylor. Atomic natural orbital basis sets for transition metals. *Theoretica chimica acta*, 86(1):13–24, 1993.

[273] C. W. Bauschlicher, S. R. Langhoff, and P. R. Taylor. *Accurate Quantum Chemical Calculations*, page 103–161. John Wiley & Sons, Inc., 2007.

[274] J. Almlöf and P. R. Taylor. General contraction of Gaussian basis sets. II. Atomic natural orbitals and the calculation of atomic and molecular properties. *The Journal of Chemical Physics*, 92(1):551–560, 1990.

[275] R. E. Thomas, C. Overy, G. H. Booth, and A. Alavi. Symmetry Breaking and Broken Ergodicity in Full Configuration Interaction Quantum Monte Carlo. *Journal of Chemical Theory and Computation*, 10(5):1915–1922, 2014. PMID: 26580521.

[276] Daniel I. Khomskii. *Transition Metal Compounds*. Cambridge University Press, 2014.

[277] G. Kotliar and D. Vollhardt. Strongly Correlated Materials: Insights From Dynamical Mean-Field Theory. *Physics Today*, 57(3):53–59, March 2004.

[278] V. J. Emery. Theory of high-$\mathrm{t_c}$ superconductivity in oxides. *Physical Review Letters*, 58:2794–2797, Jun 1987.

[279] O.K. Andersen, A.I. Liechtenstein, O. Jepsen, and F. Paulsen. LDA energy bands, low-energy hamiltonians, t', t”, $t_\perp(k)$, and $J_\perp$. *Journal of Physics and Chemistry of Solids*, 56(12):1573–1591, 1995. Proceedings of the Conference on Spectroscopies in Novel Superconductors.

[280] L. F. Mattheiss. Electronic band properties and superconductivity in $\mathrm{La_{2-y}X_yCuO_4}$. *Physical Review Letters*, 58:1028–1030, Mar 1987.

[281] M.B. Zölfl, Th. Maier, Th. Pruschke, and J. Keller. Electronic properties of $\mathrm{CuO_2}$ -planes: A DMFT study. *The European Physical Journal B - Condensed Matter and Complex Systems*, 13(1):47–53, 2000.

[282] X. Wang, L. de' Medici, and A. J. Millis. Role of oxygen-oxygen hopping in the three-band copper-oxide model: Quasiparticle weight, metal insulator and magnetic phase boundaries, gap values, and optical conductivity. *Physical Review B*, 83:094501, Mar 2011.

[283] M. S. Hybertsen, E. B. Stechel, M. Schluter, and D. R. Jennison. Renormalization from density-functional theory to strong-coupling models for electronic states in $\mathrm{Cu-O}$ materials. *Physical Review B*, 41:11068–11072, Jun 1990.

[284] J. Zaanen, G. A. Sawatzky, and J. W. Allen. Band gaps and electronic structure of transition-metal compounds. *Physical Review Letters*, 55:418–421, Jul 1985.

[285] D. Khomskii. Unusual valence, negative charge-transfer gaps and self-doping in transition-metal compounds. *eprint arXiv:cond-mat/0101164*, January 2001.

[286] A. E. Bocquet, T. Mizokawa, T. Saitoh, H. Namatame, and A. Fujimori. Electronic structure of $3d$-transition-metal compounds by analysis of the $2p$ core-level photoemission spectra. *Physical Review B*, 46:3771–3784, Aug 1992.

[287] C. Weber, K. Haule, and G. Kotliar. Strength of correlations in electron- and hole-doped cuprates. *Nature Physics*, 6(8):574–578, aug 2010. 10.1038/nphys1706.

[288] M. A. Korotin, V. I. Anisimov, D. I. Khomskii, and G. A. Sawatzky. $\mathrm{CrO_2}$. *Physical Review Letters*, 80:4305–4308, May 1998.

[289] M. Takano, J. Kawachi, N. Nakanishi, and Y. Takeda. Valence state of the Fe ions in $\mathrm{Sr_{1-y}La_yFeO_3}$. *Journal of Solid State Chemistry*, 39(1):75–84, 1981.

[290] C. Weber, A. Läuchli, F. Mila, and T. Giamarchi. Orbital currents in extended hubbard models of high-T_c cuprate superconductors. *Physical Review Letters*, 102:017005, Jan 2009.

[291] C. Weber, K. Haule, and G. Kotliar. Apical oxygens and correlation strength in electron- and hole-doped copper oxides. *Physical Review B*, 82:125107, Sep 2010.

[292] F. C. Zhang and T. M. Rice. Effective hamiltonian for the superconducting Cu oxides. *Physical Review B*, 37:3759–3761, Mar 1988.

[293] C. Weber, K. Haule, and G. Kotliar. Optical weights and waterfalls in doped charge-transfer insulators: A local density approximation and dynamical mean-field theory study of $\mathrm{La}_{2-x}\mathrm{Sr}_x\mathrm{CuO}_4$. *Physical Review B*, 78:134519, Oct 2008.

[294] V. J. Emery and G. Reiter. Mechanism for high-temperature superconductivity. *Physical Review B*, 38:4547–4556, Sep 1988.

[295] J. Oitmaa and D. D. Betts. The ground state of two quantum models of magnetism. *Canadian Journal of Physics*, 56(7):897–901, 1978.

[296] D. D. Betts, H. Q. Lin, and J. S. Flynn. Improved finite-lattice estimates of the properties of two quantum spin models on the infinite square lattice. *Canadian Journal of Physics*, 77:353–369, May 1999.

[297] P. R. C. Kent, M. Jarrell, T. A. Maier, and Th. Pruschke. Efficient calculation of the antiferromagnetic phase diagram of the three-dimensional hubbard model. *Physical Review B*, 72:060411, Aug 2005.

[298] P. Lykos and G. W. Pratt. Discussion on the hartree-fock approximation. *Reviews of Modern Physics*, 35:496–501, Jul 1963.

[299] Hank Childs, Eric Brugger, Brad Whitlock, Jeremy Meredith, Sean Ahern, David Pugmire, Kathleen Biagas, Mark Miller, Cyrus Harrison, Gunther H. Weber, Hari Krishnan, Thomas Fogal, Allen Sanderson, Christoph Garth, E. Wes Bethel, David Camp, Oliver Rübel, Marc Durant, Jean M. Favre, and Paul Navrátil. VisIt: An End-User Tool For Visualizing and Analyzing Very Large Data. In *High Performance Visualization–Enabling Extreme-Scale Scientific Insight*, pages 357–372. Oct 2012.

[300] R. T. Scalettar, D. J. Scalapino, R. L. Sugar, and S. R. White. Antiferromagnetic, charge-transfer, and pairing correlations in the three-band hubbard model. *Physical Review B*, 44:770–781, Jul 1991.

[301] J. Dutka and A. M. Oleś. Antiferromagnetism in three-band hubbard model: Local-ansatz approach. *Physical Review B*, 43:5622–5633, Mar 1991.

[302] C. Weber, T. Giamarchi, and C. M. Varma. Phase diagram of a three-orbital model for high-T_c cuprate superconductors. *Physical Review Letters*, 112:117001, Mar 2014.

[303] M. Sugihara, M. A. Ikeda, and P. Entel. Electronic structure, fermi surface, and antiferromagnetism of high-T_c cuprate materials and their doping dependence. *Physical Review B*, 57:11760–11768, May 1998.

[304] M. Sugihara, M. A. Ikeda, and P. Entel. Antiferromagnetism and electronic structure of high-T_c cuprate. *J Korean Phys. Soc. Suppl.*, 32:s11–S16, February 1998.

[305] I. W. Bulik, W. Chen, and G. E. Scuseria. Electron correlation in solids via density embedding theory. *The Journal of Chemical Physics*, 141(5):054113, 2014.

[306] P. Gersdorf, W. John, J. P. Perdew, and P. Ziesche. Correlation entropy of the H_2 molecule. *International Journal of Quantum Chemistry*, 61(6):935–941, 1997.

[307] K. Boguslawski, P. Tecmer, P. W. Ayers, P. Bultinck, S. De Baerdemacker, and D. Van Neck. Efficient description of strongly correlated electrons with mean-field cost. *Physical Review B*, 89:201106, May 2014.

[308] T. Stein, T. M. Henderson, and G. E. Scuseria. Seniority zero pair coupled cluster doubles theory. *The Journal of Chemical Physics*, 140(21):214113, 2014.

[309] N. D. Drummond, R. J. Needs, A. Sorouri, and W. M. C. Foulkes. Finite-size errors in continuum quantum monte carlo calculations. *Physical Review B*, 78:125106, Sep 2008.

[310] S. Azadi and W. M. C. Foulkes. Systematic study of finite-size effects in quantum Monte Carlo calculations of real metallic systems. *The Journal of Chemical Physics*, 143(10):102807, 2015.

[311] M. Holzmann, R. C. Clay, M. A. Morales, N. M. Tubman, D. M. Ceperley, and C. Pierleoni. Theory of finite size effects for electronic quantum monte carlo calculations of liquids and solids. *Physical Review B*, 94:035126, Jul 2016.

[312] M. Casula, C. Filippi, and S. Sorella. Diffusion monte carlo method with lattice regularization. *Physical Review Letters*, 95:100201, Sep 2005.

[313] A. Harju, B. Barbiellini, S. Siljamäki, R. M. Nieminen, and G. Ortiz. Stochastic gradient approximation: An efficient method to optimize many-body wave functions. *Physical Review Letters*, 79:1173–1177, Aug 1997.

[314] A. Harju. Stochastic gradient approximation method applied to Hubbard model. *eprint arXiv:cond-mat/0101465*, January 2001.

[315] S. Bubeck. Convex Optimization: Algorithms and Complexity. *ArXiv e-prints*, May 2014.

[316] Sebastian R. An overview of gradient descent optimization algorithms. *Computing Research Repository*, abs/1609.04747, 2016.

[317] Y. N. Dauphin, R. Pascanu, C. Gulcehre, K. Cho, S. Ganguli, and Y. Bengio. Identifying and attacking the saddle point problem in high-dimensional non-convex optimization. In *Proceedings of the 27th International Conference on Neural Information Processing Systems*, NIPS'14, pages 2933–2941, Cambridge, MA, USA, 2014. MIT Press.

[318] H. Robbins and S. Monro. A stochastic approximation method. *The Annals of Mathematical Statistics*, 22(3):400–407, 09 1951.

[319] R. M. Lee, G. J. Conduit, N. Nemec, P. López Ríos, and N. D. Drummond. Strategies for improving the efficiency of quantum monte carlo calculations. *Physical Review E*, 83:066706, Jun 2011.

[320] Ian Goodfellow, Yoshua Bengio, and Aaron Courville. *Deep Learning.* MIT Press, 2016. http://www.deeplearningbook.org.

[321] Michael A. Nielsen. *Neural Networks and Deep Learning.* Determination Press, 2015. http://neuralnetworksanddeeplearning.com.

[322] V. Dunjko, J. M. Taylor, and H. J. Briegel. Quantum-enhanced machine learning. *Physical Review Letters*, 117:130501, Sep 2016.

[323] R. A. Jacobs. Increased rates of convergence through learning rate adaptation. *Neural Networks*, 1(4):295–307, 1988.

[324] D. R. Wilson and T. R. Martinez. The need for small learning rates on large problems. In *Neural Networks, 2001. Proceedings. IJCNN '01. International Joint Conference on*, volume 1, pages 115–119 vol.1, 2001.

[325] R. S. Sutton. Two problems with backpropagation and other steepest-descent learning procedures for networks. In *Proceedings of the Eighth Annual Conference of the Cognitive Science Society*, 1986.

[326] N. Qian. On the momentum term in gradient descent learning algorithms. *Neural Networks*, 12(1):145–151, 1999.

[327] Y. Nesterov. A method of solving a convex programming problem with convergence rate $\mathcal{O}(1/k^2)$. In *Soviet Mathematics Doklady*, volume 27, pages 372–376, 1983.

[328] A. Beck and M. Teboulle. A Fast Iterative Shrinkage-Thresholding Algorithm for Linear Inverse Problems. *SIAM Journal on Imaging Sciences*, 2(1):183–202, 2009.

[329] Ilya Sutskever. *Training recurrent neural networks.* PhD thesis, University of Toronto, 2013.

[330] http://www.cs.toronto.edu/~tijmen/csc321/slides/lecture_slides_lec6.pdf. (Retrieved: 16.3.2017).

[331] I. Sutskever, J. Martens, G. Dahl, and G. Hinton. On the importance of initialization and momentum in deep learning. In *Proceedings of the 30th International Conference on International Conference on Machine Learning - Volume 28*, ICML'13, pages III–1139–III–1147. JMLR.org, 2013.

[332] A. Beck and M. Teboulle. Fast gradient-based algorithms for constrained total variation image denoising and deblurring problems. *IEEE Transactions on Image Processing*, 18(11):2419–2434, Nov 2009.

[333] W. Su, S. Boyd, and E. Candès. A Differential Equation for Modeling Nesterov's Accelerated Gradient Method: Theory and Insights. In Z. Ghahramani, M. Welling, C. Cortes, N. D. Lawrence, and K. Q. Weinberger, editors, *Advances in Neural Information Processing Systems 27*, page 2510–2518. Curran Associates, Inc., 2014.

[334] B. O'Donoghue and E. Candès. Adaptive Restart for Accelerated Gradient Schemes. *Foundations of Computational Mathematics*, 15(3):715–732, 2015.

[335] Yousef Saad. *Numerical methods for large eigenvalue problems.* Society for Industrial and Applied Mathematics, Philadelphia, rev. ed edition, 2011.

[336] Carl (Carl Dean) Meyer. *Matrix Analysis and Applied Linear Algebra [electronic resource].* Society for Industrial and Applied Mathematics, Philadelphia, 2000.

[337] Lloyd N. (Lloyd Nicholas) Trefethen. *Numerical linear algebra.* Society for Industrial and Applied Mathematics, Philadelphia, 1997.

[338] D. Scieur, A. d'Aspremont, and F. Bach. Regularized Nonlinear Acceleration. *ArXiv e-prints*, June 2016.

[339] Jane K. Cullum and Ralph A. Willoughby. *Lanczos Algorithms for Large Symmetric Eigenvalue Computations Vol II.* Birkhäuser Basel, 1985.

[340] T. Zhang and F. A. Evangelista. A Deterministic Projector Configuration Interaction Approach for the Ground State of Quantum Many-Body Systems. *Journal of Chemical Theory and Computation*, 12(9):4326–4337, 2016. PMID: 27464301.

[341] J. Duchi, E. Hazan, and Y. Singer. Adaptive subgradient methods for online learning and stochastic optimization. *The Journal of Machine Learning Research*, 12:2121–2159, July 2011.

[342] M. D. Zeiler. ADADELTA: an adaptive learning rate method. *Computing Research Repository*, abs/1212.5701, 2012.

[343] Y. N. Dauphin, H. de Vries, J. Chung, and Y. Bengio. Rmsprop and equilibrated adaptive learning rates for non-convex optimization. *Computing Research Repository*, abs/1502.04390, 2015.

[344] D. P. Kingma and J. Ba. Adam: A method for stochastic optimization. *Computing Research Repository*, abs/1412.6980, 2014.

[345] L. K. Wagner. Types of single particle symmetry breaking in transition metal oxides due to electron correlation. *The Journal of Chemical Physics*, 138(9):094106, 2013.

[346] Ken F. Riley, Michael P. Hobson, and Stephen J. Bence. *Mathematical Methods for Physics and Engineering: A Comprehensive Guide*. Cambridge University Press, 3 edition, 2006.

[347] J. Toulouse, R. Assaraf, and C. J. Umrigar. Introduction to the variational and diffusion Monte Carlo methods. *ArXiv e-prints*, August 2015.

[348] S. Sorella. Wave function optimization in the variational monte carlo method. *Physical Review B*, 71:241103, Jun 2005.

[349] L. Zhao and E. Neuscamman. A Blocked Linear Method for Optimizing Large Parameter Sets in Variational Monte Carlo. *Journal of Chemical Theory and Computation*, 13(6):2604–2611, 2017. PMID: 28514597.

[350] L. Zhao and E. Neuscamman. An Efficient Variational Principle for the Direct Optimization of Excited States. *Journal of Chemical Theory and Computation*, 12(8):3436–3440, 2016. PMID: 27379468.

[351] H. J. Changlani, J. M. Kinder, C. J. Umrigar, and G. K.-L. Chan. Approximating strongly correlated wave functions with correlator product states. *Physical Review B*, 80:245116, Dec 2009.

[352] E. Neuscamman, H. Changlani, J. Kinder, and G. K.-L. Chan. Nonstochastic algorithms for Jastrow-Slater and correlator product state wave functions. *Physical Review B*, 84:205132, Nov 2011.

[353] E. Neuscamman and G. K.-L. Chan. Correlator product state study of molecular magnetism in the giant Keplerate $Mo_{72}Fe_{30}$. *Physical Review B*, 86:064402, Aug 2012.

[354] M. P. Nightingale and H. W. J. Blöte. Gap of the linear spin-1 Heisenberg antiferromagnet: A Monte Carlo calculation. *Physical Review B*, 33:659–661, Jan 1986.

[355] D. A. Huse and V. Elser. Simple variational wave functions for two-dimensional Heisenberg Spin-½ antiferromagnets. *Physical Review Letters*, 60:2531–2534, Jun 1988.

[356] A. Gendiar and T. Nishino. Latent heat calculation of the three-dimensional $q = 3$, 4, and 5 potts models by the tensor product variational approach. *Physical Review E*, 65:046702, Apr 2002.

[357] F. Mezzacapo, N. Schuch, M. Boninsegni, and J. I. Cirac. Ground-state properties of quantum many-body systems: entangled-plaquette states and variational Monte Carlo. *New Journal of Physics*, 11(8):083026, 2009.

[358] F. Mezzacapo and J. I. Cirac. Ground-state properties of the spin-$\frac{1}{2}$ antiferromagnetic Heisenberg model on the triangular lattice: a variational study based on entangled-plaquette states. *New Journal of Physics*, 12(10):103039, 2010.

[359] F. Mezzacapo. Variational study of a mobile hole in a two-dimensional quantum antiferromagnet using entangled-plaquette states. *Physical Review B*, 83:115111, Mar 2011.

[360] K. H. Marti, B. Bauer, M. Reiher, M. Troyer, and F. Verstraete. Complete-graph tensor network states: a new fermionic wave function ansatz for molecules. *New Journal of Physics*, 12(10):103008, 2010.

[361] A. Kovyrshin and M. Reiher. Tensor network states with three-site correlators. *New Journal of Physics*, 18(11):113001, 2016.

[362] K. H. Marti and M. Reiher. New electron correlation theories for transition metal chemistry. *Physical Chemistry Chemical Physics*, 13:6750–6759, 2011.

[363] V. Stojevic, P. Crowley, T. Đurić, C. Grey, and A. G. Green. Time evolution and deterministic optimization of correlator product states. *Physical Review B*, 94:165135, Oct 2016.

[364] S. Al-Assam, S. R. Clark, C. J. Foot, and D. Jaksch. Capturing long range correlations in two-dimensional quantum lattice systems using correlator product states. *Physical Review B*, 84:205108, Nov 2011.

[365] Eric Neuscamman. *Modeling electron correlation in quantum chemistry.* Dissertation for the degree of doctor of philosophy, Cornell University, 2011.

[366] A. J. Coleman. Structure of Fermion Density Matrices. II. Antisymmetrized Geminal Powers. *Journal of Mathematical Physics*, 6(9):1425–1431, 1965.

[367] M. Bajdich, L. Mitas, G. Drobný, L. K. Wagner, and K. E. Schmidt. Pfaffian pairing wave functions in electronic-structure quantum monte carlo simulations. *Physical Review Letters*, 96:130201, Apr 2006.

[368] M. Bajdich, L. Mitas, L. K. Wagner, and K. E. Schmidt. Pfaffian pairing and backflow wavefunctions for electronic structure quantum monte carlo methods. *Physical Review B*, 77:115112, Mar 2008.

[369] S. M. Bhattacharjee. Exact matrix representation of the RVB wavefunction. *Zeitschrift für Physik B Condensed Matter*, 82(3):323–324, 1991.

[370] J. P. F. LeBlanc, A. E. Antipov, F. Becca, I. W. Bulik, G. K.-L. Chan, C.-M. Chung, Y. Deng, M. Ferrero, T. M. Henderson, C. A. Jiménez-Hoyos, E. Kozik, X.-W. Liu, A. J. Millis, N. V. Prokof'ev, M. Qin, G. E. Scuseria, H. Shi, B. V. Svistunov, L. F. Tocchio, I. S. Tupitsyn, S. R. White, S. Zhang, B.-X. Zheng, Z. Zhu, and E. Gull. Solutions of the two-dimensional hubbard model: Benchmarks and results from a wide range of numerical algorithms. *Physical Review X*, 5:041041, Dec 2015.

[371] W. J. Hehre, R. F. Stewart, and J. A. Pople. Self-Consistent Molecular-Orbital Methods. I. Use of Gaussian Expansions of Slater-Type Atomic Orbitals. *The Journal of Chemical Physics*, 51(6):2657–2664, 1969.

[372] J. Hachmann, W. Cardoen, and G. K.-L. Chan. Multireference correlation in long molecules with the quadratic scaling density matrix renormalization group. *The Journal of Chemical Physics*, 125(14):144101, 2006.

[373] T. Tsuchimochi and G. E. Scuseria. Strong correlations via constrained-pairing mean-field theory. *The Journal of Chemical Physics*, 131(12):121102, 2009.

[374] N. Lin, C. A. Marianetti, A. J. Millis, and D. R. Reichman. Dynamical mean-field theory for quantum chemistry. *Physical Review Letters*, 106:096402, Mar 2011.

[375] K. Boguslawski and P. W. Ayers. Linearized Coupled Cluster Correction on the Antisymmetric Product of 1-Reference Orbital Geminals. *Journal of Chemical Theory and Computation*, 11(11):5252–5261, 2015. PMID: 26574319.

[376] T. Nguyen Lan, A. A. Kananenka, and D. Zgid. Rigorous Ab Initio Quantum Embedding for Quantum Chemistry Using Green's Function Theory: Screened Interaction, Nonlocal Self-Energy Relaxation, Orbital Basis, and Chemical Accuracy. *Journal of Chemical Theory and Computation*, 12(10):4856–4870, 2016. PMID: 27585293.

[377] G. H. Booth, T. Tsatsoulis, G. K.-L. Chan, and A. Grüneis. From plane waves to local Gaussians for the simulation of correlated periodic systems. *The Journal of Chemical Physics*, 145(8):084111, 2016.

[378] P. Corboz, T. M. Rice, and M. Troyer. Competing states in the t-j model: Uniform d-wave state versus stripe state. *Physical Review Letters*, 113:046402, Jul 2014.

[379] P. Nataf, M. Lajkó, P. Corboz, A. M. Läuchli, K. Penc, and F. Mila. Plaquette order in the su(6) heisenberg model on the honeycomb lattice. *Physical Review B*, 93:201113, May 2016.

[380] P. Corboz. Variational optimization with infinite projected entangled-pair states. *Physical Review B*, 94:035133, Jul 2016.

[381] L. Vanderstraeten, J. Haegeman, P. Corboz, and F. Verstraete. Gradient methods for variational optimization of projected entangled-pair states. *Physical Review B*, 94:155123, Oct 2016.

[382] A. W. Sandvik and G. Vidal. Variational quantum monte carlo simulations with tensor-network states. *Physical Review Letters*, 99:220602, Nov 2007.

[383] N. Schuch, M. M. Wolf, F. Verstraete, and J. I. Cirac. Simulation of quantum many-body systems with strings of operators and monte carlo tensor contractions. *Physical Review Letters*, 100:040501, Jan 2008.

[384] L. Wang, I. Pižorn, and F. Verstraete. Monte carlo simulation with tensor network states. *Physical Review B*, 83:134421, Apr 2011.

[385] D. M. Ceperley and M. Dewing. The penalty method for random walks with uncertain energies. *The Journal of Chemical Physics*, 110(20):9812–9820, 1999.

[386] Arjun K. Gupta and Dattatraya Govind Kabe. *Theory of sample surveys.* World Scientific, 2011.

[387] M. Qin, H. Shi, and S. Zhang. Benchmark study of the two-dimensional hubbard model with auxiliary-field quantum monte carlo method. *Physical Review B*, 94:085103, Aug 2016.

[388] G. Carleo and M. Troyer. Solving the quantum many-body problem with artificial neural networks. *Science*, 355(6325):602–606, 2017.